Development of an Inverted Ring Imaging Cherenkov Micromegas

Maximilian Paul Rinnagel

München 2023

Development of an Inverted Ring Imaging Cherenkov Micromegas

Maximilian Paul Rinnagel

Dissertation
an der Fakultät für Physik
der Ludwig–Maximilians–Universität
München

vorgelegt von
Maximilian Paul Rinnagel
aus München

München, den 07.06.2023

Erstgutachter: Prof. Dr. Otmar Biebel
Zweitgutachter: Prof. Dr. Thomas Kuhr
Tag der mündlichen Prüfung: 01.08.2023

Abstract

The Cherenkov effect describes the creation of well-defined photon signatures by charged particles traversing a medium faster than the speed of light of the medium. By knowing the momentum of the charged particles, the Cherenkov effect allows the identification of the charged particles. Particle identification is one of the primary reasons for using the Cherenkov effect in large detector systems built for high energy physics. Detector systems such as LHCb at the Large Hadron Collider at CERN and BELLE II at KEKb employ Cherenkov detectors for particle identification. In reverse, this thesis aims to reconstruct a known particle's momentum by measuring its Cherenkov cone. Such a detector, called inverted RICH, has potential applications in beam diagnostics for high energy physics.

This work presents the development, construction, and characterization of the prototype detector for an inverted RICH. The detector uses a Lithium Fluoride crystal (diameter 50 mm, and thickness 20 mm with a high refractive index in the UV). The Cherenkov photons created are converted to electrons in a cesium iodide (CsI) photocathode after being transmitted through a Chromium layer (Cr). The signal is detected by a 10x10 cm^2 resistive strip Micromegas. A high voltage guides the Cherenkov electrons through the Micromegas drift region of the detector while the charged particle creates primary electrons inside the gas-filled detector. In this thesis, different radiator and photocathode materials have been studied and explored using the Geant4 simulation toolkit. LiF and MgF_2 were the most suited radiators for initial studies due to their sizeable refractive index leading to a large photon yield. CsI was the most suitable candidate for the photocathode due to its high peak quantum efficiency of 9 %. Also, the CsI photocathode is easier to use with gaseous detectors compared to, e.g. bialkali.

Detailed simulations in Garfield++ of the detector prototype were compared to measurements with the inverted RICH prototype inside a tracking detector hodoscope. Homogeneous signals are created and detected, fully covering the active area of the photocathode. Due to the cone shape of the Cherenkov signal, a significant overlap between the muon cluster and all Cherenkov photon clusters was expected and observed. The typical time signature for Cherenkov photons and muon signals is visible. A technique was developed to separate both signals. Reconstructed muon signals and the Cherenkov photons are well separated for the measured and simulated data of the entire detector prototype.

Finally, reconstruction techniques were tested that will be further developed and refined for future iterations of the detector. An analytic fit of the Cherenkov cone describes a well-defined radius working especially well for an accumulation of incident muons perpendicular and inclined up to 25° to the detector plane. This fit was also tested on measured data sampled with the detector hodoscope, which strongly agrees with the theoretical and simulated radius.

Despite some operational instabilities in cluster charge, the detector showed reasonable spatial resolution and allowed for the separation of the photon from the muon signal. Possible optimizations are proposed to improve the spatial reconstruction of multiple incident particles, enhance the detector's photodetection efficiency, and adjust the detectable kinetic energy range to eliminate ambiguities.

Kurzfassung

Der Cherenkov-Effekt beschreibt die Erzeugung von Photonen verteilt entlang eines Kegels um geladene Teilchen, die ein Medium schneller als mit Lichtgeschwindigkeit durchqueren. Durch die Kenntnis des Impulses der geladenen Teilchen ermöglicht der Cherenkov-Effekt die Identifizierung der geladenen Teilchen. Die Identifizierung von Teilchen ist einer der Hauptgründe für die Nutzung des Cherenkov-Effekts in großen Detektorsystemen, die für die Hochenergiephysik gebaut werden. Detektorsysteme wie LHCb am Large Hadron Collider am CERN und BELLE II am KEKb nutzen Cherenkov-Detektoren zur Teilchenidentifikation. In der vorliegenden Arbeit soll der Impuls eines bekannten Teilchens durch die Messung seines Cherenkov-Kegels rekonstruiert werden. Ein solcher Detektor, der als invertierter RICH bezeichnet wird, hat potenzielle Anwendungen in der Strahldiagnostik für die Hochenergiephysik.
In dieser Arbeit wird die Entwicklung, Konstruktion und Charakterisierung des Prototyps eines invertierten RICH-Detektors vorgestellt. Der Detektor verwendet einen Lithiumfluoridkristall (Durchmesser 50 mm und Dicke 20 mm mit einem hohen Brechungsindex im UV Bereich). Die erzeugten Cherenkov-Photonen werden in einer Cäsiumjodid (CsI)-Photokathode in Elektronen umgewandelt, nachdem sie durch eine Chromschicht (Cr) geleitet wurden. Das Signal wird von einem 10x10 cm^2 Widerstandsstreifen Micromegas erfasst. Eine applizierte Hochspannung leitet die Cherenkov-Elektronen durch den Driftbereich des Micromegas, während das geladene Teilchen Primärelektronen in dem gasgefüllten Detektor erzeugt. In dieser Arbeit wurden verschiedene Radiator- und Photokathodenmaterialien untersucht und mit Geant4 erforscht. LiF und MgF_2 waren aufgrund ihres großen Brechungsindexes, der zu einer hohen Photonenausbeute führt, die am besten geeigneten Radiator für Prototypstudien. CsI war aufgrund seiner hohen Quanteneffizienz von 9 % im Maximum der geeignetste Kandidat für die Photokathode. Außerdem ist die CsI-Photokathode im Vergleich zu z.B. Bialkali einfacher mit gasförmigen Detektoren zu verwenden.
Detaillierte Simulationen des Detektorprototyps in Garfield++ wurden mit Messungen mit dem invertierten RICH-Prototyp in einem Detektorhodoskop verglichen. Es werden homogene Signale erzeugt und detektiert, die den aktiven Bereich der Photokathode vollständig abdecken. Aufgrund der Kegelform des Cherenkovsignals wurde eine signifikante Überlappung zwischen dem Myonencluster und allen Photonenclustern erwartet und beobachtet. Die typische Zeitsignatur für Cherenkov Photonen und Myonensignale ist sichtbar. Es wurde eine Technik entwickelt, um beide Signale zu trennen. Die rekonstruierten Myonensignale und die Cherenkov-Photonen sind für die gemessenen und simulierten Daten des gesamten Detektorprototyps gut getrennt.
Schließlich wurden Rekonstruktionstechniken getestet, die für künftige Iterationen des Detektors weiterentwickelt und verfeinert werden sollen. Ein analytischer Fit des Cherenkov-Kegels beschreibt einen wohldefinierten Radius, der besonders gut für eine Ansammlung von einfallenden Myonen unter geraden und bis 25° zur Detektorebene geneigten Teilchenspuren. Dieser Fit wurde anhand von Daten getestet, die mit dem Hodoskop des Detektors gemessen wurden und die mit dem theoretischen und simulierten Radius gut übereinstimmen.
Trotz einiger betrieblicher Instabilitäten hinsichtlich der Clusterladung zeigte der Detektor eine angemessene räumliche Auflösung und ermöglichte die Trennung des Photonencluster vom Myonencluster. Es werden mögliche Optimierungen vorgeschlagen, um die räumliche Rekonstruktion von gleichzeitig einfallenden Teilchen zu verbessern, die Photodetektionseffizienz des Detektors zu erhöhen und den detektierbaren kinetischen Energiebereich anzupassen.

Contents

1 Ring Imaging Cherenkov Detectors **1**

1.1 The Cherenkov Effect . . . 2

1.1.1 Photon Yield: Frank Tamm Formula . . . 4

1.2 Photon Interaction with Matter . . . 7

1.3 Photoeffect and Photocathodes . . . 8

1.4 Working Principle of RICH Detectors . . . 10

2 The Micromegas Detector **13**

2.1 Energy Loss of Charged Particles in Matter . . . 13

2.2 Free Charge Carriers in Gases . . . 15

2.2.1 Drift in Electric Fields . . . 15

2.2.2 Gas Amplification . . . 16

2.3 Working principle of the Micromegas . . . 17

2.4 Picosec Micromegas . . . 18

2.5 Inverted RICH Micromegas . . . 19

2.6 Secondary Avalanche Processes . . . 22

3 Signal Analysis and Methods **25**

3.1 Readout Electronics: APV25 SRS-Hybrid . . . 25

3.2 Raw Data Signals . . . 26

3.3 Position and Timing Reconstruction Methods . . . 27

3.3.1 Signal Reconstruction . . . 27

3.3.2 Position Reconstruction . . . 28

3.3.3 Timing Reconstruction . . . 28

3.4 Particle Tracking . . . 29

3.5 Simulation Packages . . . 31

3.5.1 Geant4 . . . 31

3.5.2 Garfield++ . . . 31

4 Production of the Detector Prototype **33**

4.1 Production of the Photocathode Layers 33
4.2 Detector Assembly in Dry Environment 34

5 Design Studies for the Cherenkov Micromegas 37
5.1 Geant4: Simulation of the Cherenkov Cone 38
5.2 Choice of the Photocathode 39
5.3 Studies of the Chromium Adhesion Layer 42
5.3.1 Resistivity Measurement of the Cr Layers 42
5.3.2 Transmission Measurement of Cr Layers with Varying Thickness . . . 43
5.4 The Ideal Cherenkov Radiator 45
5.4.1 Momentum Detection of High Energy Muons 45
5.4.2 Refractive Index and Photon Yield 47
5.4.3 Variation of the Radiator Thickness 51
5.5 Energy Variation of the Incident Muons 52
5.6 Summary 55

6 Simulation of the Detector Characteristics 57
6.1 Combined Simulation Workflow 57
6.2 Number of Drift Electrons 59
6.2.1 Muon Drift Electrons 59
6.2.2 Photoelectrons 61
6.3 Position Distribution of the Photons 62
6.4 Strip and Cluster Distribution 65
6.5 Cluster Charge and Cluster Timing 68
6.6 Summary 70

7 Measurements of Cherenkov Photons Using Cosmic Muons 71
7.1 Measurement Setup 71
7.2 Individual Muon Detector Signals 74
7.3 Charge Distribution 75
7.4 Position Reconstruction of the Radiator 78
7.5 Muon Tracking 80
7.6 Cluster and Strip Multiplicity 82
7.7 Timing Distribution for the Detectors 86
7.7.1 Leading Charge Timing Distributions 86
7.7.2 Timing Distributions - Muon Cluster Separation 91
7.7.3 Two-Dimensional Timing Distributions 96
7.8 Summary 98

8 Cherenkov Cone Reconstruction 99
8.1 Analytical Cherenkov Cone Fit . . . 100
8.2 Energy Variation . . . 101
8.3 Comparison of Garfield++ Simulation and Measured Data . . . 103
8.4 Variation of the Muon Incidence Angle . . . 104
8.5 Incidence Angle Reconstruction . . . 108
8.6 Energy and Incidence Angle Variation . . . 110
8.7 Summary . . . 110

9 Potential Detector Optimizations 111
9.1 Ambiguity of the Position Reconstruction . . . 111
9.2 Detection Efficiency . . . 112
9.3 Kinematic Range . . . 113

10 Characterization of a 10x10 cm^2 Pixel Micromegas 115
10.1 Measurement Setup . . . 116
10.2 Raw Signal . . . 118
10.3 Pixel and Cluster Charge . . . 119
10.4 Hit Position and Pixel Multiplicity . . . 122
10.5 Crosstalk between Neighboring Pixels . . . 124
10.6 Summary . . . 126

11 Conclusion 127

A Detector Alignment 129

B Detector Resolution for Different Particle Energies 133

C Outlook: Neural Networks for Momentum Reconstruction 135

D Momentum Reconstruction with a Bigaussian Fit 139

E List of Abbreviations 141

Bibliography 141

Chapter 1

Ring Imaging Cherenkov Detectors

Cherenkov detectors are a widely used detector type utilizing the Cherenkov effect for the detection mechanism. They find their application for particle identification in high energy particle physics. Typically large detector systems incorporate them besides many other detector subsystems. A branch of Cherenkov detectors is called Ring Imaging Cherenkov Detectors (RICH). These detectors can reconstruct a charged particle's mass by recognizing the radiation pattern. The momentum of a particle has to be determined in another detector. The position and spatial distribution of Cherenkov photons is typically reconstructed by RICH on a ring (e.g., LHCb RICH located at the LHC[1] in Geneva) [Adinolfi et al., 2013].
Micro Pattern Gaseous detectors are well-studied gaseous detectors. These detectors are characterized by their microelectronic structures [Pinto, 2010]. They achieve high position and time resolution while also being simple to produce. Micro-Mesh Gaseous Structure detectors (Micromegas) were developed by Giomataris et al. [1996]. Due to their high rate durability, they are used in a wide field of high rate applications, e.g., in the muon spectrometer of the ATLAS[2] New Small Wheel experiment. Here the large area detectors are utilized for tracking muons created in high energy collisions [Kawamoto et al., 2013]. Micromegas are also incorporated in the COMPASS experiment to be used as charged particle trackers and in another version as RICH readout structure in combination with Thick GEMs [Abbon et al., 2007]. ATLAS and COMPASS are both situated at CERN in Geneva.
Depending on the specific requirements for a Ring Imaging Cherenkov Detector (RICH), various designs are applied in high energy physics, ranging from differences of the Cherenkov radiator, such as the material, which can be solid, liquid, or gaseous, to different detector designs. In DIRC detectors, the total reflection of photons inside the material is exploited [Ratcliff, 2003].
Conversely, the prototype of this thesis seeks to combine the RICH principle and MPGDs into a prototype called Inverted RICH Micromegas. The idea is to create a detector solution to determine the position of a traversing muon and its momentum. Applications of this detector are of various scopes due to the adaptability of the design. An evident example is a compact detector measuring the energy and shape of particle beams used in high energy physics.
The goal of this thesis is to build a prototype of this Cherenkov Micromegas and to verify that Cherenkov photons can be reconstructed by the prototype. This prototype detector is used as a foundation for future iterations to determine the momentum of an incident-charged particle.
In the following, the interaction process for Cherenkov detectors is discussed. First, the creation of Cherenkov photons is explained in Section 1.1 and, afterward, the photoconversion in a photocathode to photoelectrons (see Section 1.3). Chapter 2 focuses on electron detection

[1] Large Hadron Collider
[2] A Toroidal LHC Apparatus

in the Micromegas. Finally, the RICH working principle is explained.

1.1 The Cherenkov Effect

Similar to an aircraft breaking the speed of sound, a charged particle surpassing the velocity of light in a specific medium $c_n = \frac{c}{n}$ with the refractive index $n > 1$ and speed of light c_n the Cherenkov effect is the equivalent for electromagnetic waves instead of acoustic waves. Čerenkov [1937] described the Cherenkov effect first, while the energy loss and emission of photons were theoretically described by Frank and Tamm [1937].
A charged particle polarizes the medium locally. In the case of $v < c_n$, the medium is polarized symmetrically. The influence of the dipole integrated over the size of the medium results in a net neutral electric field.
When a charged particle crosses the speed of light c_n inside a given medium, this leads to an interference of the electromagnetic field in a constructive way. The dipoles orient and are thus not axial symmetric along the flight axis of the traversing particle anymore (see Figure 1.1).

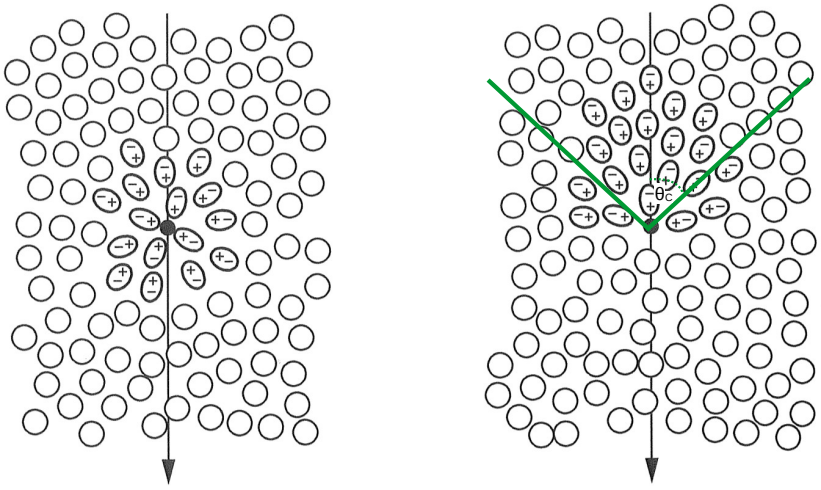

Figure 1.1: Illustration of a muon traversing a medium with velocity $v < c_n$ (left) and with velocity $v > c_n$ (right). In the second case, the muon induces a constructive interference leading to a photon emission in a conic shape - along the Cherenkov angle θ_C. Taken from Kolanoski and Wermes [2016].

This constructive behavior leads to the emission of radiation in the form of photons (see Figure 1.2). The Huygens principle can be applied to retrieve the Cherenkov angle θ_C.
Along the particle's track, elementary waves are created during the passage of the medium. For velocities lower than the speed of light in the medium, the elementary waves destructively interfere with each other thus, no photoemission occurs. After overcoming this velocity c_n, the particle traverses a distance $x = c_n t$ at the same time as the charged particle $y = tc\beta$. The radiated light is emitted in a conic shape with the opening angle θ_C (Cherenkov angle) and can then be calculated with $\beta = \frac{v}{c}$

$$\cos\theta_C = \frac{x}{y} = \frac{1}{n\beta} \tag{1.1}$$

The calculation of the Cherenkov angle excludes quantum mechanical effects of the photon recoil, which can be neglected [Nappi and Seguinot, 2005]. For example in case of photons with wavelength $\lambda = 200\,\text{nm}$ created by a cosmic muon with the momentum of $p = 4\,\text{GeV}$ or $\beta = 0.9997$ in a medium with refractive index $n = 1.44$ the correction gives the following

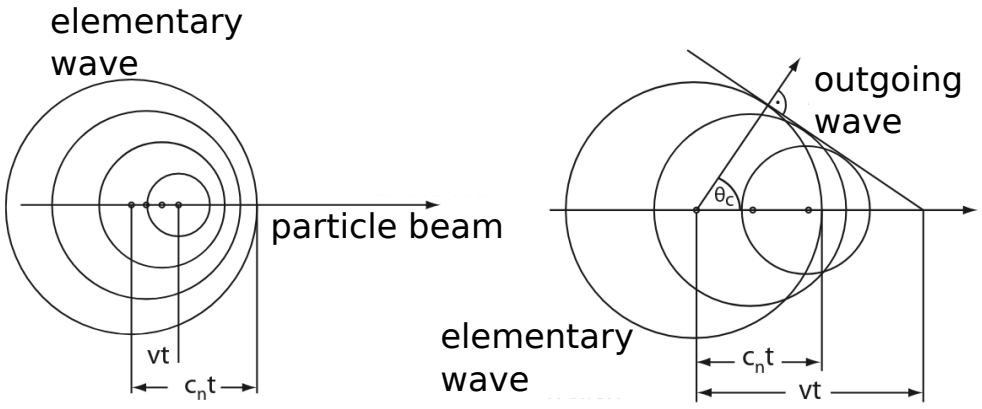

(a) $v < c_n$ (b) $v > c_n$

Figure 1.2: Particle tracks of a charged particle traversing a material (fig. (a)) with $v < c_n$ and (fig. (b)) with $v > c_n$. The elementary waves are visualized after the Huygens principle. In fig. (a), the elementary waves do not interfere with each other. No electromagnetic waves are emitted. In fig. (b), electromagnetic waves are interfering constructively. Adapted from [Kolanoski and Wermes, 2016].

result, where h represents the Planck constant:

$$\cos(\theta_C) = \left(\frac{1}{n\beta}\right) + \left(\frac{h}{\lambda p}\right) \cdot \left(\frac{n^2 - 1}{2n^2}\right) = 0.694653 + 1 \cdot 10^{-12} \tag{1.2}$$

The velocity threshold for an incident particle to be crossed for Cherenkov light production is reached for $\theta_C > 0$. This can be expressed in terms of the Lorentz factor γ or β

$$\gamma_t = \frac{1}{\sqrt{1 - \frac{1}{n^2}}} \text{ with } \beta_t = \frac{1}{n} \tag{1.3}$$

On the other hand, the limit of the maximum angle θ_{max} that can be created inside a Cherenkov medium (radiator) when the particle approaches the speed of light ($\beta \to 1$) is $\theta_{max} = \arccos\left(\frac{1}{n}\right)$. A small maximum angle needs a much finer spatial resolution required by the detector to resolve the created Cherenkov cone. For gaseous materials or variable materials such as aerogel (explained in Section 5.4.1) with a refractive index close to one, the Cherenkov angle is much smaller than for liquid or solid media (see Table 1.1). High granular detectors are needed to resolve these minor differences produced by a Cherenkov cone. In return, the threshold energy of the medium (radiator) is also much smaller in solid radiators than in gases such as Argon.
The projection at the bottom plane of a transversed Cherenkov medium leads to photons distributed in a circular shape (see Figure 1.3). The number of photons on each circular segment is constant as the photons are homogeneously emitted to each path element Δz (see Figure 1.5).
Due to the geometry of the effect, the photons emitted close to the top of the Cherenkov media have a larger distance from each other when projecting the position in 1D. The effect leads to an accumulation of Cherenkov photons in the center where the charged particle traversed the radiator (see Figure 1.4). The simulation is explained in Section 5.1.

Medium	n	β_t	γ_t	$E_{\mu,t}\,[MeV]$	$\theta_{max}\,[^\circ]$
Argon	1.0003	0.9997	57.74	5995	1.4
low density aerogel	1.006	0.994	9.17	857	6.26
high density aerogel	1.2	0.8333	2.449	154	33.6
water	1.396	0.7163	1.878	93	44.2
LiF	1.460	0.6849	1.7815	83	46.8
MgF_2	1.445	0.6920	1.802	85	46.2
NaF	1.449	0.6901	1.796	85	46.4
CaF_2	1.604	0.6234	1.6296	67	51.4
BaF_2	1.599	0.6254	1.6338	68	51.3
SiO_2	1.586	0.6305	1.645	69	50.9

Table 1.1: For different media with refractive index n evaluated at $\lambda = 200\,\text{nm}$ the threshold factors β_t and energies γ_t for a cosmic muon and the maximum Cherenkov angle θ_{max} are calculated. $E_{\mu,t}$ is the kinetic energy of a muon. The refractive indices are taken from various papers (see [Malitson, 1963], [Radhakrishnan, 1947], [H.H.Li, 1976], [Li, 1980], [Nappi and Seguinot, 2005] [Bellunato et al., 2008] and [Bideau-Mehu et al., 1981]).

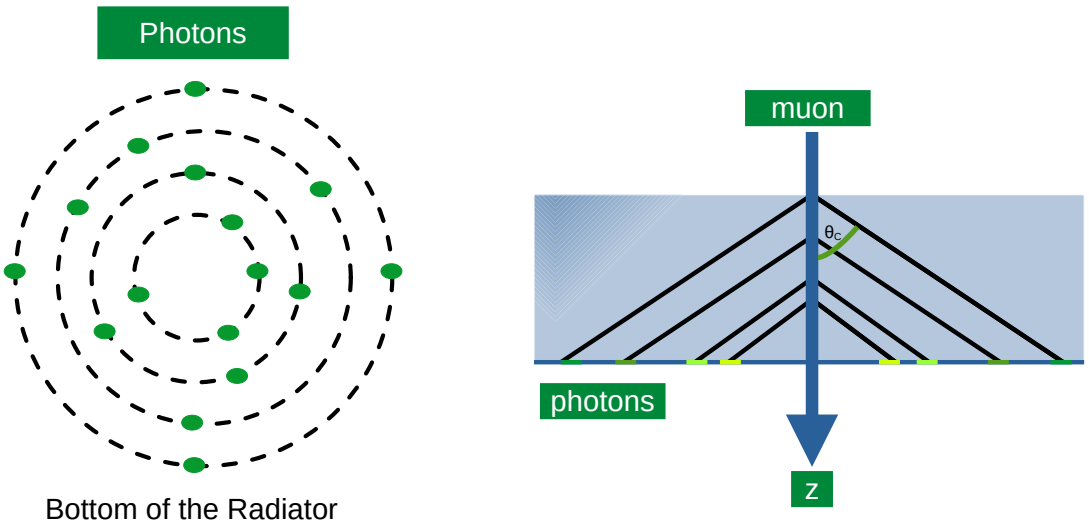

Figure 1.3: Schematic of Cherenkov cones with angle θ_C created by a charged particle (blue) on the right. The bottom view (left) shows the circular segments where the number of Cherenkov photons is constant on every circle and given by the Frank-Tamm formula.

1.1.1 Photon Yield: Frank Tamm Formula

Photons for different wavelengths λ (or frequency ω with energy $E_\gamma = \hbar\omega = \frac{hc}{\lambda}$) are experiencing different refractive indices $n = n(\lambda)$ due to the dispersion inside a given material. The complex refractive index is defined as $n = n_R + in_I$. The real part n_R defines the velocity of the electromagnetic wave inside this medium as discussed in Section 1.1. The extinction coefficient n_I describes the absorption of the electromagnetic wave in the medium (see [Zinth and Zinth, 2018]).

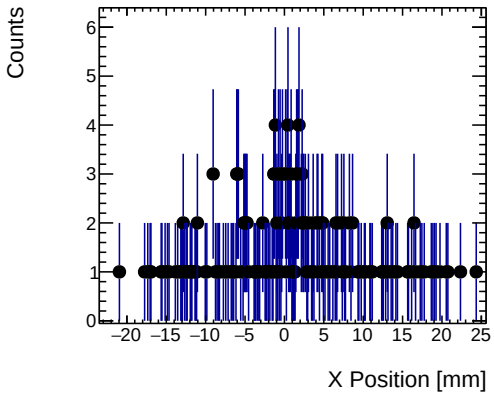

Figure 1.4: Simulated distribution along the x axis of a created Cherenkov cone for an 4 GeV incident cosmic muon in LiF $n = 1.46$ with a 20 mm thickness at the conversion layer.

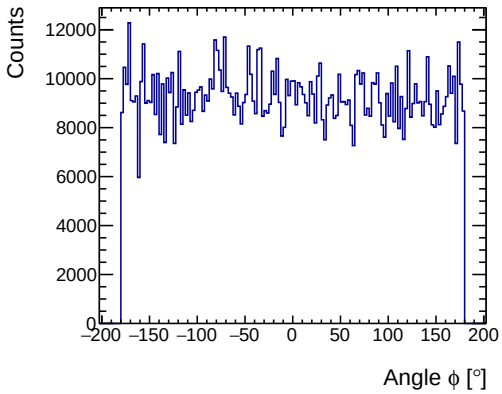

Figure 1.5: Simulated radial distribution for an accumulation of muons for Cherenkov photons. It is nearly constant along the circular segments.

The medium in the example transmits photons in the visible region (see Figure 1.6). The absorption due to emission bands leads to a decrease of transmitted photons in the UV when approaching a resonance ω the extinction coefficient n_I increases (see Figure 1.7).
This behavior is typical for materials transmissive in the visible region such as SiO_2 or LiF. Hence a significant increase in the refractive index n^2 is visible until the material completely absorbs photons at the material-specific resonances ω_1 and ω_2.

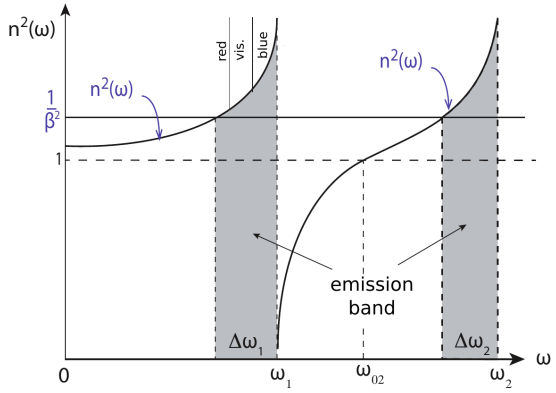

Figure 1.6: Illustration of the refractive index n^2 with photon frequency for a generic material. A radiator transmissive in the optical has an absorption edge typical in the UV, e.g. ω_1 and ω_2 (gray area). Here the photons are absorbed. Adapted from [Kolanoski and Wermes, 2016].

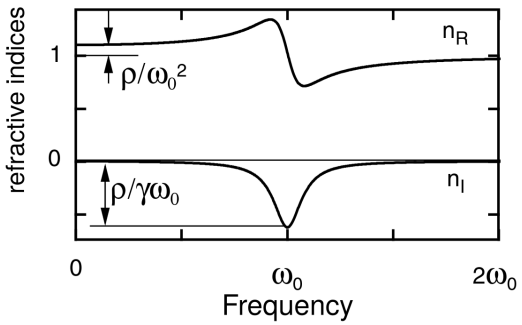

Figure 1.7: When reaching a resonance frequency of the material, the refractive indices n_R and n_I change. The real part n_R increases close to the resonance frequency while the complex part n_I deviates from zero. n_I quantifies the absorption of photons. Schematic taken from [Zinth and Zinth, 2018].

The transmission range of the medium for different wavelengths defines the observable photon wavelengths from the Cherenkov effect. A large variation of n^2 leads to a variation of the Cherenkov angle as visible from Equation 1.2. The energy spectrum of the Cherenkov effect is derived from the Maxwell equations with a relativistic charged particle moving through a medium.

The Frank Tamm formula derived by Frank and Tamm [1937] calculates the radiated energy E per photon wavelength interval $d\lambda$ and distance dx with a particle of charge z and the dielectric constant ϵ_0:

$$\frac{d^2E}{d\omega dx} = \frac{z^2e^2}{4\pi\epsilon_0 c^2}\omega\left(1 - \frac{1}{\beta^2 n^2(\omega)}\right) = \frac{z^2e^2}{4\pi\epsilon_0 c^2} \cdot \omega \cdot \sin^2(\theta_C(\omega)) \tag{1.4}$$

This emission spectrum for photons is of continuous form. It depends on the particle's velocity due to β, the refractive index of the medium n , and the frequency of the emitted photon ω. The number of Cherenkov photons N created per photon frequency interval $d\omega$ and distance dx is defined by Equation 1.4 substituting by $\omega = \frac{2\pi c}{\lambda}$ with the fine structure constant $\alpha = \frac{e^2}{4\pi\epsilon_0 c^2}$:

$$\frac{d^2N}{d\lambda dx} = \frac{2\pi z^2\alpha}{\lambda^2}\left(1 - \frac{1}{\beta^2 n^2(\lambda)}\right) = \frac{2\pi z^2\alpha}{\lambda^2}\sin^2(\theta_C(\lambda)) \tag{1.5}$$

The number of created photons is proportional to $\frac{d\lambda}{\lambda^2}$. Simulated examples of the emission spectrum for different kinetic muon energies in LiF with $n = 1.46$ are shown in Figure 1.8. Section 5.1. discusses the simulation in detail. Here multiple emission spectra are shown as a function of the emitted photon energy E_{ph} produced by muons of varying kinetic energies in LiF $n = 1.44$. The shape of the graphs stays similar. However, the total amount of photons emitted per incident muon increase with higher muon kinetic energy and photon energy as expected from Equation 1.4.

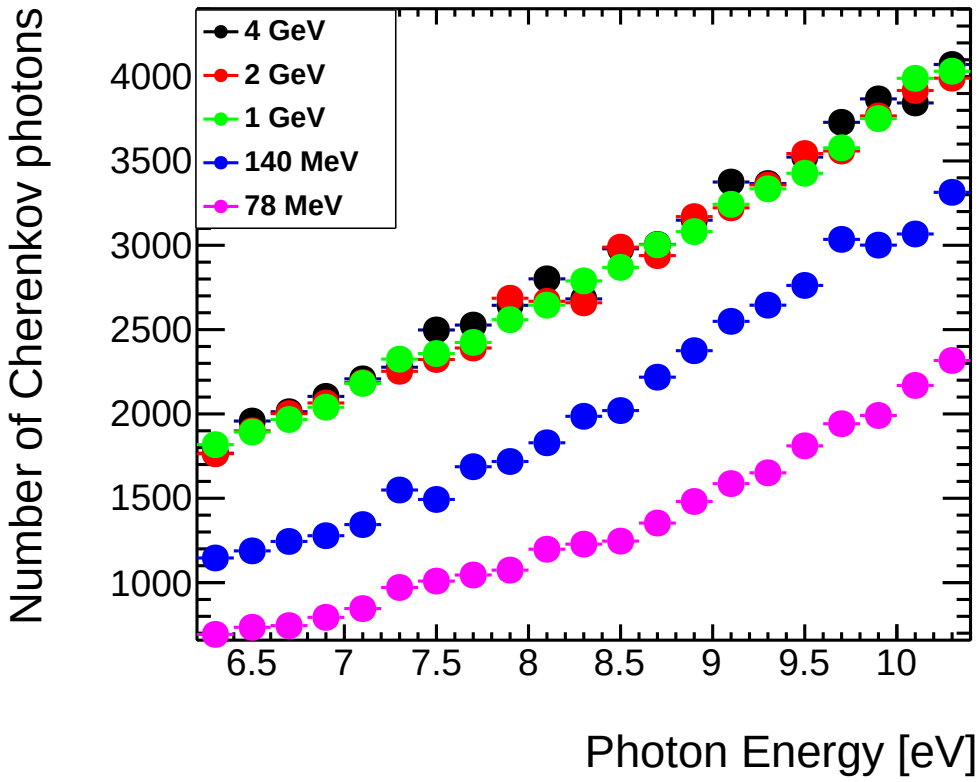

Figure 1.8: The number of created photons $\frac{dN}{dx}$ per energy interval in a 20 mm thick LiF $n = 1.46$ radiator for 5000 cosmic muons with different kinetic energies from 78 MeV to 4 GeV. The spectrum as a function of the photon energy is similar for various muon energies. However, the total amount of photons created increases with muon energies close to the Cherenkov threshold. For the working principle of the simulation (see Section 5.1).

To calculate the total photon yield inside a material for a wavelength interval, e.g., between 100 nm and 200 nm, the Frank Tamm formula has to be integrated over the wavelength and the length L of the medium

$$\frac{dN_{VUV}}{dx} = \int_0^L dx \int_{100\,\mathrm{nm}}^{200\,\mathrm{nm}} d\lambda \cdot \frac{2\pi z^2 \alpha}{\lambda^2} \sin^2(\theta_C(\lambda)) = 2295 \cdot z^2 L \sin^2 \theta_C \tag{1.6}$$

Here the assumption was made that the Cherenkov angle θ_C stays constant in this wavelength interval. A constant Cherenkov angle is untypical in the UV region for most media transmissive in the visible range (see Section 5.4.2). Thus Equation 1.6 is only a rough estimation of the photon yield as θ_C is typically not constant in this region (see Figure 5.14). In the visible range between 400 nm and 700 nm this estimation becomes more accurate as here, for most media, the refractive index does not vary too broadly:

$$\frac{dN_{vis}}{dx} = \int_0^L dx \int_{400\,\mathrm{nm}}^{700\,\mathrm{nm}} d\lambda \cdot \frac{2\pi z^2 \alpha}{\lambda^2} \sin^2(\theta_C(\lambda)) = 491 \cdot z^2 L \sin^2 \theta_C \tag{1.7}$$

The number of photons deduced from Equation 1.6 increase with the energy of the traversing particle. The increase from the Frank Tamm formula is shown in Figure 1.8. The photons have to be converted to electrons to achieve a signal in the detector.

1.2 Photon Interaction with Matter

Depending on the energy regime of the photon, multiple effects exist that mediate an interaction between it and matter. These processes are the photoeffect, Compton scattering, and pair creation (see Figure 1.9).
The strength of the mass attenuation coefficient $\frac{\mu}{\rho}$ for each process determines the probability that a photon interacts with matter via one of the processes. In a medium with size x with density ρ and attenuation factor μ the intensity of a photon beam after a distance x inside a medium with starting intensity I_0 is given by the Lambert-Beer Law which is [Kleinknecht, 1992a]:

$$I(x) = I_0 \cdot \exp\left(-\frac{\mu x}{\rho}\right) \tag{1.8}$$

The photoelectric effect is the most dominant process for low energy photons such as Cherenkov photons or photons from a ^{55}Fe source at 5.9 keV. The photons from ^{55}Fe are used for test measurements with a pixelated detector (see Chapter 10). For energies between 100 keV and 2 MeV, the Compton effect becomes dominant where the photon ionizes an electron, transferring kinetic energy in the process and getting scattered by the Compton angle. Pair production becomes relevant for energies larger 2 MeV.

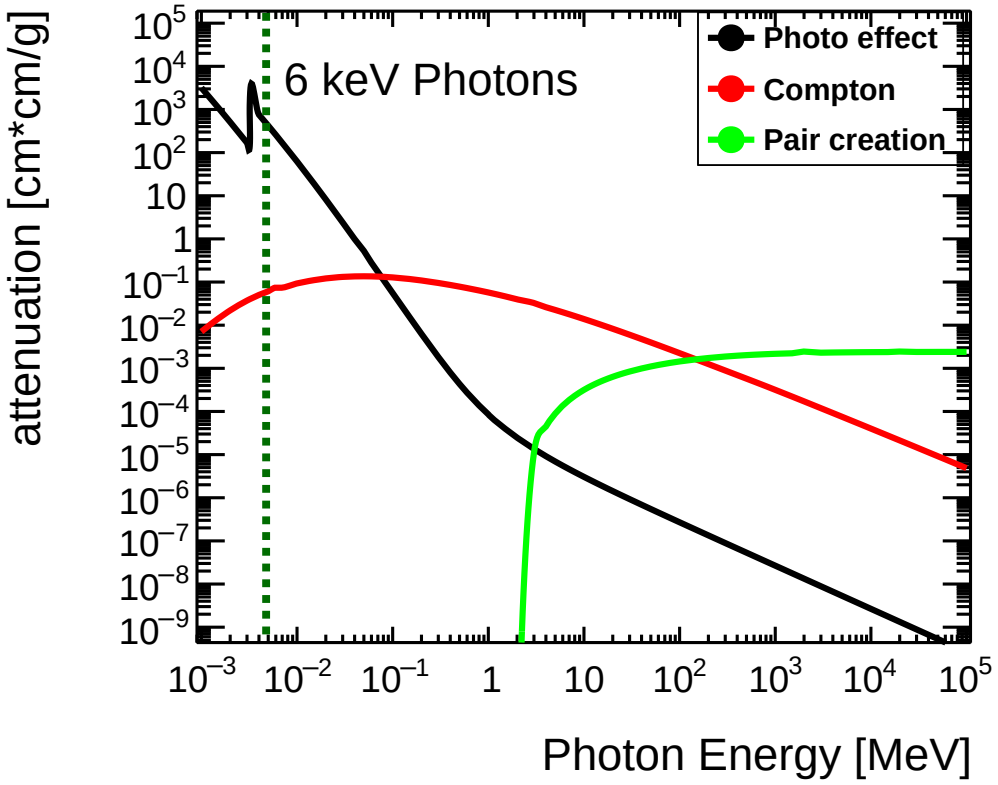

Figure 1.9: Mass-attenuation coefficient against photon energy E_{ph} in Argon. The different interaction processes for photons are shown. For low energies, the photoelectric effect (black line) is the strongest. With increased photon energies, other effects start to become dominant. The green dashed line indicates a 5.9 keV photon produced by a ^{55}Fe source that is used for detector characterization (see Chapter 10). Cherenkov photons are below the indicated energy range, typically around a few eV. Values are taken from [The National Institute of Standards and Technology]

1.3 Photoeffect and Photocathodes

The dominant process for low-energy photons is the photoeffect. It is the dominant process in this thesis for photons interacting with matter and the process to convert Cherenkov photons to electrons inside of a so-called photocathode to achieve an electron signal.
Einstein [1905] first described the photoeffect where an incoming photon with photon energy $E_{ph} = \hbar\omega$ ionizes an electron of a solid. An electron can escape from an atomic shell, carrying the kinetic energy E_{kin}. The work function ψ is the energy required to elevate an electron into the free state. Electrons that are extracted in this way are called photoelectrons.

$$E_{kin} = E_{ph} - \psi \tag{1.9}$$

This phenomenological model has been refined later by Berglund and Spicer [1964] called the "Three Step Model of Photoemission" to be applied to the photoemission of solids. The process for the photoeffect is shown in Figure 1.10.
Photocathodes can be described in the band model. In the band model (see Figure 1.10), the energy gap (EG) is not possible to be occupied by electrons between the vacuum barrier and the valence band. The electron affinity (EA) is the energy between the conduction band and vacuum level [Hamamatsu, 2007].
In step 1, the photon is either reflected with the probability R or absorbed. The photon with a probability P_ν is absorbed by an electron excited to a state higher than the vacuum level. k is the coefficient with that a photon becomes fully absorbed.
The electron is transported towards the surface of the photocathode in the second step. This

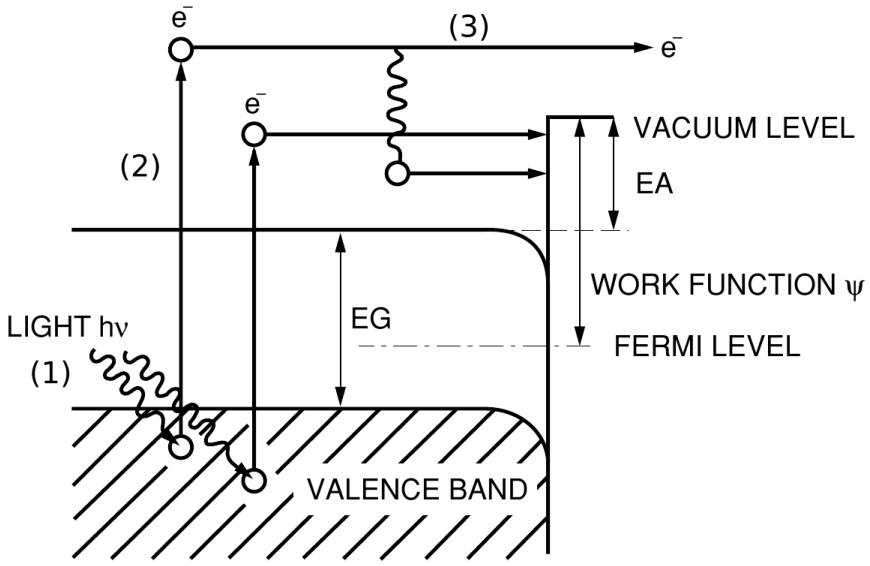

Figure 1.10: A sketch of the photoeffect in a Bialkali photocathode visualizes the band model. An incident photon (1) with a large enough energy leads to an electron emission (2). The electron has to emerge to the surface and overcome the potential barrier of the material (3). The steps in the "Three Step Model of Photoemission" are indicated. Adapted from [Hamamatsu, 2007].

process depends on the electron's mean free path length Λ.
In the third step, the electron has to overcome the vacuum barrier, leaving the photocathode as photoelectrons with a probability P_S. As this is a statistical process, a rate for extracting a photoelectron from a Cherenkov photon can be determined by the quantum efficiency $QE(\nu)$ taken from Hamamatsu [2007]

$$QE(\nu) = (1 - R)\,\frac{P_\nu}{k} \cdot \left(\frac{1}{1 + \frac{1}{k \cdot \Lambda}}\right) P_S \tag{1.10}$$

The additional variables are the photon frequency ν and the photon absorption coefficient k inside the material. Typical photocathode materials are shown and discussed in this thesis (see Section 5.2).
In the case of using a reflection photocathode, the electron does not have to cross the whole area inside the radiator, increasing the quantum efficiency compared to a transmission photocathode (see Figure 1.11). For transmissive photocathodes, the challenge for the production is that the layer may neither be too thick nor too small [Francke and Peskov, 2016].

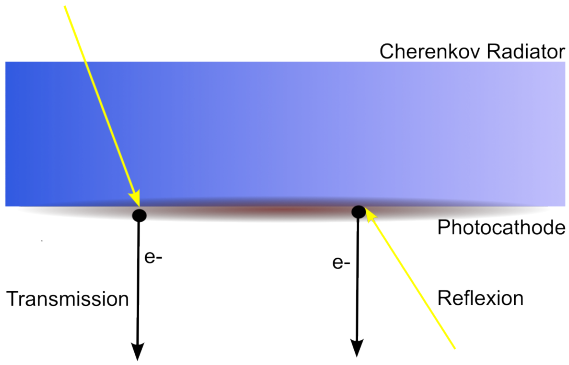

Figure 1.11: A photocathode working in transmission or reflection mode is visible. In the case of the reflective photocathode, the escape length an electron has to traverse through the cathode material is decreased. For this reason, the quantum efficiency is increased for reflection mode.

1.4 Working Principle of RICH Detectors

Detectors based on the Cherenkov effect can be utilized to identify particles when the momentum or kinetic energy has been determined. Photons are created in a Cherenkov radiator. The designs range from simple photon proportionality counters to complex machines measuring the radius of the created Cherenkov cones.
The Cherenkov angle θ_C or photon yield n can be directly accessed via the reconstructed Cherenkov cone. This section focuses on Ring Imaging Cherenkov detectors (RICH). Seguinot and Ypsilantis [1977] pioneered this detector type. RICH finds its application in the identification of particles in large detector systems.
Exemplarily explained is the ARICH detector (see Figure 1.12) in the Belle II particle identification system.
The Belle II detector uses a RICH detector with aerogel as a radiator aligned in a tile-like fashion (see Figure 1.13). The Cherenkov radiation created inside the aerogel material traverses through a $d = 160\,\text{mm}$ sized vacuum. The refractive index in a vacuum is $n = 1$, no photons are created here, and the Cherenkov cone becomes a ring (see Figure 1.14).

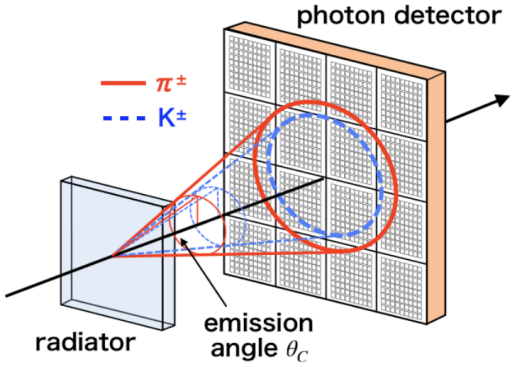

Figure 1.12: Schematic of the Belle II ARICH. Photons created inside the radiator create a ring on the detector area. The photons form a ring because they drift in a vacuum (n=1). Figure taken from Yonenaga [2020]

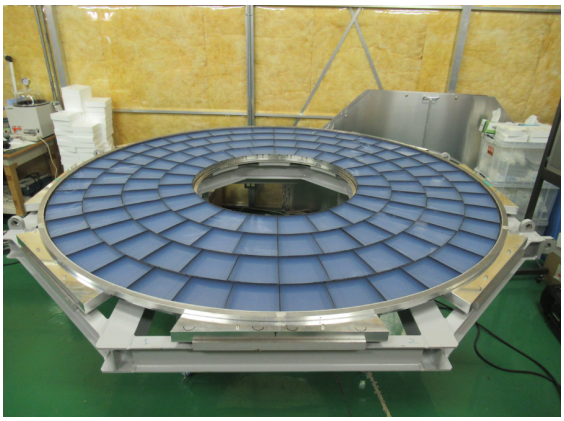

Figure 1.13: Radiator tiles on top of the ARICH detector of Belle II. Figure taken from Yonenaga [2020]

The photons are converted to electrons inside the photon detector, where pixelated detectors determine a 2D position information. The Cherenkov angle θ_C of this ring with radius r can be then determined by

$$\tan\theta_C = \frac{r}{d} \tag{1.11}$$

For thin radiator media, the RICH detector achieves a high resolution for the Cherenkov angle of the particle.
Via the equation of the Cherenkov angle θ_C (see Equation 1.2), the momentum information determined by other detectors can be included. The particle with mass m can then be identified by measuring θ_C taken from Kolanoski:

$$m = \frac{p}{c}\sqrt{(n\cos\theta_C)^2 - 1} \tag{1.12}$$

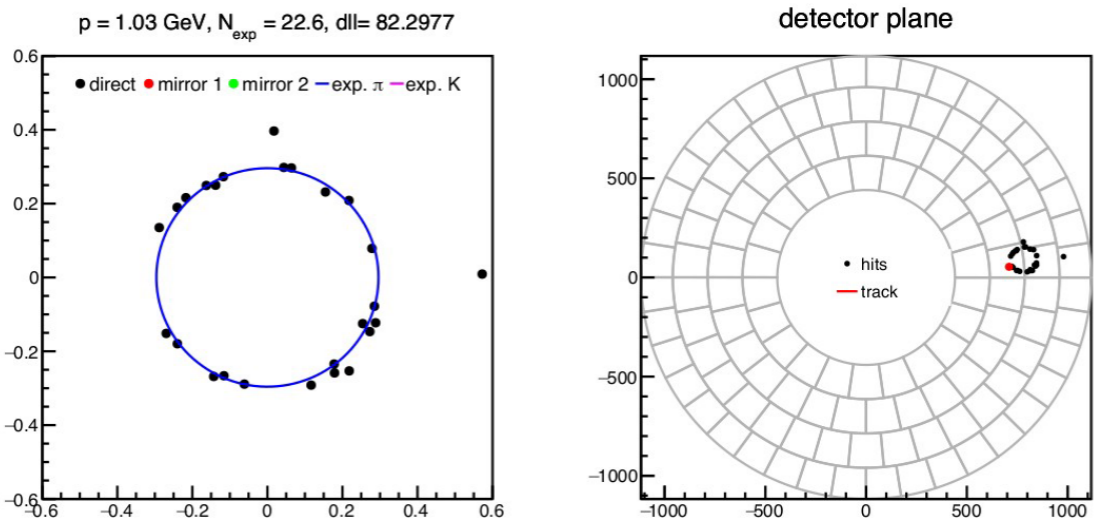

Figure 1.14: Event display of the Aerogel RICH (ARICH) of the Belle II detector. As described, the radius of the Cherenkov cone makes it possible to determine the radiation's emission angle θ_C. The measurable angle allows to identify the particle, in this case, a pion. Taken from Hartbrich [2019]

For a material with refractive index n for particles with higher masses m, the energy threshold is increased for Cherenkov radiation to be emitted (see Figure 1.15). For the calculation exemplarily, LiF material was used. The different particles can be distinguished if the particle does not reach the maximum Cherenkov angle $\theta_{max} = 46.8°$.
In reverse with a known particle mass m, the particle momentum can also be determined, which is the goal of the detector prototype discussed in this thesis.

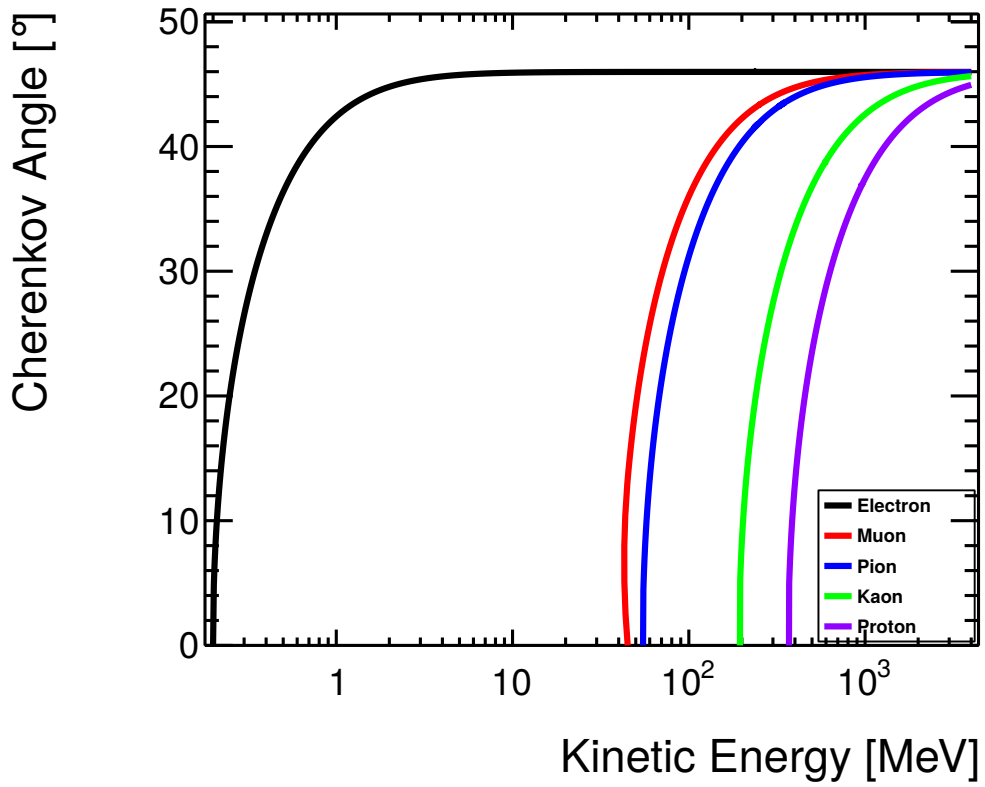

Figure 1.15: Calculated Cherenkov angles θ_C of differently charged particles (masses taken from M. Tanabashi et al. (Particle Data Group) [2018]) for various kinetic energies of the muon in LiF (with a Cherenkov threshold of $\beta = 0.7$). The threshold when Cherenkov photons are emitted is given by the value when the particle reaches $v > c_n$.

Chapter 2

The Micromegas Detector

Micro Pattern Gaseous Detectors (MPGDs) are defined by their micro-structured design, e.g., visible in the spacing of readout structure [Pinto, 2010]. These detectors measure the position and timing of ionizing radiation traversing through the gaseous active area of the detector. The underlying physical processes in these detector types are gas ionization and gas amplification.
The Micromegas detector is a type of MPGD invented by Giomataris et al. [1996]. It can be applied in medical and high-energy particle physics [Bortfeldt et al., 2017]. Special areas of application are the ATLAS New Small Wheel or the COMPASS experiment used for muon tracking.
These detectors possess excellent spatial and time resolution while operating in high-rate environments [Kawamoto et al., 2013].
In medical physics, their design is ideal as they are composed of low material budget so that ion beams for therapy are not losing significant energy inside the gas [Bortfeldt, 2014]. Before an overview of the Micromegas working principle is given, the underlying physical processes in the detector are explained.

2.1 Energy Loss of Charged Particles in Matter

Inside a Micromegas detector, a charged particle loses energy by interacting with the material, particularly with the gas volume. The Bethe-Bloch formula describes the average energy loss in matter (see Table 2.1) [M. Tanabashi et al. (Particle Data Group), 2018]:

$$-\langle\frac{dE}{dx}\rangle = Kz^2\frac{Z}{A}\frac{1}{\beta^2}\left[\frac{1}{2}\ln\frac{2\gamma^2 m_e c^2\beta^2 T_{max}}{I^2} - \beta^2 - \frac{\delta(\beta\gamma)}{2} - 2\frac{C}{Z}\right] \tag{2.1}$$

The stopping power is defined as $\frac{dE}{dX} = \frac{dE}{\rho\cdot dx}$, which is independent of the material's density. The stopping power of a muon in copper is plotted as a function of the particle's momentum and $\beta\gamma$ in Figure 2.1.

In this thesis, cosmic muons in the range of a few MeV to a few GeV are measured. The cosmic radiation below 1 GeV is statistically rarely occurring compared to high energies. The most probable energy of the cosmic muon distribution is around 2 GeV and is close to the region of minimum ionization [M. Tanabashi et al. (Particle Data Group), 2018].

parameter	definition	value/unit
K	$2\pi\rho r_e^2 m_e N_A$	eV/m
ρ	mass density	g/m^3
$m_e c^2$	electron mass $\cdot c^2$	0.511 MeV
r_e	classical electron radius	$1.818\,10^{-15}$m
N_A	Avogadro constant	$6.022 * 10^{23}$ 1/mol
Z, A	atomic number, mass number	1
z	particle charge	1
$T_{max} = \frac{2m_e c^2 \beta^2 \gamma^2}{1+2\gamma\frac{m_e}{M}+(\frac{m_e}{M})^2}$	maximum kinetic energy transfer	eV
M	mass of the particle	kg
δ	density correction	1
C	correction due to the atomic core	1
I	ionization energy of an atom	eV

Table 2.1: Parameters of the Bethe-Bloch formula

For thick detectors, the energy loss inside a material for a beam of particles is typically Gaussian distributed. For thin detectors, $\frac{dE}{dx}$ follows a Landau shape with a long tail towards high energy loss [Grupen and Shwartz, 2008]. The muon is hardly scattered in angle when traversing the detector. When the traversing media is low-density, large momentum transfers are possible in thin-layered detectors.

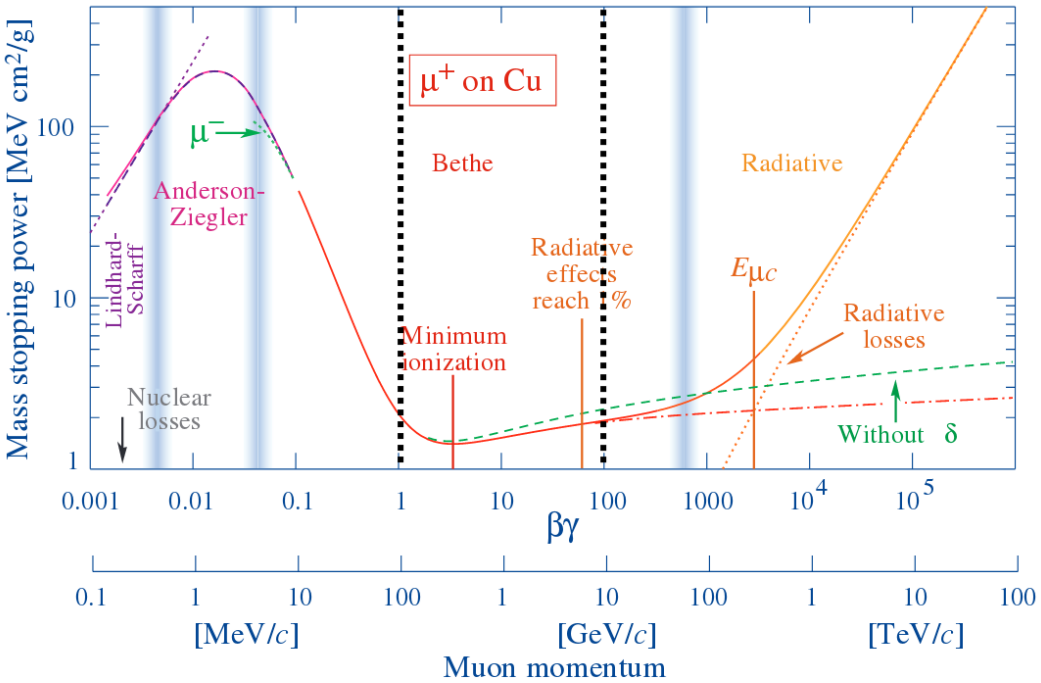

Figure 2.1: The stopping power for muons in copper for different values of $\beta\gamma$ and the muon momentum is visible. The particle shows a high energy loss for small $\beta\gamma$ at 0.01 to 0.1. At $\beta\gamma$ =3-4 the particle becomes minimum ionizing. Radiative losses dominate at larger $\beta\gamma$. The muons measured in this thesis are close to the valley of minimum ionization. The dashed lines indicate the momentum range. Figure taken from [M. Tanabashi et al. (Particle Data Group), 2018].

The energy loss of the particle, according to the Bethe Bloch formula, is typically several magnitudes larger compared to the energy loss due to the Cherenkov effect. Calculating energy loss induced by the Cherenkov effect with Equation 1.5 for a 4 GeV muon in a solid medium like LiF with a refractive index ($n \approx 1.44$) gives $\frac{dE_{FT}}{dx} \approx 4.3\,\frac{\text{keV}}{\text{cm}}$. In comparison, the mean energy loss predicted by Bethe Bloch for high energy particles is $\frac{dE_{BB}}{dx} \approx 5.28\,\frac{\text{MeV}}{\text{cm}}$ using $\rho \approx 2.64 \frac{g}{\text{cm}^3}$ from Korth [a].

2.2 Free Charge Carriers in Gases

Typical gaseous detectors operate with noble gas mixtures based on Ar, Ne, or Xe. The few atomic energy levels of noble gases can lead to an emission of UV photons into the gas. UV photons can create secondary electrons that do not have to necessarily coincide with an incident particle's signal (discussed in Section 2.6).
An admixture of molecular quenching gases such as CF_4 or CO_2 reduces this behavior due to their broad molecular absorption spectra [Kolanoski and Wermes, 2016]. UV photons excite non-radiative vibrational and rotational inside these gases.
In the following section, the effects of free charge carriers inside the gas detector are discussed.

2.2.1 Drift in Electric Fields

In gaseous media with weak electric fields ($E_d < 10\,\text{kV/cm}$), an ionized electron drifts along the electric field lines to the anode. At the same time, the positive ions are pushed toward the cathode of the detector.
The electrons gain more energy from the electrical field in gas than ions. In the region of eV, quantum mechanical interference effects, e.g., the Ramsauer effect, lead to a non-linear behavior of the electron velocity (see Figure 2.2).
Above the Ramsauer minimum for high electric fields, only a slow increase follows in pure, noble gases [Kleinknecht, 1992b].
The admixture of molecular gases increases inelastic collisions for low electric fields achieving high electron velocities [Kleinknecht, 1992b].
Furthermore, electrons experience transverse diffusion when following an electric field in a gas, influencing the reconstructed position. At the time t the spread of the electron cloud perpendicular to the drift direction is given:

$$\sigma = \sqrt{2D_e t} \tag{2.2}$$

where D_e is the gas diffusion coefficient.
The produced ions are a factor 10^{2-3} slower in their mobility than electrons because of their high mass. The ion drift velocity increases linearly with the quotient $\frac{E}{p}$ of the electric field E and gas pressure p. The ion mobility is μ_+ and $p_0 = 760\,\text{Torr}$ [Kleinknecht, 1992b].

$$< v_+ >= \mu_+ \frac{E \cdot p_0}{p} \tag{2.3}$$

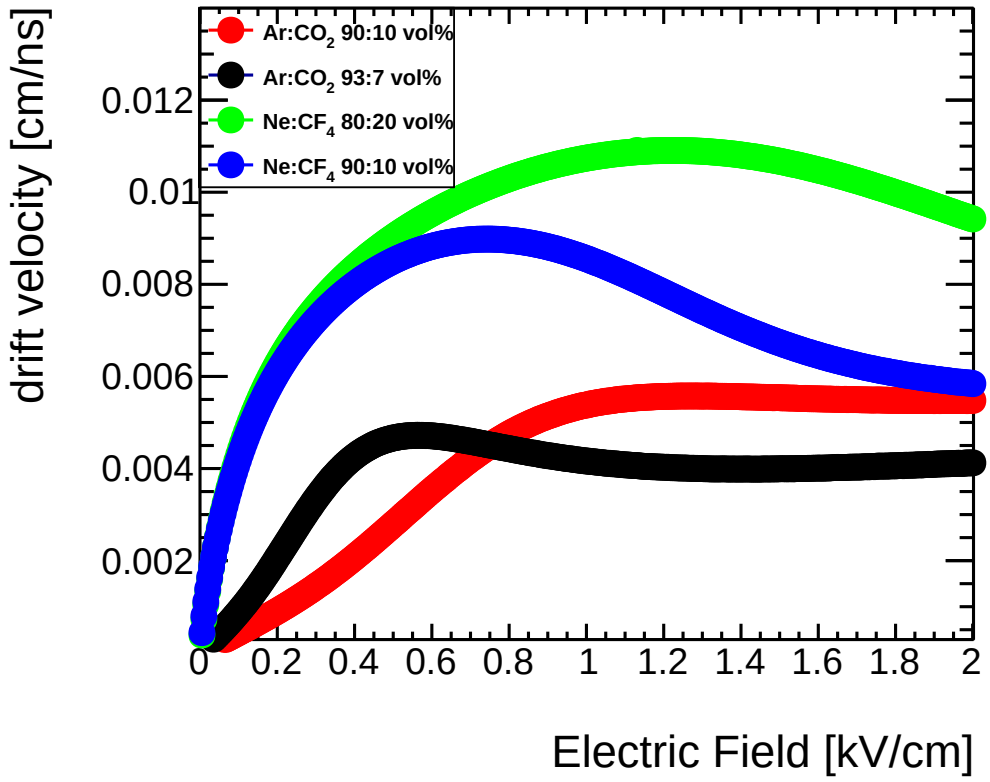

Figure 2.2: Electron drift velocities in different gaseous media simulated by MAGBOLTZ [Biagi, 2023] for different mixtures of Ar:CO_2 and Ne:CF_4.

2.2.2 Gas Amplification

The primary process in MPGDs to create a measurable signal is gas amplification requiring high electric fields. The acceleration inside the electric field leads to multiplying the initial free charges [Kleinknecht, 1992b].
Discovered by Townsend [1910] the avalanche process starts with an electron ionizing another electron from gas atoms or molecules.
After a collision, two electrons are free after the initial electron.
The initial electron is accelerated again and again to kinetic energies $E_{kin} > E_I$ during the avalanche process. This process also repeats for ionized electrons, thus achieving an avalanche effect. The number of created avalanche electrons depends on the first Townsend coefficient α at the position x.

$$\frac{dn}{dx} = \alpha(x)n(x) \tag{2.4}$$

Integrating over the amplification path x:

$$N = N_0 \cdot \exp(\int dx\alpha(x)) = N_0 \cdot G \tag{2.5}$$

With A and B being detector and gas dependant while p is the pressure, E is the electrical field, and T is the temperature, the gas gain can be expressed as [Korff, 1946].

$$G = \exp\left(A \cdot \frac{p}{T} \exp\left(-B \cdot \frac{p}{TE} d\right)\right) \tag{2.6}$$

G is called the gas gain and quantifies the signal amplification in a detector. The constants A and B of Micromegas were determined by Lippert [2012].

An exponential increase is expected with a larger distance x and higher electric field E (see Equation 2.6). In Micromegas detectors, typical gas gains are 10^2 up to 10^4. Above the Raether limit reached at $\alpha x = 20$, a conducting plasma is created inside the detector leading to discharges limiting the operation of a detector [Raether, 1964].

2.3 Working principle of the Micromegas

Micromegas (Micro-Mesh Gaseous Structure) detectors have a fine spatial resolution $\approx 50\,\mu m$ and very fast signals of orders of 100 ns. Thus they might be perfectly suited as photoelectron detectors for a Cherenkov detector so that the spatial distribution of the Cherenkov photons can be resolved.
Micromegas consist of three conductive planes: a cathode, a thinly woven mesh, and an anode usually made out of an industrially mass-producible printed circuit board (PCB) (see Figure 2.3). The investigated detectors of this thesis are filled with Ar:CO_2 93:7 vol% gas mixture.
At the top, the cathode is placed. Between the cathode and the mesh distanced $\sim$ a few mm from each other, an electric field $E_{drift} \approx 0.1 - 1\text{kV/cm}$ is applied. This space is called the drift region. The electrically grounded micro-mesh is situated about 100 - 150 µm above the anode.
An incident charged particle traverses through the Micromegas detector's drift region. The particle's energy is deposited according to the Bethe-Bloch formula, leading to gas ionization. The freed electrons in this process drift towards the micro-mesh following the low electric field. At the micro-mesh, the electric field funnels electrons into the amplification region of the detector.

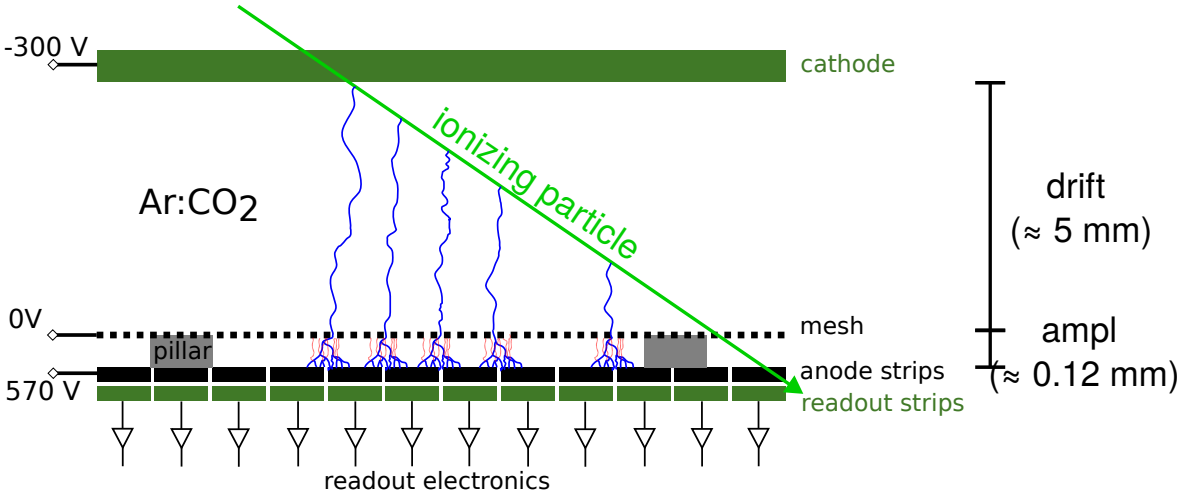

Figure 2.3: Sketch of a 1D resistive strip Micromegas detector. It consists of drift and amplification regions with a high electric field separated by a thin, conductive micro-mesh. A traversing particle will ionize the gas. The electrons drift to the amplification gap creating avalanches which are then collected at the readout strips. Figure taken from [Jagfeld, 2023]

The transparency $\xi = \frac{E_{amp}}{E_{drift}}$ for electrons at the micro-mesh depends on the ratio of the applied electric field in the drift region E_{drift} and the amplification field E_{amp}.
High electron mesh transparency close to unity can be reached for high amplification fields and low electric drift fields [Loesel, 2017]. This thesis uses electron transparency close to 100 % for the simulations.

The anode and a micro-structured readout below bound the amplification region. A high electric field of $E_{ampl} \approx 40\text{-}60\,\mathrm{kV/cm}$ is applied in this region. Small printed pillars on top of the anode PCB support the micro-mesh.
These pillars define the size of the amplification region with a typical size of 120 µm.
In the amplification region, the drift electrons create secondary electrons via gas multiplication according to the above-described Townsend avalanches (see Section 2.2.2). On the readout strips, a measurable signal is produced where the position and timing of an incident particle can be reconstructed. The single electron detection efficiency is close to 100 % [Derré et al., 2000].
The usual signal strength at the anode of Micromegas detectors is in the order of $\sim$ fC. The raw signal is then amplified, shaped, and digitized for signal reconstruction. The signal reconstruction is discussed in Section 3.3.
Anode strips made out of resistive material (MΩ/cm) on top of the readout strips prevent the detector from operational instabilities because of, e.g., significant particle background inside the detector [Alexopoulos et al., 2014]. The particle background would lead to the detector reaching the Raether limit locally, where discharges flow between the micro-mesh and anode.
Up to two layers of crossed readout strips allow for a two-dimensional readout (see Figure 2.4). The strip layer orthogonal to the resistive layer experiences a time-dependent flow of the charge accumulated on the anode strips. In this case, the signal form for both layers is negative.
The signal is an induced v shape on the readout strips. The signal is pulled towards the HV connection of the detector. In this direction, the v shape is more dominant [Klitzner, 2019].

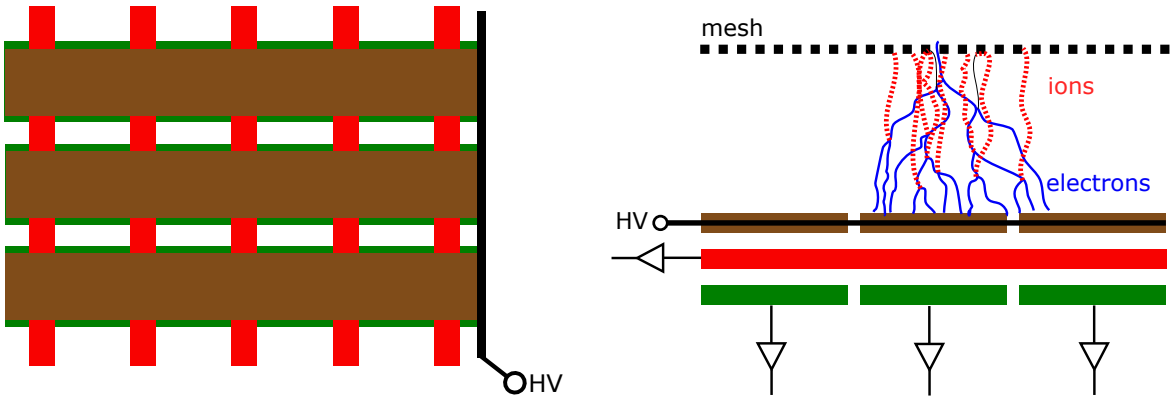

(a) Schematic from top of the anodes

(b) Schematic from the side

Figure 2.4: The resistive strips (brown) in a 2D layout is situated on top of an orthogonal readout strip x layer (red) made of copper (see fig. (a)). Below this readout strip layer, another layer (y layer, green) parallels the resistive strips. A signal can spread along the resistive strips creating a stretched signal on the x strip layer (see fig. (b)). Figures taken from Jagfeld [2023].

2.4 Picosec Micromegas

For a satisfactory timing resolution required in high-rate environments such as the High Luminosity LHC, the Picosec collaboration of RD51 at CERN investigated a potential Micromegas development. They created the Picosec Micromegas to reach time resolution in the orders of a few ps.
The detector uses a thin Cherenkov radiator made of a magnesium fluoride crystal a few mm thick (see Figure 2.5). The Cherenkov light is instantaneously produced. The created photons are converted by a Cesium Iodide (CsI) photocathode $\approx 15\,\mathrm{nm}$ thickness on the bottom of the radiator.

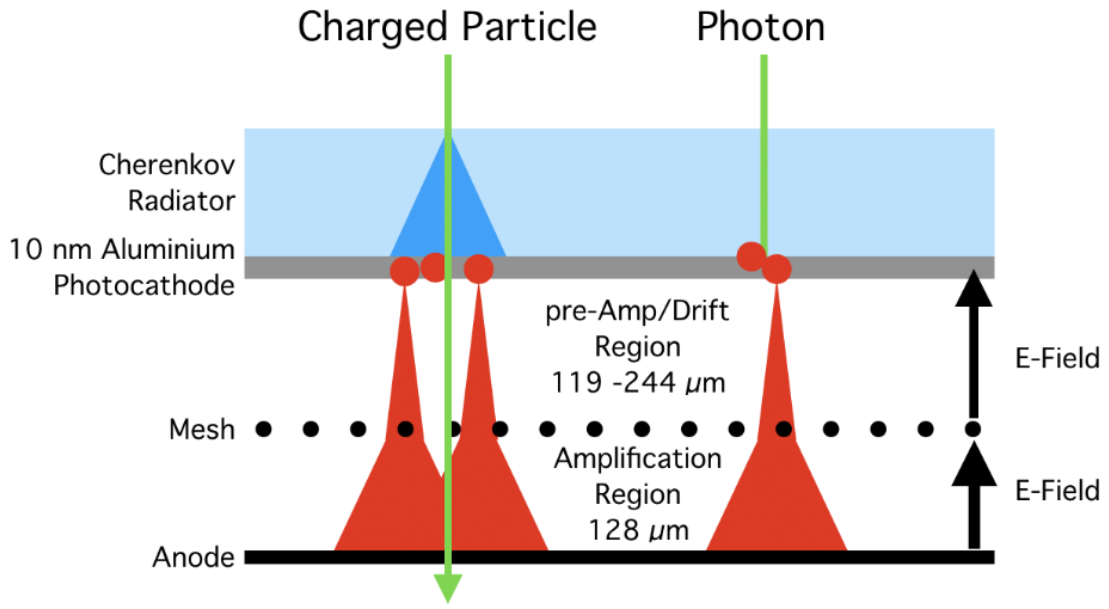

Figure 2.5: Schematic of the Picosec Micromegas. The signal of this detector is used for a high timing resolution of a few ps achieved by the time scale of the photon signals. Schematic taken from [Sohl et al., 2020].

The drift region acting as a pre-amplification region is much smaller than regular resistive strip Micromegas, thus minimizing the signal time. Here photoelectrons create already avalanches. The charged particle creates a signal through the Cherenkov photons, thus achieving this ps time resolution mostly dependent on the time response of the photocathode. The detector uses a gas mixture 80 %Ne +10 %C_2H_6+ 10 %CF_4 with electron drift velocities between 9 up to 16$\frac{\text{cm}}{\mu\text{s}}$ [Bortfeldt et al., 2018].

2.5 Inverted RICH Micromegas

In the following, the detector prototype produced and tested in the scope of this thesis is discussed. The Picosec Micromegas detector inspired a design not focused on the excellent time resolution but on determining the spatial distribution of the Cherenkov cone and the position of traversing charged particles.
The goal of this setup is to simultaneously determine the position and momentum of a muon in a very compact design. This setup could be applied as an energy filter for cosmic muons or a compact beam profile measurement system, which can also measure the particle's kinetic energy. A potential application is the CRF in Garching [Loesel, 2017], where detector systems for future experiments and upgrades can be tested with cosmic radiation. The built detector prototype uses a 20 mm thick Cherenkov radiator consisting of a lithium fluoride crystal (LiF) creating $\mathcal{O}(2000)$ Cherenkov photons per muon events (see Figure 2.6).
These photons arrive at a conductive layer of Chromium of 4 nm with transmission $T \approx 0.5$ [Ghosh et al., 2009]. If the photons are not transmitted through the Chromium, they are reflected or absorbed. The Chromium layer is used as the HV contact of the photocathode. The photons reaching the 15 nm thick CsI photocathode are converted to electrons via the photoeffect (see Section 1.3). The highest efficiency of photons converted within a CsI cathode is $QE = 9\,\%$ at a photon energy of 9 eV [Hamamatsu, 2007]. For semi-transparent photocathodes a film thickness of 10 - 15 nm is the optimum [Francke and Peskov, 2016].

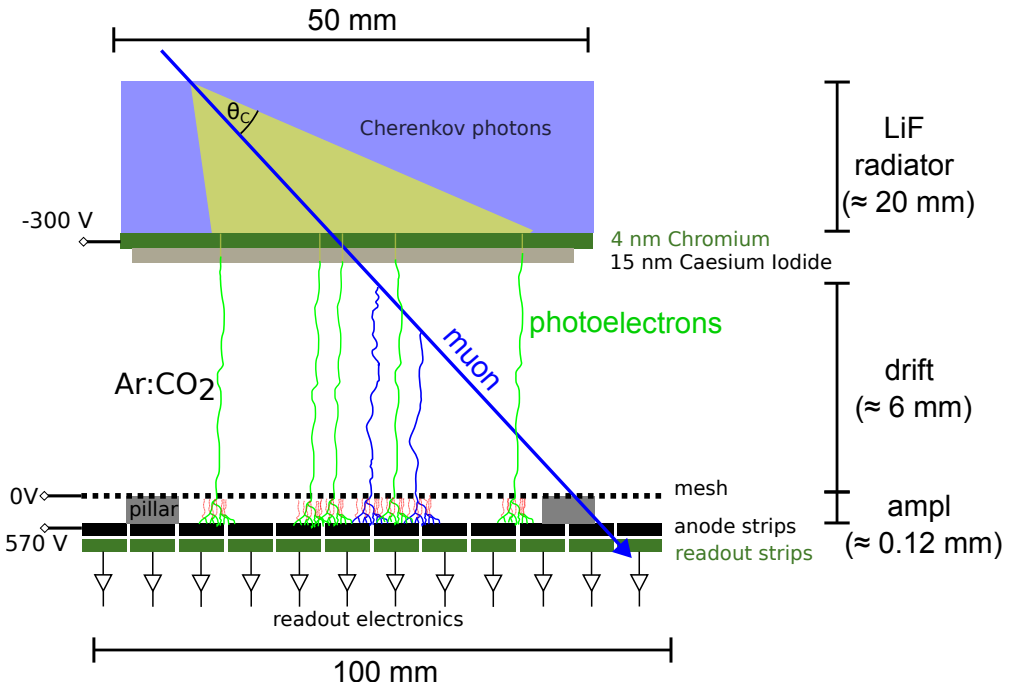

Figure 2.6: Schematic of the Cherenkov Micromegas prototype. It consists of a Cherenkov radiator, a photocathode, and a resistive strip Micromegas with a 2D readout. Created photons (yellow) are converted into electrons (green) drifting towards the amplification region of the Micromegas, where a measurable signal is created at the strips. The muon also creates drift electrons inside the drift region (blue). Typical voltages for a resistive strip Micromegas are indicated.

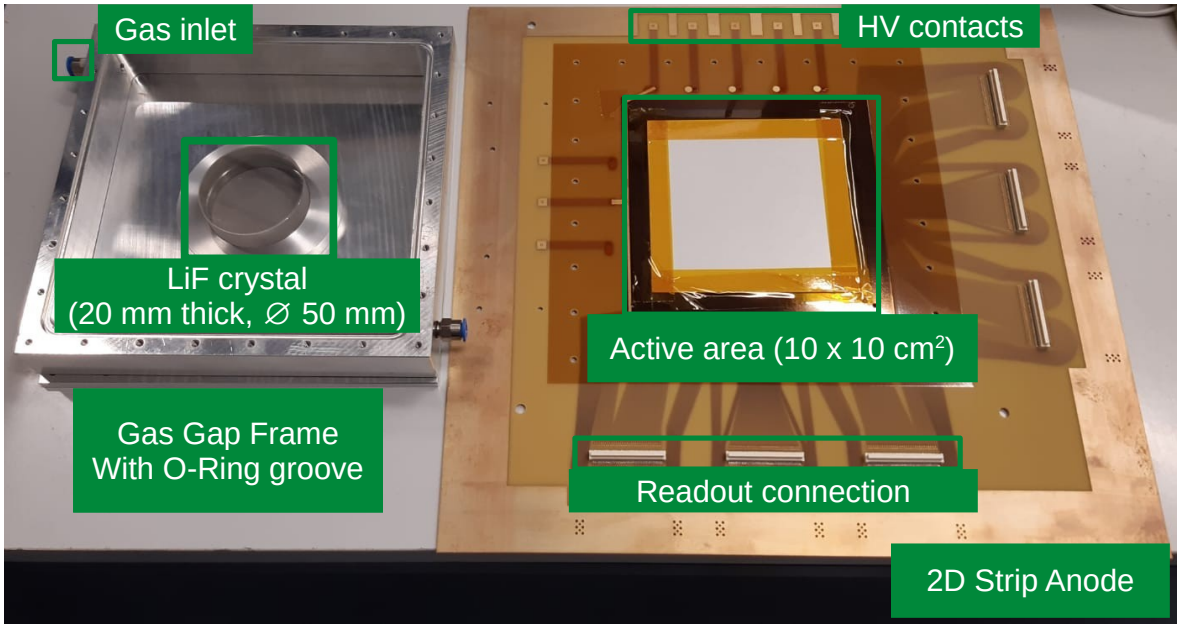

Figure 2.7: The two-dimensional strip anode (used for this thesis) on the right has an active area of 10x10 cm^2. The active area consists of 360 readout strips in the x and y plane with three APV25 readout chips attached (not shown). The pitch between the readout strips is 0.250 mm resulting in a very fine spatial resolution $\approx 50\,\mu m$. On the left, the gas gap frame is shown used for the vital gas tightness for this detector achieved by an O-Ring. Special to this gas gap frame is an attached LiF Cherenkov radiator with a 4 nm Cr layer (CsI is missing here). This radiator also defines the size of the drift region.

This percentage of photoelectrons now has to cross into the gas volume of the detector while not being backscattered into the cathode. Typical drift voltages of 350 V up to 550 V and a drift region of 6 mm are used with a gas mixture of Ar:CO_2 93:7 vol%.
The drift region of the Micromegas detector is defined by the distance between the micro-mesh the radiator attached to the detector lid and the drift voltage as here the conductive Cr thin layer is evaporated, which is $\sim$ 4 nm in size (see Figure 2.7). The amplification region is 120 µm large.
A traversing charged particle will also create primary electrons inside the drift region. The photoelectrons and the muon drift electrons are subjected to the avalanche process in the resistive strip Micromegas. The photoelectrons create a reconstructable Cherenkov cone, while the muon ionization electrons create a significant signal at the readout strips. The muon signal is expected to overlap with the Cherenkov electrons at the bottom of the cathode.
The active drift area of this 2D strip detector is smaller than its anode with 100 cm^2. It is limited due to the cylindrical LiF radiator with a diameter 50 mm. 50 mm correspond to 200 strips. Primary drift electrons of the muon are rarely created outside this diameter. Small signals are detected if a muon ionizes in the non-drift area and electrons are created close to the micro-mesh. Amplification in this area still is possible (see Figure 2.8).

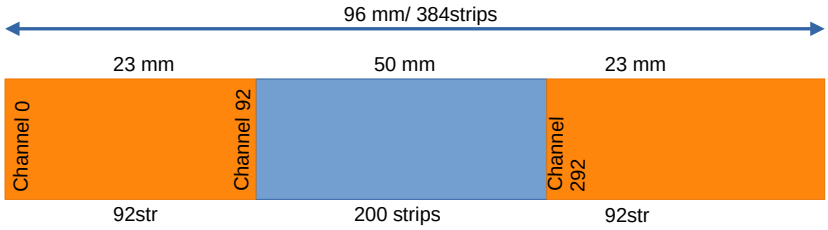

Figure 2.8: Schematic of the LiF radiator position in the detector frame. By the Cr cathode, 200 anode strips are covered. Due to the CsI not being evaporated on the borders because of the HV contacting, the strips covered by the CsI are about 192. Only in this region can photoelectrons be extracted.

A challenge this detector faces is the two-dimensional reconstruction of the particle's position. For one particle traversing the detector at once, the position is unambiguous. However, as soon as multiple particles traverse the detector at once using only the position information of the particles in the case of a strip detector, it becomes impossible to correctly assign an x position to a y coordinate (see Figure 2.9).
Especially for the reconstruction of the Cherenkov cone where a multiple of 10 electrons per charged particle is expected, this becomes difficult for two-dimensional reconstruction.
A 2D readout with a strip detector requires complex algorithms. In the first step, the challenge has to be tackled in a one-dimensional case.

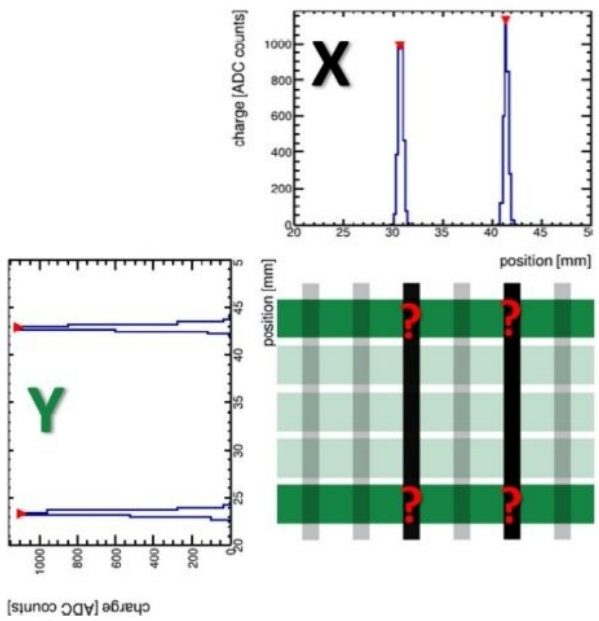

Figure 2.9: For a two-dimensional detector, correlating x and y hits is not uniquely possible if two or more particles hit the detector simultaneously.

2.6 Secondary Avalanche Processes

Secondary effects inside the gaseous volume also lead to amplification effects which can eventually be problematic for the signal reconstruction of the Cherenkov photons. In addition to gas ionization, the avalanche electrons in the detector's avalanche region excite atoms and molecules. The excited atoms and molecules emit photons. These effects can also induce macroscopic electrical discharges (see Figure 2.10).

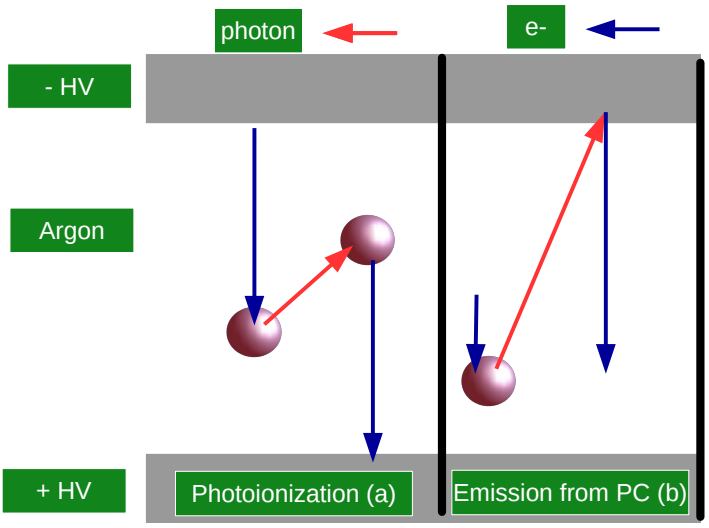

Figure 2.10: Sketch of possible secondary electron creation effects inside a gaseous detector. These effects lead to the secondary emission of electrons which can be uncorrelated to the position of the particle and its timing.

One of these effects is the photoionization of the gas (see Figure 2.10 (a)), where deexcited atoms emit photons. These, in return, will ionize another atom in the gas leading to a secondary drift electron.
Another possibility is that the photons at a time t_γ emitted by the atom hit the photocathode (see Figure 2.10 (b)). Recombination of electron-ion pairs primarily in the detector's avalanche region also leads to the emission of a photon. This effect is also used for the optical readout of Micromegas detector [Rolandi et al., 2008].
Photons created by the recombination have a high chance of arriving at the detector's photocathode and, thus are converted to photoelectrons. The effect that these secondary photoelectrons are creating a signal is called photon feedback/afterpulsing. It leads to an arrival time of the photoelectron τ of the detectors signal inside the drift region d_{drift} and an electron drift velocity v_{drift} duration:

$$\tau = t_\gamma + \frac{d_{drift}}{v_{drift}} \tag{2.7}$$

The electron extraction efficiency ϵ from the photocathode into the gas depends on the electric field E/p inside the gas and the initial photon energy. When the photoelectron escapes the photocathode into the gas after a few collisions, it may enter the photocathode again due to back diffusion inside and is absorbed here [Francke and Peskov, 2016]. Typically with the addition of quenching gases such as CO_2, CF_4, CH_4 improvements are visible in the extraction efficiency (Figure 2.11)[Escada et al., 2009] [Covita et al., 2011].
In this case, the probability of extracting a photoelectron depends on the photocathode efficiency QE in a vacuum and the extraction probability into the gas.

$$QE_{gas} = QE \cdot \epsilon\left(\frac{E}{p}, E_\nu\right) \tag{2.8}$$

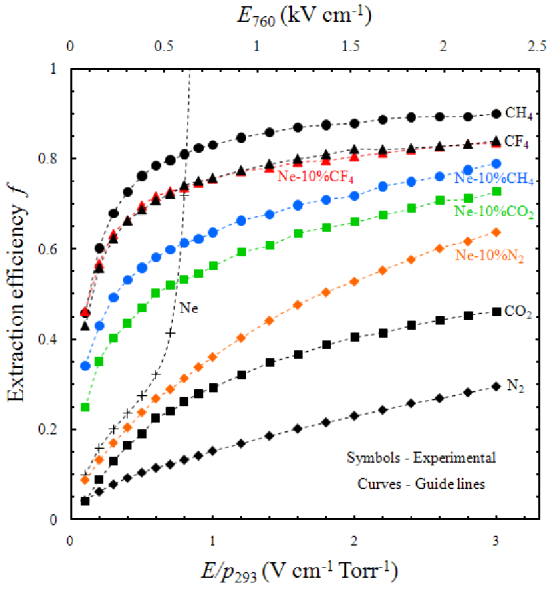

(a) Electron extraction efficiency of different Ne mixtures

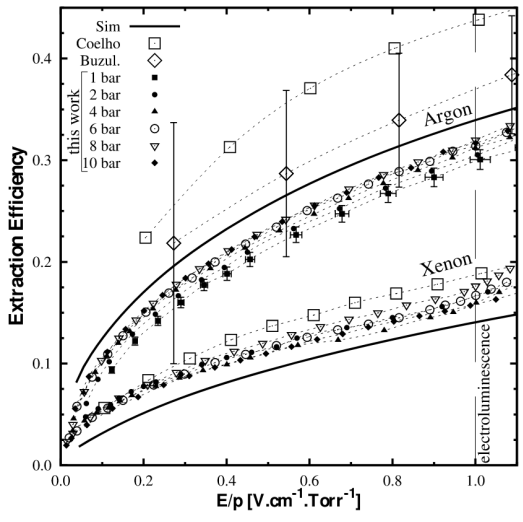

(b) Electron extraction efficiency of pure Ar and Xe at different gas pressures

Figure 2.11: The electron extraction efficiency for different quencher admixtures in fig. (a) and for pure Ar and Xe of varied pressures in fig. (b). The number of photoelectrons is large when reaching high electric field values for pure, noble gases. Figures taken from [Escada et al., 2009] and [Covita et al., 2011]

Chapter 3

Signal Analysis and Methods

The following chapter discusses the readout electronics used for data acquisition and the principle of the recorded data's signal analysis using photon and muon clusters. These methods are applied for a detector hodoscope testing the Cherenkov Micromegas prototype using cosmic muons (see Chapter 7) and for a pixelated Micromegas tested with a ^{55}Fe source (see Chapter 10).
The libraries Geant4 [Agostinelli et al., 2003] and Garfield++ [Veenhof, 1998] employed to simulate the detector behavior are discussed.
Finally, the principle of the neural network used for the reconstruction of the Cherenkov angle is explained.

3.1 Readout Electronics: APV25 SRS-Hybrid

The raw signal of the Micromegas on the detector strips is read out and has to be prepared for the final reconstruction of muons and for photon identification. The APV25 front-end hybrids retrieve a signal from the detector that can be digitized for further analysis (see Figure 3.1).
The APV25 has 128 input channels. Each channel is connected to a detector readout strip. The charge signal on a strip is converted into a voltage, and the voltage signal is shaped, amplified, and finally sampled in 25 ns steps in up to 27 consecutive data points. The amplification is required as the typical Micromegas signal is in the order of a few fC.
Mounted on hybrid chip-carrier boards of the Scalable Readout System (SRS), the chip is protected against discharges and too high signal currents with a diode network (see [Martoiu et al., 2013]). The APV25 hybrid (see Figure 3.1) is based around the APV25 readout chip designed initially for silicon microstrip detectors of CMS. The hybrid's input circuit has been adapted for micro-pattern gaseous detectors by the RD51 SRS collaboration [Jones et al., 1999].
A hybrid is attached to a detector via a 128-pin Panasonic connector connected to the detector's readout strips. A second APV hybrid board can be attached to the first one creating a data link (master/slave connection). The measured pulse height saturates at around 1500 - 1800 ADC counts. A 192-cell deep storage register stores up to 27 sampled data points of a signal for each of the 128 channels. The register accommodates the trigger latency. A maximum latency of $4.8\,\mu s = 192 \cdot 25\,ns$ is thus allowed. The time granularity of the APV chip corresponds to a 25 ns timing window where the chip integrates the collected charge per channel. Here, 24 consecutive time bins sample the signal for analysis.
After a trigger, the data samples corresponding to the trigger latency are transferred to the ADC card and digitized. HDMI cables connect the APV25 hybrid front-end board to the

ADC card. The timing, charge, and strip information is sent to the front-end concentrator card.
For this experiment, the data stream of up to 12 APVs (two 2D detectors with 360 strips per layer) is synchronized by 1 FEC card. The data of 2 FEC cards are sent via Ethernet to the data acquisition computer.
The so-called scalable readout unit (SRU) synchronizes multiple FECs. The feature of the complete readout system called scalable readout system (SRS) is the modularity of its design. It is easily possible for a small system to be scaled up (see Figure 3.2).

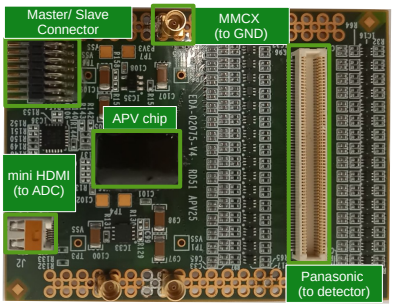

Figure 3.1: The APV25 hybrid measures the charge arriving at the 128 readout strips. The addressed channel, charge, and signal timing are buffered and forwarded to the digitizer card (ADC card) if coinciding with a trigger signal.

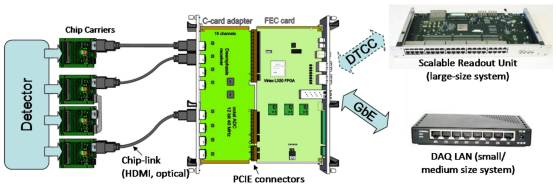

Figure 3.2: A schematic of the readout chain of the SRS system from Martoiu et al. [2013]. The APV 25 hybrids (FE ASIC) are connected in master-slave pairs with an HDMI cable attached to the ADC card (Front-End Adapter). The digitized data is sent to a computer afterward.

3.2 Raw Data Signals

The data is taken using two data acquisition programs called MMDAQ and SRUDUMP. MMDAQ is used for the data acquisition with the pixel detector described in Chapter 10 [Byszewski, 2012]. SRUDUMP is used for the readout of multiple FECs as discussed in Chapter 7 [Flierl, 2018]. Both programs function similarly, while MMDAQ can not handle the readout of multiple FECs. In both programs, an offset subtraction (pedestal) is included (see Figure 3.3 (a)). The programs select only strips higher in collected charge than 1.5 times the measured standard deviation over the pedestal value (see Figure 3.3 (b)). Otherwise, the strip is discarded [Flierl, 2018].

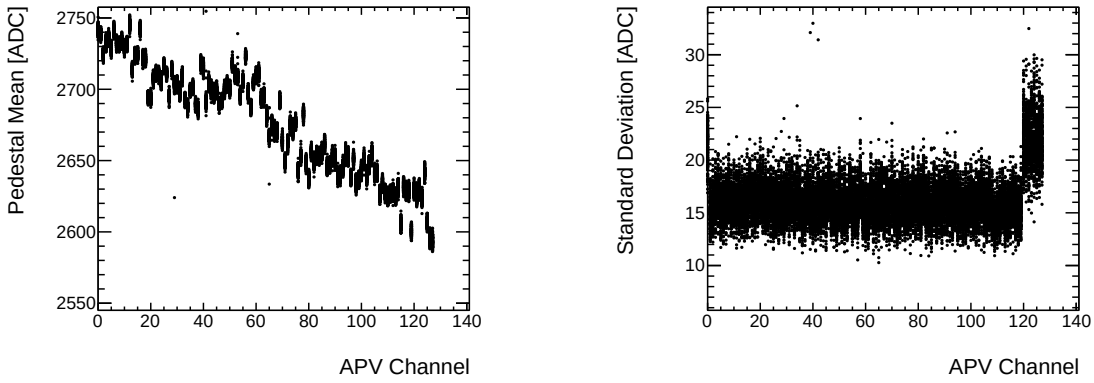

(a) APV Pedestal **(b)** APV Standard Deviation

Figure 3.3: For the pixelated Micromegas, the readout software MMDAQ calibrates the APV measuring the offset (pedestal) (see fig. (a)) and the standard deviation of the pedestal (see fig. (b)) for all APV channels before taking data with a ^{55}Fe source. For all other experimental setups, this calibration is done before data acquisition. The last eight channels in fig. (b) are not connected to the detector leading to a higher standard deviation.

3.3 Position and Timing Reconstruction Methods

After digitizing the signals, they are processed to determine the incident particle's position, timing, and charge deposition.
The analysis programs are written in C++. In the case of the pixelated Micromegas, the analysis is based on Bortfeldt [2014] and Klitzner [2019] while being further adapted for pixel detectors (see Chapter 10).
For the measurements with the Micromegas hodoscope and the Cherenkov Micromegas, the analysis was adapted from Jagfeld [2023] and Loesel [2017] with a focus on the separation of muon and photon clusters for the test Cherenkov Micromegas detector (see Chapter 7).

3.3.1 Signal Reconstruction

The information to be extracted from the APV data for an incident particle is the detected charge, signal timing, and channel number corresponding to the responding strip (see Figure 3.4). Using the integrated signal of the APV25, the charge and time information of the signal is determined by an inverse Fermi fit to the signal of each strip above the threshold (see Figure 3.5). As the time information t_0 of an addressed strip is used and as strip pulse height q_0 is used. The difference between q_0 and the offset q_{Offset} results in the total charge collected on the strips:

$$q(t) = \frac{q_0}{1 + \exp\left(\frac{t_0 - t}{\Delta t}\right)} + q_{offset} \tag{3.1}$$

As avalanches of one particle subsequentially lead to multiple responding strips, it is necessary to consider all neighboring strips with their charge information to reach an acceptable spatial resolution and good timing information.
For perpendicular incident muons, a typical strip number is around 2-3 hit strips. In the case of the pixel detector analysis, no inverse fermi fit is performed. Instead, the mean of three consecutive time bins with the highest charge on this strip is used for the strip charge and timing.

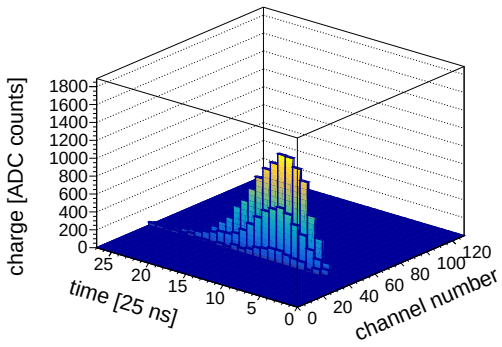

Figure 3.4: Offset-corrected and zero-suppressed raw signal of a 5.9 keV photon for a pixelated Micromegas. The zero suppression improves the electronic noise created by the APV25 electronics. The signal structure on the 24 consecutive time bins peaks around 11. This peak height is a measure of the accumulated charge on a strip. The cluster charge is given by the sum of all peak values on strips in a cluster.

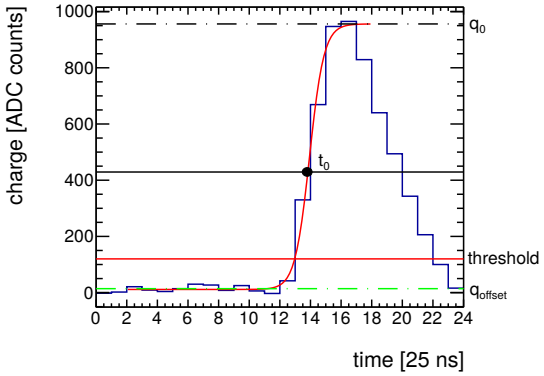

Figure 3.5: Raw signal of a single APV25 readout channel of a traversing cosmic muon in a strip segmented Micromegas fitted with an inverse Fermi function. The fit parameters determine the timing and charge on a detector strip.

3.3.2 Position Reconstruction

The Centroid method determines an incident particle's position via weighting each hit's strip charge q_{strip} (see Equation 3.2). It is used to reconstruct the position inside the detector. The adjacent strips x_{strip} responding after the traversal of a particle with charge q_{strip} form a cluster with the charge $q_{Cluster}$

$$q_{Cluster} = \sum_{strip} q_{strip} \tag{3.2}$$

The particle's position x_{cen} is measured relative to the middle plane of the drift region of the detector:

$$x_{cen} = \frac{\sum_{strip} q_{strip} \cdot x_{strip}}{q_{cluster}} \tag{3.3}$$

The Centroid method, however, shows decreasing spatial resolution for inclination angles above $\alpha > 8°$ [Ntekas, 2016].

3.3.3 Timing Reconstruction

The start of the signal time t_{first} of a cluster has the information if a signal starts late or early compared to the trigger time window.
It quantifies if a particle arrived late or early compared to the data acquisition window.
The duration of a cluster signal is given by $\Delta t = t_{first} - t_{last}$ with t_{first} being the time of the first responding strip and t_{last} the time of the last strip in a cluster.
Weighting all the strip times to the charge of a cluster gives the cluster timing relative to the data acquisition window:

$$t_{weight} = \frac{\sum_{strip} q_{strip} \cdot t_{strip}}{q_{cluster}} \tag{3.4}$$

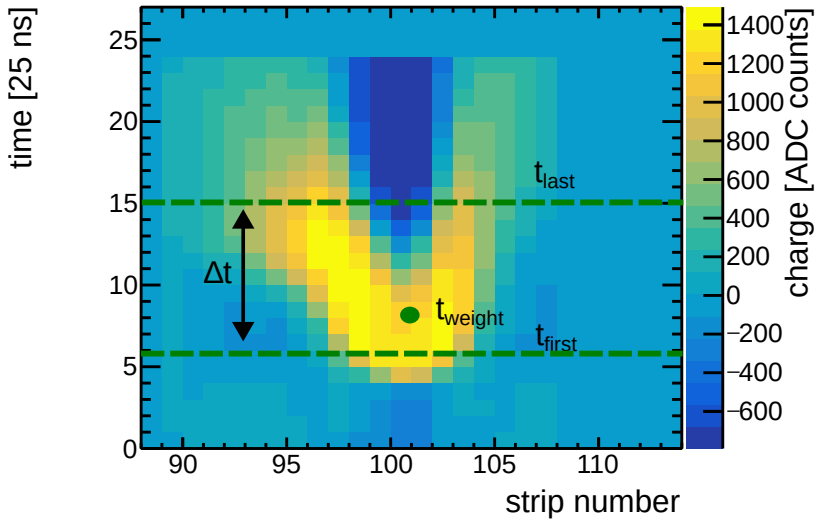

Figure 3.6: Exemplary event display of the addressed strips, their timing and charge of zero-suppressed raw data for a resistive strip Micromegas on the upper detector layer x with a visible v shape (see section 2.3). The different timing definitions are indicated, such as the time of the first strip t_{first}, the signal duration Δt, and the weighted cluster time t_{weight}.

3.4 Particle Tracking

Typically, detector hodoscopes are employed to build a reference position x_{ref} inside a test detector. This reference position is used in Chapter 7 to determine the muon's reference position x_{ref} in the test detector and to differentiate the muon cluster from photoelectron clusters. By using two detectors with a known spatial resolution σ_R a reference position of the test detector x_{ref} can be determined via a line fit through the measured positions of the tracking detectors (see Figure 3.7).

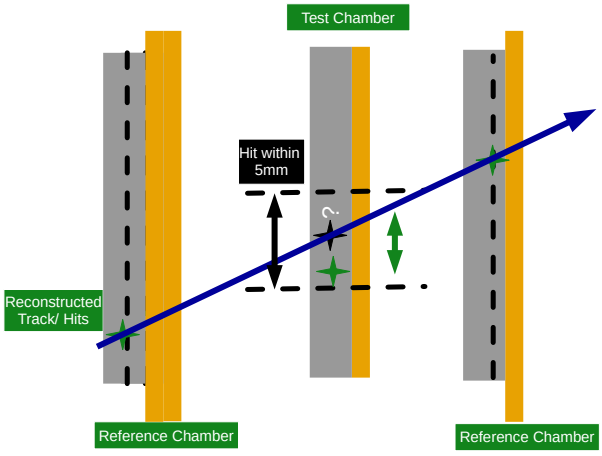

Figure 3.7: Example of a tracking hodoscope. The reference detectors are used to define a line fit through the test detector. The line fit at the position of the test detector determines a reference position x_{ref} to separate muon and photon clusters.

The accuracy of the constructed tracks can be calculated by the geometric mean method, which uses the spatial resolution of the tracking detectors by Horvat [2005]. In Figure 3.8, it is visible that for the hodoscope setup in Chapter 7 resolutions of $\sigma_{track} = 105\,\mu m$ can be

reached.
The determination of the test detector's spatial resolution σ_{SR} is possible when subtracting the track uncertainty from the detector's exclusive residual width:

$$\sigma_{SR} = \sqrt{\sigma_{ex}^2 - \sigma_{track}^2} \tag{3.5}$$

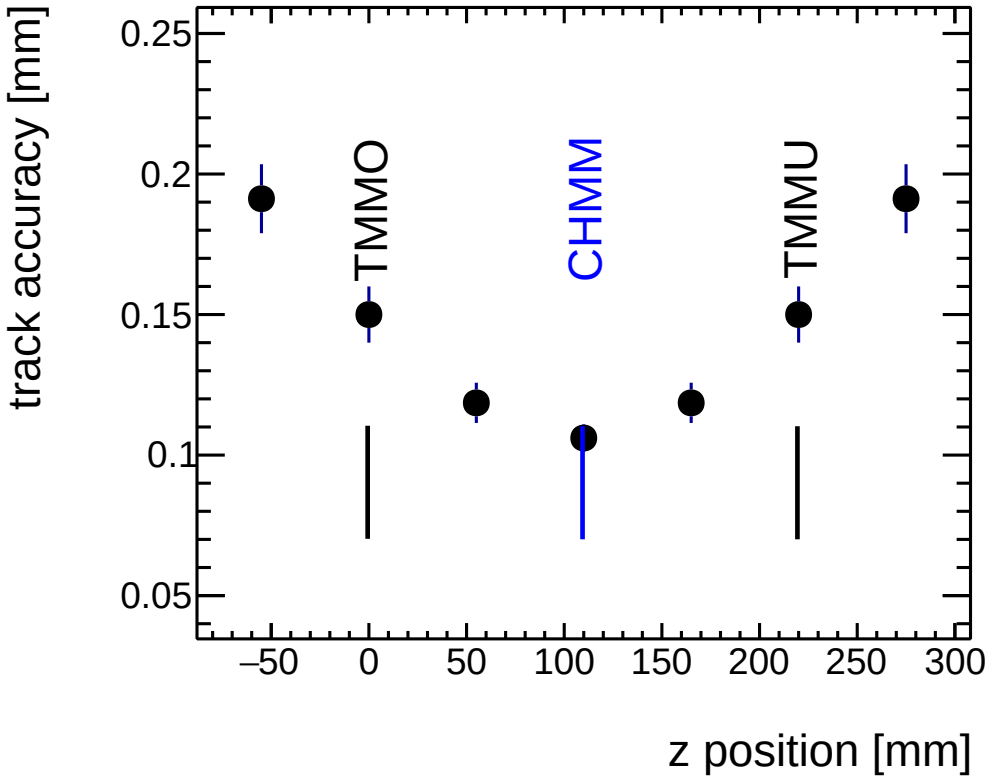

Figure 3.8: The track accuracy is determined by the geometric mean method for the detector hodoscope used to test the Cherenkov Micromegas (blue line). The track accuracy inside of the test detector CHMM is 105 μm with an assumed spatial resolution of σ_{SR} =150 µm for the reference detectors (see Chapter 7).

The residual $\Delta x = x_{ref} - x_{hit}$ is determined for the test detector. With a reasonable alignment, the residual is centered at 0. A double Gaussian fit comprises the tail Gaussian influenced especially by delta electrons and multiple scattering, and the core Gaussian gives the resolution of an ideal detector (as described in Loesel [2017]):

$$\begin{aligned} f(x) &= gauss_{core}(x) + gauss_{tail}(x) \\ &= A_{core} \exp\left(\frac{(x - \Delta x_{core})^2}{2\sigma_{core}^2}\right) + A_{tail} \exp\left(\frac{(x - \Delta x_{tail})^2}{2\sigma_{tail}^2}\right) \end{aligned} \tag{3.6}$$

Weighting the distributions gives a combined residual σ_{ex}:

$$\sigma_{ex} = \frac{\sigma_{core} \int gauss_{core} + \sigma_{tail} \int gauss_{tail}}{\int gauss_{core} + \int gauss_{tail}} \tag{3.7}$$

Furthermore, a detection efficiency ϵ_{5mm} within 5 mm of the hit position of the reference can be determined for the test detector

$$\epsilon = \frac{\#\text{Hits}_{\text{test,5 mm}}}{\#\text{tracks}} \tag{3.8}$$

A suitable detector alignment is necessary to determine the detector's spatial resolution and to separate muon and photon clusters (see Appendix A).

3.5 Simulation Packages

The two simulation packages used for this work, Geant4, and Garfield, are discussed in the following. Geant4 simulates the Cherenkov photons inside the radiator, accounting for the photoconversion to electrons.
In Garfield++, the drift and avalanche processes of the photoelectrons are simulated. The position, time, and energies of the photoelectrons are imported from Geant4 and produced in the active gas volume of the Micromegas.

3.5.1 Geant4

Geant4 is a simulation toolkit for the interaction and passage of particles in matter. The focus lies primarily on high energy physics [Agostinelli et al., 2003] [Allison et al., 2016] [Allison et al., 2006]. For the simulation performed with Geant4, the example `/extended/optical/LXe` was used as a foundation for the simulation of the detection of Cherenkov photons.
As Cherenkov photons are typical of a few eV in energy, a particular treatment is required in Geant4 with `OpticalPhotons`. For these objects to interact with any material defined in Geant4 within a given geometry, it is essential to specify the photon energy and refractive indices as parameters in ascending order [Dietz-Laursonn, 2016]. The simulation keeps records of the created photons' and the traversing muon position, angle, and energy, which can later be exported to Garfield++.

3.5.2 Garfield++

Garfield++ [Veenhof, 1998] specializes in the interaction and signal creation in gaseous detectors and incorporates the HEED and MAGBOLTZ package.
For the simulation of a Micromegas, MAGBOLTZ simulates first the electron and ion mobility in a gas mixture, taking into account scattering cross section, energy losses, and excitation level from a database [Biagi, 2023].
The HEED program generates then a track for a particle in the detector volume [Smirnov, 2005] and the primary electrons from ionization.
The position and timing of all avalanche electrons are determined at the anode. Garfield simulates the drift of the primary electrons as well as their amplification.

Chapter 4

Production of the Detector Prototype

The following chapter discusses the detector assembly of the Cherenkov Micromegas prototype. This prototype is used as a test chamber inside the detector hodoscope (see Chapter 7). As the radiator, a 20 mm thick and 50 mm diameter sized LiF crystal is used. The detector prototype uses a resistive strip Micromegas anode with a calendared micro-mesh creating a drift region of 5 mm and an amplification region of 120 µm.
The delicate step of the production at Technical University Munich (TUM) of the 4 nm Chromium layer and the 15 nm CsI layer is discussed first. Due to its hygroscopic properties, the CsI photocathode has to be prepared in a dry environment. The assembly is then explained in the last step, which occurs in a dry environment of a glove box.

4.1 Production of the Photocathode Layers

The photocathodes are produced in two steps at TUM: First, the 4 nm Chromium layer is evaporated with a metallic mask. Afterward, a mask a few mm smaller in diameter (see Figure 4.1 (a)) is used to evaporate the CsI layer onto the radiator. The small rim of pure Cr is used as HV contact. A thin Cr layer leads to an improved photon transmission. For the CsI layer in transmission mode, the optimal layer thickness is found to be 10 - 15 nm (see Francke and Peskov [2016]).
The evaporation mask containing the crystal samples (substrate) is inserted into the machine. For the production of detector samples, first, Cr and afterward CsI is evaporated. For the transmission and conductivity studies, only Cr layers are applied. After creating a vacuum with a cryo pump, pressures of $p \approx 10^{-6} - 10^{-5}$ Pa are reached. An electron beam with magnetic deflection has an acceleration voltage of 5 kV. A defocusing effect is achieved with a 13 mm wide filament and via the magnetic field. The vessel (ship) containing the CsI or Cr is hit.
CsI/Cr is hit by the electron beam. When the CsI/Cr inside the vessel is finally heated enough, it evaporates toward the substrate. The vessel is also water-cooled to reduce the reaction between the vessel's copper and the CsI. A piezo element at the position of the shutter can measure the thickness of the layer in Å. After reaching the desired layer thickness, the shutter blocks the substrate from further CsI vaporization.
The sample is then transported from TUM to LMU inside a desiccator with a vacuum to avoid absorbing water vapor due to the hygroscopic nature of the CsI layer.

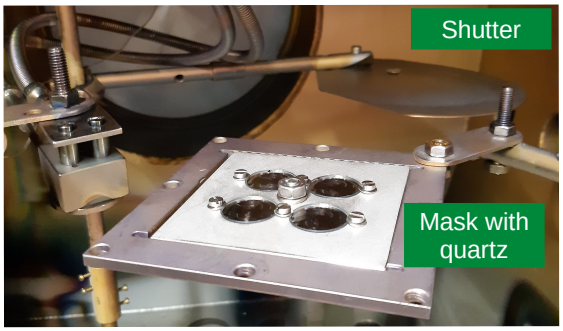

(a) Small SiO_2 samples were inserted in an evaporation mask and placed into the evaporation machine. Also visible is the shutter used for blocking the substrate after evaporation. The procedure is the same for larger samples.

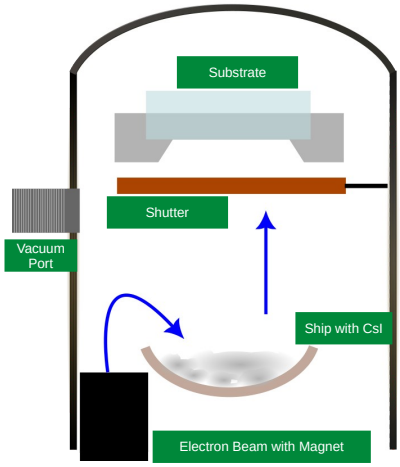

(b) Sketch of the evaporation machine used at TUM as described in [Bauer, 1995]. Missing in the sketch is the piezo element at the position of the shutter measuring the layer thickness.

Figure 4.1: The evaporation machine is used to produce a thin layer of Chromium/CsI using an electron beam to heat the material to be evaporated onto the substrate. After the desired thickness is reached, measured by a piezo element, the shutter is used to protect the finished substrate from becoming too thick. The machine is described in [Bauer, 1995] and [Maier-Komor et al., 1995].

4.2 Detector Assembly in Dry Environment

When working with CsI, it is important to keep the material off air humidity during the assembly of the detector due to its hygroscopic nature. The detector is assembled inside an Ar filled glove box (see fig. 4.2). After transporting the radiator within a desiccator, the Micromegas is already placed inside the glove box, so only the radiator has to pass the floodgate. After inserting the radiator, the vacuum pump applies a vacuum to the floodgate to pump out the humid air.
To get the residual air out of the floodgate, liquid nitrogen is used as a heavy gas after the vacuum pump's valve is closed. After reaching equal pressure between the floodgate and glove box, the radiator can enter the Argon atmosphere in the glove box. To prevent humid air from entering the glove box through the exhaust line and contaminating the CsI layer, a column is installed behind the glove box outlet.
The lid and anode with an attached gas gap frame are already situated inside the glove box before the assembly, while the radiator has to be guided inside the glove box, as explained above. The anode is prepared, including a micro-mesh and an already attached lid. The lid only prevents dust from falling into the detector and on top of the micro-mesh. Once this lid is removed from the top of the detector, the lid containing the crystal can be attached.

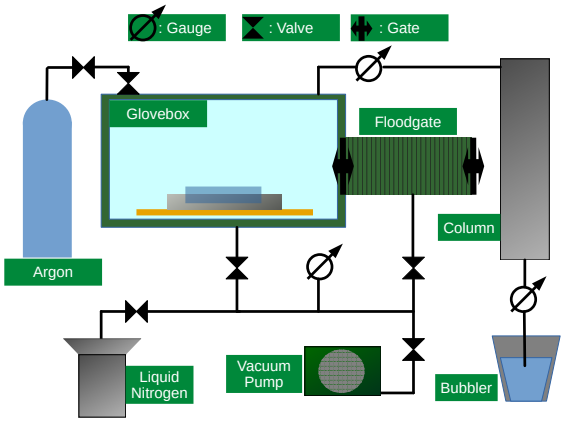

(a) Schematic of the glove box with all relevant valves and gates indicated.

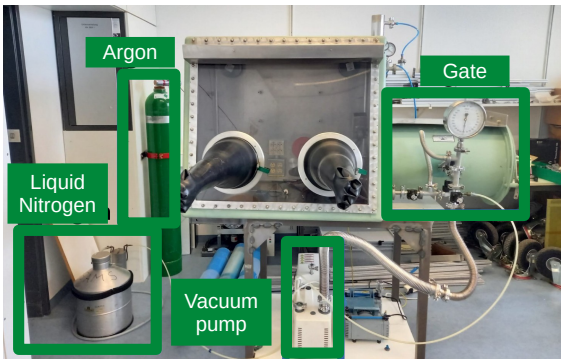

(b) Picture of the glove box to store the CsI evaporated samples and to assemble the detector. The column is used as an outlet for the system is not visible.

Figure 4.2: The schematic (see fig. (a)) and picture (see fig. (b)) show the setup of the glove box. To bring samples into the glove box, the floodgate is pumped out after placing the sample and filled with liquid nitrogen. After this procedure, the sample can be introduced to the Argon environment of the glove box. A column outside the glove box is used to avoid air humidity in the volume.

The crystal is placed in a lid structure with $\approx 0.1\,\text{mm}$ tolerance compared to its diameter (see fig. 4.3). Below the crystal, an O-ring fitting to the crystal's diameter is situated.
The most crucial step is now the attachment of the HV for the photocathode. After a Teflon ring with an O-Ring is pressed between the lid, the Cr part of the cathode is now contacted with silver conductive lacquer and a copper strip to guarantee a fine connection.
The lid has to be closed afterward with attention to the HV cable. After the detector is made gas-tight, it can be removed from the glove box.

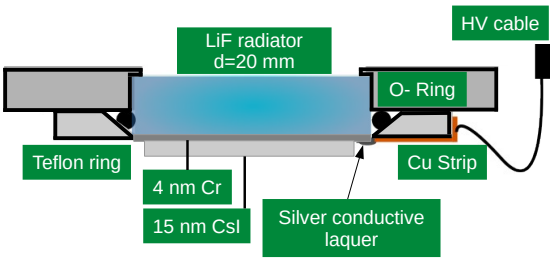

(a) Sketch of the detector lid with the radiator attached between the Teflon ring and the lid.

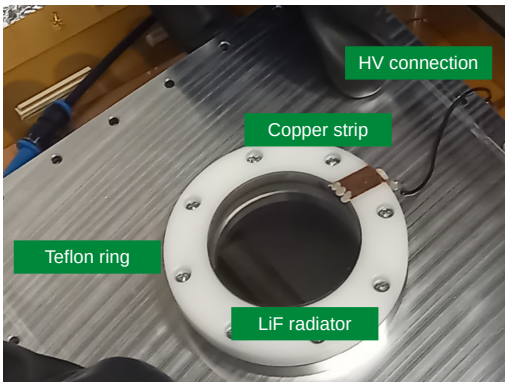

(b) Picture of the detector lid with the Teflon ring used as a seal between the metal and LiF at the top.

Figure 4.3: The detector is designed for particles to traverse through the radiator detector. To achieve gas tightness which is important due to the hygroscopic nature of the CsI layer, an O-ring is pressed between the detector lid, the radiator, and a Teflon ring.

Chapter 5

Design Studies for the Cherenkov Micromegas

For RICH detectors, very different designs exist that use different Cherenkov media (radiators) and photocathodes.
The choice of the radiator determines the detectable energy range of a particle and how large the maximum Cherenkov angle is (see Section 1.1). The potential materials for the detector design introduced in Section 2.5 are described and studied in this chapter.
The prototype's primary goal is to resolve the Cherenkov photons produced in the radiator below the Micromegas cathode (working principle discussed in Section 1.4).
It is, therefore, essential to achieve a large number of produced photons and a high number of photoelectrons entering the gas volume of the detector. Optimization of the photon/ photoelectron yield is the focus of this chapter.
Furthermore, the energy regions resolvable with this detector are explored. The radiator and photocathode materials must be selected for this prototype (see Section 2.5). The geometric design is similar to the Picosec Micromegas detector (as discussed in Section 2.4) [Bortfeldt, 2014] [Manthos et al., 2020].
A crystal with a photocathode layer is attached to the lid of the prototype (see Figure 5.1). The distance between the mesh and photocathode defines the 6 mm drift gap. The anode of the detector is a typical resistive strip Micromegas with a two-dimensional readout (see Section 2.3). The 2D readout strips (pitch $p_s = 250\,\mu m$) detect the muon as well as the photoelectrons from Cherenkov photons with an excellent spatial resolution $O(h) \approx 100\,\mu m$.

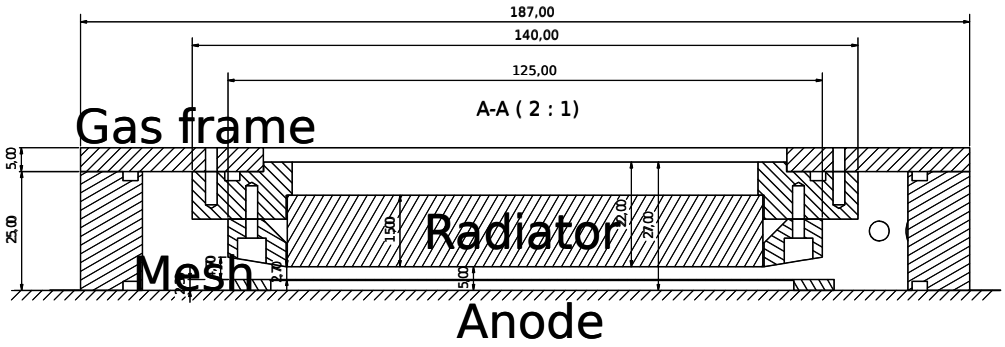

Figure 5.1: Sketch of a first Cherenkov Micromegas design. The LiF Teflon holder is missing from this sketch, which presses the LiF via an o-ring in place without damaging the crystal. The micro-mesh is placed above the anode. The measure shown here is indicated for a 15 mm radiator and different drift gap size, while the detector discussed in Chapter 7 uses a 20 mm radiator.

First, the principle of the simulation performed with Geant4 is considered. Then the choice of the photocathode and radiator is discussed as follows.

5.1 Geant4: Simulation of the Cherenkov Cone

The simulation of a muon creating Cherenkov photons inside a radiator was performed using the Geant4 package (see Section 3.5.1). Parameters such as muon energy, radiator thickness, and material are varied to investigate the behavior of the Cherenkov photons inside the radiator. The diameter is fixed at 100 mm. A muon traverses a radiator where materials chosen were MgF_2, SiO_2, CaF_2, BaF_2, LiF and NaF_2 (see Figure 5.2). The muon inside the radiator creates Cherenkov photons, which are either transmitted or reflected toward the photocathode. Reflected photons repeat the previously mentioned step. Otherwise, the photocathode absorbs the photons and counts them as transmitted photoelectrons. In reality, these photoelectrons would enter the gas volume.
The refractive indices (see Figure 5.14), as well as the quantum efficiency of the photocathode (see Figure 5.5), are used as parameters in the simulation. The photocathode is set then as the sensitive volume that counts the arriving photons and determines their position and angle. This photocathode consists of a conductive 4 nm Cr layer as well as 15 nm CsI layer for the prototype detector. The simulation tracks the position and energy of every particle.

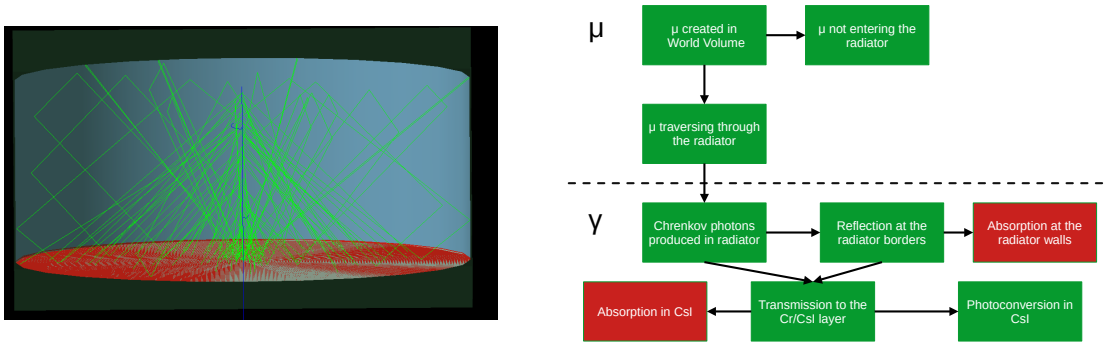

Figure 5.2: Left: The radiator with the attached photocathode is realized in Geant4. The muon (dark blue track) creates inside the radiator (light blue) the (green) photons. The photons are converted at the (red) photocathode. Right: Flow of the simulation for a muon as the primary particle.

In Geant4 also distances between the muon position r_{muon} and photon position r_{ph} are calculated in terms of a radius at the bottom of the radiator (see Figure 5.3). The average radius over all Cherenkov photons N: $r_N = \sum_N \frac{r_{ph} - r_{muon}}{N}$.
The question is whether the photons farthest from the muon can be used similarly to standard RICH detectors with an elliptic or ring-shaped fit to determine the particle's momentum. Issues might arise due to the reflection mentioned above and low statistics. For this reason, three and ten of the most outer photons are used to determine a radius with these $n = 3, 10$ outer photons $r_n = \sum_n \frac{r_{ph} - r_{muon}}{n}$
Also visible is that the Cherenkov photons accumulate close to the muon position as photons are equally distributed on ring segments leading to a higher number at the center of the distribution along a 1D projection (see Section 1.1). The Geant4 simulation is a basis for the whole detector simulation (see Chapter 6).

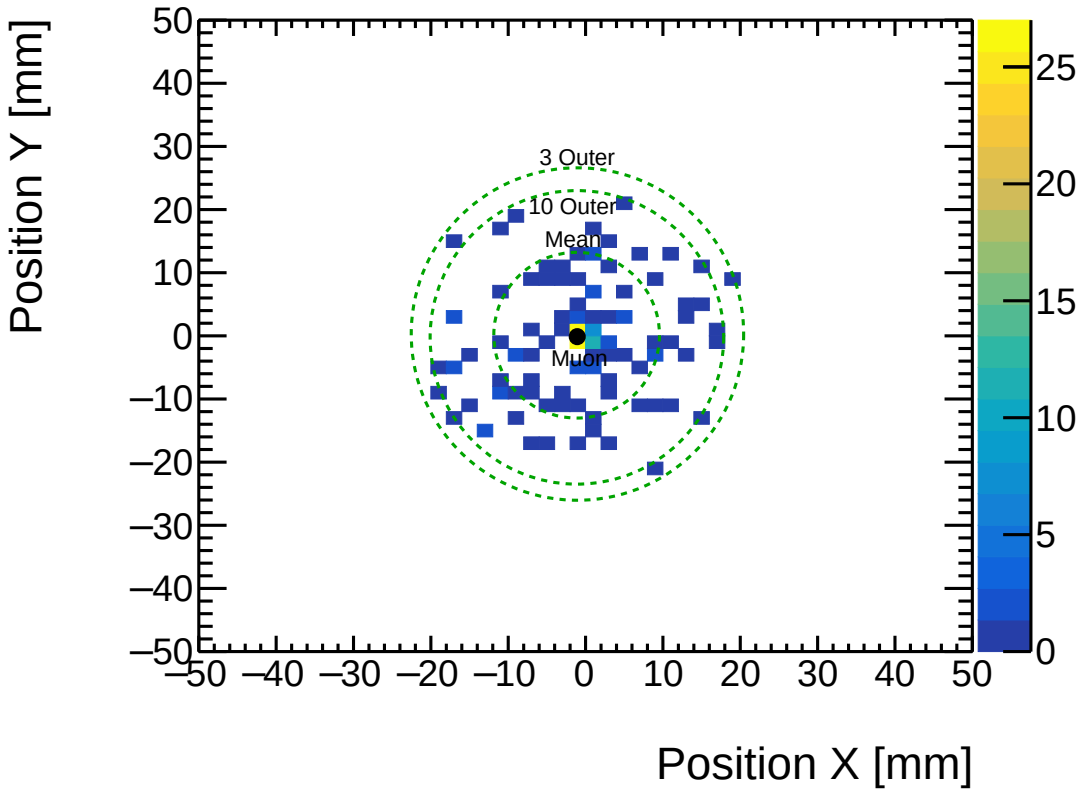

Figure 5.3: The simulated Cherenkov photoelectrons by a 600 MeV muon were simulated by Geant4. The different radii or distances of the ten or three outer photoelectrons and the average radius are indicated.

5.2 Choice of the Photocathode

The photocathode converts the photons created by the Cherenkov effect into photoelectrons via the photoeffect. It covers a wavelength λ or energy region $E_{ph} = \hbar\omega$ starting with E_A the minimum energy at which an electron is elevated to the conduction band (see Section 1.3).
The photocathode selects the photons depending on their wavelength (or energy). For this reason, the photocathode is discussed before the choice of the Cherenkov radiator, as the photocathode rules out some materials that absorb light in the photocathode's conversion range.
Figure 5.4 features an overview of potential candidates used as a photocathode.
The selection of photocathodes is indicated by their operational wavelength region, and their respective peak quantum efficiency at the energy of the highest conversion probability is shown in Figure 5.4.

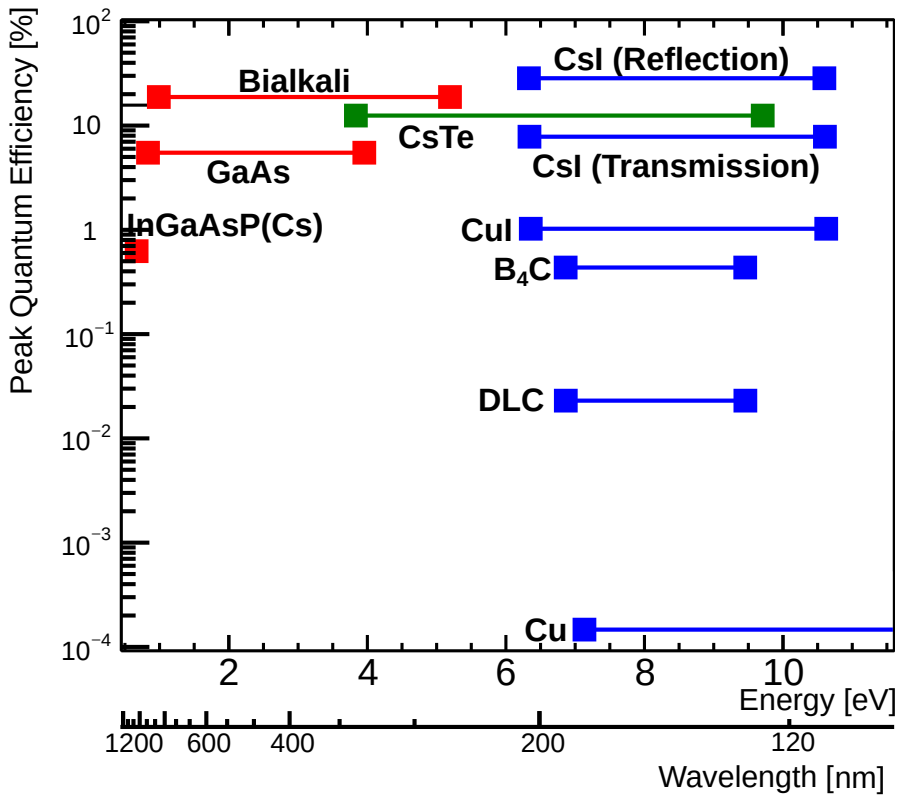

Figure 5.4: Different photocathodes (shown as bars) operate in different wavelength regions. The peak quantum efficiency (taken from [Hamamatsu, 2007], [Sohl, 2020], [Henneken et al., 2000]) of each photocathode is indicated. The far UV region (blue bar) is attractive for usage in a Cherenkov detector due to the high predicted photon yield (see Equation 1.6) while the infrared (red bar) and visible region (green bar) have here a lower number of created photons.

Some of the most interesting photocathode shown in Figure 5.4 are:

- Bialkali: This cathode operates in the visible spectrum with a high quantum efficiency. The region is attractive as most Cherenkov media have here a lower angle uncertainty $\Delta\theta_C$ than in the vacuum ultraviolet (VUV) region. However, its reactivity with air and manufacturing makes it not feasible as a photocathode for the prototype detector [Nappi and Seguinot, 2005].
- GaAs/ InGaAs: The photon sensitivity of GaAs/InGaAs is in the red to the visible spectrum, making it unattractive for Cherenkov detectors with a goal of high photon yield [Hamamatsu, 2007].
- DLC: Diamond-like Carbon is an attractive candidate that is also tested by the Picosec collaboration due to its high durability in high-rate environment [Sohl, 2020].
- Cu: Metallic photocathodes are very durable compared to other materials. However, they lack a high quantum efficiency due to their shallow escape depth [Henneken et al., 2000]. Metallic photocathodes are not ideal candidates because a large quantum yield is essential.
- CsI: Cesium Iodide is typically applied in RICH with gaseous detectors due to the high quantum efficiency and higher tolerance to contact with air compared to, e.g., Bialkali. It also covers the VUV region, making it attractive due to the high photon yield in this region (see Equation 1.6) [Nappi and Seguinot, 2005].

Typically for photocathodes, a compromise must be made between high quantum efficiency and low reactivity that makes comfortable handling possible during the manufacturing and detector assembly. In addition, non-metallic photocathodes are susceptible to an aging process. The aging of photocathodes leads to decreased quantum efficiency over time. Several factors accelerate this process. In the detector, ion backflow influences this process, for example. Ions from the avalanche region drift towards the cathode, where a too-large current can destroy the material [Braem et al., 2005].
Another factor to consider during the manufacturing process and detector operation is gas pollution, e.g., by water vapor, which in the case of CsI, leads to water adsorption on the surface due to its hygroscopic nature. Water adsorption also leads to an aging effect as well [Di Mauro et al., 2005].
In the end, CsI was chosen as the photocathode material for the prototype as it can be handled more easily compared to bialkali during and after the production process. Further, its conversion range into the VUV spectrum increases the usable photon yield (see Figure 5.5). Comparing the photon yield in the VUV spectrum N_{VUV} according to the Frank Tamm formula (100 nm to 200 nm: see Equation 1.5) to the photons produced in the visible spectrum N_{vis} (400 nm to 700 nm: see Equation 1.7) gives:

$$\frac{N^{VUV}}{N^{vis}} = \frac{2295 \cdot z^2 L \sin^2 \theta_C}{491 \cdot z^2 L \sin^2 \theta_C} = 4.67$$

Thus the photon production is expected to be a factor 4.67 higher in the VUV range, making the VUV more desirable for the prototype. This calculated photon yield is a rough approximation as the refractive index increases towards the VUV region.

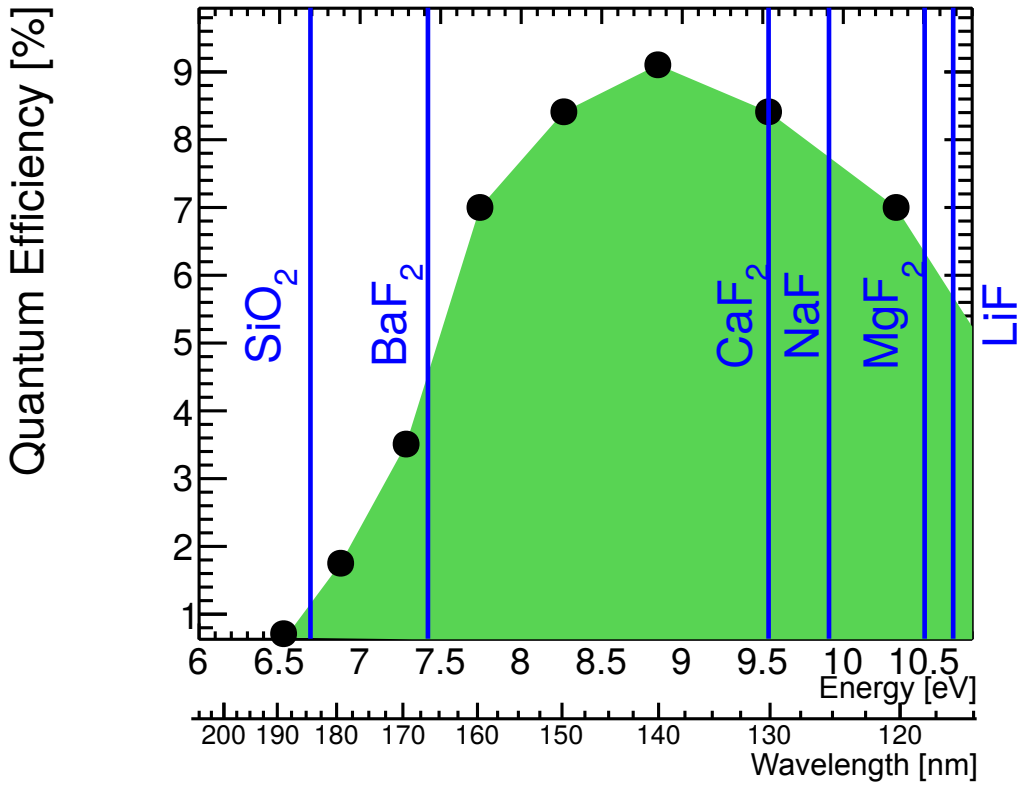

Figure 5.5: Quantum efficiency for a transmissive Cesium Iodide photocathode (green area) from Hamamatsu [2007]. The blue bars indicate the absorption edge where the internal absorption surpasses 50 %. The absorption edges were acquired from [Korth, c], [Korth, b], [Korth, a].

In Figure 5.5, the peak quantum efficiency (green) increases up to 9% for a CsI cathode in a transmissive mode according to Hamamatsu [2007]. The conversion range for this photocath-

ode is between 6.5 eV up to 10.5 eV or 100 nm to 200 nm depending on the absorption edge of the radiator material [Hamamatsu, 2007] [Bauer, 1995]. O_2 molecules in the air absorb photons in this wavelength region.
The choice of the photocathode also limits the options for the radiator. The radiator material should allow transmitting as many photons as possible for an optimal photon yield. For this reason, materials such as CaF_2, NaF, MgF_2, and LiF are desirable for a CsI photocathode that absorbs photons mostly in the VUV range.
For a semi-transparent photocathode, an ideal thickness between 10 nm - 15 nm was determined as for thicker layer electrons have a decreasing probability of escaping the medium while for thinner layers photons are transmitted through the photocathode without conversion to electrons [Francke and Peskov, 2016].

5.3 Studies of the Chromium Adhesion Layer

In addition to the CsI layer, the thin layer of Cr that is part of the photocathode must also be optimized. The layer can not be reliably simulated by the packages Geant4 and Garfield++, so it is important to measure that a homogeneous layer can be used and the layer's transparency is determined.
The Cr layer is situated between the radiator and the CsI layer (see Figure 5.6). Photons have to transmit through the layer for conversion. It is used for HV contacting to create an electric field in the drift gap between the CsI layer and the micro-mesh to create an electric field. Furthermore, it is an adhesive layer for the CsI on the crystals.

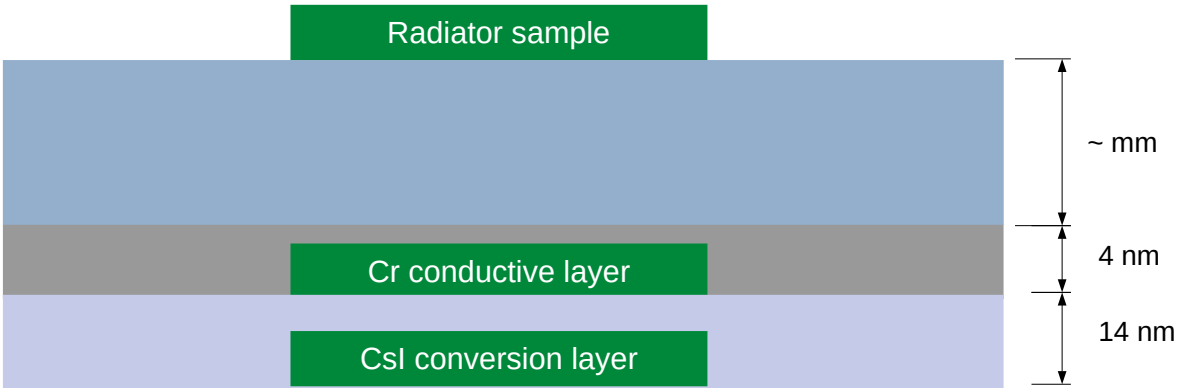

Figure 5.6: The radiator samples are evaporated as explained in Chapter 4 with a conductive layer made out of 4 nm thick Cr and the conversion layer of 15 nm thick CsI.

5.3.1 Resistivity Measurement of the Cr Layers

Chromium layers were evaporated onto small samples of SiO_2 with a thin layer of varying thickness for resistivity tests (see Figure 5.7). The focus in the production of this layer is thus providing a layer as thin as possible for maximum transmission while maintaining good HV distribution properties. The material must be conductive so that the photoelectrons created in the CsI layer drift toward the drift region of the detector.
Cr layers of varying thicknesses were produced on 20 mm diameter small SiO_2 with a thickness of 2 mm at LMU as well as TUM workshops.
The samples' sheet resistance R was measured with two spring contacts attached to a Fluke 289 True-rms multi-meter [FLUKE, 1993] averaged over four different points of the surface. Visible in Figure 5.8 are the electrical resistivities measured for the samples also partly shown

in Figure 5.7. The resistivity values ρ values were calculated from the measured resistances R and the Cr layer thicknesses d, yielding $R = \frac{\rho}{d}$. The reciprocal of ρ is the conductivity.
For the sample with $d \approx 4\,\text{nm}$, there is a high measurement uncertainty due to the two step production process. Here the sample's first layer was produced with 4 nm, and a second ring structure was created afterward for more accessible contact about 1.4 µm thick. The drawback is a loss of active conversion area on the photocathode. Unfortunately, the ring has not sustained but has peeled off (see Figure 5.7).

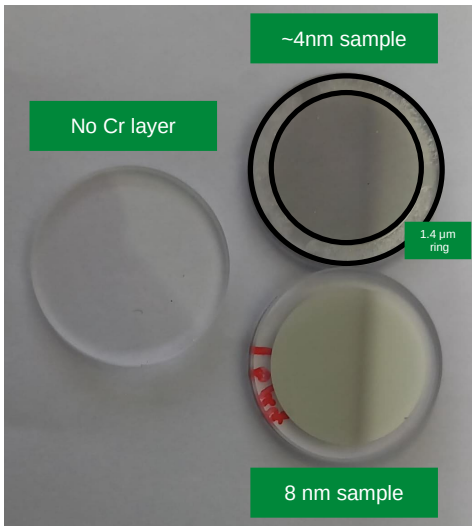

Figure 5.7: A picture of different SiO_2 samples with different Cr layer thicknesses. At 8 nm thickness, an already significant reflection is visible. The ≈4 nm sample contains a ring of thickness 1.4 µm Cr layer on the outside.

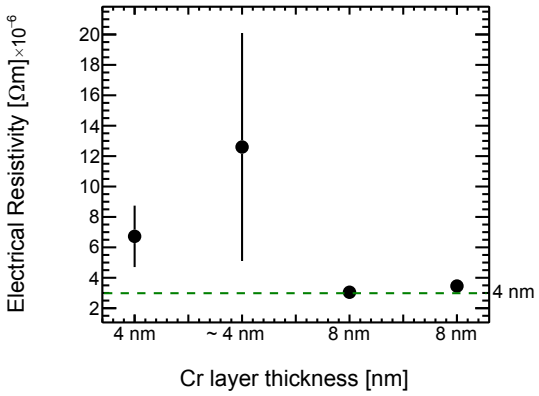

Figure 5.8: The resistivity for different Cr layer samples was measured on three points on the border of the small samples. The ≈ 4 nm layer produced by another machine than the other layers is not very homogeneous leading to a significant variation. A thicker metallic layer leads to better conductivity. The green line indicates data measured by Rajani et al. [2010].

The higher conductivity for 8 nm Chromium layers is observable compared to the 4 nm sample, as there is now a thicker conductive layer. The measured values' uncertainty is the smallest for the largest thickness of 8 nm while higher variations are visible for 4 nm samples. The literature value indicated by the green line agrees with the measured resistivity for the 8 nm samples [Rajani et al., 2010].
Likely, this is due to a high contribution of contact resistance which becomes much lower at 8 nm thick Cr layers and due to the handling of the spring contacts.
Ultimately, the three samples produced with the same method show a low variance in conductivity, meaning that there is a low variance in resistivity on the whole surface. The actual resistivity of the material is not of the highest importance as long as a homogenous electric field is created.

5.3.2 Transmission Measurement of Cr Layers with Varying Thickness

The second important property of the Cr layer is the transmission of photons. For this purpose, a measurement setup at TUM (see Figure 5.9 (b)) was used to quantify the photocurrent measured by a FGAP71 photodiode from Thorlabs (with an active area of 2.5 x 2.5 mm^2) [Thorlabs, 2017].
The emitted light is created by a deuterium lamp (h2 lamp) in the wavelength range of 100 nm - 200 nm [Hamamatsu, 2007]. Via a filter, only light with a wavelength of 192 nm

can reach the radiator and the photodetector. The whole setup has to be put under vacuum ($p \approx 10^{-5}$ mbar) otherwise the photons get absorbed by the air.
The resulting photocurrent was measured with a Keithley Digital multi-meter. The radiator with the Cr layer to be tested for transmission is placed directly above the photodiode. The sample is illuminated via the indicated hole of a few mm diameter so that only a small portion of the Cr layer transmits light (see Figure 5.9 (b)).

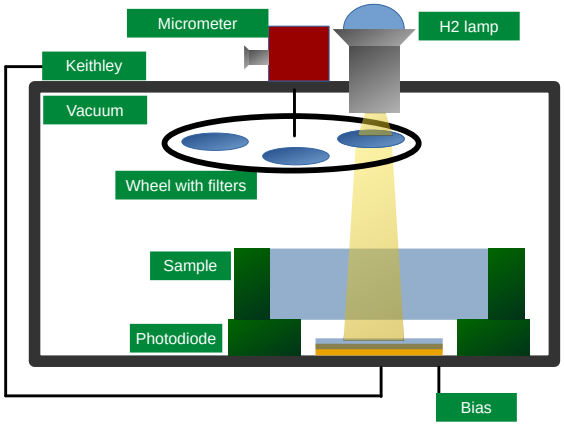

(a) Sketch of the transmission measurement setup at TUM.

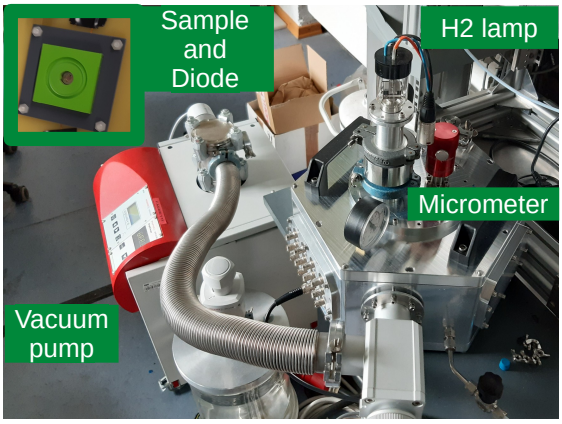

(b) A picture of the transmission measurement setup at TUM. The zoom in the top left shows the sample placed on the photodiode.

Figure 5.9: Setup for transmission measurements at TUM as a sketch (see fig. (a)) and (see fig. (b)) as a picture. The deuterium lamp (H2 lamp) illuminates the sample through 192 nm filter. The photocurrent created in the diode can be measured via a Keithley digital multi-meter and is proportional to the relative transmission.

Thus the transmission is proportional to the photocurrent of the photodiode at the selected wavelength ($T \propto I_{ph}$). The relative transmission for an uncoated sample is assumed as $T = 1$. Thus the transmission is calculated as $T_{rel} = \frac{I_{ph}}{I_{ph,uncoated}}$.

These values are shown for multiple Cr layers in Figure 5.10 measured for the relative transmission. The values measured agree with the values taken from [Ghosh et al., 2009]. Applying the Lambert-Beer law $I = I_0 e^{-ax}$ (see Section 1.2) with the extinction coefficient a from a fit to the data $a = (0.17 \pm 0.05)$ nm which agrees with the literature value of $a = (0.10 \pm 0.02)$ nm. The intensity becomes half of its intensity at $x = \frac{ln2}{\alpha} = 4$ nm. Thus 4 nm of Cr layer seems to be a good starting point between transmission and conductivity.

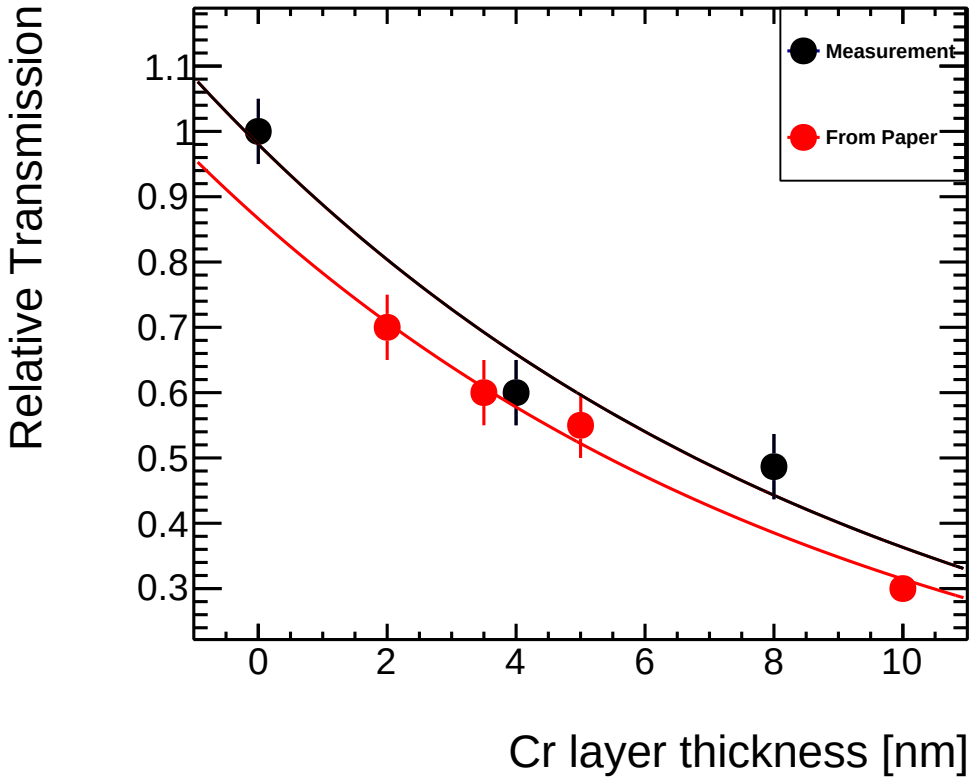

Figure 5.10: To test the relative light transmission T_{rel} through the Chromium part of the photocathode, small radiator samples were covered with a thin nm thick Cr layer. The measured relative transmission for different thicknesses of Chromium evaporated onto SiO_2 was fitted exponentially with a slope of $a = 0.17 \pm 0.05\,\text{nm}$ is in agreement with literature $a_{ghosh} = 0.10 \pm 0.02\,\text{nm}$. This transmission decreases according to the Lambert-Beer law exponentially.

5.4 The Ideal Cherenkov Radiator

The material's emission range is studied in the following in the VUV range as the photocathode used is CsI (see Section 5.2). The parameters of interest are the number of created photons N_{ph} and photoelectrons N_{pe} that will determine how well-defined the Cherenkov radius is for reconstruction methods. Furthermore, the Cherenkov angle θ_C of the photons and the distance of the photons from the muons are determined and discussed.

5.4.1 Momentum Detection of High Energy Muons

Since the main goal for the prototype is to reach a high number of photons sufficient for reconstruction. The choice is solid radiators due to their large photon yield. A solid radiator also simplifies the design because the radiator and photocathode can be directly attached to the detector lid. The liquid and gaseous radiator would require a more complex design to contain the radiator.
While liquid, gaseous radiators, and aerogel with small refractive indices have the merit to resolve high momentum particles as visible in Figure 5.11, the downside to them is the low number of created photons due to the low refractive index n according to the Frank-Tamm-formula (see Equation 1.5).
Aerogel, which is amorphous SiO_2, is a porous structure with voids between the atoms. If the voids are filled with air and since the porous structure, it can be produced with a refractive index between 1.0006 (low) and 1.2 (high) [Nappi and Seguinot, 2005]. Because the air does

not transmit in the wavelength interval 100 nm - 200 nm, such air-filled aerogels are not usable with a CsI photocathode.
With a refractive index $n = 1.2$ for aerogel the Cherenkov angle reaches its maximum already around at 1 GeV while with $n = 1.0006$ for aerogel around 4 GeV can be resolved. The maximum achievable Cherenkov angle of this material is, however, small. Pure gases such as Argon allow distinguishing higher energies (see Section 1.1).
According to the formula of the Cherenkov angle, different Cherenkov angles and, thus, different energies can be resolved by choosing different refractive indices n. To determine the resolution for different energies, the derivative of $\frac{d\theta_C}{dE}$ is calculated and solved for fixed values of the kinetic energy of the muon E and $\frac{d\theta_C}{dE}$ using that the Cherenkov angle θ_C is dependent on $\beta = \sqrt{1 - \frac{1}{\gamma^2}}$ and $\gamma = \left(\frac{E}{E_0} + 1\right)$ with E_0 the rest energy of the muon.

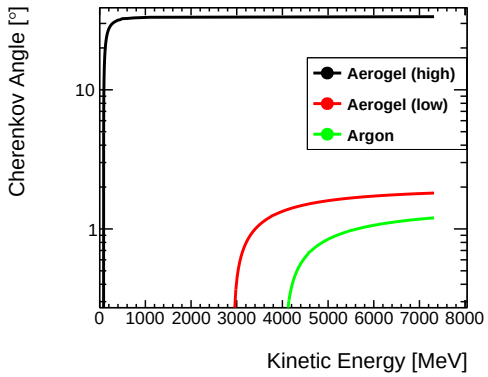

Figure 5.11: For different muon energies, the theoretical Cherenkov angle (log scale) of aerogels and Argon are calculated. To distinguish kinetic energies between 500 MeV up to 4 GeV, a combination of these radiators is required. When the Cherenkov angle reaches its maximum, no separation can be made. Refractive index values taken from [Nappi and Seguinot, 2005] [Bellunato et al., 2008] and [Bideau-Mehu et al., 1981].

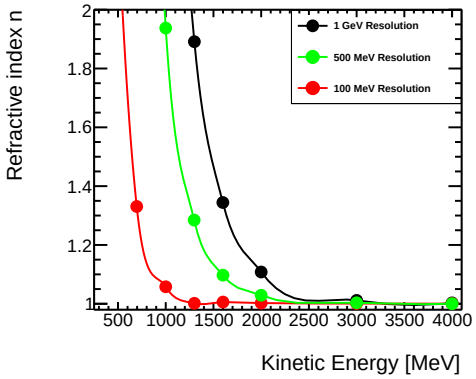

Figure 5.12: The required refractive index that is needed for the kinetic energy to be resolvable within an energy interval ΔE of 1 GeV, 500 MeV and 100 MeV for the spatial resolution of a Micromegas of $\sigma_R = 50\,\mu m$. Very low refractive indices are required to resolve a few GeV of kinetic energy for a muon.

Expressing then θ_C (see Equation 1.2) in terms of E gives:

$$\theta_C = \arccos\left(\frac{1}{n\beta}\right) = \arccos\left(\frac{1}{n\sqrt{1-\frac{1}{\gamma^2}}}\right) = \arccos\left(\frac{1}{n\sqrt{1-\frac{1}{(\frac{E}{E_0}+1)^2}}}\right) \tag{5.1}$$

The derivative of Equation 5.1 yields:

$$\frac{d\theta_C}{dE} = \left(n \cdot E_0 \cdot (\frac{E}{E_0}+1)^3 \cdot \left(1 - \frac{1}{\left(\frac{E}{E_0}+1\right)^2}\right)^{\frac{3}{2}} \cdot \sqrt{1 - n^{-2} \cdot \left(1 - \frac{1}{\left(\frac{E}{E_0}+1\right)^2}\right)}\right)^{-1} \tag{5.2}$$

The Cherenkov angle θ_C creates in a radiator of thickness d a cone of radius size:

$$R_C = d \cdot \tan(\theta_C) \tag{5.3}$$

In terms of spatial resolution, the cone diameter in a $d = 20\,\text{mm}$ thick radiator has to be larger than the spatial resolution of the Micromegas detector typically around $\sigma_{SR} = 100\,\mu\text{m}$, which is the lower limit to resolve a Cherenkov cone.

$$\sigma_{SR} = 2d \cdot \tan(\theta_{C,min}) \rightarrow \Delta\theta_C = \arctan\left(\frac{\sigma_{SR}}{2d}\right) = 0.143^\circ \tag{5.4}$$

$\frac{\Delta\theta}{\Delta E} = \frac{0.143^\circ}{\{100\,\text{MeV},500\,\text{MeV},1\,\text{GeV}\}}$ is considered for $\Delta\theta_C = 0.143^\circ$ (from Equation 5.3). This is the minimum angle resolution of the Micromegas for Cherenkov cones. Equation 5.1 is then rearranged to n and solved for fixed values of E visible in Figure 5.12.

$$n = f(E)|_{\Delta\theta=0.143^\circ} \cdot \Delta E \tag{5.5}$$

For different kinetic energies E of the muon, the refractive index n is shown as a function of the muon kinetic energy for energy intervals of $\Delta E = \{100\,\text{MeV}, 500\,\text{MeV}, 1\,\text{GeV}\}$.
Especially to resolve the energy of muons between 1 GeV and 4 GeV, multiple layers of aerogels and gaseous volumes like Argon are required.
Several layers of the materials could be used in one design to resolve the whole energy region at once.
Solid and liquid media can satisfy a high energy resolution at lower energies. However, even to get a coarse resolution starting at 2 GeV for the muon, a gaseous medium with $n \lll 1.1$ is necessary.

5.4.2 Refractive Index and Photon Yield

The compromise for the high momentum resolution of materials with low refractive index is a low number of photons. In solids, the refractive index is large, leading to a large amount of created photons which is important for the prototype. However, photons of different wavelengths experience different θ_C because of a variation in refractive index.
In case of no dispersion ($\Delta\theta = 0$ in Figure 5.13), the Cherenkov photon's position at the readout plane retains considerable uncertainty with increased dispersion. Also, this will broaden the Cherenkov cones and the resulting spatial distribution as some photons are emitted at larger angles than the average Cherenkov angle (see Section 1.1). Large deviations for the Cherenkov angles $\theta_C(\lambda)$ due to dispersion inside the material will lead to deviations of the reconstructed radii in Geant4 (see Section 5.1) and will influence the reconstruction.

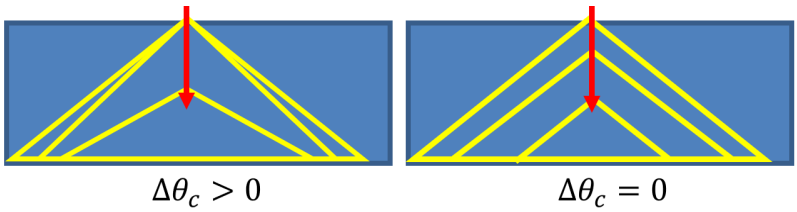

Figure 5.13: The sketch demonstrates the challenge resulting from the dispersion of photons in a given medium: In the right case, the photons (yellow lines) have no uncertainty on their position $\Delta\theta_C = 0$. A high variance $\Delta\theta_C > 0$ leads to many angles for the Cherenkov photons and, thus at different positions at the bottom of the detector when two photons with different wavelengths are produced at the same point.

A small $\Delta\theta$ is desired to achieve an unambiguous reconstruction of the photons and, thus, a satisfactory particle momentum resolution.
To calculate the expected Cherenkov angle θ_C and the photon or photoelectron yield, measured experimental parameters from various papers (see [Malitson, 1963], [Radhakrishnan,

1947], [H.H.Li, 1976], and [Li, 1980]) are evaluated by the Sellmeier formula which gives the refractive index as a function of the wavelength or energy:

$$n(\lambda) = \sqrt{\left(1 + \sum_i \frac{B_i^2}{\lambda^2 - C_i}\right)} \tag{5.6}$$

The Sellmeier formula is valid only for small n_I where absorption is negligible. These values are shown in Figure 5.14 (a) with their corresponding Cherenkov angle (see Figure 5.14 (b)) for a 4 GeV muon.
Materials such as SiO_2 and BaF_2 have only a small overlap with the conversion range of the photocathode due to their absorption edge. For this reason, they only allow a low number of photons to transmit and have a lower photon yield than the other listed materials.

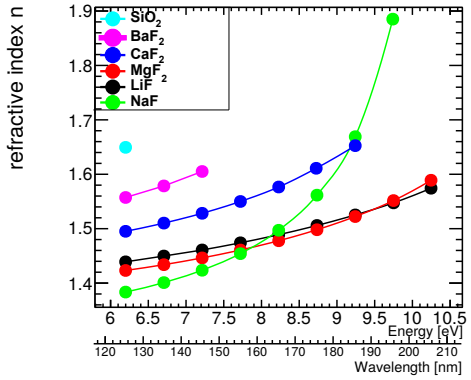

(a) Refractive index of potential Cherenkov radiators concerning the created photon wavelength or energy.

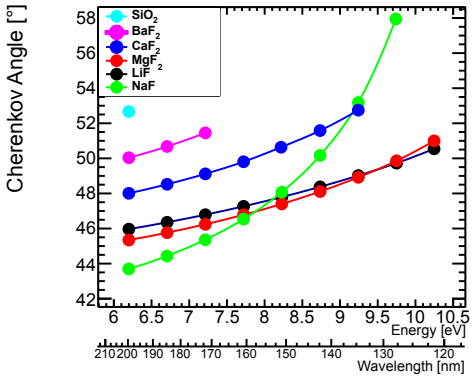

(b) Calculated Cherenkov angle of potential Cherenkov radiators concerning the created photon wavelength or energy.

Figure 5.14: The variance of the refractive index n in the VUV region (see fig. (a)) and the variance of the Cherenkov angle θ_C (see fig. (b)) are shown as a function of the photon energy in different materials. Achieving a high refractive index n with a small variance is desirable for a high photon yield with good energy resolution.

A significant deviation of the refractive index Δn e.g., in NaF, leads to a high variance in angle $\Delta\theta$ decreasing the reachable momentum resolution. This effect is due to the dispersion of the photons inside the material since each photon energy experiences a different refractive index (chromatic aberration, see Section 1.1.1).
The mean detected Cherenkov angle and its variance for these materials are visible in Figure 5.15 (a) for 10000 muons with 4 GeV traversing a 20 mm thick radiator, is simulated in Geant4 (see Section 1.1.1). The mentioned error also leads to significant ambiguity in measuring the radius (see Figure 5.15 (b)) visible in the case of NaF.
The mean radius and radii for the three or ten photons furthest away from the muon center (see Section 5.1) are determined by the simulation based on Geant4 except for the theoretically calculated radius. The theoretical radius is calculated according to Equation 1.11. The other radii using the most outer ten and three photons are nearly constant due to internal reflection inside the radiator.
In Figure 5.2, it is visible that the photons can be reflected from the radiator's walls. The photons' origin is most likely from the center of the cone. These reflected photons are also converted to photoelectrons but arrive at different positions than predicted by the Cherenkov angle. Thus these reflections have to be considered for the reconstruction of the angle, otherwise leading to miss reconstruction from the theoretically expected angle. The average radius is the closest radius to the theoretical radius. It is expected to be smaller than the theoretical radius as most photons sit in the center of the hit distribution close to the muon.

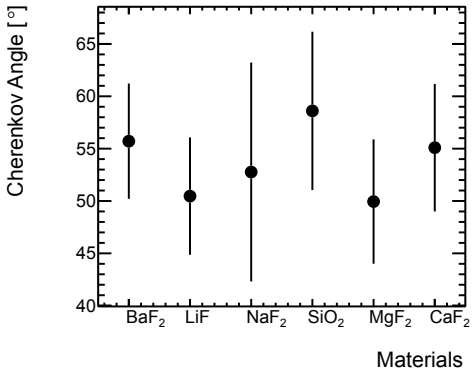

(a) Simulated average Cherenkov angles

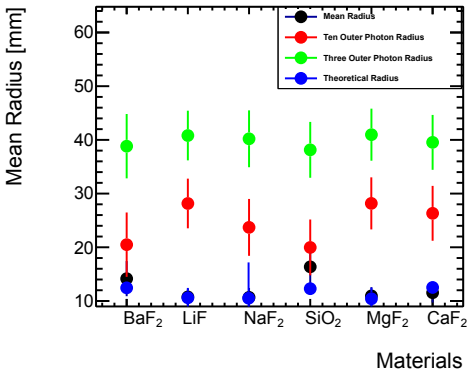

(b) The simulated three or ten most outer photons and mean radius of all photons per muon are compared to the theoretically calculated radii.

Figure 5.15: A high variation in the Cherenkov angle, error bars in (see fig. (a)) is less desirable since the error on the expected measured radius (see fig. (b)) leads to strong deviation for the determined radius from 10000 muon events in different radiators by Geant4. The solid radiators with $d = 20\,\text{mm}$ and diameter 100 mm have comparable radii. Due to the reflective properties, the radius stays constant for the three photons farthest from the muon. The theoretical radius is calculated according to Equation 1.11.

As previously stated, the photon radius is strongly dependent on chromatic aberration because it leads to a variance in the Cherenkov angle. The accuracy σ_β of the determined velocity β and can be expressed in terms of percentage where Δn is the variation of the refractive index and $\Delta\theta_C$ the contribution of the variation of the Cherenkov angle. $\left(\frac{\sigma_\beta}{\beta}\right)$ can be given by differentiating the Cherenkov angle (see Equation 1.2) [Nappi and Seguinot, 2005]:

$$\left(\frac{\sigma_\beta}{\beta}\right)^2 = (\tan(\theta_C)\Delta\theta)^2 + \left(\frac{\Delta n}{n}\right)^2 \tag{5.7}$$

Material	θ_C	$\Delta\theta$	n	Δn	$\frac{\sigma_\beta}{\beta}$ [%]
LiF	50	6	1.5	0.2	18.3
MgF_2	50	6	1.4	0.2	18.9
NaF	52	10	1.4	0.7	54.2
CaF_2	55	6	1.6	0.1	16.2
BaF_2	55	6	1.6	0.1	16.2
SiO_2	58	8	1.6	0.4	33.5

Table 5.1: The velocity uncertainty $\left(\frac{\sigma_\beta}{\beta}\right)$ of each radiator is calculated via the mean Cherenkov angle θ_C for a 4 GeV muon taken from Figure 5.15 (a) traversing the material. The variance of the angle $\Delta\theta$ and of the refractive index Δn is due to chromatic aberration.

For 4 GeV muons, the smallest uncertainty on the determined particle velocity is around 16% in the wavelength range of 100 - 200 nm. For a material with an absorption edge in the conversion region such as NaF, this leads to even higher uncertainties due to the increased refractive index.
To decrease this ambiguity while using the same radiators, a photocathode with a range in the visible region can be used since this range is very far from the absorption edge of the medium leading to a lower variance of the Cherenkov angle.
The BaF_2 and CaF_2 have lowest velocity uncertainty. BaF_2 is, unfortunately, unsuited for

a Cherenkov radiator because of its scintillating properties producing a large number of scintillation photons. The scintillation photons are irradiated in 4π direction. Compared to other materials, its scintillation emission spectrum becomes significant in the conversion region of the photocathode (around 200 nm) [Vladimirov et al., 2001]. LiF, MgF_2 and CaF_2 seem similar regarding uncertainty.
Via the refractive index as a function of the wavelength $n(\lambda)$ of a medium, the number of photons can be calculated in a radiator with thickness $d = 20\,mm$ more precisely, especially for the VUV region for every photon wavelength interval $\Delta\lambda$ using the Frank Tamm formula with the Cherenkov angle $\theta_C(\lambda)$ is now dependent on the wavelength (see Equation 1.5):

$$\frac{\Delta N}{\Delta \lambda} = \frac{2\pi z^2 \alpha}{\lambda^2} \sin^2(\theta_C(\lambda)) \cdot d \tag{5.8}$$

The number of photons within a wavelength region is determined over 100 intervals and is cut off at the absorption edges of the material (see Figure 5.5). The Cherenkov photons created for each wavelength interval are shown in Figure 5.16. While Figure 5.16 (a) shows the visible spectrum from 400 nm to 700 nm, the VUV region between 100 nm to 200 nm is shown in Figure 5.16 (b).
In the visible region, the photon yield stays nearly constant due to low variations of the refractive index as expected (see Section 1.1.1). The theoretical value determined by Equation 1.7 agrees with the number of photons created e.g., for LiF 20 mm thick with $\theta_{C,vis} = 48°$. The result for LiF with the integrated Frank Tamm formula (see Equation 1.7) yields 472 photons, while the sum above gives 472 photons.
In Figure 5.16 (b) a substantial increase is visible due to the close absorption edge, here the values of the rough approximation of Equation 1.6 (2439 photons with $\theta_C = 48.6°$ see Figure 5.14) does not agree with the shown values acquired from the summation over wavelength intervals (1860 photons). However, a significant contribution is due to the absorption edges in Equation 5.8. Also, NaF especially shows a large increase as it is close to the absorption edge of the material where n_I increases (see Section 1.1.1).

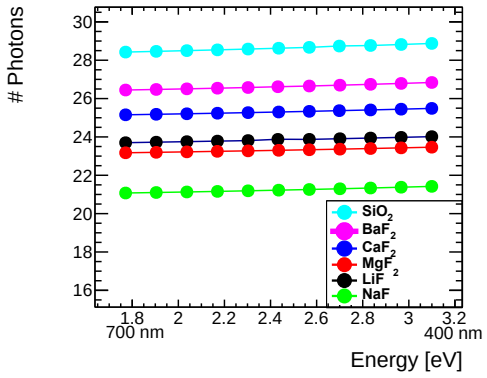

(a) Number of Photons per wavelength interval between 400 nm to 700 nm

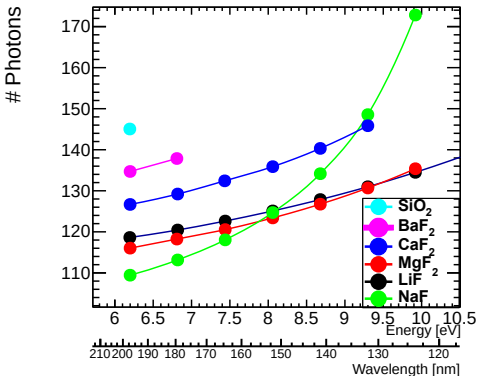

(b) Number of photons per wavelength interval between 100 nm to 200 nm

Figure 5.16: The refractive index (see Figure 5.14) is used to determine the number of created photons per wavelength interval via the Frank-Tamm formula. In the optical region from 400 nm to 700 nm (see fig. (a)), the number of created Cherenkov photons stays constant in comparison to the VUV region (see fig. (b)). Here a steep increase due to a close absorption edge is visible.

A way to verify the simulation results by Geant4 is to compare the simulated photon yield to the above-calculated values. 10000 muons with perpendicular incidence were simulated to traverse through 20 mm of different radiator material (see Figure 5.17). The number of photons (see Figure 5.17 (a)) produced in Geant4, e.g., in LiF with 2114±500 photons, is within error agreement with the above calculations. LiF also has the largest photon yield

compared to all materials. For this reason, LiF was chosen as the radiator material for the prototype detector. It has a high refractive index with a small angle variance and extensive coverage in the VUV region, while MgF_2 and CaF_2 are also considered relevant materials.
The number of photoelectrons (see Figure 5.17 (b)) created is determined by the number of photoelectrons entering the gas volume. For the radiator, it depends on the transmission of the radiator (T_R) for every photon per energy interval ($\frac{dN_{ph}}{dE}$) as well as the transmission through the Chromium layer (T_{Cr}) between the radiator and the photocathode.
Not taken into account inside the radiator is the electron extraction efficiency between CsI and the detector gas. For 4 nm thin layered Chromium 50 % transmission was assumed taken from [Ghosh et al., 2009]. Finally, the quantum efficiency of photocathode QE determines the number of converted electrons given by the final number of photoelectrons N_{pe}.

$$N_{pe} = \int N_{ph} \cdot T_R \cdot T_{Cr} \cdot QE \cdot dE \tag{5.9}$$

The number of photoelectrons left in case of 20 mm thick LiF is 70±10, which is the highest yield compared to all materials (see Figure 5.17).
The overall conversion efficiency to photoelectrons with LiF using the photons and photoelectrons from above $QE = \frac{70\,\text{photoelectrons}}{2214\,\text{photons}} = (3 \pm 1)\%$. It is close to agreeing with the theoretical consideration when using a peak quantum efficiency of 9 % and a Chromium transmission of $\approx$ 50 % [Hamamatsu, 2007] [Ghosh et al., 2009]. Using both values would be theoretically equal to $\approx 4.5\%$. In the simulations, $T_R \neq 1$ is accounted for, which yields a lower quantum efficiency than expected.

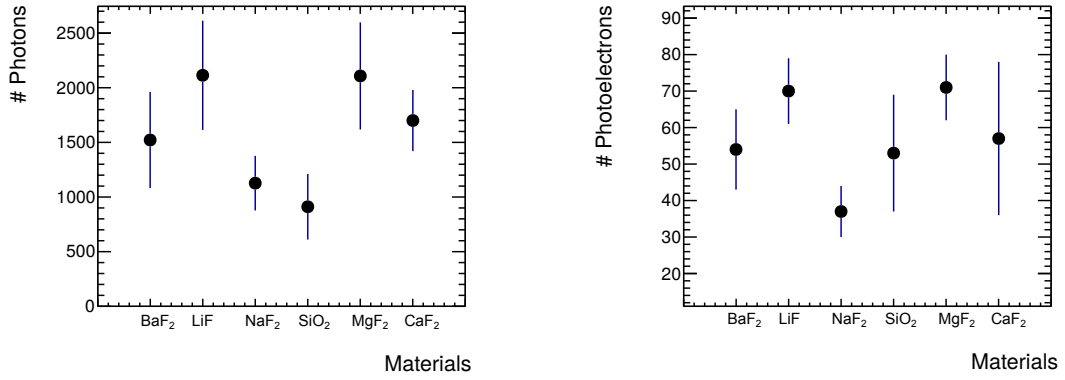

(a) Simulation of the average amount of generated photons

(b) Simulation of the average number of created photoelectrons

Figure 5.17: The number of created photons for 10000 muons in 20 mm thick materials in fig. (a) and number of photoelectrons in fig. (b) are the largest when a material has the highest overlap with the photocathode's conversion region such as MgF_2 and LiF.

5.4.3 Variation of the Radiator Thickness

Varying the radiator thickness will linearly increase the photon yield according to the Frank-Tamm formula (see Equation 1.5). As the radiator thickness increases, its cost also increases. Optimization according to the number of detectable photoelectrons has to be made.
The radius of the Cherenkov cone depends on the material thickness as well. The cone diameter should not exceed a few cm because the anode is 10x10 cm^2 large.
In the same Geant4 simulation for LiF with a diameter of 100 mm the thickness of the radiator was varied to determine the spatial photon distribution with the kinetic energy of the muon fixed at 4 GeV. The muon starts at the top of the radiator's center, traversing

the radiator without an inclination angle α. The different radii for various thicknesses are shown in Figure 5.18. A theoretical radius is determined with $\theta_C = 46.8°$ from Table 1.1 using Equation 1.11.

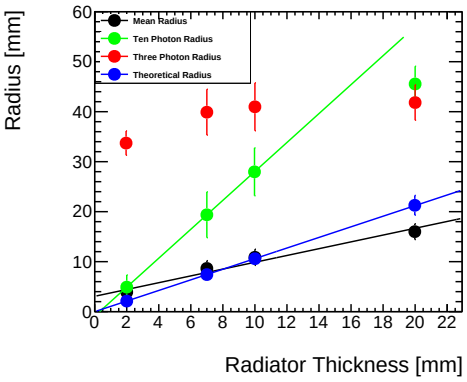

Figure 5.18: The simulated three or ten most outer photons and mean radius of all photons per muon are compared to the theoretically calculated radii as a function of different radiator sizes in LiF for 10000 muons. The theoretical radius and the mean radius increase linearly (with a slope of a =1.06±0.06 for the theoretical, a =0.89±0.2) with the thickness. For the outer photons this saturates at about 40 mm.

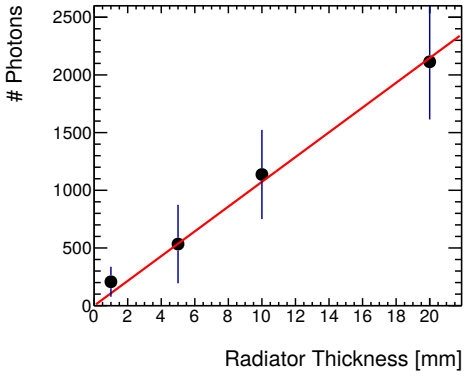

Figure 5.19: The number of Cherenkov photons created for 10000 muons inside the LiF radiator increases linearly as expected for different thicknesses. A line fit $a \cdot x$ gives a slope $a = (110 \pm 20)\frac{\text{photons}}{\text{mm}}$. This value is close to the calculated value from the Frank-Tamm formula with 113 $\frac{\text{photons}}{\text{mm}}$ (see Equation 1.6).

The theoretical radius, mean radius, and the radius given by the ten most outer photons increase linearly.
The radius for the three outer and ten outer photons increases to a maximum radius of 40 mm for a 100 mm sized radiator. A continuous increase would be expected for an infinitely large radiator for the outer photon radii. The radius for the three outer photons here is also consistent with the three outer photon radii shown in Figure 5.15 (b), where the value stays constant independent of the material.
Per mm of a radiator, a radius $r_{Ch} = d\tan(\theta_C)$ is expected. A linear function $a \cdot x + b$ is fit to the average, theoretical, and outer ten photons' radius. It results in a slope of a =1.06±0.06 for the theoretical, a =0.89±0.2 for the mean and a =2.9±0.6 for the ten most outer photon radius.
The reflected photons outside the original Cherenkov can explain the substantial radius difference for the ten and three outer photons to the theoretical consideration.
In Figure 5.19, the number of created photons with increasing radiator thickness is shown. The number of Cherenkov photons generated in the LiF radiator increases linearly as the radiator thickness varies. By performing a line fit $a \cdot x$, a slope of $a = (110 \pm 20)\frac{\text{photons}}{\text{mm}}$ is obtained. This value is quite similar to the computed value of 113 $\frac{\text{photons}}{\text{mm}}$ based on the Frank-Tamm formula, as demonstrated in Equation 1.6.

5.5 Energy Variation of the Incident Muons

In the following, the impact of varying the kinetic energy of a muon inside the 20 mm thick LiF radiator used in Chapter 7 is discussed.
A low number of photoelectrons or large angle deviation will decrease the accuracy of potential analytic fits (see Chapter 8).

The average value of created photons and photoelectrons varies with the kinetic energy reaching up to a maximum of 2214 photons (see Figure 5.20 (a)) for muons when approaching $\beta \to 1$. This increase is expected according to the Frank Tamm formula (see Equation 1.6). In Figure 5.20 (b), the number of created photoelectrons is shown, reaching at maximum 65 photoelectrons. The photoelectrons increase similarly and are convolved with the quantum efficiency of the photocathode.

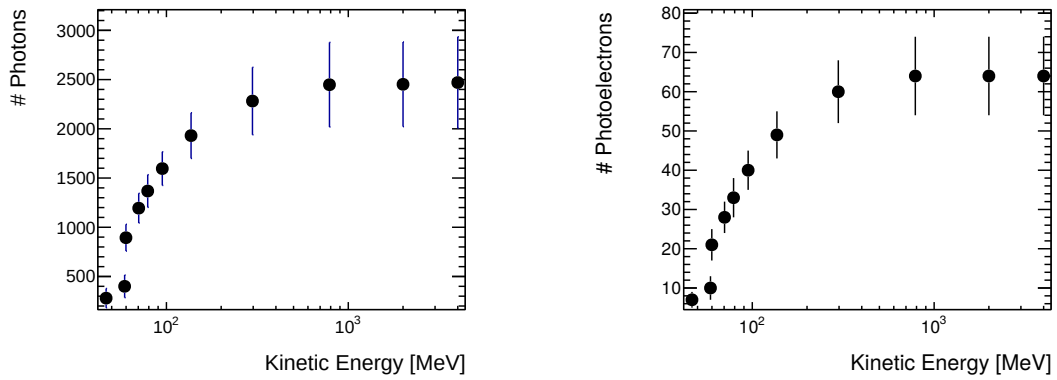

(a) Simulation of the average amount of generated photons for 10000 muons in 20 mm thick LiF.

(b) Simulation of the average amount of generated photoelectrons

Figure 5.20: The number of photons (see fig. (a)) and photoelectrons (see fig. (b)) increases with the energy of the traversing muons for 10000 muons in 20 mm thick LiF readout in the CsI layer. The maximum number reached in 20 mm thick LiF is 2250 photons and 65 photoelectrons at the photocathode.

For the Cherenkov angle θ_C an increase with the particle velocity (see fig. 5.21 (a)) or the muon's kinetic energy occurs (see fig. 5.21 (b)). In both cases, the simulated angle agrees with the theoretically calculated values within the errors. The mean radius of the Cherenkov cone increases from 5 mm to 20 mm.

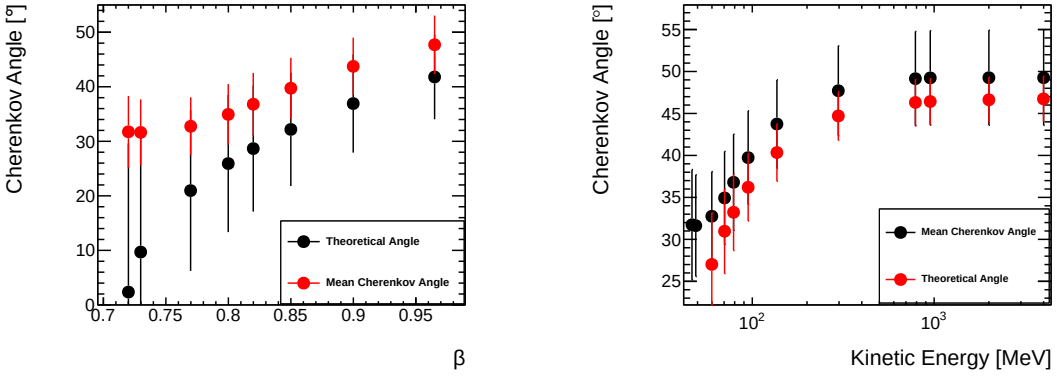

(a) Cherenkov angle as function β

(b) Cherenkov angle as a function of the kinetic energy

Figure 5.21: For increasing β in fig. (a) or increasing kinetic energy in fig. (b), the Cherenkov angle reaches around 47° (at 500 MeV or $\beta = 0.95$). Low velocities with low amounts of created photons lead to a variance deviating from the theoretical angle within errors.

In contrast, the radius of ten outer photons increases from 10 mm up to 40 mm (see Figure 5.22 (a) as a function of β and fig. (b) as a function of the kinetic energy). An explicit dependency of all radii except the three outer photons (green) is visible with increasing energy. The outer three or ten photons agree when approaching $\beta \to 1$, consistent with Figure 5.18. The average radius agrees with the calculated radius, while the radius for the ten outer photons shows a similar trend when the beforementioned radii are used.
Particle velocities higher than $0.9997c$ or starting at 1 GeV kinetic energy can not be resolved this way because the maximum Cherenkov angle has been reached.

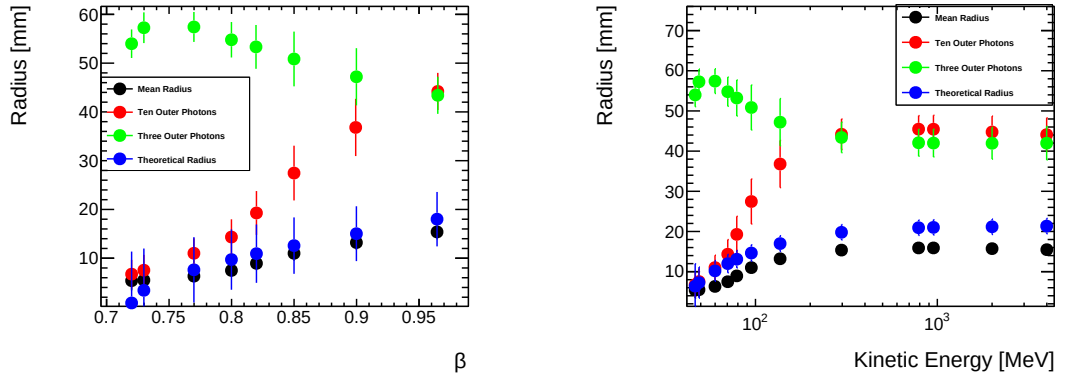

(a) Radii for different values of β.

(b) Radii for different values of kinetic energy

Figure 5.22: Simulated radii in 20 mm thick LiF comparing the three or ten most outer photons created by a single muon as well as the mean radius of all photons per muon to the theoretically calculated angle for different values of β (see fig. (a)) and kinetic energy (see fig. (b)). The average radius and the radius of the ten most outer photons show a similar behavior regarding the general course.

For the potential radiators of the Cherenkov Micromegas, the energy resolution ΔE was determined by applying Equation 5.3 to the refractive indices of CaF_2, MgF_2 and LiF (see Table 5.1) shown in Figure 5.23. The equation can be then solved for ΔE:

$$\Delta E = \Delta\theta \cdot \frac{dE}{d\theta}(E) \tag{5.10}$$

The kinetic energy E is compared to the minimum resolvable angle difference for Cherenkov photons $\Delta\theta_C = 0.143°$ (see Equation 5.3). MgF_2, CaF_2 LiF have a comparable refractive index. Here the refractive index variance is not included in the calculations. After reaching a kinetic energy of 1 GeV, the energy becomes hardly resolvable as ΔE becomes comparable to E to the kinetic energy. Not included in this is the angle variance due to the chromatic aberration inside the medium. This effect is taken into account by the Geant4 simulation. The kinetic energy of two particles can be differentiated when the spatial resolution of the detector is sufficient (see discussion in Appendix B).

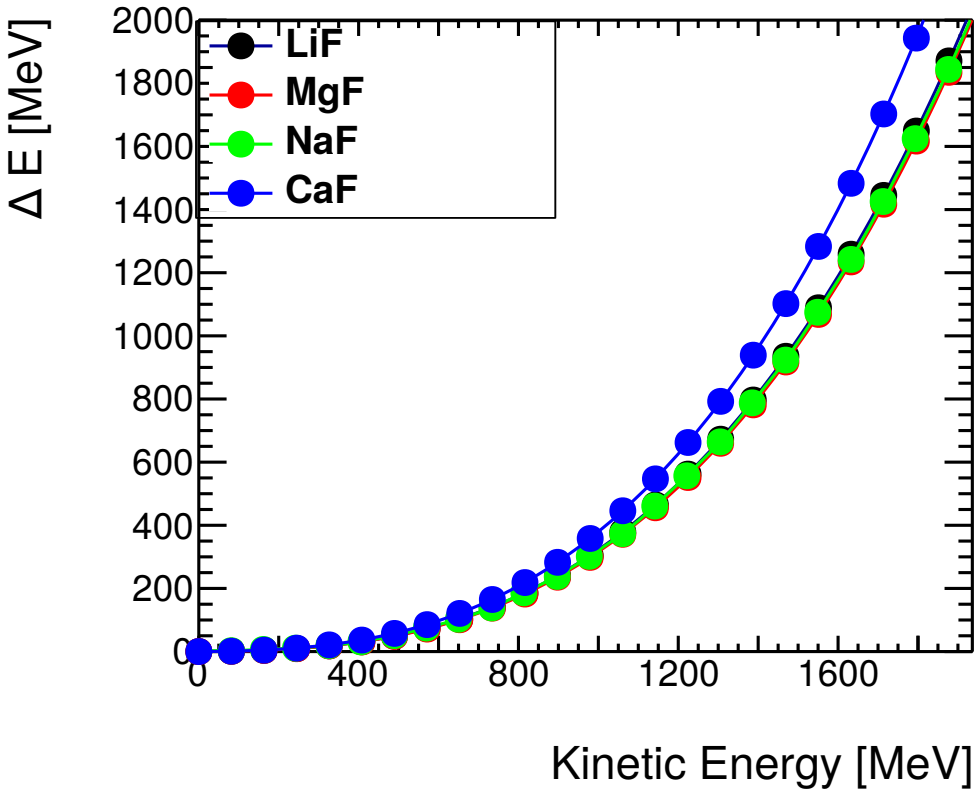

Figure 5.23: The energy difference ΔE is calculated by using Equation 5.5 with the material's refractive indices. At around E =1 GeV the energy difference using a spatial resolution of 50 µm becomes too high to differentiate different muons.

5.6 Summary

For the Cherenkov Micromegas detector, a CsI photocathode in transmission mode is used because of the high quantum efficiency in the VUV range of 100 nm - 200 nm while also being more facile in production compared to e.g., Bialkali.
As ideal radiator materials LiF, MgF_2 and CaF_2 have been determined due to their high photon yield in the far UV region. For a better momentum resolution, the material must be improved, e.g., by using liquids or solids, which is necessary to resolve high energy muons above $\approx$ 600 MeV. The Chromium adhesion layer is conductive, and its transmission agrees with literature values.
The combined quantum efficiency of the CsI 15 nm and Cr 4 nm cathode is 4.1 %.
A clear dependence of the average radius is visible for the kinetic energy or β. A similar dependency is shown for the number of produced Cherenkov photons or photoelectrons. Both parameters (radius and number of produced photons) could be potentially applied for the momentum reconstruction.

Chapter 6

Simulation of the Detector Characteristics

In this chapter, the geometry of the Cherenkov detector prototype is included in the following study to understand the signal based on the Geant4 and Garfield++ simulation (see Section 5.1). The expanded simulation includes the electron drift and avalanche processes provided by Garfield++. Further explored is the signal form of the muon cluster and photoelectron cluster.

6.1 Combined Simulation Workflow

The whole Micromegas detector with a 20 mm thick radiator using a diameter 50 mm LiF crystal is simulated by combining two programs, Geant4 and Garfield++. The first step uses a Geant4 simulation as explained in Section 3.5.1 with the output creating the x and y positions of the photoelectrons on the CsI plane.
The Garfield++ part lets the created photoelectrons drift in an Ar:CO_2 93:7 vol% mixture (see Figure 6.1). The reference position of the muon tracks x_{true} is assumed at half of the drift region of the detector. The starting point for the time is when the muon enters the gaseous volume. The electronic influences, e.g., readout electronics, are not assessed. The required number of hit strips for a cluster to be considered is two strips. The strip pitch of the detector is $p = 0.250\,\text{mm}$.
The photon feedback from the electron-ion pair recombination is not included in the simulation. This recombination mainly occurs in one or two mean free path lengths of an electron above the anode (see section 2.6). The applied voltages are $U_{Drift} = 350\,\text{V}$ and $U_{Amp} = 550\,V$ The used electrical fields are for the drift $E_{Drift} = 0.5\,\text{kV/cm}$ and $E_{Amp} = 43\,\text{kV/cm}$ for the anode for all simulations.
The drift region of the detector is 7 mm and the drift velocity of electrons $E_{Drift} = 0.5\,\text{kV/cm}$ voltage is determined as $0.47\frac{\text{mm}}{\text{ns}}$ which leads to a maximum drift time of 149 ns. The simulated drift size is different from the detector prototype's drift size of 6 mm which must be considered when comparing the results. In the avalanche region of size 0.128 mm, the Monte Carlo simulation produces the avalanche electrons.

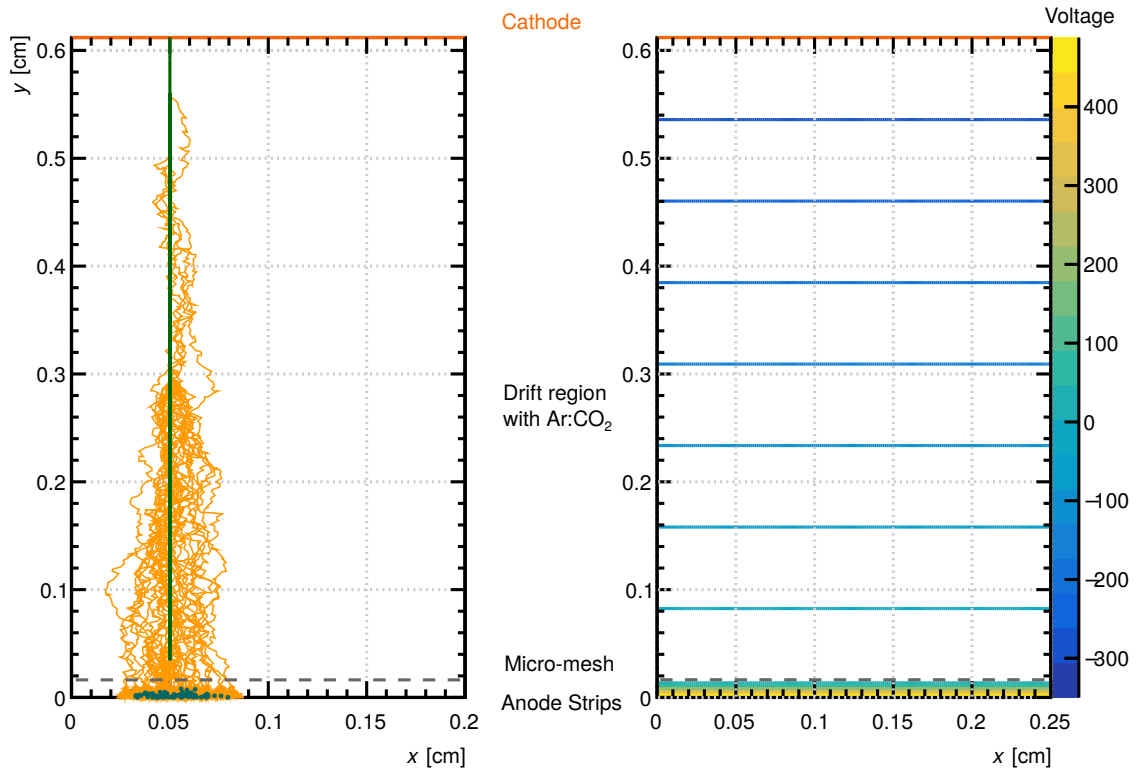

Figure 6.1: On the left, a Micromegas geometry implemented into Garfield++ with a muon traversing through the drift region in the Micromegas afterward, muon electrons and photoelectrons create Townsend avalanches. On the right, the electrical field is indicated. The applied electric field or voltages are for $E_{Drift} = 0.5\,\mathrm{kV/cm}$ and $U_{Amp} = 550\,\mathrm{V}$ for the anode.

As information, the charge, x, and y position, and the signal timing of the created avalanche electrons are recorded (see Figure 6.2 (b)). Afterward, the position information is converted into strip information to determine the cluster position in Garfield++. Typically, muon clusters overlap spatially with photoelectron clusters (see Figure 6.2 (a)).

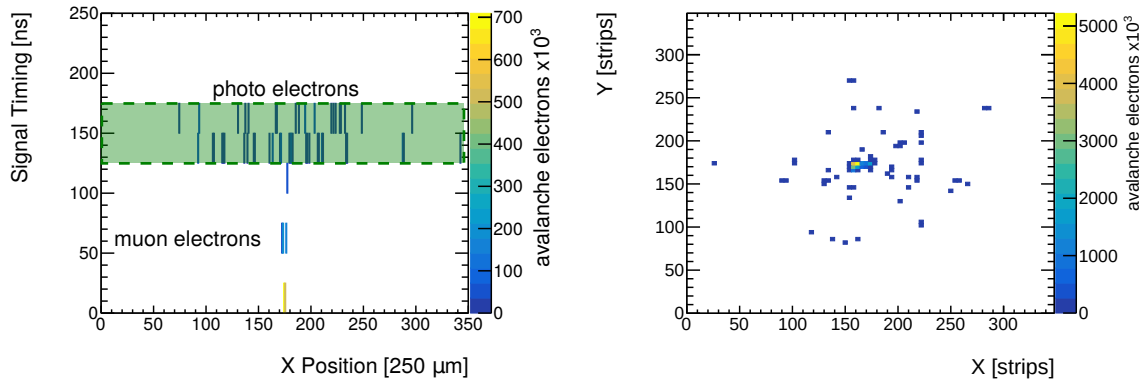

(a) 1D hit information

(b) 2D hit information

Figure 6.2: The raw event of a 4 GeV muon and its photoelectrons is visualized. The applied electric field or voltages are for $E_{Drift} = 0.5\,\mathrm{kV/cm}$ and $U_{Amp} = 550\,\mathrm{V}$ for the anode. Examples of simulated photoelectrons in Garfield++ fig. (a) are shown for segmented 1D strip information, and fig. (b) shows the 2D hit information.

6.2 Number of Drift Electrons

Firstly, the Micromegas is simulated without photoelectrons passing through it before moving on to events with photoelectrons. The simulation results are then compared to those including photon clusters to determine any overlap.

6.2.1 Muon Drift Electrons

According to the Bethe-Bloch formula, a cosmic muon creates the primary electrons inside a Micromegas due to gas ionization (as discussed in Section 2.1).
Compared to perpendicular particles, muons inclined by an incidence angle α traverse a larger region inside the detector (see Figure 6.3). The deposited charge is expected to increase linearly with the path length L inside the detector $Q \propto \frac{\mathrm{dE}}{\mathrm{dx}}$:

$$L = \frac{d_g}{\cos \alpha} \tag{6.1}$$

The theoretically hit multiplicity of the addressed strips N_s can be calculated with the drift space size $d = 7\,\mathrm{mm}$ and using the pitch of the detector $p_s = 0.25\,\mathrm{mm}$. It also depends on the incidence angle α:

$$N_s = \frac{\Delta x}{p_s} = \frac{d}{p_s} \cdot \tan(\alpha) \tag{6.2}$$

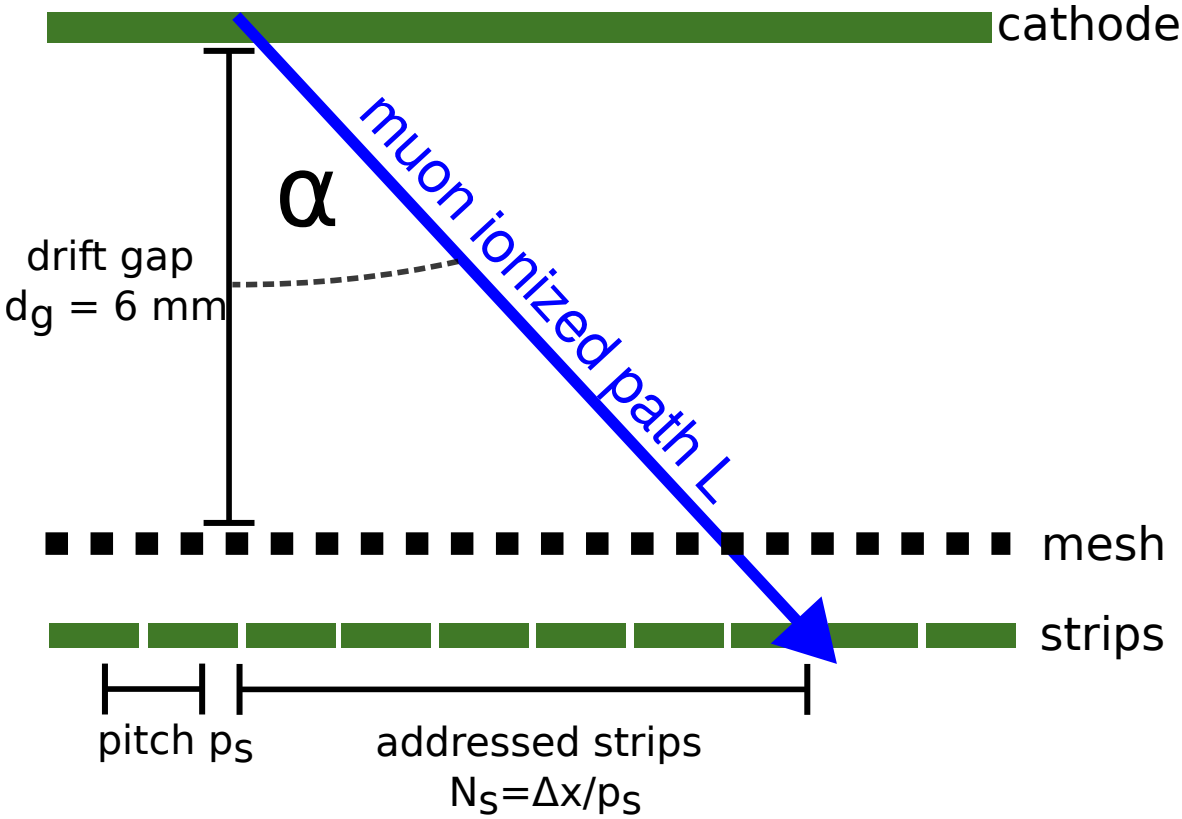

Figure 6.3: When a muon traverses the drift region of a detector with an inclination α, the length it can ionize the gas is $L = \frac{d_g}{\cos(\alpha)}$. This distance is increased compared to the perpendicular case. Thus also the number of created electrons is larger. Similarly, a muon cluster's number of addressed strips is larger for an inclination angle α (see Equation 6.1).

As a comparison, 10000 muons at 4 GeV are propagated through the detector for different angles of incidence in Garfield++. A Landau shape is expected for the number of drift electrons, as discussed in Section 2.1. The Landau distribution is fit to the simulation, and the most probable value is used (see Figure 6.4 (a)).
Visible is that the number of drift electrons produced increases according to expectation marginally at about 4 electrons when the angle increases to 25°. The increase is proportional to $\frac{1}{\cos\alpha}$ (see Equation 6.1). The influence of the angle is small concerning the number of drift electrons. The number of created drift electrons deviates from Bortfeldt [2014] where 49 e have been measured in Ar:CO_2 93:7 vol.% in 6 mm. for 80 GeV muons. A reason for this discrepancy is the larger energy loss expected from the Bethe Bloch formula (see Section 2.1) when compared to 4 GeV muons leading to a larger number of primary electrons due to gas ionization.
The number of hit strips increases from a mean value of 5 to 15 at maximum (see Figure 6.4 (b)). The theoretical values range from 2 strips at 5° to 13 strips at 25° (see Equation 6.2). The theoretical calculation (black points) is purely geometric, so no point exists at 0°. Missing in this consideration is the extension of the electron avalanches.

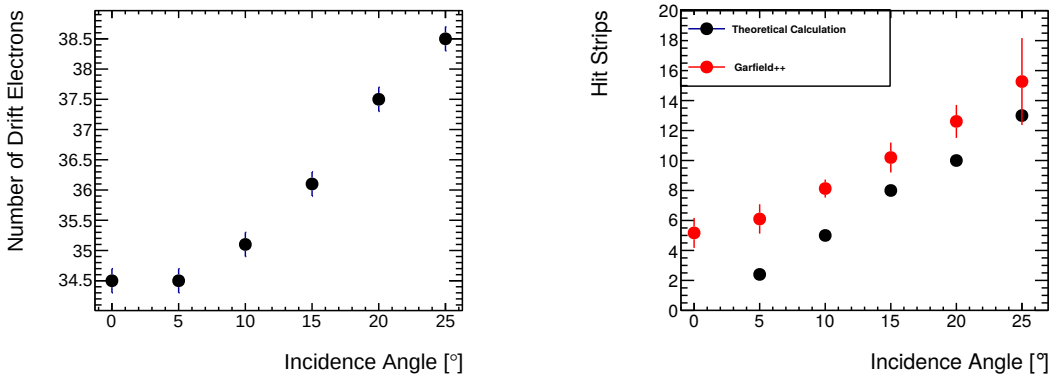

(a) Amount of drift electrons simulated by Garfield++

(b) Number of hit strips simulated by Garfield++

Figure 6.4: For different muon incidence angles, the number of created drift electrons (see fig. (a)) and hit strips (see fig. (b)) in a Micromegas with a drift gap of 7 mm were simulated. The number of adressed strips for a muon ranges from 5 to 15. The difference between the theoretical calculation of the two strips is due to the missing avalanche extension in the geometric considerations.

A low number of muon electrons might be of interest to studying the photoelectron signal thoroughly so that a low overlap exists between the muon cluster and the photoelectron cluster.
The ionization electrons in detectors with various drift sizes while using a drift voltage of $U_{drift} = 350\,\text{V}$ is shown in Figure 6.5. The number of electrons created by a muon in the drift region changes linearly, with the length in the drift region increasing. A linear fit $a \cdot x + b$ yields a slope of $a = 5.0 \pm 1$ electrons per mm.

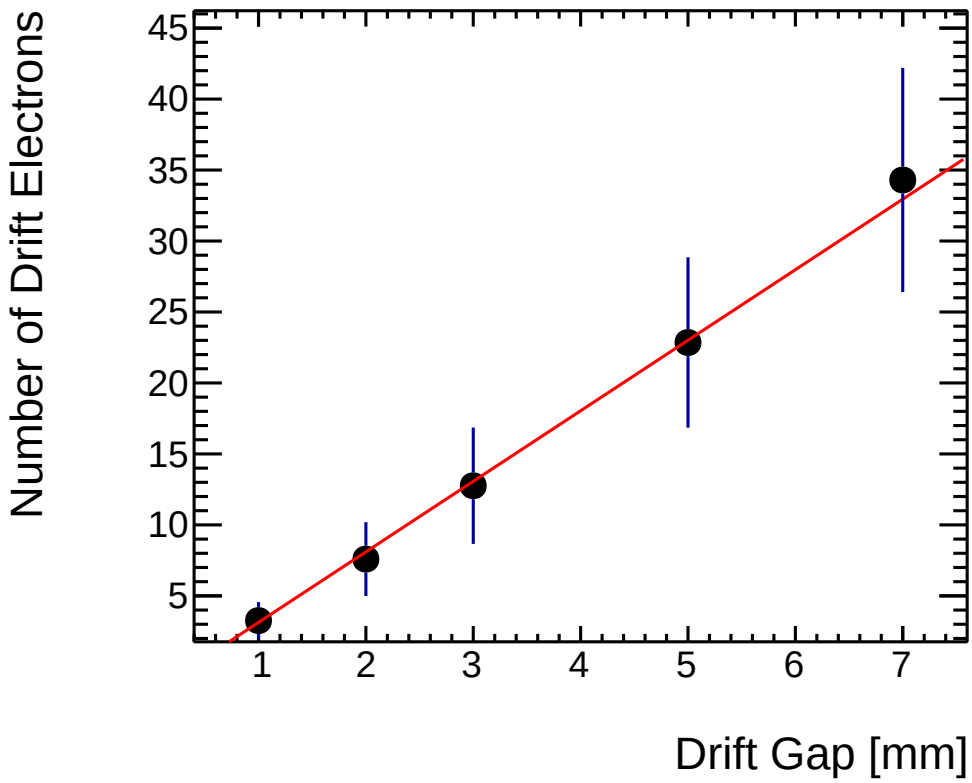

Figure 6.5: For distances between the cathode and mesh, the number of created drift electrons were simulated for a drift voltage $U_{drift} = 350\,\text{V}$. The number of created photoelectrons is indicated in green (see Section 6.2.2). The linear fit result has a $a = (5.0 \pm 1)$ electrons/mm slope.

6.2.2 Photoelectrons

Finally, the photoelectrons are accounted for in the combined simulation with Garfield++ and Geant4. As stated, the incidence angle α varies between $\pm 25°$ according to a $\cos^2 \alpha$.
A Gaussian distribution with a mean energy of 2 GeV is used as energy distribution. Higher energies show no significant change in the production of Cherenkov photons inside the radiator (see Section 1.1).
The number of photoelectrons created in the 20 mm thick CsI layer yields an average of 70 ± 12 photoelectrons (see Figure 6.6 (a)). The number of photoelectrons agrees with the calculated values from Section 5.5. Due to the radiator's size, reflections decrease the number of extracted photons. For this reason, the distribution is not Gaussian.
The number of extracted photoelectrons into detector gas decreases from an average of 89 photoelectrons in CsI to $N_{pe} = 39 \pm 9$ (see Figure 6.6 (b)).
The extraction efficiency of photoelectrons into a vacuum would be 100%. Due to elastic backscattering of electrons, especially in noble gases, however, the extraction efficiency is reduced (see Section 2.6) [Di Mauro et al., 1995]. The backscattering effect leads to a simulated cathode-to-gas extraction efficiency of $\epsilon = 55\%$ between Figure 6.6 (a) and (b). The whole detector's total single photon detection efficiency is $4.1\% \cdot 55\% = 2.28\%$ with the quantum efficiency from Section 5.4.2.
The number of muon electrons created by the muon via gas ionizations is around $N_\mu = 31 \pm 8$ muon electrons (see Figure 6.6 (b)). This number is similar as discussed in Section 6.2.1. The number of muon electrons is in the shape of a Landau distribution due to the $\frac{dE}{dx}$ loss (see Section 2.1).

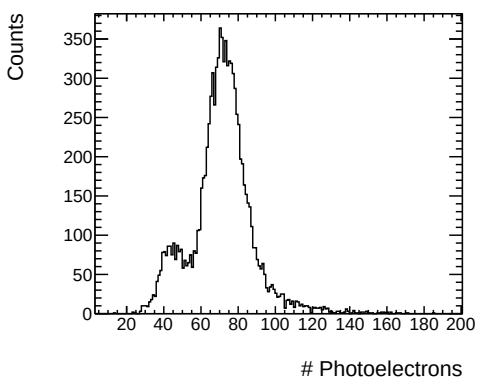

(a) Created photoelectrons (Geant4).

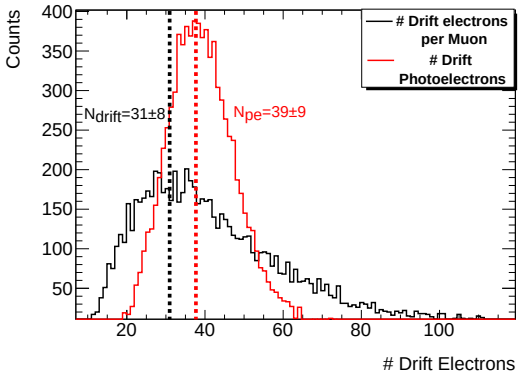

(b) Muon electrons for muons and photoelectrons extracted into the gas (Garfield++).

Figure 6.6: The extracted Cherenkov photoelectrons for 20000 muon events of a d =20 mm radiator with an average of 70 ± 18 photoelectrons of the simulation (see fig. (a)). A small tail toward fewer photoelectrons is visible due to internal reflections. In fig. (b), the photoelectrons $N_{pe} = 39 \pm 9$ extracted into the gas are compared to the ionization electrons created by the muon $N_{drift} = 31 \pm 8$ with a strong tail to larger values.

As the number of electrons produced is proportional to the deposited charge inside a detector, the factor f_{ele} is used to compare the pulse height created by photoelectrons and muon later in the experiment (see Chapter 7):

$$f_{ele} = \frac{N_{pe}}{N_{\mu}} = \frac{39 \pm 9}{31 \pm 8} = 1.3 \pm 0.4 \tag{6.3}$$

6.3 Position Distribution of the Photons

The photoelectrons produced inside the photocathode by Geant4 are shown as a projection along the x axis of the detector in Figure 6.8. For this reason, studying the spatial distribution of photons simulated by Geant4 is of interest. Two LiF radiators of diameter 50 mm and 100 mm were simulated to differentiate border effects. For the $\cos^2 \alpha$ law of cosmic muons, most enter the detector with $\alpha = 0°$. At the borders of the radiator, the acceptance decreases due to reflections occurring, leading to a lower number of detected photons for the same number of incident muons (red curve in Figure 6.8).

The average photon distance (see Section 5.1) for the ten outermost photons is shown in Figure 6.7 (a). Here a strongly defined peak is visible for a radiator of size d =50 mm at a distance of (23.68 ± 0.05) mm and for a radiator of d = 100 mm at a distance of (48.66 ± 0.07) mm. A Gaussian distribution is also visible below the peak for the larger radiator. These photons are not reflected at detector walls due to the larger size of the radiator. Here the photons have a mean distance of 43 ± 5 mm.
Inside a radiator with radius r_{rad} and thickness d, the rough position of a reflection photon $x_{refl} = r_{rad} - \Delta_{refl}$ can be estimated (see Figure 6.9). An incident photon created at the position z_{ph} with Cherenkov angle θ_C can be reflected according to Snell's law by the same angle [Zinth and Zinth, 2018]. For a photon created in the center of a LiF ($\theta = 46.8°$ see Table 1.1), two reflections are expected.

According to Equation 1.11 the distance after creation r_{ph} and after the first reflection r_C is

$$r_C + r_{ph} = (d + z_{ph}) \cdot \tan \theta_C \tag{6.4}$$

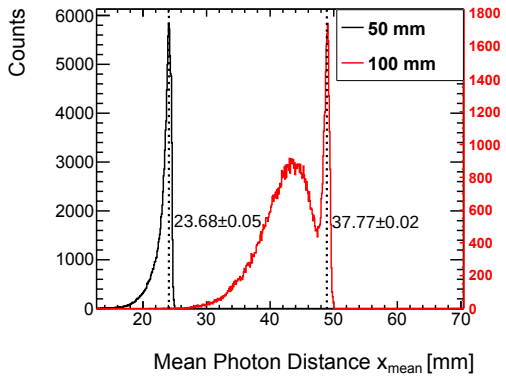

Figure 6.7: The simulated photoelectron distance relative to the position of the cosmic muon inside the radiator averaged over the ten outer photons. Evident in both distributions is a dominant peak because of reflections at the radiator walls and borders.

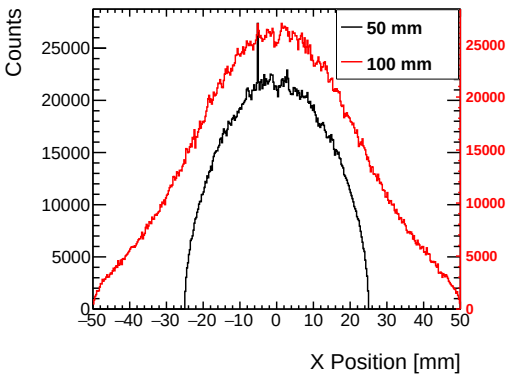

Figure 6.8: The histograms show the individual positions of all created photoelectrons arriving in the CsI. For the 50 mm case, the distribution is cut off at the border of the radiator at ±25 mm. This simulation is produced by Geant4.

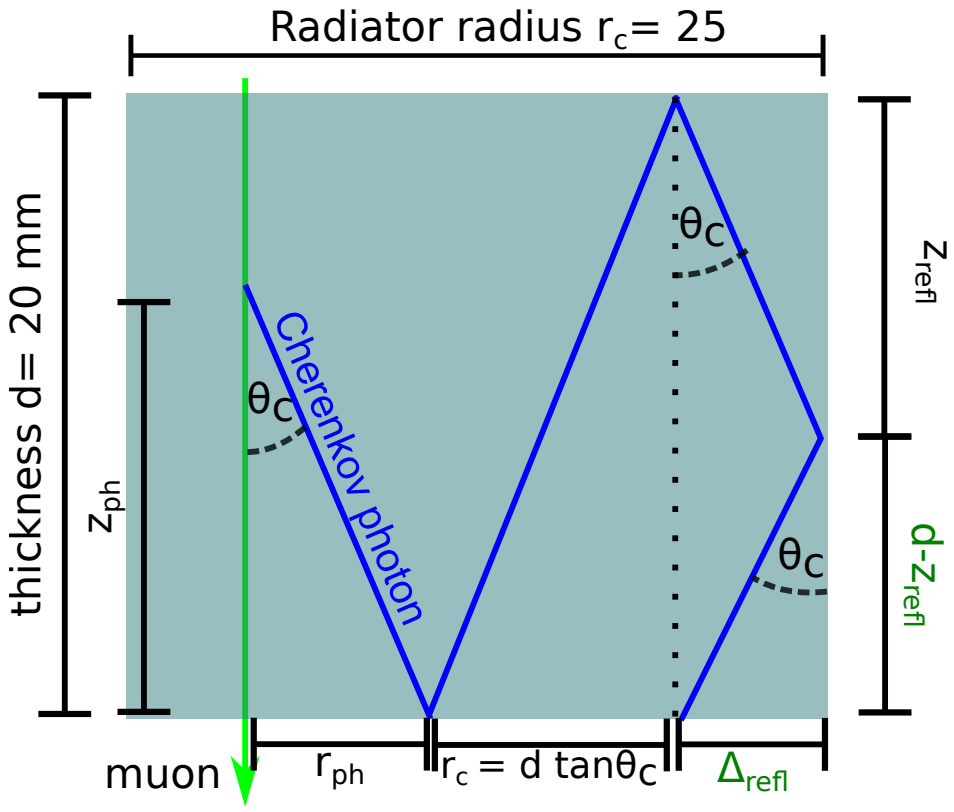

Figure 6.9: The position of the reflected photon at the radiator's center $x_{refl} = d - \Delta_{refl}$ can be calculated for a Cherenkov photon created at z_{ph}. Depending on z_{ph}, the position where the photon is reflected from the radiator wall can be determined.

Similar to the position z_{refl} where the photon is reflected from the wall can be determined as

$$z_{refl} \cdot \tan\theta_C = r_{rad} - r_{ph} - r_c \rightarrow z_{refl} = \frac{r_{rad} - r_{ph} - r_c}{\tan\theta_C} \tag{6.5}$$

Finally the position of a reflected photon is

$$x_{refl} = r_{rad} - \Delta_{refl} = r_{rad} - z_{refl} \cdot \tan\theta_C = r_{ph} + r_C = (z_{ph} + d)\tan\theta_C \tag{6.6}$$

The reflected photon position of a radiator with size 50 mm is then calculated for a $z_{ph} = (0-2)$ mm as most projected photons are here (see Figure 1.4) with the angle variation of $\Delta\theta = 5°$ (see Table 5.1) is $x_{refl} = (20\pm6)$mm. For a radiator with size 100 mm the position is around $x_{refl} = (42\pm6)$mm. This value agrees with the reflection peaks in Figure 6.7.
In the following, the Geant4 data is inserted into Garfield++. The radiator used to investigate the detector's energy resolution is of size 100 mm.
The result for the residual $(x_{mu} - x_{pred})$ of the photoelectron clusters to the muon position on a strip anode is shown (see Figure 6.10). The muon is incident around 0 mm of the hit distribution. This is the reason for the gaps in the following histograms showing the residual of the photoelectrons as the photoelectrons adjacent to the muon are cut. In Figure 6.10 (a), the reconstructed position was determined by varying only the energy with a constant angle $\alpha = 0°$ incoming at the center of the radiator (black curve) and also varying both the angle according to the $\cos^2\alpha$ distribution as well as the incidence position on the radiator surface (red curve). In the first case, the Gaussian standard deviation is (11.47 ± 0.03) mm while including angle and positional variance (15.77 ± 0.03) mm are reached. For large angles above 15°, the distribution becomes slightly asymmetric (see Figure 6.10 (b)).

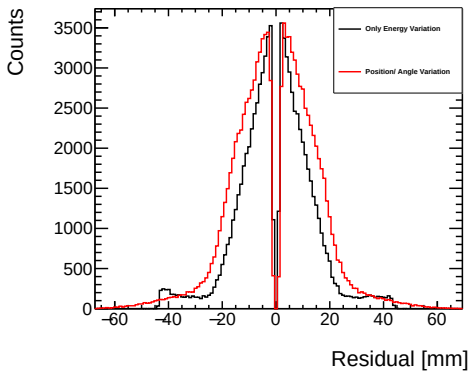

(a) Cluster distance of all photoelectrons in Garfield++

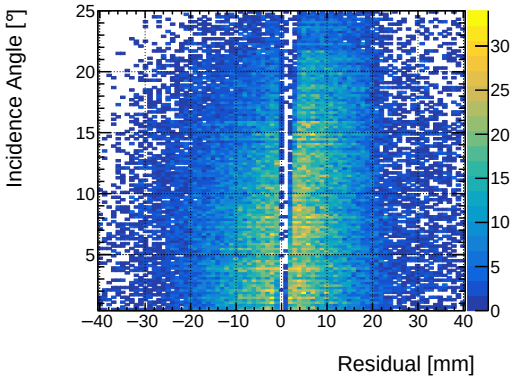

(b) Cluster distance as a function of the angle in Garfield++

Figure 6.10: The position of the photoelectron clusters relative to the muon is the residual shown for a LiF crystal with 50 mm, and 100 mm diameter has a standard deviation of $\sigma = 11.45 \pm 0.03$ mm for perpendicular cosmic muons of different energies determined via Gaussian fit. Introducing the positional variation across the radiator and the $\cos^2\alpha$ angle spectrum yields a larger standard deviation $\sigma = (15.77 \pm 0.02)$ mm. The residuals slightly become asymmetric for $\alpha > 15°$ visible in fig. (b). As the muon cluster is filtered, a gap is created around 0 mm.

The muon and photoelectron residual Δx is determined via the centroid method (Section 3.3.2) and compared to the strip multiplicity (see Figure 6.11 (a)). The muon cluster is reconstructed close to the actual position with a width of (120 ± 17) µm determined by a Gaussian fit of the 1D projection. The expected spatial resolution is around 50 µm [Alexopoulos et al., 2014]. Using the centroid method becomes problematic for an angle above 8° [Ntekas, 2016]. In the experimental setup (see Chapter 7), the use of the centroid method will also influence the reconstruction accuracy as angles up to 22° are allowed by the geometry.
The photoelectron cluster show, as expected, a prominent peak at the center and a decreasing amount of addressed strips towards larger relative positions (see Figure 6.11 (b)). Also important to note is that the distribution is broadened due to the avalanche behavior inside the detector. Finally, the question is how much the spread of the Cherenkov cone behaves with increasing energy in the Micromegas detector, as the goal of the detector is to determine the particle's energy.

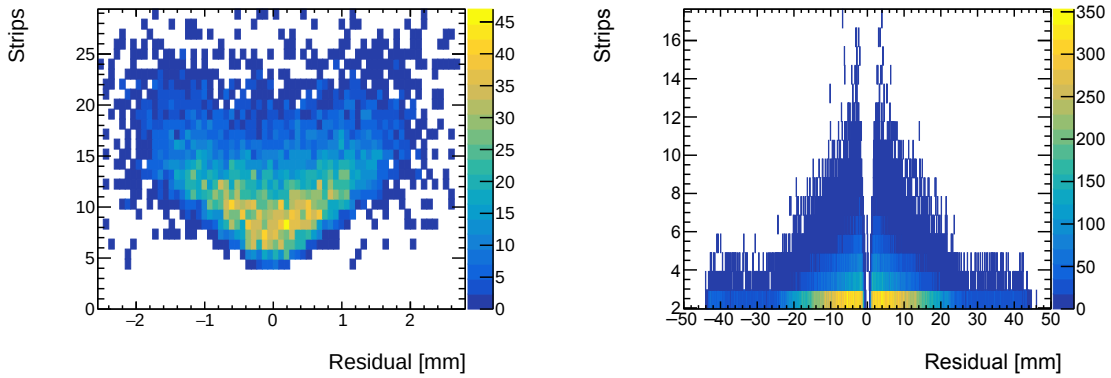

(a) Muon cluster in Garfield++

(b) Photon cluster in Garfield++

Figure 6.11: The residual of the muon (see fig. (a)) increases in a parabolic shape number of addressed strips. The photon clusters (see fig. (b)) show a decrease with larger residuals due to the expected decrease with further distance from the muon.

For different energy values, 1000 cosmic muons and the created photoelectrons were simulated in the gas gap region of the Micromegas with Garfield++ (see Figure 6.12 (a)). An increase in the cone size is visible with increasing energy according to expectation (see Figure 5.22). As a measure for the size of the Cherenkov cone, the standard deviation of the photoelectron position is used (see Figure 6.12 (b)). The standard deviation saturates at around 15 mm at around 600 MeV, meaning higher energies can no longer be distinguished. As expected from calculations, the difference above 600 MeV in kinetic energies can, thus, not be resolved with this radiator (see Figure 5.23). However, a cone size difference can be determined below this energy. The possible application for reconstruction methods is further studied in Chapter 8.

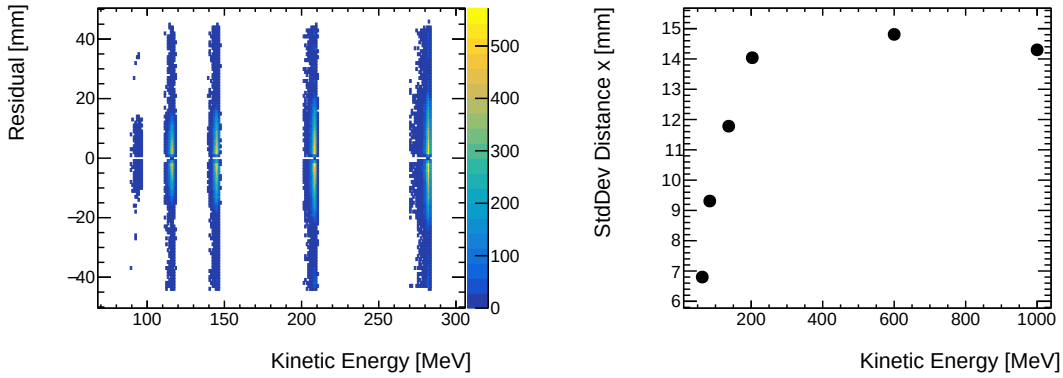

(a) Relative photoelectron position per energy in Garfield++

(b) The standard deviation of the relative photoelectron position along x

Figure 6.12: The relative position of photoelectrons to the muon varies with the energy reaching a plateau at around 600 MeV for 1000 muons. The muon cluster is excluded. The most probable value for the muon is at 2 GeV. Such high energies will become difficult to resolve by measuring cosmic muons.

6.4 Strip and Cluster Distribution

The strip and cluster multiplicity inside the detector is compared in the next step.
These properties can be used for the separation of muon and photoelectron clusters. Furthermore, as the number of photons created by a muon is $\propto E_{kin}$ the number of clusters could also be $\propto E_{kin}$ (see Equation 1.6), which should be helpful for the momentum reconstruction.

The number of strips reconstructed forming the muon cluster only and all clusters created by photoelectrons and muons are visible in Figure 6.13 (a). The number of strips in the muon clusters ranges from 5 to 16 strips as expected from Figure 6.4 averaging at 11 ± 3 strips.
The number of the strips addressed by photons ranges from 2 to 4 strips. This number is similar to the simulated muon with a perpendicular track through the detector (see Figure 6.4 (b)).
Also, the avalanches of photoelectrons closer to the muon overlap leading to a higher strip count different from 2 or 4 strips. The number of clusters formed by only the photons is 20±4 clusters per event (see Figure 6.13 (b)).

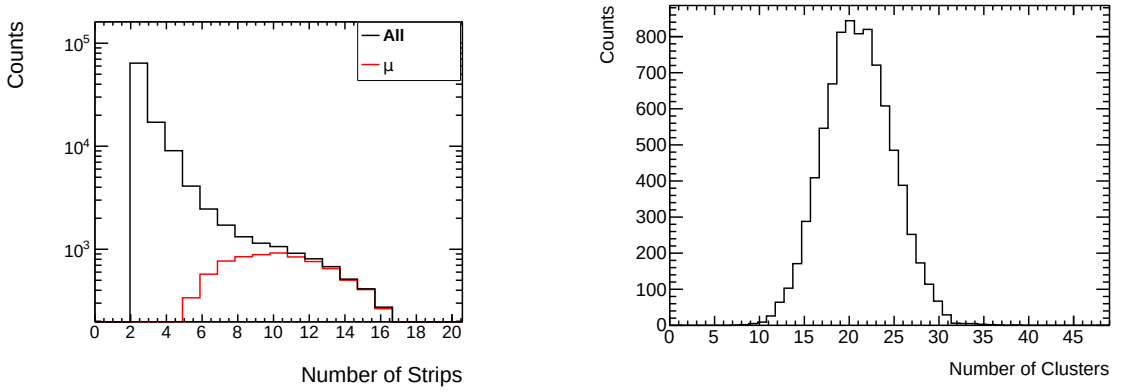

(a) Number of strips per cluster in Garfield++ **(b)** Number of clusters per event in Garfield++

Figure 6.13: The average number of hit strips for a muon cluster is 11 ± 3 strips, while for photoelectron clusters are 2-4 hit strips (see fig. (a)). The average number of clusters (b) is 21 ± 4 per event (see fig. (b)).

The average number of clusters for 1000 muon is determined via Gaussian fit for each energy. These values are shown as a function of energy in Figure 6.14. For low kinetic energies, the number of clusters that can be detected is low since the deposited charge in the detector $Q \propto N_{pe}$.
The number of cluster N_C is expected to increase with the kinetic energy E_{kin} according to the Frank-Tamm formula $N_C \propto N_{pe} \propto \left(1 - \frac{1}{n^2 \cdot \beta^2}\right)$ (see Figure 6.14). Thus a fit function can be used to determine the maximum number of clusters $N_{C,max}$ including the rest energy of the particle E_0

$$N_C(E) = \frac{N_{C,max}}{1 - n^{-2}} \cdot \left(1 - \frac{1}{n^2 \cdot \beta^2}\right) = \frac{N_{C,max}}{1 - n^{-2}} \cdot \left(n^{-2} - \frac{1}{(1 - \left(1 + \frac{E_{kin}}{E_0}\right)^{-2}}\right) \tag{6.7}$$

Upwards of 600 MeV, the number of clusters reaches a plateau at the average of about 26 ± 3, and the rest energy of the muon $E_0 = (110 \pm 30)$ MeV is in agreement with the nominal value $E_0 = 105$ MeV from M. Tanabashi et al. (Particle Data Group) [2018] determined by the fit. Thus, it agrees with the theory as the number of photons increases according to the Frank-Tamm formula (see Equation 1.5). The refractive index for LiF of $n = 1.41 \pm 0.8$ determined by the fit also agrees with the refractive index $n = 1.46$ (see Section 5.4.2).
As the muon electrons overlap with photoelectrons at the center of the photon distribution along one coordinate, the number of these masked photoelectrons is determined in Figure 6.15. Using the fit defined in Equation 6.7 shows an agreement with the expected increase according to the Frank-Tamm formula (see Equation 1.5).
The fit result yields for the masked photo electrons $N_{pe,max} = 16 \pm 2$. The refractive index $n = 1.41 \pm 0.8$ and the rest energy of the muon $E_0 = (42 \pm 65)$ MeV agree with the nominal

values above. However, a large uncertainty of E_0 and n is likely due to the few photoelectrons. The number of photoelectrons not overlapping with the muon cluster is then $N_{pe,unmask} = 23 \pm 9$ with the extracted photoelectrons of $N_{pe} = 39 \pm 9$ from Figure 6.6 at E_{kin} =4 GeV. Thus (59±26)% of the extracted photoelectrons do not overlap with the muon cluster and can be easily used to reconstruct the kinetic energy.

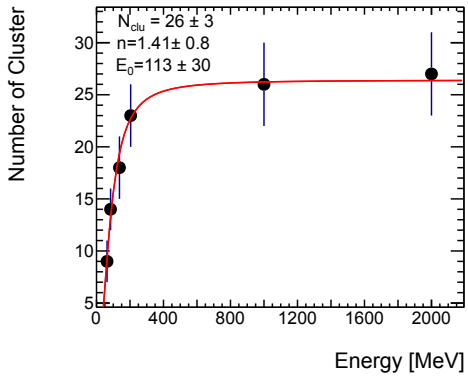

Figure 6.14: The number of clusters N_C created in the Cherenkov detector increases with the kinetic energy of the muon as this property is proportional to the number of created photoelectrons by Garfield++. The maximum number of clusters determined by fit is $N_{C,max}$ =26±3 and the determined rest energy of the muon $E_0 = (110 \pm 30)$MeV is in agreement with its nominal value of 105 MeV from M. Tanabashi et al. (Particle Data Group) [2018].

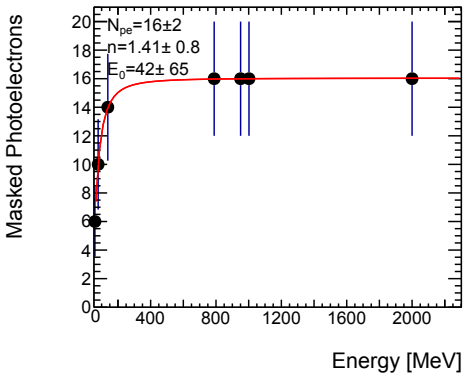

Figure 6.15: The photoelectrons created in Garfield++ masked by the muon $N_{pe,max} = 16 \pm 2$ increase according to the Frank-Tamm formula. The determined refractive index $n = 1.41 \pm 0.8$ and the rest energy of the muon $E_0 = (42 \pm 65)$ MeV agree with the nominal values but have a large uncertainty.

For different incident muon angles, the strip multiplicity changes as explained before for a muon cluster in Figure 6.16 (a). The number of strips is larger than for pure muon clusters, as photoelectron clusters overlap with the muon electrons. A parabolic shape is visible for increasing angles. For the photon cluster (see Figure 6.16 (b)), there is, however, no angular dependence visible as expected.

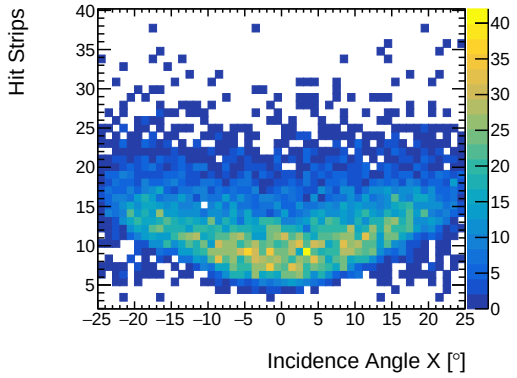

(a) Muon cluster in Garfield++

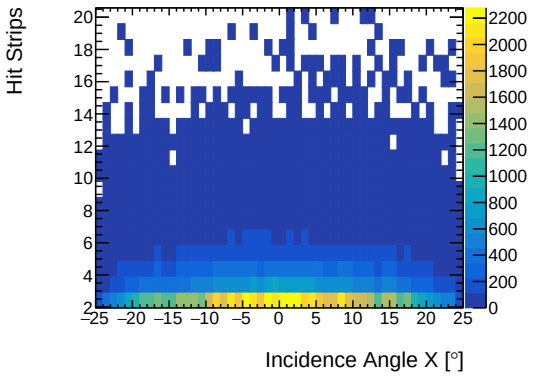

(b) Photon cluster in Garfield++

Figure 6.16: The number of hit strips by the muon in a cluster increases with the incidence angle (see fig. (a)). No cluster variation is observed for the photoelectrons, as expected (see fig. (b)).

6.5 Cluster Charge and Cluster Timing

Another feature that can be measured in the detector and possibly used to separate the muon and photon clusters is the cluster charge deposited inside the detector (see Figure 6.17). As it is proportional to the amount of produced electrons, a difference between the muon cluster and the many separated photon cluster should be visible in the Garfield++ simulation.
The cluster charge of the photoelectrons averages around $N_{aval,pe} = 24400 \pm 80$ avalanche electrons, and for the Landau distributed cluster charge of the cosmic muon $N_{aval,\mu} = (1.1 \pm 0.1) \cdot 10^6$ avalanche electrons created. The charge deposited by the photoelectron cluster thus is about a factor ≈ 100 lower than for the muon cluster.
For $N_{prim} = 39 \pm 8$ (see Figure 6.6) a simulated gain $G_{sim} = \frac{N_{aval,\mu}}{N_{prim}} = (2.8 \pm 0.6) \cdot 10^4$ which is within the region of the typical gas gain for a Micromegas (see Section 2.3).
The drift electrons arrive between time 0 to 150 ns of the signal timing in the 7 mm sized drift region. The cluster time does only rarely reach this value as the cluster weighted time (see Section 3.3.3) is shown in Figure 6.18. As visible for the photon cluster, they arrive at 150 ns, the latest point in the drift gap, as they all stem from the point most distant from the anode. A Gaussian fit of the photon peak yields a standard deviation of (3.558±0.001) ns.

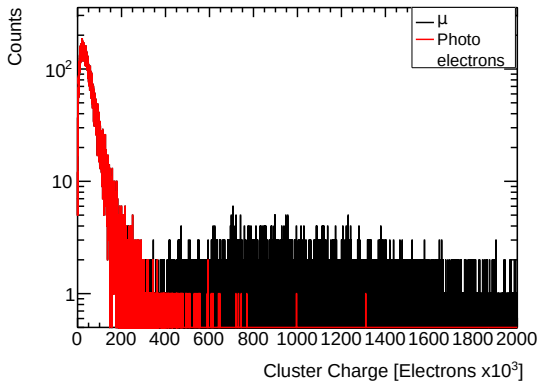

Figure 6.17: Simulated cluster charge for the muon and photoelectrons detected at the anode strips with a logarithmic scale on the y axis. The average charge of the photon clusters is several magnitudes lower than the muon cluster in Garfield++.

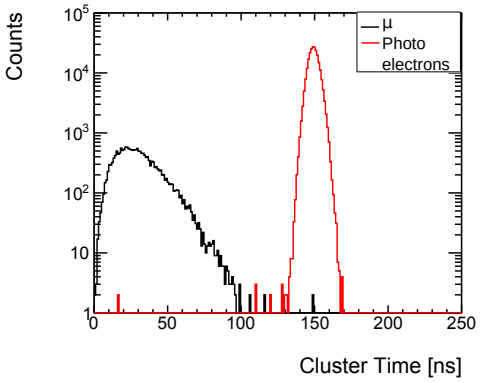

Figure 6.18: Weighted cluster timing for muon and photoelectrons with a logarithmic scale on the y axis. It is visible that some muon clusters are separated from the main cluster as the photoelectrons are expected to hit simultaneously. The standard deviation of the photon peak is $\sigma = 3.558 \pm 0.001$ ns in Garfield++.

For the photoelectrons, some clusters are found below a cluster of 150 ns. Likely a few muon cluster electrons are wrongly accounted for as muons as visible in the tail. For a high acceptance angle, the path through the drift gap increases the chance of creating muon ionization (e.g. δ-electrons) far apart, producing multiple clusters.

In Figure 6.19 (a), the first strip addressed of a cluster is shown. Muon electrons (black curve) can be created close to the mesh, peaking at 0 ns. The photoelectron (red curve) again shows a dominant peak at 150 ns as the photoelectrons have to traverse the longest path through the gas gap region.
The signal duration (see Figure 6.19 (b)) defined by the difference of the last and first strip of a photon cluster conversely shows that most photons have a short signal timing around 0 ns. The signal duration of most muon clusters ranges towards the 150 ns peak as expected as muon electrons are ionized over the whole drift region.

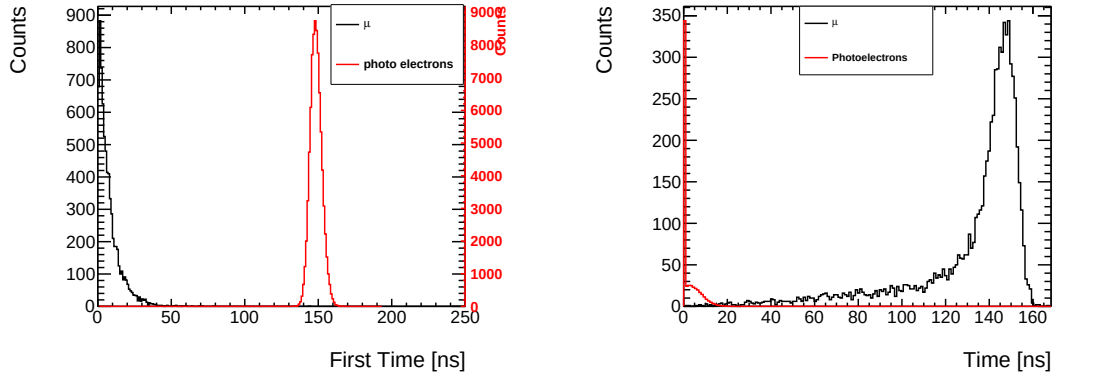

(a) Timing of the first strip in Garfield++ **(b)** Timing of First - Last Strip in Garfield++

Figure 6.19: The first strips of a cluster (see fig. (a)) show as expected that all photoelectrons arrive at the same timing (150 ns), which can also be seen in the signal cluster as a peak at zero in fig. (b). Here the muon creates electrons across the whole drift space. It leads to a broadening effect for the signal.

The residual between the reconstructed and muon positions is compared to the cluster time for the muon in Figure 6.20 (a) and photon clusters shown in Figure 6.20 (b).

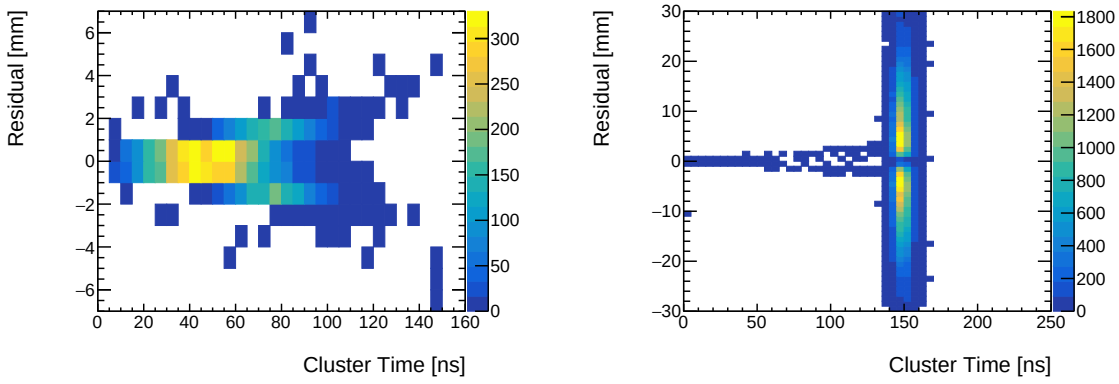

(a) Muon cluster in Garfield++ **(b)** Photon cluster in Garfield++

Figure 6.20: Residual distribution of the incident muon and photon clusters. Both result in a different signature in the detector, as is to be expected. The standard deviation of the muon residual is $\sigma = (0.120 \pm 0.003)$mm.

Finally, the distribution of hit strips increases for the muon linearly with increasing cluster time up to the maximum drift time of 150 ns (see Figure 6.21 (a)). The photon clusters (see Figure 6.21 (b)) show a peak along the timing distribution at 150 ns with a low strip multiplicity. The clusters accounted for as photons with a cluster time lower than 150 ns are again likely the muon electrons created far from the primary muon cluster due to steep angles.
These two-dimensional distributions can also be used to check whether the Cherenkov Micromegas works (see Chapter 7).

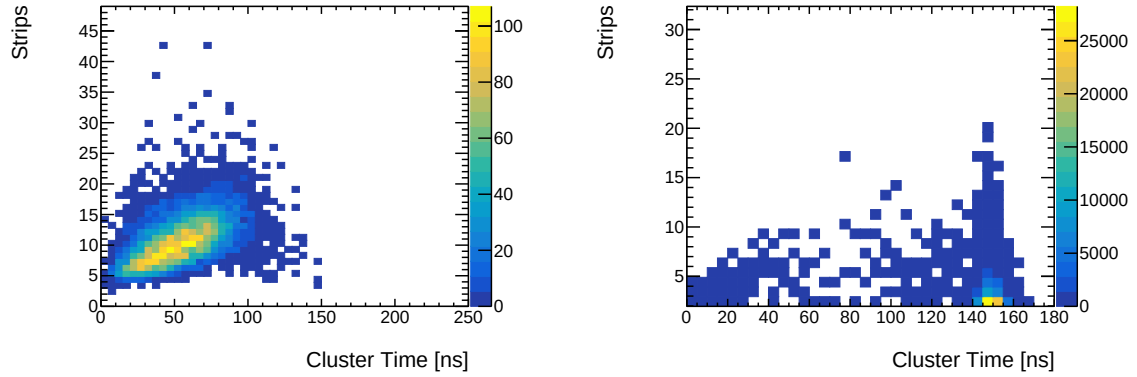

(a) Muon cluster in Garfield++ **(b)** Photon cluster in Garfield++

Figure 6.21: The number of hit strips increases linearly (slope $= 0.196 \pm 0.002$strips/ns) with cluster time for a cosmic incident muon as visible while for the photons, a distinct peak is seen as expected at 150 ns.

6.6 Summary

This chapter discusses the implication of the drift size on the produced muon electrons and can be used for further detector optimization.
Simulation in Garfield++ demonstrated clear signals for Cherenkov photons and muon clusters, which can be used to identify and separate these clusters in the next chapter (see Chapter 7). The cluster timing shows a clear photon peak that can be separated. Moreover, the strip multiplicity for photoelectrons is generally low, particularly far away from the incident muons.

Chapter 7

Measurements of Cherenkov Photons Using Cosmic Muons

The following chapter describes the measurements with the Inverted RICH Micromegas prototype, focusing on the timing reconstruction and separation of the photon and muon cluster. The measurements are compared to simulations produced by Geant4 and Garfield++ (see Chapter 6).

7.1 Measurement Setup

The inverted RICH Micromegas prototype (CHMM) with a 20 mm thick LiF sample of diameter 100 mm is tested with a detector hodoscope using two 2D reference detectors. The hodoscope provides the track of the muon. The track is interpolated into the CHMM. The goal is to separate the muon cluster from the photon cluster via the determination of the track through the detector hodoscope. The closest cluster in the CHMM to the interpolated position is then identified as the muon cluster.

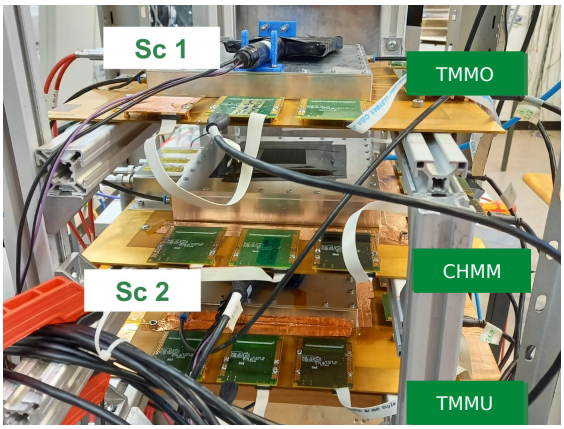

(a) Picture of the detector hodoscope with the test Cherenkov Micromegas.

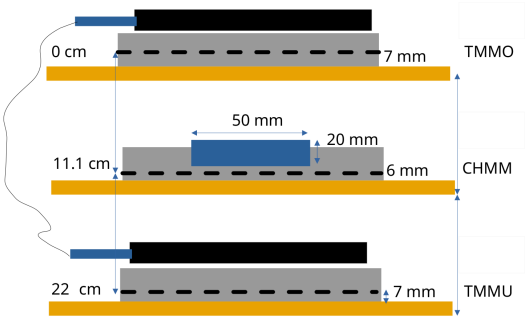

(b) Sketch of the detector hodoscope.

Figure 7.1: The detector hodoscope setup with a 22 cm distance between the trigger scintillators allows for an angle acceptance of 20°. The reference detectors are the upper (TMMO) and lower (TMMU) detectors, while the detector to be investigated is in the middle of the hodoscope (CHMM). The active area of the detectors is 10x10 cm^2 and for the CHMM, the area is restricted by the LiF crystal to $A_{CH} = \pi \cdot (2.5)^2\,cm^2 = 19.6\,cm^2$. They cover a maximum acceptance angle $\alpha = \tan(\frac{9\,cm}{22\,cm}) = 22.2°$ given by the trigger scintillators.

The detectors used for the tracking are two resistive strip Micromegas (TMMO and TMMU, see Figure 7.1). The spatial resolution of the tracking detector is assumed to be 150 µm due to the allowed angle acceptance. The tracking accuracy was determined to be 105 µm which is accurate for the separation of muon and photon clusters in the CHMM (see Figure 3.8).
All detectors are spaced with 11 cm distance along the z axis relative to each other. Each TMMO and TMMU is equipped with a scintillator on top. A coincident trigger signal initiates data acquisition.
The entire setup can also be inverted so that the photocathode and radiator face away from the incoming muon. The reversed setup is used later for timing studies to determine if the Cherenkov photons can leave the radiator (see Section 7.7.2). The air surrounding the radiator material is anticipated to absorb the photons.
The drift gap of the TMMO and TMMU is 7 mm, and CHMM is of 6 mm height. The voltages chosen for the TMMs are $U_D = 650\,\mathrm{V}$ ($E_{drift} = 0.92\,\mathrm{kV/cm}$) and an amplification voltage of $U_{amp} = 565\,\mathrm{V}$ while for the CHMM $U_{drift} = 550\,\mathrm{V}$ ($E_{drift} = 0.93\,\mathrm{kV/cm}$) and an amplification voltage of $U_{amp} = 550\,\mathrm{V}$. The drift velocities of all detectors are $0.0422\frac{\mathrm{mm}}{\mathrm{ns}}$ determined by MAGBOLTZ (see Figure 6.4).
Choosing a higher anode voltage for the CHMM is not possible due to the risk of charging up effects that result in discharges on the detector anode.
The readout chain for the telescope is sketched in Figure 7.2. The trigger signal is obtained by 9x9 cm^2 scintillators on top of the Micromegas. The advantage of these detectors is a fast signal with a good timing resolution of a few ns. For this reason, they are ideal to use as timing detectors.

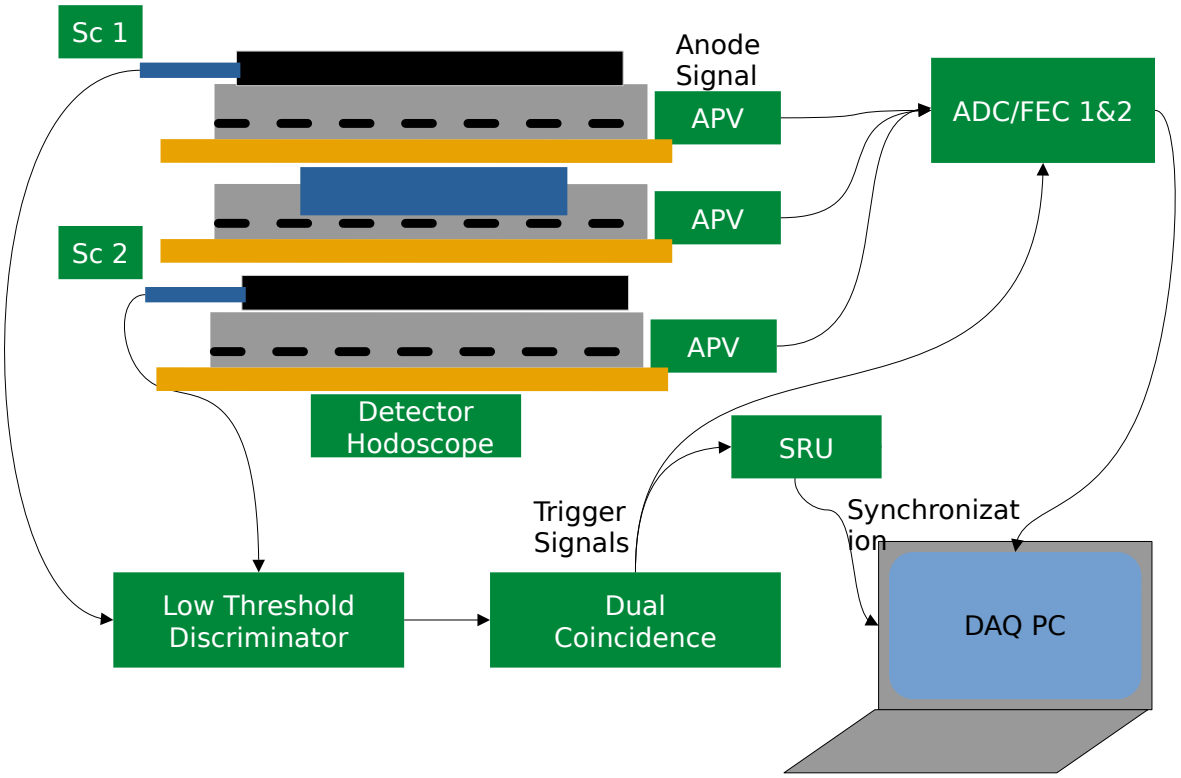

Figure 7.2: The readout chain for all measurements with a detector hodoscope to measure cosmic muons. Two coincident scintillators give the FEC the trigger signal to acquire data. Due to the many APV25s used, multiple FECs are required to receive a synchronization pulse from the SRU. The trigger signal is obtained by $9x9\,\mathrm{cm}^2$ scintillators on top of two Micromegas.

A CAEN discriminator to a NIM signal converts a trigger signal from the scintillators [CAEN, 2011].
The APV25 chip sends the data to a FEC, which sends the taken data to a data acquisition computer.
The requirement for successful particle tracking is a well behaving active area of the reference detectors. The CHMMs active area is considerably smaller than the other detectors by a factor of

$$\frac{A_{CHMM}}{A_{TMM}} = \frac{\pi r^2}{10 \cdot 10\,\mathrm{cm}^2} = 0.19 \tag{7.1}$$

The smaller active area is expected to affect the number of addressed strips and the number of recorded events. During tracking between strips 92 to 292, a cut is applied for the active area. The two-dimensional position of the leading cluster was reconstructed via the centroid method (see Figure 7.3). It is shown here without applying the cut mentioned earlier to visualize the homogenous distribution along the active area of the reference chambers.
The white lines in both detectors (see Figure 7.3 (b)) at strip 220 and (see Figure 7.3 (a)) strip 320 are due to APV25 defects while the white borders are occurring because of the trigger scintillators position.

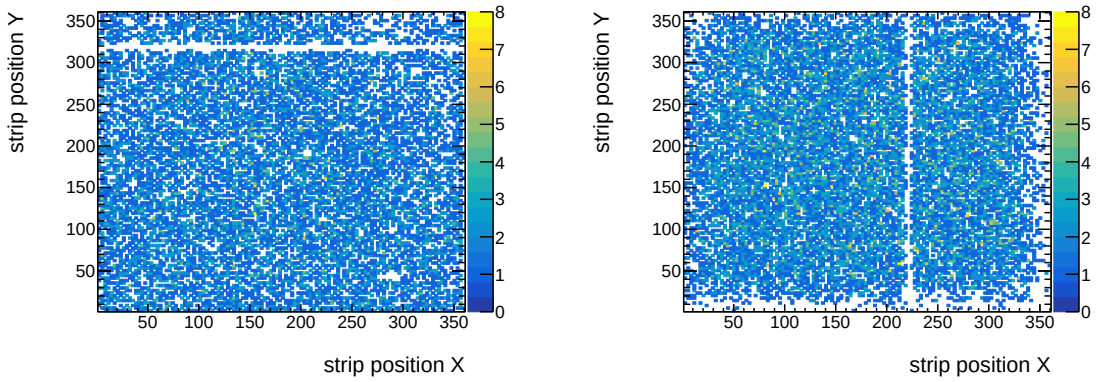

(a) TMMO **(b)** TMMU

Figure 7.3: The two-dimensional cluster position (in strips) of TMMO (see fig. (a)) and TMMU (see fig. (b)) for the cluster with the highest charge. The hits are homogeneously distributed as expected across the detector except for dead APV channels (white). The active area cut is not applied for these plots.

Due to the scintillator size and their distance to each other, a maximum acceptance angle $\alpha = \tan(\frac{9\,\mathrm{cm}}{22\,\mathrm{cm}}) = 22.2°$ results at the edges of the scintillators.
The track angle is a $\cos^2\alpha$ distribution validated by a fit function $a \cdot \cos(b \cdot \alpha)$. The acceptance angle reaches a maximum of 21° along the x and y layer of all detectors (see Figure 7.4). Determining the zero crossings for the fit values $b_x = 4.136 \pm 0.002$ and $b_y = 4.519 \pm 0.008$ with $x_0 = \frac{90°}{b}$ gives $\alpha_x = 21.95°$ and $\alpha_y = 19.92°$. This is a good indicator that the particle tracking via the reference detectors works.

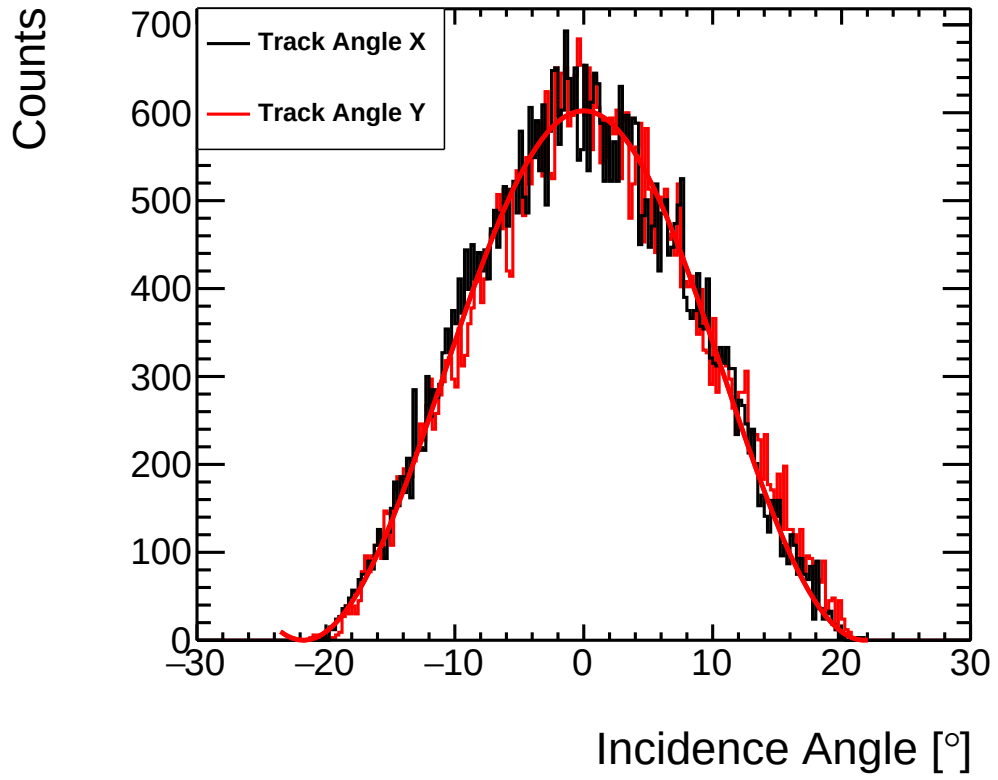

Figure 7.4: The angle is extracted from the track slope of the two reference detectors for the x (black) and y (red) layers. A fit is applied to the distribution $a \cdot \cos(b \cdot \alpha)$ along both axes. Along x, the fit yields $a = 599 \pm 2$ and $b = 4.136 \pm 0.002$. Along y, the fit yields $a = 575 \pm 2$ and $b = 4.519 \pm 0.008$.

7.2 Individual Muon Detector Signals

This section will discuss the signal produced by a typical muon passing through the detector at a small angle of incidence α, specifically in the resistive strip detectors TMMO and the Cherenkov Micromgas CHMM.
The signals discussed are detected on the x layer. Here the signal is stronger at the upper x layer of the detector than at the y layer. However, as the x layer is perpendicular to the resistive strips, this leads to the v shape effect as explained (see Section 2.3). Due to the signal's v shape, more strips are addressed. Due to the drift on the resistive strips, the charge arrives later than at the strips the avalanche electrons arrived.
The event shown in Figure 7.5 is an incident muon at 10° at the TMMOX layer. Compared to the simulation (see Figure 6.4 (b)), the number of addressed strips at 10° would be around 8 strips whereas in this example, it is 12 strips.
In Figure 7.6 a single muon with a strongly expressed v shape (green) is visible with three additional photon clusters on the CHMM x layer that arrive at a later time compared to the muon cluster (of TMMO and CHMM).
These clusters arrive close to the expected photon clusters' timing at 150 ns, and an increased number of clusters per event compared to the reference detectors is visible. This behavior is further investigated for multiple muon events (see Section 7.7).

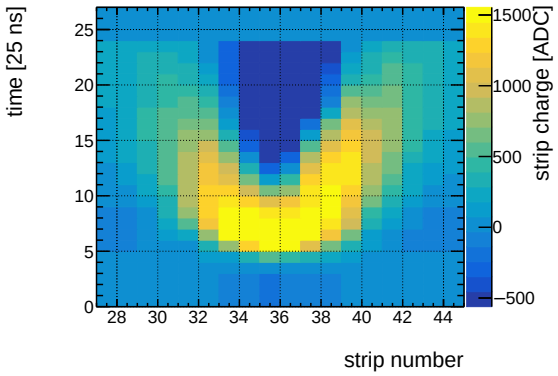

Figure 7.5: The incident muon signal is spread on 12 strips on the TMMOX layer for $\alpha = 10°$. Mostly, only one cluster per acquired event is expected for the reference detector.

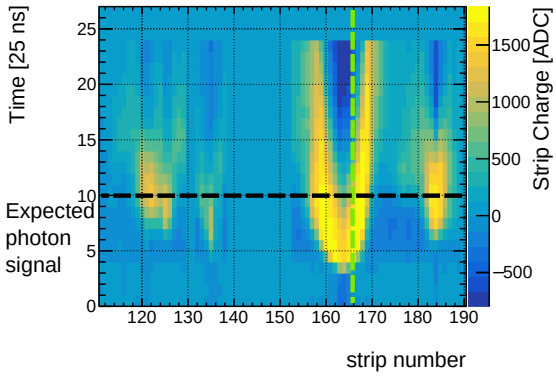

Figure 7.6: A signal from an incident muon at 10° with three additional clusters on the CHMMX layer. The muon cluster exhibits a strong v shape coinciding with the reference position (green) and is similar to the TMMOX event (see Figure 7.5). The other clusters arrive slightly later, close to the time when the photoelectrons are expected (black).

7.3 Charge Distribution

The strip and cluster charge distributions are discussed to showcase the performance of all detectors in the following. The charge q_0 (see Equation 3.1) detected by each strip for all events created by traversing cosmic muons is similar to a Landau distribution (see Figure 7.7). In this section, the before-mentioned active area cut is not applied yet.

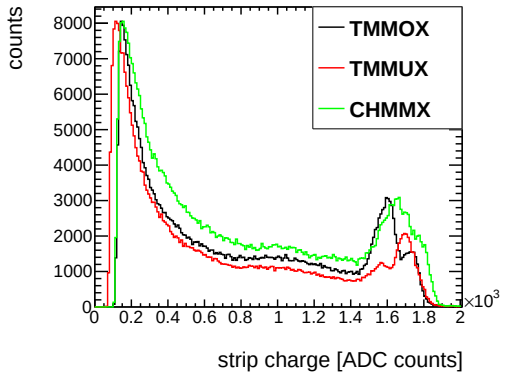

(a) x layer (layer with V shape)

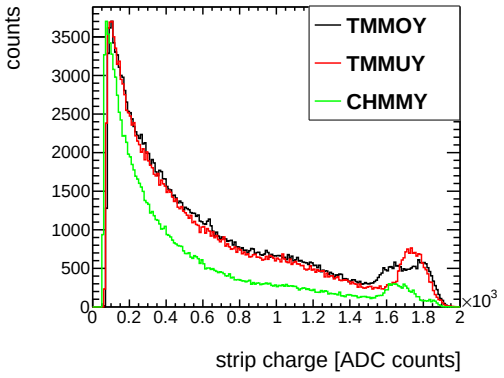

(b) y layer

Figure 7.7: Measured strip charge on the x layer (see fig. (a)) and on the y layer (see fig. (b)) measured for all anode readout layers with $U_{amp} = 550\,\text{V}$ for the Cherenkov Micromegas (CHMM) and $U_{amp} = 565\,\text{V}$ for the remaining Micromegas detectors (TMM). All detectors behave similarly with only a small amount of saturation. The active area cut is not applied in this section.

A larger number of addressed strips is expected along the x axis than the y axis. For all detectors, the strip charge distributions behave well for all detector layers. The strip charge starts at the respective threshold (see Table 7.1).
The strip charge has, as expected, a large peak at the start and ranges over the whole dynamic range of the APV25. At around 1800 ADC counts, a small peak due to saturation is visible. A high percentage of saturated strips is problematic for position reconstruction as the charge weights will be falsely considered. The fraction of saturated strips and the cut on the strip charge is shown in Table 7.1.

	TMMO	TMMU	CHMM
strip charge cut x	120	80	120
strip charge cut y	80	75	60
strip saturation x	16%	10%	17.7%
strip saturation y	10%	7%	5.8%

Table 7.1: The charge cuts applied to the strip charge in the analysis and the relative saturation of the strip charge. A strip is counted as saturated if its charge is above 1600 ADC counts.

It is essential to find the right balance between a high detector gain to achieve a high detection efficiency with a satisfactory track reconstruction and the limits of the detector electronics. The right balance is crucial for the CHMM, where a lower gas gain results in a loss of detectable photoelectrons.
As the whole deposited charge inside the detector has to be considered, the cluster charge is calculated by adding the charge of neighboring strips (see Section 3.3.2). It is assumed that the muon will deposit the largest charge in the detectors. The rate of muons passing through the 10x10 cm^2 detectors is below 1 Hz, so the likelihood of two simultaneous muons traversing the hodoscope is low. Inside the Cherenkov detectors, the simulation predicts that the photoelectron cluster is much lower in charge (see Figure 6.17). Because of these reasons, the cluster with the highest charge of the detectors can be assumed to be the muon cluster for performance studies (see Figure 7.8).

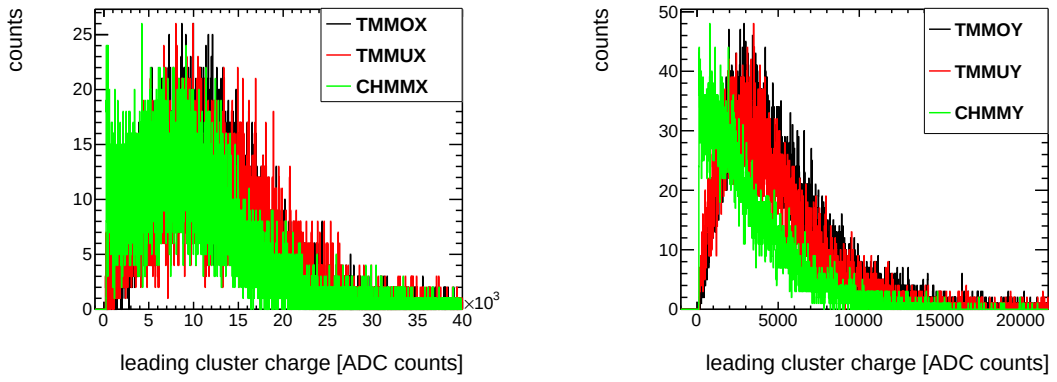

(a) x layer **(b)** y layer

Figure 7.8: The cluster charge is shown for the cluster with the highest charge for 22000 incident muons for all detector layers with $U_A = 550\,V$ for CHMM and $U_A = 650\,V$ for the TMMs. The most probable value of the CHMM is lower for all layers than for the TMMs.

The cluster charges are comparable as similar electric fields are applied, and the detectors are similar in construction. The most probable values were determined via the fit of a Landau distribution to the leading cluster charge. The most probable values of the fit are listed Table 7.2. In general, on the x layer (see Figure 6.17 (a)), a more considerable amount of charge is detected than on the y layer as the x layer is above the y layer (see Figure 6.17 (b)). The number of clusters reconstructed in each detector's x and y layers are similar, and the Landau distribution fits the cluster charge distribution well. Thus all layers of all detectors are working.
Relatively speaking, the TMMU reconstructed slightly fewer clusters than TMMO due to the setup's geometry of the placed trigger scintillators.
For the CHMM, significantly fewer reconstructed events would be expected from the calculation of Equation 7.1. Possibly on the outside of the active area, events are still reconstructed due to a not negligible electric field close to the micro-mesh.

	TMMO	TMMU	CHMM
Q_{clu} x [ADC counts]	8717 ±49	8362±63	6107±7
Q_{clu} y [ADC counts]	3236±9	2617 ± 19	1405±20
F_{clu}	2.69±0.02	3.20±0.03	4.35±0.06
reconstructed clusters x	21868	18264	19088
reconstructed cluster y	21857	18172	18965

Table 7.2: The leading cluster charge for the different detector layers as MPV and the quotient F_{clu} of the MPV determined by the Landau fit, and the number of cluster are shown here. Here the number of events is retrieved without the active area cut.

The reference detectors have both a similar fraction $F_{clu} = \frac{Q_x}{Q_y}$ when using the MPV value of the cluster charge for Q_x,Q_y between the x/y layer. The fraction indicates how much larger the signal is measured on the x than on the y axis. The fraction indicates the detector's stability if it is possible to reconstruct a signal in two dimensions reliably. Due to the induction of the signal from the x to y strips, this fraction can not reach 1.
The amplification of the CHMM is significantly lower than the reference detectors. Additionally, $F_{clu} = 4.35 \pm 0.06$, a signal on the y layer is much weaker than on the x layer. As shown in Chapter 6, the charge magnitudes of the photoelectrons are lower than for the muon ionization electrons. If the factor F_{clu} is too low, a Cherenkov photoelectron can, in the worst case, not be reconstructed on both detector layers. Therefore, it is crucial to consider the weaker charge detection on the y layer when analyzing the data. As a result, the CHMM primarily focuses on particle detection on the x layer.
The leading cluster charges of both readout strip layers are expected to correlate (see Figure 7.9). On both the TMMO (see Figure 7.9 (a)) and the CHMM detector (see Figure 7.9 (b)), a linear increase is visible.

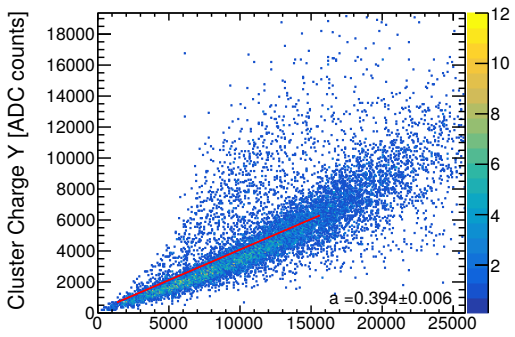

(a) 2D Cluster Charge TMMO

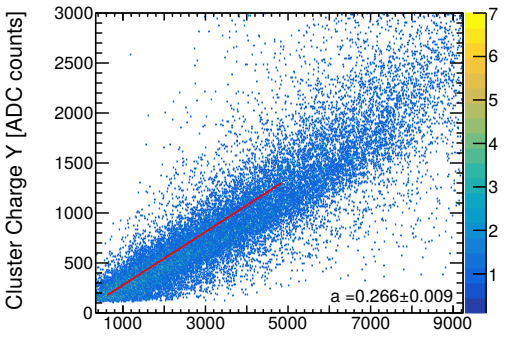

(b) 2D Cluster Charge CHMM

Figure 7.9: Leading cluster charge of the x and y layer of the TMMO (fig. (a)) and the CHMM (fig. (b)) with a linear fit included in the two-dimensional histogram for 17000 muons. The cluster charge along x for the TMMO is much higher than along the CHMM detector. On both detectors, data points mostly follow the expected linear increase. The determined slope of the fit is $m_{TMMO} = 0.394 \pm 0.006$ and $m_{CHMM} = 0.2660 \pm 0.009$. The inverse of the fit slope gives the charge factor $f_{TMMO} = 2.54 \pm 0.04$ and $f_{CHMM} = 3.8 \pm 0.1$.

Also clearly visible are data points that deviate from this linear course. The data points are attributed to larger y values further away from the linear fit. Electronic noise issues of the readout electronics could induce a larger amount of charge due to APV25 behavior leading to this discrepancy.

From a linear fit to the distributions, an identical cluster charge factor should be possibly determined. The slope m of the linear fit is the inverse of the x/y ratio f_{Det} (see Table 7.2 for the MPV). The slope determined by a line fit for the detectors yields $m_{TMMO} = 0.394 \pm 0.006$ and $m_{CHMM} = 0.2660 \pm 0.009$. The inverse of both slopes gives then $f_{TMMO} = 2.54 \pm 0.04$ and $f_{CHMM} = 3.8 \pm 0.1$. The values determined from the MPV of the leading cluster charge is $F_{TMMO} = 2.69 \pm 0.02$ for the TMMO and $F_{CHMM} = 4.35 \pm 0.06$ (see Table 7.2).
For the TMMO, the determined factor is deviating. However, it is roughly on the same order of magnitude, which is likely as for the MPV method, only the maximum of the distribution is accounted for.
The CHMM's factors deviated to a much higher degree by 0.7. Also visible is more considerable uncertainty on the factor determined via fit due to a broad distribution of the cluster charges. Either the leading cluster of the x layer is falsely combined with the y layer cluster, or due to the much weaker signal on the y axis the electronic noise may influence this.

7.4 Position Reconstruction of the Radiator

For the Cherenkov detector to function correctly, it needs a consistent position reconstruction throughout its photocathode.
The reconstructed hit position is expected inside a circle with a diameter of 200 strips or 50 mm which is indicated green in Figure 7.10. The detector demonstrates such behavior. Outliers exist which are more dominant along the x position than on the y position. On the one hand, the small electrical field close to the micro-mesh can induce outliers. Closer to the radiator, this electrical field is stronger, leading to excess hits beyond the circle.

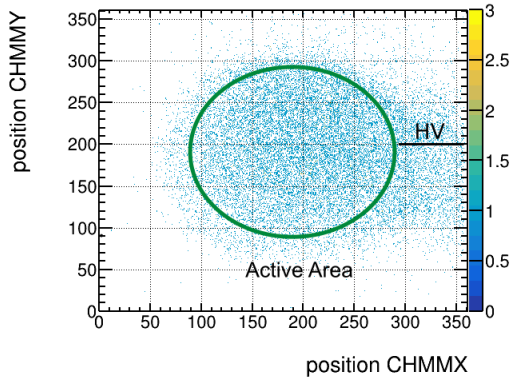

Figure 7.10: The two-dimensional cluster position of CHMM across the whole area of the detector. As expected, the circular shape of the radiator and the Chromium cathode can be reconstructed between strips 90 and 292 (indicated in green). The HV connection (indicated in black) possibly induces an additional electric field leading to detection outside the radiator.

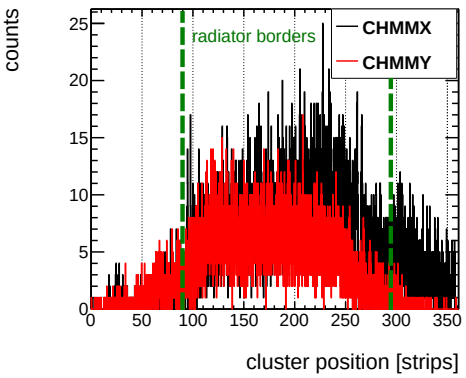

Figure 7.11: Projection of Fig. 7.10 on the x layer of the CHMM (black) and the y layer (red). It is visible that most events are within strips 90-292 (green). However, some hits are visible in the x layer from strips 290 to 350 where the HV cable is situated. Thus the cable and the connection could induce an electric field at the position. Also, the divergence of the signals by the v shape could contribute to the excess hits.

On the x axis the additional electric field is exhibited as a tail between 290 to 350 strips which are more clearly visible in a 1D projection (see Figure 7.11). This is possibly induced by a HV connection (black line). Effectively this increases the detector's active area and leads to a larger detection probability than calculated by Equation 7.1. At the center of the detector, most clusters are expected, as at this position, most angles are allowed by the geometry.

The muon strip position can be separated via the strip timing into different intervals (see Figure 7.12). In the active area of the detector, the timing intervals are indicated (a) the muon drift timing, (b) the photon peak, (c) overlapping with the afterpulsing and the v shape of the signal (Section 2.6).
The muon drift is located across the active area and is nearly equally distributed in intervals from 5 to 11 time bins ($\Delta t = 6\,\text{time bins} = 150\,\text{ns}$). According to the simulation, the photo peak (b) is expected to cover the photocathode completely visible at time bin 10. However, due to a few mm defect of the photocathode (strip 260 - 290), the signal does not cover the crystal with CsI.

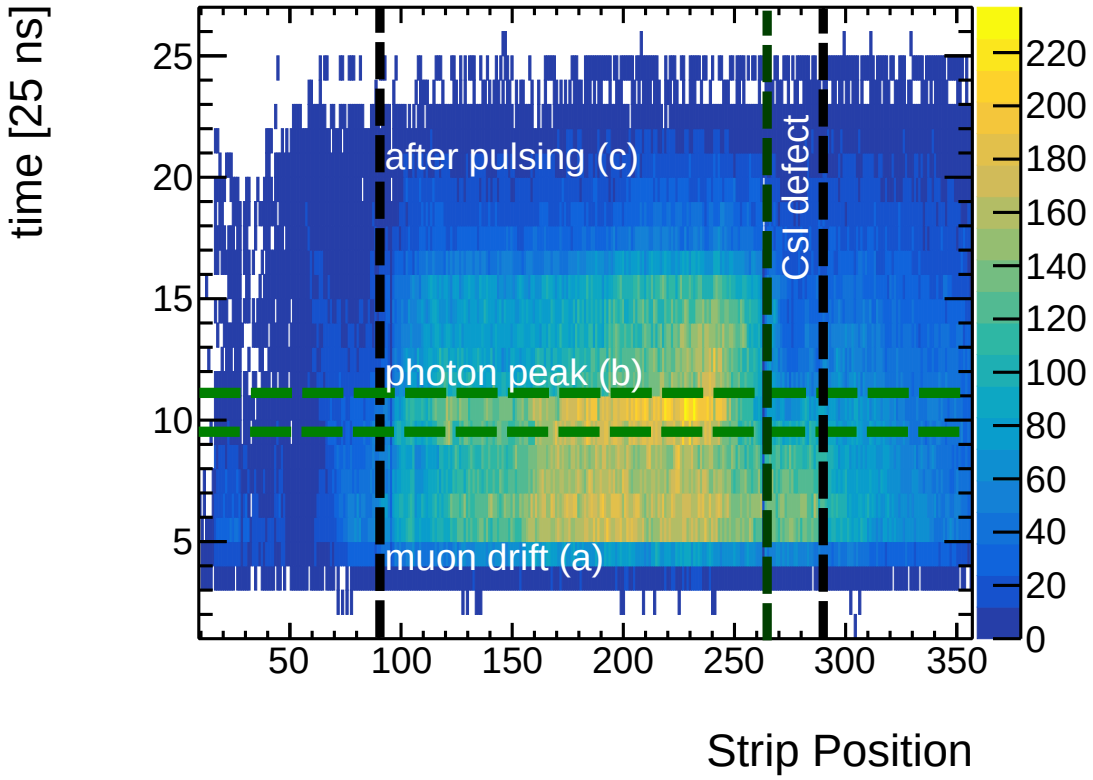

Figure 7.12: The strip timing of the x layer of CHMM shows a dominant peak (b) at around 10 time bins in the active Cr cathode area as well as an expected muon signal (a) between time bins 5 to 11. The late entries (c) are influenced by the electrons drifting on the resistive strips and an afterpulsing effect (see Section 2.6). Defects of the CsI of a few mm are visible as the photon peak abruptly stops at strip 260 even if the radiator spans to strip 292.

An afterpulsing effect (see Section 2.6) creates photons reaching the photocathode later. Photons are created in the avalanche region when electrons and ions recombine. The photocathode converts the photons to photoelectrons which have to traverse the whole detector volume again, leading to a delay time of $\frac{6\,\text{mm}}{0.0422\frac{\text{mm}}{\text{ns}}} = 142\,\text{ns}$.[1] The timing of the muon drift (a) with around $6\,\text{time bins} \cdot 25\,\text{ns} = 150\,\text{ns}$ agrees with the above calculation.
In the following, a cut on the active area of the LiF crystal (strip 92-292) is applied. Only events that are reconstructed in this area are used. The reference detectors are also only allowed to have a signal around strips 92-292.

[1] This clear difference from the simulated muon drift time is expected as here the drift gap size and electrical field is different leading to a time of 150 ns for the photopeak. In the following thus the drift times are calculated with the drift velocities from MAGBOLTZ (see Figure 2.2).

7.5 Muon Tracking

For accurate separation of the clusters inside the test detector, the spatial resolution of the detector is first probed. A line fit determines the reference position x_{ref} inside the CHMM predicted by the reference detectors (TMMO and TMMU) to measure the spatial resolution. The actual reconstruction position is x_{ref}. Comparing both positions yields a residual $\sigma = x_{ref} - x_{pred}$ that can be used to determine the spatial resolution of the detector (see Section 3.4). When the tracking is applied, only muon tracks are counted where TMMO and TMMU detected one single cluster.
The closest cluster to the interpolated track is identified as the muon cluster. All other clusters are classified as secondary clusters. The resulting residual distributions are Gaussian-like for the muon (see Figure 7.13).
To determine the CHMM's detection efficiency for muons and spatial resolution with the position of the cluster x_{pred} and the position determined by the reference tracker x_{ref} a spatial residual $\sigma = x_{ref} - x_{pred}$ is calculated for the x layer (see Figure 7.13 (a)) and the y layer of the detector (see Figure 7.13). A double Gaussian fit is applied to both residual distributions.

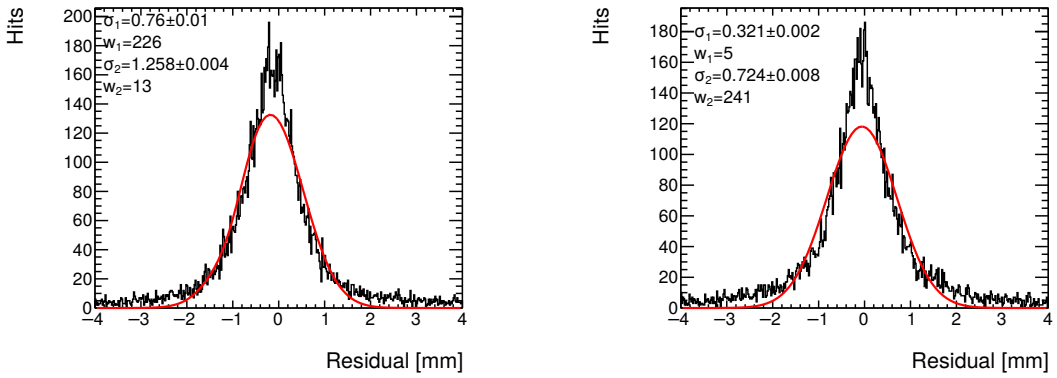

(a) x layer **(b)** y layer

Figure 7.13: The position of the cluster x_{pred} and the position determined by the reference tracker x_{ref} are used to determine the residual σ for the x layer (see fig. (a)) and for the y layer (see fig. (b)) of the CHMM. A double Gaussian determines the detector's spatial resolution by weighting the area of the Gaussian. The weighted residual $\sigma = x_{ref} - x_{pred}$ calculated yields $\sigma_{comb,x} = (716 \pm 8)$µm (see fig. (a)) and $\sigma_{comb,y} = (790 \pm 10)$µm (see fig. (b)). The number of determined tracks $N_{track} = 17645$.

From the width of both Gaussian distributions σ_1, σ_2 and of their weights w_1, w_2 the combined residual can be calculated (see Section 3.4). The fit results are shown in Table 7.3. The equation yields $\sigma_{comb,x} = (716 \pm 8)$µm (see Figure 7.13 (a)) and $\sigma_{comb,y} = (790 \pm 10)$µm (see Figure 7.13 (b)).
The actual spatial resolution of detector is then determined as $\sigma_{det,x} = (708 \pm 8)$µm (see Figure 7.13 (a)) and $\sigma_{det,y} = (780 \pm 10)$µm (see Figure 7.13 (b)). From the simulation, around 120 µm would be expected (see Figure 6.20). The spatial resolution of the CHMM is bad as only two reference detectors are used, likely leading to worse track uncertainties than expected. The detector properties, such as a small cluster charge measured in the CHMM detector, may also worsen the spatial resolution (see Section 7.3).

	x	y
σ_1	(321 ± 2)µm	(760 ± 1)µm
w_1	5 ± 1	226 ± 8
σ_2	(724 ± 8)µm	(1258 ± 4)µm
w_2	241±5	13±2
σ_{comb}	(716 ± 8)µm	(790 ± 10)µm
σ_{det}	(708 ± 8)µm	(780 ± 10)µm
ϵ	77.0 %	76.9 %

Table 7.3: The fit results by a double Gaussian (Gaussian 1 and Gaussian 2) fit from Figure 7.13 are listed. With the weights w and σ_1, σ_2 the combined spatial resolution σ_{comb} can be calculated. Subtracting the track accuracy σ_{track} gives the detector's spatial resolution σ_{det}. Also, the 5 mm reconstruction efficiency is shown.

With the tracking cluster N_{track} =17645 and the number of detected events in the CHMM N_{CHMMX} = 13570 and N_{CHMMY} = 13578, a detection efficiency $\epsilon = \frac{N_{CHMM}}{N_{track}}$ for the muon clusters can be determined. This equates to a detector efficiency of ϵ_X = 76.90 % and ϵ_Y = 77.0 %. The detection efficiency seems small but is expected as the area cut across the radiator $d = 50$ mm is rectangular, leading to a percentage of detected muons of $P_{cut} = \frac{\pi \cdot (d/2)^2}{d^2} = \frac{\pi}{4} = 78$ % of the rectangular area.
In Figure 7.14, the muon residual (red) in the CHMM is compared to the residual of reconstructed clusters inside the CHMM, including the photon cluster. In Figure 7.14 (a), the x layer, and in Figure 7.14 (b), the y layer is shown. It is visible that the distribution, including all photon clusters, is spread more expansive, nearly across the whole detector.
Also, the photon cluster should contribute to a large peak at the center, which is visible as the number of entries close to the reference position is increased between the black and red curves on both detector layers. A single Gaussian was fit to the background of the residual (black) that extends up ±15 mm. With photon clusters included the Gaussian width is $\sigma_x = 6.78 \pm 0.02$ mm and $\sigma_y = 6.53 \pm 0.02$ mm. As expected, the photons are detected over the full CHMM area. The momentum reconstruction with the measured data shown in Figure 7.13 is pursued in Chapter 8.

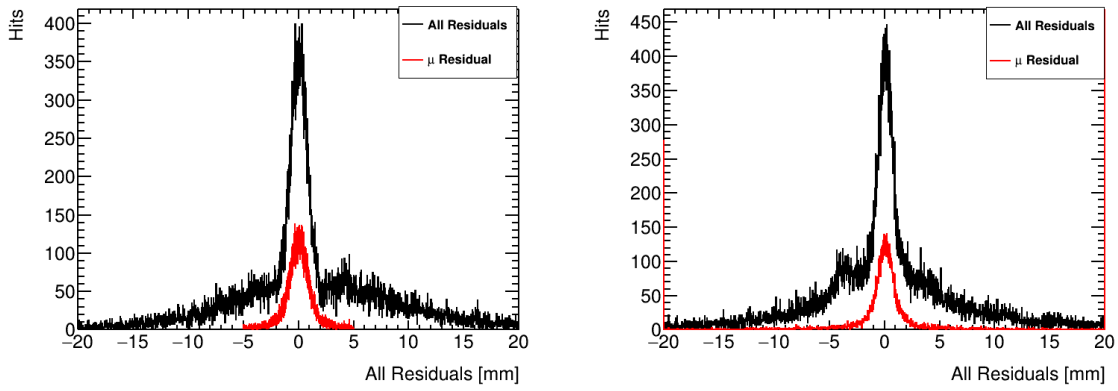

(a) x layer **(b)** y layer

Figure 7.14: The residuals for the muon cluster (red) are overlaid with the residuals for all clusters (black). The photon cluster contributes to the black curve to more events at the center of the muon and a steep decrease further away from the muon's position. In fig. (a), the x layer, and in fig. (b), the y layer is shown. A single Gaussian was fit to the background of the residual (black) that extends up ±15 mm. With photon clusters included the Gaussian width is $\sigma_x = (6.78 \pm 0.02)$ mm and $\sigma_y = (6.53 \pm 0.02)$ mm.

7.6 Cluster and Strip Multiplicity

The cluster multiplicity was already discussed in the simulation where an average of 21±4 clusters would be expected for the CHMM detector with inclined incident muons (see Figure 6.14).
The tracking cut for only one cluster in the reference detector is not applied in Figure 7.15 so that the reference detectors can also be included for comparison. However, the area cut on the radiator's surface of 50 mm corresponding to 200 strips of the detectors is included.
For the reference detectors (TMMO and TMMU) along the x layer (see Figure 7.15 (a)) and along the y layer (see Figure 7.15 (b)) mostly 0 or 1 cluster were detected inside the detector when the area cut is applied as is expected. A larger number of clusters detected rarely occurs and is accountable to cosmic showers or residual electronic noise.
The CHMM shows along the x layer (see Figure 7.15 (a)) and along the y layer (see Figure 7.15 (b)) for a higher number of clusters which is accountable to photoelectron clusters stemming from the photocathode. This tail to additional clusters is not visible for the reference detectors.

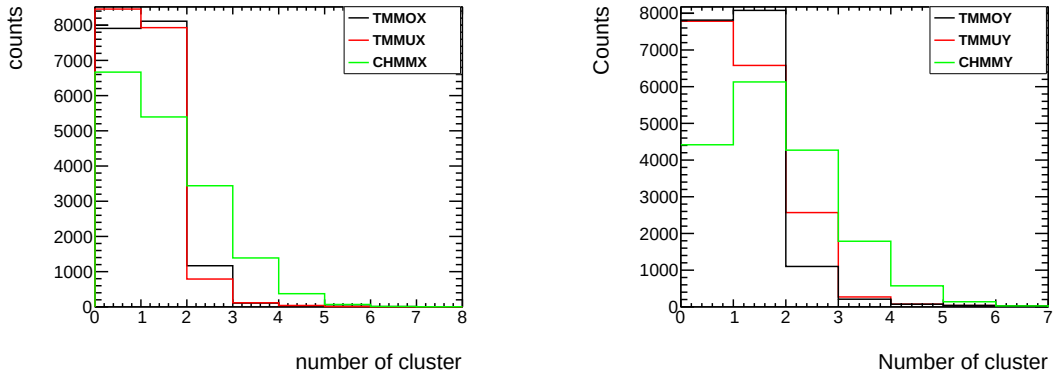

(a) x layer **(b)** y layer

Figure 7.15: The number of clusters for 17000 muons detected in the x (fig. (a)) and y layer (fig. (b)) of the detector. The entries at zero cluster in all detectors result from the area cut on the central 200 strips of each detector.

The average measured cluster multiplicity is shown in Table 7.4. Here it is visible that the reference detector detects a slightly lower number of clusters than the CHMM.
However, the measured cluster multiplicity of 2±1 for the CHMM on both layers does not agree with the simulated values 21±4 when counting photoelectrons as well (see Figure 6.13).

	TMMO	TMMU	CHMM
Cluster Mean x	1.1 ±0.6	1.1 ±0.6	2±1
Cluster Mean y	1.3 ±0.8	1.2 ±0.8	2±1
Strip Mean x	18 ±6	21 ±7	15 ±9
Strip Mean y	9 ±3	8 ±4	10 ±6

Table 7.4: Average cluster multiplicity for the x and y (see Figure 7.15) and strip multiplicity for the x and y layer of all detectors (see Figure 7.16).

There are two explanations for the low number of detected clusters per event inside the CHMM. On the one hand, the photoelectrons deposit less charge than the muon drift electrons. They require a large gain beyond the working point of the detector. The second part is that the CsI photocathode might have been exposed to contamination by, e.g., water vapor.

Related to the cluster multiplicity is the strip multiplicity. The strip multiplicity for all detectors is shown for the x layer (see Figure 7.16 (a)) and for the y layer (see Figure 7.16 (b)). Along the y layer (Figure 7.16 (b)), the shape of the strip multiplicity is very similar for all detectors. Along the x layer, the strip multiplicities differ visibly for each detector. The peak of the distribution for the CHMM is smaller than for both reference detectors. However, the CHMM has a more distinct tail toward a higher number of strips.
The simulated number of hit strips increases from 4 up to 14 strips for an incident muon with incidence angle α up to 20° (see Figure 6.4 (b)). The simulated values are indicated as green dashed lines.

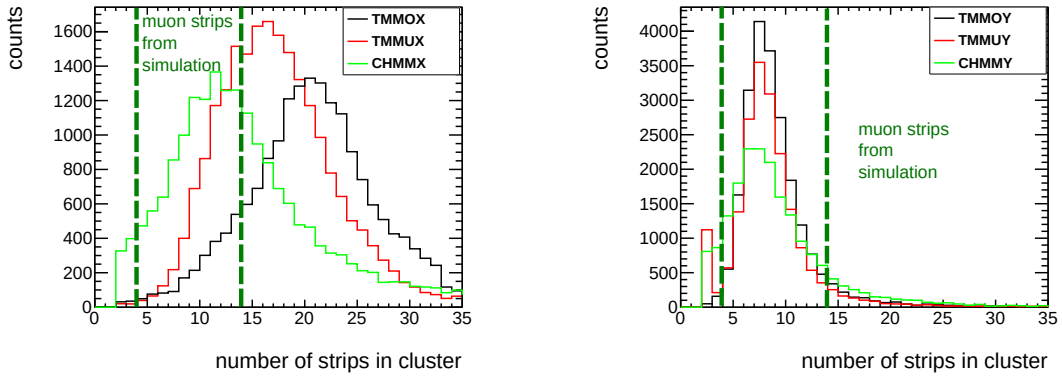

(a) x layer **(b)** y layer

Figure 7.16: The number of strips on the x layer (fig. (a)) and y layer (fig. (b)) of the cluster with the highest charge for 22000 muon events. For an incidence angle of 20°, simulated hit multiplicities are indicated as green dashed lines (see Figure 6.4 (b)). The measured strips on the y layer agree with this value within errors. The x layer shows a much higher number of hit strips due to the v shape of the signal along the resistive strips. Compared to the tracking detectors, the overall hit multiplicity of the Cherenkov detector should be larger for the x and y layers due to the overlapping photoelectrons. This is unfortunately not observed.

On the x layer (see Figure 7.16 (a)) of the detectors a higher value is expected due to the v shape expansion of the signal across the resistive strips leading to a larger strip multiplicity than simulated. The y layer (see Figure 7.16 (b)) is, however, in agreement with the simulation. Here the strip multiplicity for all detectors tends towards larger values of strip multiplicity (see Table 7.4) due to the $\cos^2 \alpha$ angular distribution of incident muons.
The strip multiplicity of CHMM is in a similar range as for the other detectors along the x and y layers. Expected would be a slightly increased strip multiplicity due to the overlapping photoelectrons. However, due to the inclination of the muons, this effect might be suppressed.
For a more thorough investigation of the CHMM's strip multiplicity, the tracking cut is now applied, and muon and photon clusters are separated from each other (see Figure 7.17).
The tracking requires only one detected cluster per tracking detector and a reconstructed position inside the photocathode area.
The number of addressed strips is visibly increased on the x compared to the y layer for both muon and photon clusters due to the v shaped signal spread as mentioned above (see Table 7.5).
The strips on the y layer that were analyzed for the muon cluster showed a tail in the data, which suggests that multiple photoelectrons were overlapping with a single muon cluster. Additionally, the number of strips measured agrees with the simulated muon cluster overlapping with the muon (see Figure 6.13 (a)).

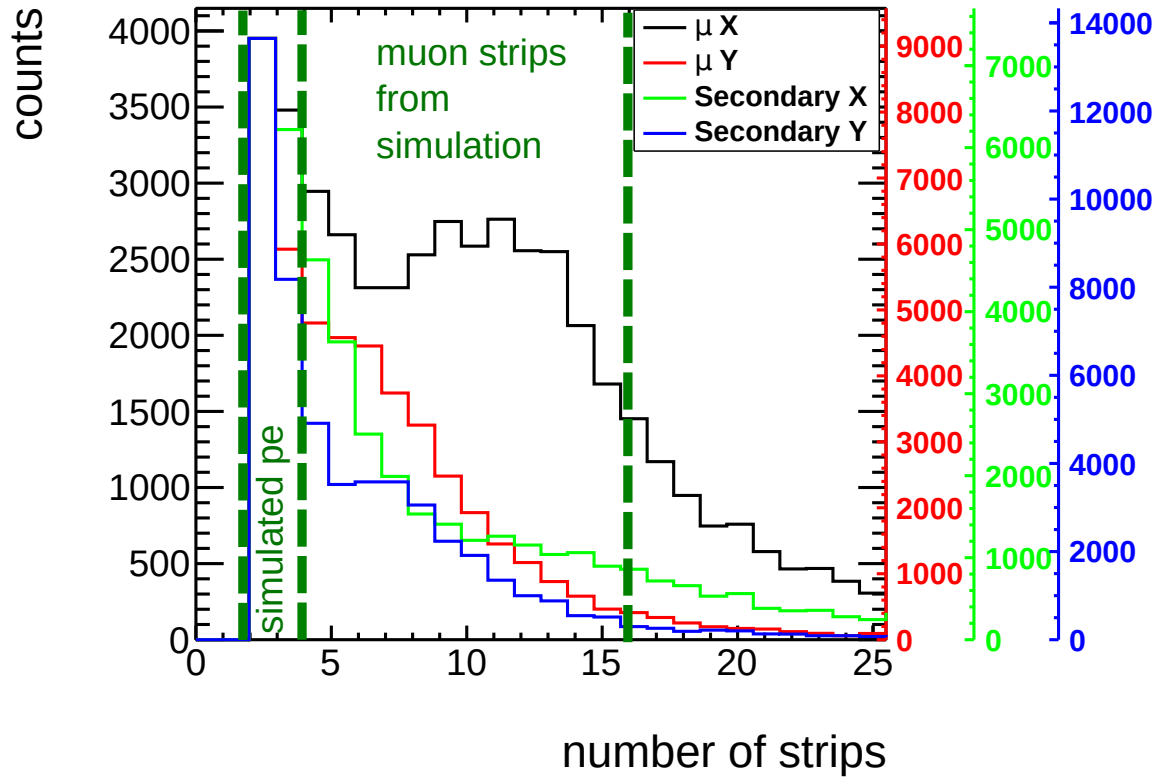

Figure 7.17: With the tracking cut applied, the clusters detected for 17000 muons in the CHMM detector is shown for the x and y layer. The tracking separates the clusters into secondary clusters containing photoelectrons and muon clusters. The simulated addressed strips for the photoelectron and the muon clusters with photoelectron overlap are indicated by dashed lines (see Figure 6.13 (a)).

	X normal	Y normal	simulated
muon	15±9	10±6	11 ±3
secondary	4±2	3±1	2±1

Table 7.5: Strip multiplicity of the closest clusters to the muon track and all secondary clusters in the normal and upside down CHMM compared to the simulated case.

The symmetric two-dimensional distribution between the track angle and the strip multiplicity (see Figure 7.18) is similar in the secondary and muon cluster case. For the addressed number of strips in a cluster, a dependency of the incidence angle was simulated, resulting in a parabolic dependency with the increasing angle (see Figure 6.16 (a)). The simulated number of strips for photoelectrons does not depend on the angle (see Figure 6.16 (b)). The measured muon clusters of the y layer are shown (see Figure 7.18 (b)) for TMMO and (see Figure 7.18 (a)) for CHMM. Here a parabolic increase is visible in both detectors. The effects seem, however, weak for the CHMM detector, for which photoelectrons overlapping with the muon are contributing. This is in agreement with the simulation (see Figure 6.16 (a)). In addition, for secondary clusters, it is essential to note that the strip multiplicity (as shown in Figure 7.18 (c)) does not increase as the incidence angle increase. This finding is consistent with the simulation results.

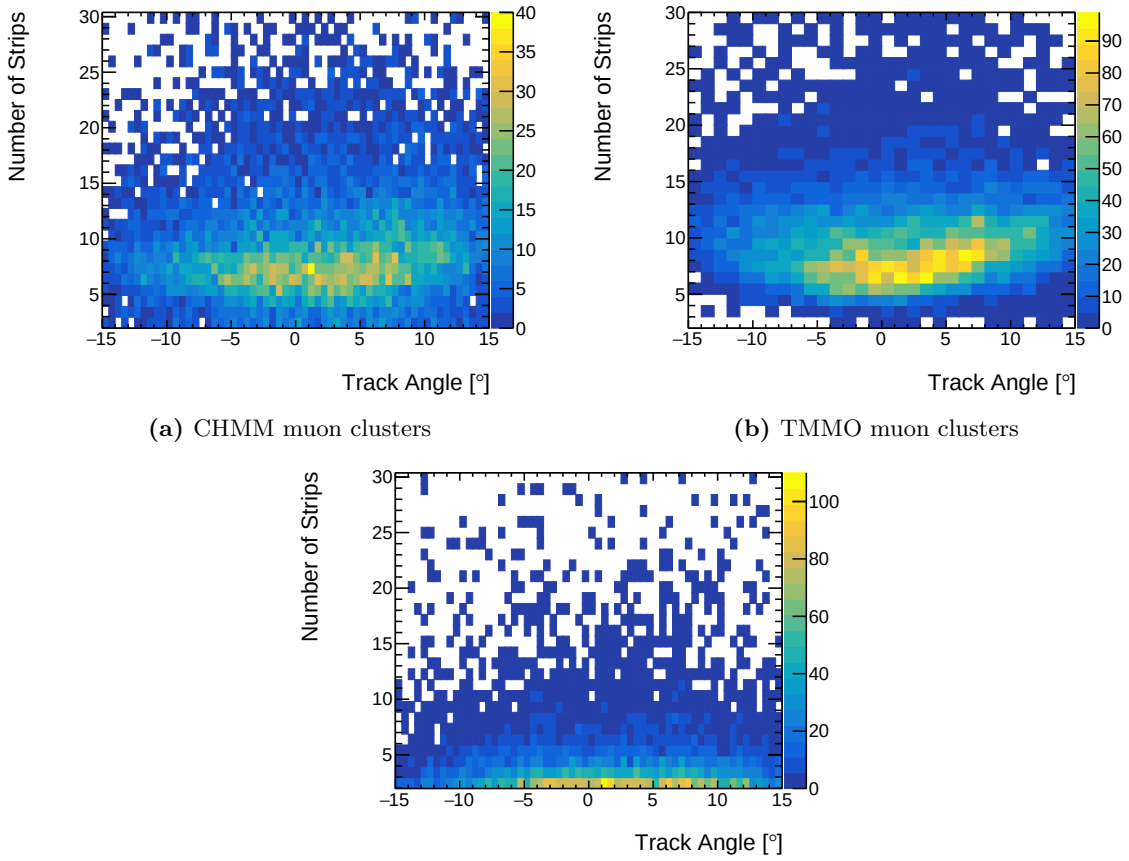

(a) CHMM muon clusters

(b) TMMO muon clusters

(c) CHMM photon clusters

Figure 7.18: The number of strips in a cluster is compared to the predicted track angle for the muon clusters in CHMMY (see fig. (a)), in TMMOY (see fig. (b)), and for the photoelectron clusters (see fig. (c)). In fig. (a) and (b), the expected parabolic shape with increasing incidence angles α is visible while the number of strips of the photoelectrons nearly stays constant. The y layer is shown as the x layer exhibits the v shaped spread leading to a smearing effect of the parabolic increase.

Another signature related to the detector's strip multiplicity that can be compared to the simulation is strip multiplicity and the detector's residual. The residual distributions for the CHMM of the muon (see Figure 7.19 (a)) and photon (see Figure 7.19 (b)) are shown.
In Fig. (a), the muon clusters found at the center of the residual are centered around 10 strips which have also been discussed before. The distribution resembles the simulation (see Figure 6.11 (a)). The photon clusters' distribution (see Figure 7.19 (b)) has the highest number of addressed strips close to the muon at around 0. Due to the geometry of the Cherenkov photon emission, such a behavior is expected, and a decrease is visible toward a higher distance from the muon cluster according to expectation and simulation (see Figure 6.11 (b)).

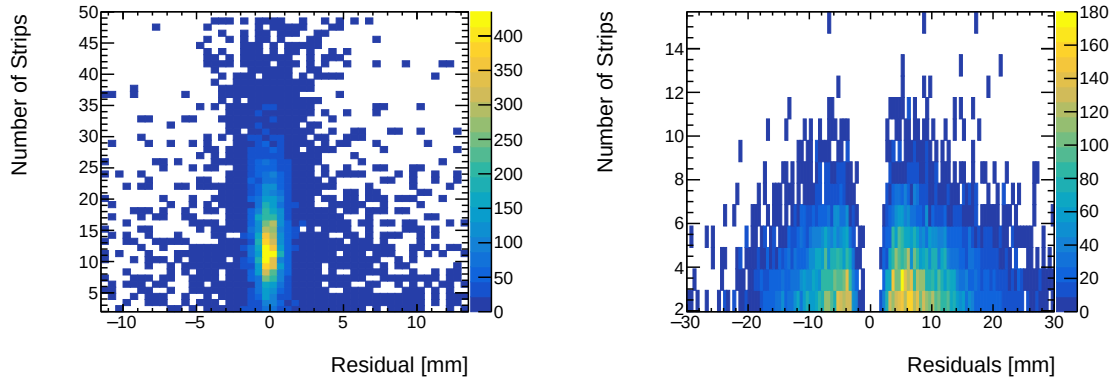

(a) Muon clusters **(b)** Secondary clusters

Figure 7.19: The number of strips in a cluster is compared to the residual for CHMMX. The muon clusters' distribution is much less extensive (see fig. (a)) than that of the secondary cluster (see fig. (b)). This is also expected from simulation for the muon and photoelectron clusters (see Figure 6.11).

7.7 Timing Distribution for the Detectors

The timing of the signal is the vital characteristic of distinguishing between muons and photoelectrons. The simulation shows that a distinct photo peak is expected for all photoelectrons due to all photons traversing the whole drift region. The timing of the muon signal is then expected to be distributed across the whole drift space of the detector (see Figure 6.18).
The following signal timings also include an offset from the trigger timing of 4.5 time bins in length. It has to be subtracted if compared to the simulation, which begins at signal timing = 0. First, the strip and cluster timing distributions without tracking are discussed.
Afterward, the tracking is applied to better separate the muon and photon clusters. Here the detector setup is also reversed to verify that the Cherenkov photons stem from the photocathode at which they should be absorbed in the reversed case.

7.7.1 Leading Charge Timing Distributions

The strip timing distribution for all hodoscope detector layers is shown without an applied tracking cut (see Figure 7.20). In each subfigure, the leading cluster charge is highlighted in red. The secondary clusters are shown in green, and the combined clusters are displayed in black.
The muon signal is visible on all detector layers along x (see Figure 7.20 (a), (c), (f)) and along y (see Figure 7.20 (b), (d), (e)) roughly at 5 to 12 time bins ($\Delta t = 7\,\text{time bins} = 175\,ns$) for TMMO, TMMU and 5 to 10 for the CHMM. On the y layer (see fig. (b) for TMMOY, (f) for TMMUY) of the detectors, only the muon drift time is visible in the form of a box-like distribution. The drift velocity of all detectors is $v_D = 0.0422\frac{\text{mm}}{\text{ns}}$ determined by MAGBOLTZ (see Figure 6.4). For the reference detectors with a $d_{Ref} = 7\,\text{mm}$ drift region, the expected width of the muon drift time $t_{D,Ref}$ equates to

$$t_{D,Ref} = \frac{d_{Ref}}{v_D} = \frac{7\,\text{mm}}{0.0422\frac{\text{mm}}{\text{ns}}} = 165.80\,\text{ns} = 6.6\,\text{time bins} \tag{7.2}$$

The calculated value agrees with the visible period of 5 to 12 time bins ($\Delta t = 7\text{time bins} = 175\,ns$) from fig. (b) and fig (f). A similar timing behavior (see Figure 7.20 (a), (b), (e), (f)) is visible from the few secondary clusters inside the reference detector, which hint,e.g., at cosmic showers. Alternatively, it is possible, due to a large incidence angle α of a muon, that it creates multiple clusters.

Along the x layer of the reference detectors (see Figure 7.20 (a), (e)) for a timing > 10 time bins the v spread of the signal is visible in the timing. This effect contributes for these detectors to 22-25% of all strips.

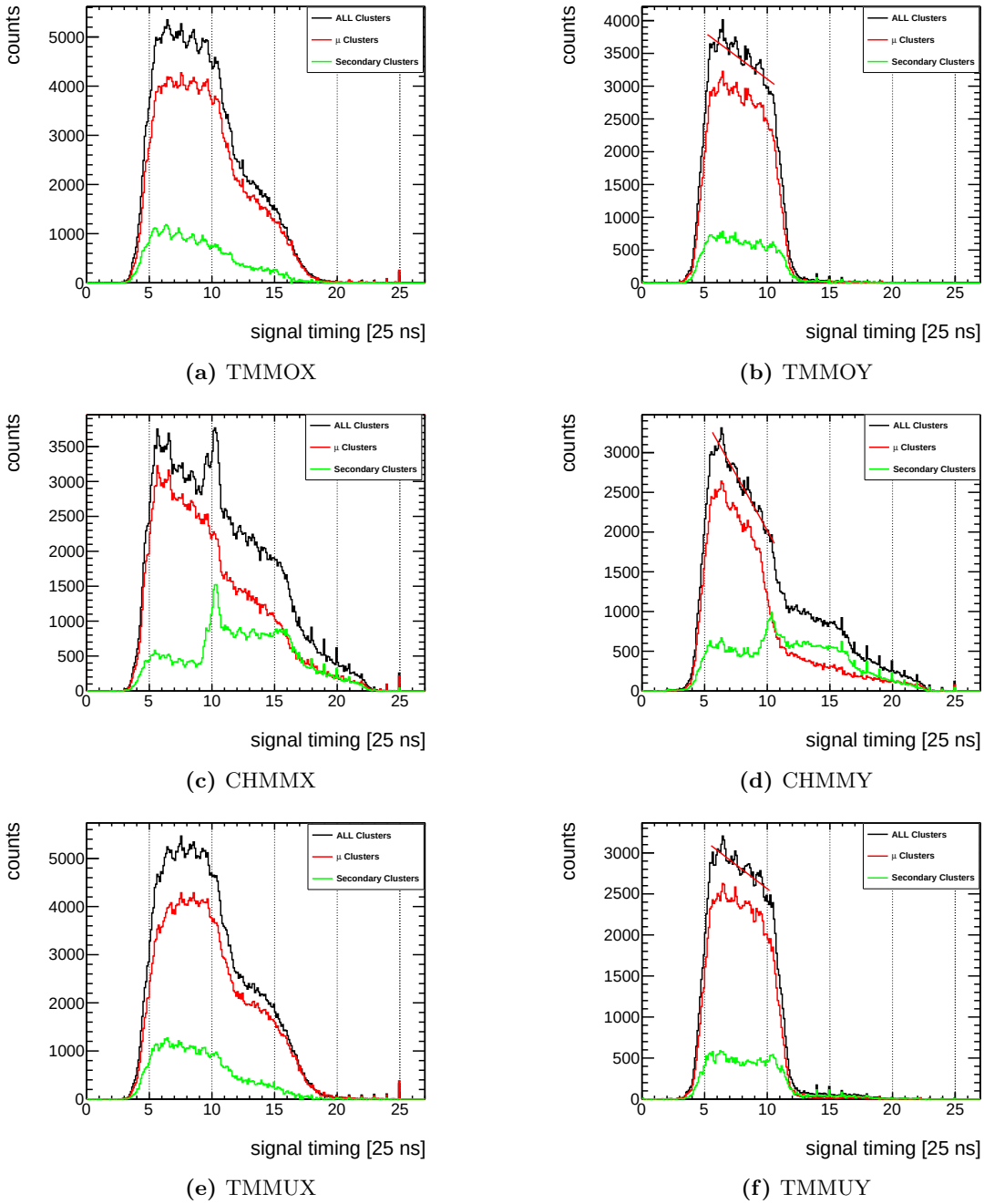

(a) TMMOX **(b)** TMMOY

(c) CHMMX **(d)** CHMMY

(e) TMMUX **(f)** TMMUY

Figure 7.20: The strip timing is shown for all detectors of the hodoscope and their respective x layers (left) and y layers (right). The muon cluster is expected between time bins 5-12 ($\Delta t = 7$ time bins $= 175\,ns$) for the reference detectors and 5-11 time bins ($\Delta t = 6$ time bins $= 150\,ns$) for the CHMM. The x layers of all detectors additionally show above 10 time bins the effect of the v shape (see fig. (a), (c), (e)). On the CHMM layer (see fig. (c), (d)), a tail is visible due to photon feedback. The peak at time bin 10 for the CHMMX layer likely corresponds to the Cherenkov photons (see fig. (c)). An unexpected linear decrease of counts with time is visible for all layers, indicated by a line fit (red).

For the CHMM with a $d_{Ref} = 6$ mm drift region Equation 7.2 yields for the width of the muon ionization drift time $t_{D,CHMM} = 142.11$ ns $= 5.7$ time bins. On both CHMM detector

layers (see fig. (c) and (d)), this calculated value is in agreement with the measured period of 5-11 ($\Delta t = 6\,\text{time bins} = 150\,ns$) time bins.
On the x layer of the CHMM (see Figure 7.20 (c)) at time bin 10, a peak is visible for all clusters and more dominantly for the secondary clusters. The effect is also slightly visible in the muon clusters as a step at time bin 10. This peak corresponds to the detected photoelectrons that arrive all from the photocathode. The weaker peak in the muon cluster is expected for the photoelectron clusters to overlap with the muon clusters.
Also a difference from the reference detectors visible in the CHMMX (see Figure 7.20 (c)) but more strongly visible in Figure 7.20 (d) for the CHMMY are intervals between 11 - 17 and 17 - 23 time bins ($\Delta t = 6\,\text{time bins}$).
Especially along the y layer (see Figure 7.20 (b), (d), (f)) of all detectors, a decrease for the strips is visible and unexpected. Expected would be a constant behavior such as seen in (see Figure 7.20 (e)) for TMMUX. The two effects hint at electronegative O_2 impurities inside the detector gas leading to recombination of the primary electrons with emission of photons inside the drift region as the negative slope is visible in all y spectra. This effect leads to a strong afterpulsing effect only inside the CHMM, as the photocathode creates photoelectrons. A line fit $a \cdot x + b$ for the negative slopes a yields $a_{CHMMY} = -10.3 \pm 0.2 \frac{1}{\text{ns}}$, $a_{TMMOY} = -7.36 \pm 0.2 \frac{1}{\text{ns}}$, $a_{TMMUY} = -3.8 \pm 0.2 \frac{1}{\text{ns}}$ and for the constant offset b yields $b_{CHMMY} = 4674 \pm 42$, $a_{TMMOY} = 4768 \pm 10 \frac{1}{\text{ns}}$, $a_{TMMUY} = 3524 \pm 38 \frac{1}{\text{ns}}$.
For the y layer of the CHMM, the two afterpulsing intervals between 11 to 17 and 17 to 23 time bins are also fitted with a linear function to determine the percentage of afterpulsing (see Figure 7.21). The afterpulsing intervals are expected to be as long in width as the original maximum muon drift time as the photoelectrons originating from electron-ion-recombination have to traverse the whole drift gap region (see Section 2.6). This effect happens two times. The fits are only viable with the y layer as the x layer exhibits the v shaped signal spread. The fit parameters of $f(x) = ax + b$ visible in Table 7.6 are determined via the linear fit. The negative slope shows that the number of hit channels decreases with time.

	muon drift	1st afterpulsing	2nd afterpulsing
slope a [1/25 ns]	-228 ± 5	-64 ± 3	-79.4 ± 0.8
intercept b	4383 ± 38	1789 ± 5	1845 ± 19
integration [25 ns]	15354	5358	1542
F_A	-	34.9 %	28.8%

Table 7.6: Parameters of the linear fit $a \cdot x + b$ of the CHMMY layer's strip timing. The line fit is integrated to determine the amount of afterpulsing. The fraction F_A determines the relative amount of afterpulsing for the muon drift and afterpulsing 1 and afterpulsing 1 to afterpulsing 2. Both values are relatively close to each other.

Each region's line fit is integrated to $F(x) = 0.5 \cdot ax^2 + bx$ and evaluated at the respective interval borders. The integrated values for each interval I_i are then divided to determine the relative amount of afterpulsing $R_{after1} = \frac{I_{after1}}{I_{drift}} = 34.9\%$ and $R_{after2} = \frac{I_{after2}}{I_{after1}} = 28.8\%$ where for R_{after2} the first afterpulsing has to be compared to the second afterpulsing as only the electrons created by first afterpulsing contribute to second afterpulsing (see Table 7.6). The relative amount of afterpulsing is for both intervals similar. This means that the effect is likely a constant detector parameter that underlines potential gas impurities by O_2.

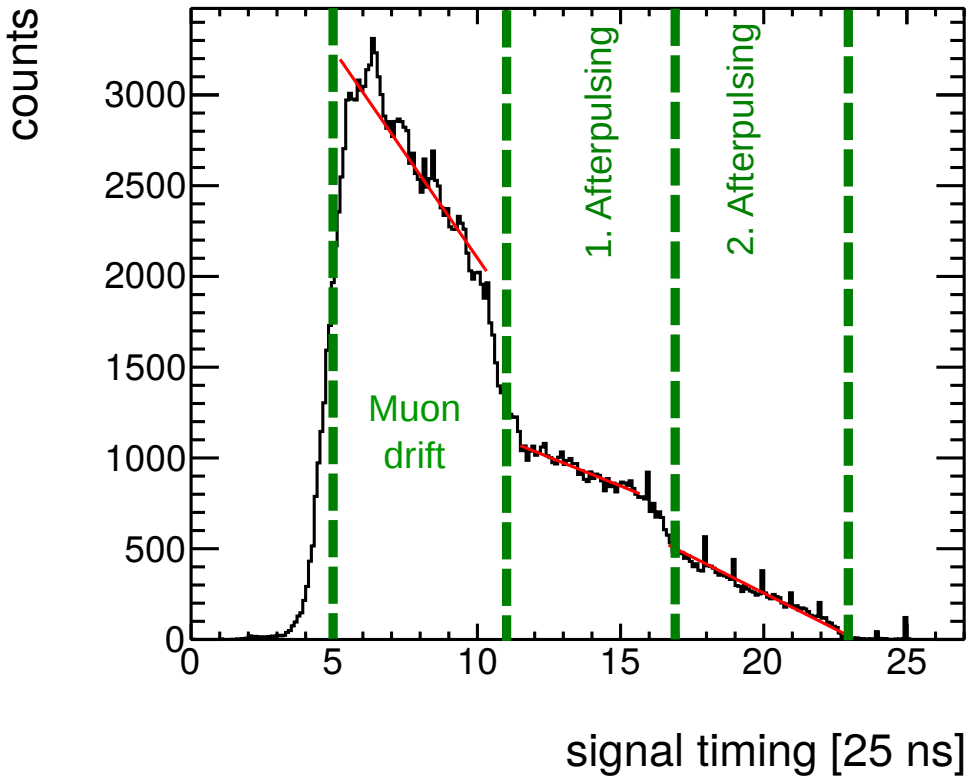

Figure 7.21: The signal timing of the addressed strips is exemplarily shown for CHMMY. The linear fits (red) are indicated to determine the afterpulsing parameters shown in Table 7.6. The dashed lines show the subdivision into the muon drift 5 to 11 time bins, the first afterpulsing (11 to 17 time bins) due to the photon feedback (see Section 2.6) and the second afterpulsing interval (17 to 23 time bins). They have the duration as the original muon drift timing as expected.

The effect of the afterpulsing is also visible, then comparing it to the measured strip charge Figure 7.22 in the CHMMX detector. The time intervals are again subdivided into the respective muon drift $(5-11)$ time bins, first afterpulsing $(11-17)$ time bins, and second afterpulsing interval $(17-23)$ time bins. The photon peak appears around 10 time bins, and there is a noticeable charge accumulation due to muon drift. The muon drift causes the strip charge to saturate, as shown in Figure 7.7. The charge decreases during the afterpulsing intervals. The photon peak is surrounded by the muon drift time and generally has a low charge (up to 400 ADC counts).
Combining the strip time information with the cluster time information yields the cluster timing (see Section 3.4) shown in Figure 7.23.
For all layers of the TMMO in Figure 7.23 (a) and (b), a Gaussian distribution is expected with the center at the drift region's center around $3.3 + 5 = 8.3$ time bins $= 208\,\text{ns}$ (half of Equation 7.2) with an offset of 5 time bins. On the x layer, a small tail exists due to the v shape of the signal. The width of the distribution along the x and y layer corresponds to the 7 time bins also determined for the strip distribution in Figure 7.23 (a) and (b) for the TMMOX and TMMOY.

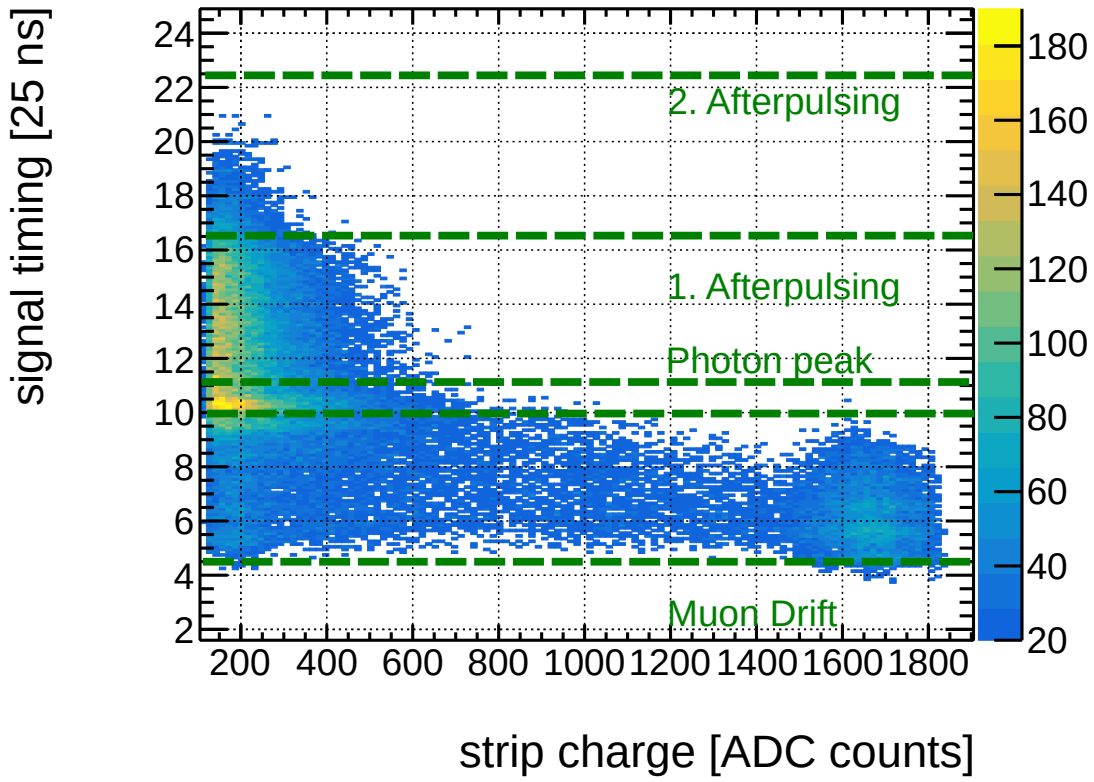

Figure 7.22: The strip signal timing for the CHMMX detector is shown against the strip charge. The dashed lines show the subdivision of drift intervals 6 time bins (= 150)ns into the muon drift 5 to 11 time bins, the first afterpulsing (11 to 17 time bins) due to the photon feedback (see Section 2.6) and the second afterpulsing interval (17 to 23 time bins). The photon peak is indicated at around 10 time bins. Visible a large amount of accumulated charge for the muon drift. The muon drift contributes solely to the saturation of the strip charge (see Figure 7.7). The charge decreases for the after pulsing intervals. The photon peak is enveloped by the muon drift time and is generally low in charge (up to 400 ADC counts).

Along CHMMX (see Figure 7.23 (a)) a second peak is visible at $10 + 6 = 16$ time bins, where the 6 time bins correspond to an electron traversing the whole drift region again. The afterpulsing effect is significant enough to replicate the first photopeak in the first afterpulsing interval. For the Cherenkov detector (see Figure 7.23 (a) and (b)) the photopeak at 10 time bins is visible. The photopeak is not expected for the muon clusters as the muon cluster should overlap with the photoelectrons so that the discrete peak smears out. A better separation algorithm must be applied to separate muon and photon clusters via muon tracking.

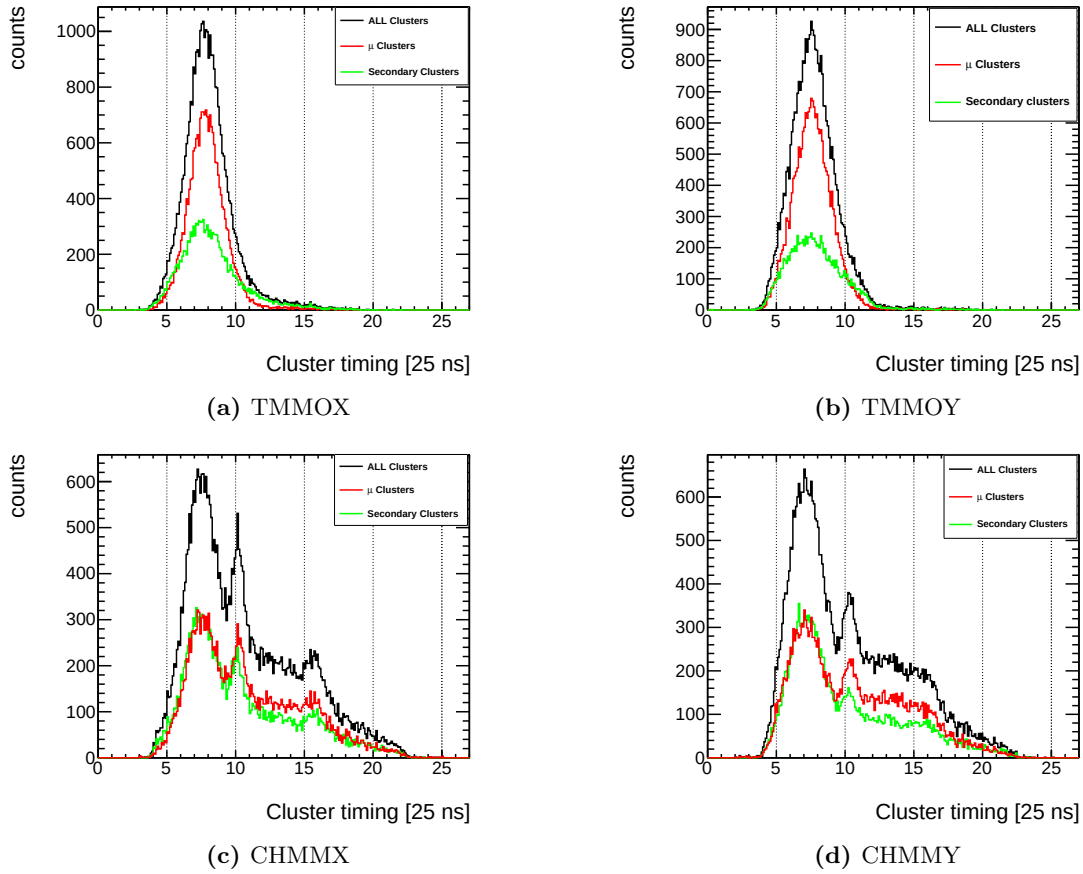

(a) TMMOX **(b)** TMMOY

(c) CHMMX **(d)** CHMMY

Figure 7.23: The weighted cluster timing is calculated from the strip timing (see Figure 7.23). In fig. (a) TMMOX , fig. (b) TMMOY, fig. (c) CHMMX, and fig. (d) CHMMY are visible. The distributions for the TMMO (see fig. (a) and (b)) have their maximum around $3.3 + 5 = 8.3$ time bins. The CHMM layers also feature this but have a distinct peak at 10 time bins and a tail with a smaller peak at 16 time bins. A clear separation is not possible with the selection criteria of the highest charge cluster. Full muon tracking is needed.

7.7.2 Timing Distributions - Muon Cluster Separation

The interpolated track position determined by the reference detectors can achieve a finer separation between the muon and photon clusters.
The timing distributions are shown for the CHMM with separated muon clusters along x (black) and along y (red) as well as the secondary clusters along x (green) and along y (blue) in Figure 7.24 (a) - (d) with the definitions for the timing used in Section 3.3.3.
The signal duration (see Figure 7.24 (a) green and blue graph) corresponding to the photoelectron cluster has a dominant peak for all secondary clusters identified as the photoelectron cluster. Photoelectrons arrive all at the same. For this reason, the time difference $t_{last} - t_{first}$ peaks at zero. The large tail includes wrongly accounted muon clusters and noise. The signal duration potentially allows for further filtering of the photoelectrons.
The muon clusters (see Figure 7.24 (a) red and black graph) are in contrast spread over the whole drift region leading to a large time difference with a maximum of 165.8 ns (from Equation 7.2) expected. Larger values can be attributed to the v spread along the x axis and potential noise.
The distribution of the first strip timing (see fig. (b)) and of the cluster timing (see fig. (d)) look similar. The muon clusters (red and black) can be well separated without a leftover photon peak. With the timing of the first strip, a better separation between muon drift time and photon peak is possible than cluster timing. Also, the shapes of distribution fig. (a), (b),

and (d) are similar to their simulated equivalents, e.g., the first strip timing (see Figure 6.19 (a)), the timing difference between first and last strip (see Figure 6.19 (b)) and the weighted cluster timing (see Figure 6.18).

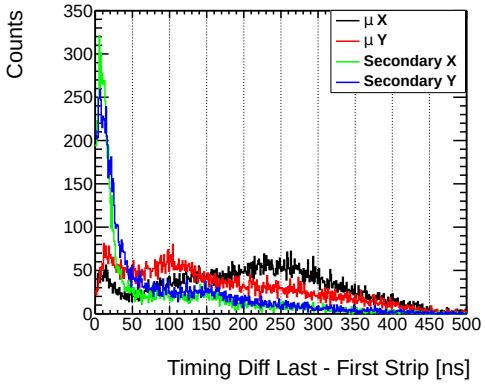

(a) Difference last and first strip

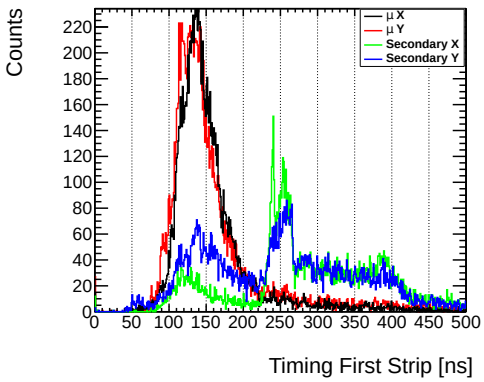

(b) First Strip

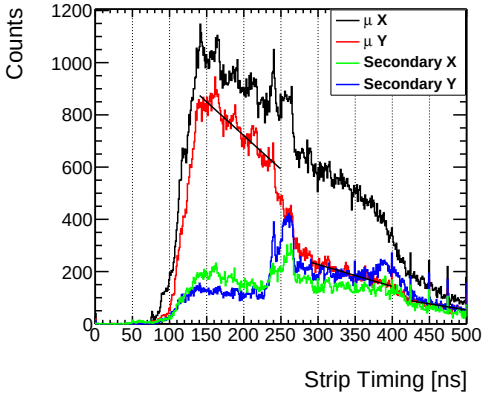

(c) Strip Timing

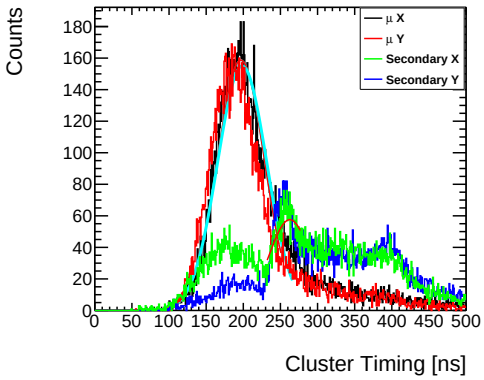

(d) Weighted cluster timing

Figure 7.24: The different timing definitions show significant differences in behavior between the muon and secondary clusters in the CHMM detector for both the x and y layer. In Fig. (a), the timing difference between the last and first strip shows a peak for the secondary photons corresponding to the photopeak. Fig. (b), the timing of the first strips, shows a similar behavior as fig. (d), the weighted cluster timing, and fig. (c), the strip timing where a photon peak is visible at around 10 time bins=250 ns. In fig. (c), the strip timing is fit with a linear function to determine the amount of afterpulsing (similar as Figure 7.21). The muon drift timing and photon peak (in fig. (d)) were fit with a Gaussian to determine the relative amount of detected photon clusters compared to the muon.

The cluster timing distributions (see fig. (d)) of the photon and muon clusters fit each with a Gaussian distribution to determine the relative amount of photoelectrons detected compared to the muon drift electrons. The determined value can then be compared to the simulation (see Equation 6.3).

The integrated values for the Gaussian and its fit parameter are shown in Table 7.7. The relationship D_i between photoelectrons N_{pe} and muon drift electrons N_μ is $D_x = \frac{N_{pe}}{N_\mu} = \frac{2793}{11900} = 24$ for the x layer and for the y layer $D_y = \frac{N_{pe}}{N_\mu} = \frac{3192}{12050} = 0.25$. However, the simulation determined 1.3 ± 0.4 (see Equation 6.3). The simulated average cluster timing values (see Figure 6.18) would be expected for the muon at $t_\mu = 25\,\text{ns} + 4 + 25\,\text{ns}$ and for the photoelectrons at $t_{pe} = 150\,\text{ns} + 4 + 25\,\text{ns} = 250\,\text{ns}$. The value for the photoelectrons agrees with the simulation, whereas the muon drift electron differs from the simulation. Deviations from the expected result could be due to the different electrical drift fields.
Multiple effects could influence detection efficiency than expected: Aging of the photocathode

	C	Mean [ns]	σ [ns]	Integral [ns]
Muon cluster x	158 ± 2	196.6 ± 0.4	-31.5 ± 0.3	11900
Photoelectron cluster x	63.1 ± 1.8	258.6 ± 0.7	19.3 ± 1.1	2793
Muon cluster y	15.5 ± 1.7	198.4 ± 0.4	33.0 ± 0.3	12050
Photoelectron cluster y	57.5 ± 1.5	262.5 ± 0.8	28.1 ± 1.2	3192

Table 7.7: The cluster timing (see Figure 7.24) is fit with a Gausian distribution. The mean μ, the standard deviation σ, and the constant C are shown. The Gaussian is integrated in the section of the muon drift and the photoelectron peak (see Figure 7.22).

influences the quantum efficiency [Va'vra et al., 1997]. Another effect might be gas pollution inside the detector as an environmental effect leading to an overall worse extraction efficiency into the detector gas (see Section Section 2.6). On the other hand, in the simulation, a different electric field was used, leading to another drift velocity that could be chosen too high, thus leading to further discrepancies.
The strip timing of the clusters visible in Figure 7.24 (c) shows that the muon clusters (black and red) still have a small number of photon residues which is expected due to the overlap between clusters of muons and photoelectrons. The photon peak is dominantly visible for the secondary cluster at 250 ns, including the afterpulsing. The before discussed second photopeak during the first afterpulsing is also visible at 400 ns as expected (see Figure 7.24 (c)). The layer was fit with a linear function for the interval of the muon drift, first and second afterpulsing (as in Figure 7.21). The fit results are considered in the discussion for Figure 7.25.

The hodoscope was also reversed (see Section 7.1). In this scenario, it is expected that the same behavior is visible in the tracking detectors. The idea of the reversed experimental setup is: The Cherenkov photons are now created in reversed direction.
They should all hit the top of the radiator and cathode where no CsI is deposited and only very few photons reach the CsI. Either the photons are transmitted and directly absorbed by the air, or after the reflection, these photons are either reflected at the radiator's walls or by the Cr. Alternatively, a low amount of photons can be transmitted through Cr. Then no photon peak or only a slim one is expected at 150 ns.
All timing distributions for the reversed setup are visible in Figure 7.25. The time distributions (fig. (a) - (d)) for the muon behave similarly (see Figure 7.25). The second broadened peak in all distributions after 250 ns is due to the afterpulsing effect.
Conversely the secondary clusters do not have the significant timing peak at 250 ns except for Figure 7.25 (a) where a peak at the time difference zero could be likely created because of the afterpulsing effect.

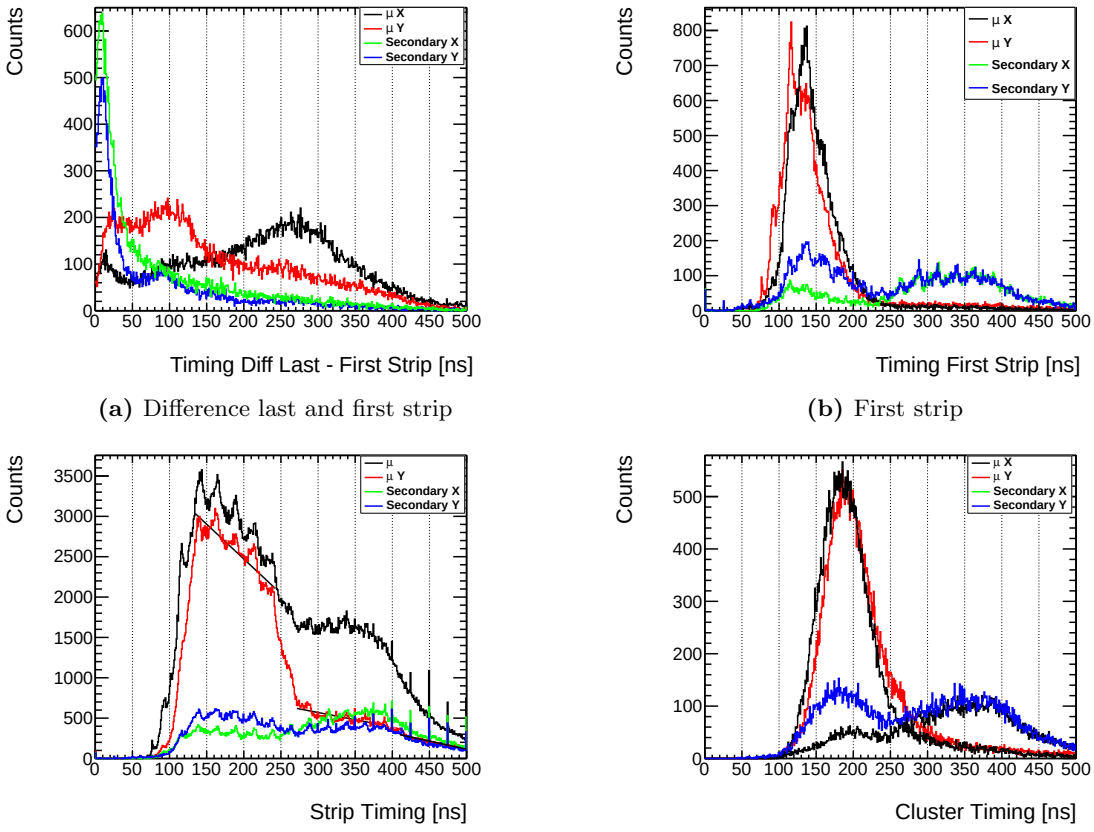

(a) Difference last and first strip

(b) First strip

(c) Strip timing

(d) Cluster timing

Figure 7.25: The timing distributions for the reversed setup are shown. It is mostly visible that the Cherenkov photon peak in the strip timing (fig. (c)) and the cluster timing (fig. (d)) is missing. A linear fit was applied to muon clusters of the strip timing (fig. (c)) to quantify the afterpulsing.

A linear fit is applied to the strip timing when the detector is in the normal configuration (see Figure 7.24 (c)) and in the reversed configuration (see Figure 7.25 (c)) to determine the relative amount of afterpulsing for the reversed hodoscope and compare it with the normal experimental setup.

	a [1/ns]	b	Integral [ns]
Muon drift	-2.5 ± 0.8	1224 ± 15	117975
1. afterpulsing x	-0.84 ± 0.04	479 ± 15	30900
2. afterpulsing	-0.47 ± 0.04	288 ± 21	9712
Rev. muon drift	-8.6 ± 0.2	419 ± 29	247188
Rev. 1. afterpulsing x	-1.78 ± 0.07	1105 ± 23	78742
Rev. 2. afterpulsing	-2.01 ± 0.06	1120 ± 27	24832

Table 7.8: A linear fit $a \cdot x + b$ is integrated to determine the relative amount of afterpulsing in the detector for the strip timing distribution when the detector is in the normal configuration (see Figure 7.24 (c)) and in the reversed configuration (see Figure 7.25 (c)).

In case of the normal configuration the factor R_i afterpulsing yields for the normal configuration $R_{after1,norm} = \frac{30900}{117975} = 26.1\%$, $R_{after2,rev} = \frac{9712}{30900} = 31.4\%$ and $R_{after1,rev} = \frac{78742}{247188} = 31.8\%$, $R_{after2,rev} = \frac{24832}{78742} = 31.5\%$ for the reversed configuration. The values are mostly consistent with each other except for $R_{after1,norm} = 26.1\%$, which is probably influenced by the photon peak contributing to the addressed strips of the muon drift. Thus the value of afterpulsing is around 32 % inside the CHMM detector.

7.7.3 Two-Dimensional Timing Distributions

The separation of the muon and photoelectron clusters and the afterpulsing of the two-dimensional timing distributions of the CHMM are further investigated to characterize the photon peak. Also, the two-dimensional distributions can be compared to the expectations from the simulation (see Chapter 6).
In Figure 7.26, the timing distribution for the muon cluster (see fig. (a)) and the photoelectron clusters (see sfig. (b)) in the standard configuration as well as for the reversed configuration (muon: fig. (c) and photoelectron: fig. (d)) are shown.
As was also visible in Section 7.7.1, the muon cluster distribution is similar in the standard configuration Figure 7.26 (a) and the reversed configuration Figure 7.26 (b). The muon drift expands across the whole drift region visible by large $t_{last} - t_{first}$ and also includes the v shape of the signal along the x axis. The afterpulsing for a strip timing $> 250\,\text{ns}$ has a comparatively short signal duration. This effect is more discernible in the secondary clusters in the standard configuration (see Figure 7.26 (c)) and the reversed configuration (see Figure 7.26 (d)). The most noticeable difference between the two plots is that the photon peak is missing, as expected in reversed configuration.

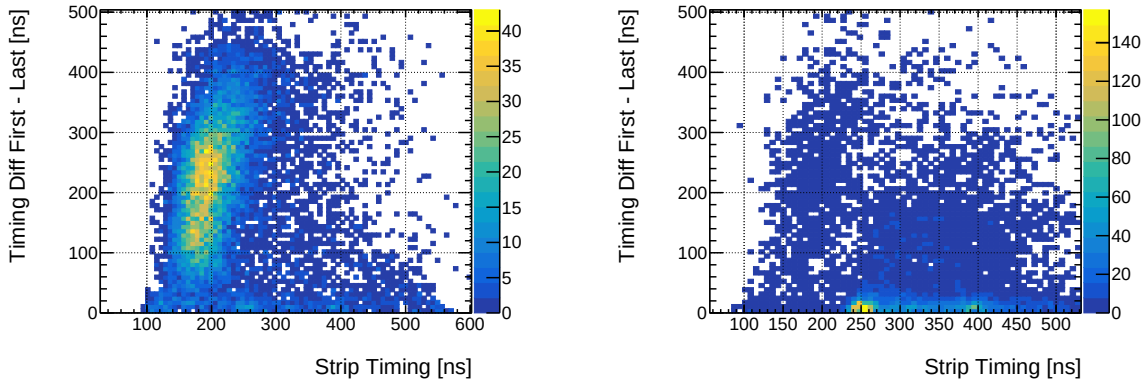

(a) Muon cluster x

(b) Secondary cluster x

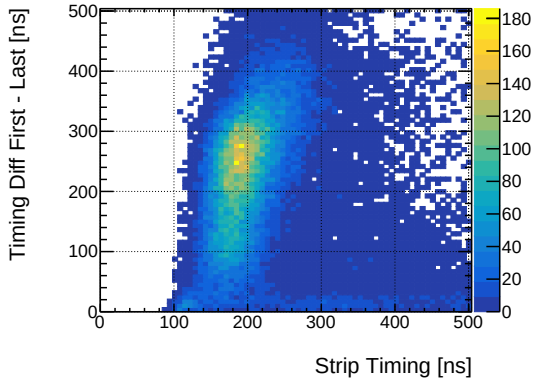

(c) Muon x reversed

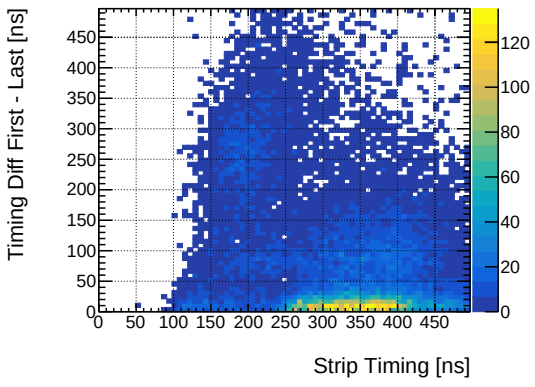

(d) Secondary x reversed

Figure 7.26: The strip timing compared to the time difference of the first and last strip of the muon cluster for the normal (se fig. (a)) and the reversed setup (fig. (c)) are similar in shape. The secondary cluster in fig. (b) contains the Cherenkov photon visible at strip timing 250 ns arriving simultaneously. Also, at the same time, (visible in fig. (b) and (d)) most of the afterpulsing signal is arriving as the created cluster stem from the photocathode but from different positions in the drift region.

The muon cluster inside the detectors is expected to be the closest to the reconstructed particle track compared to all detector clusters.
The timing distributions are shown in Figure 7.27 against the tracking residuals for the muon cluster (see fig. (a)) and the photoelectron clusters (see fig. (b)) in the standard configuration as well as for the reversed configuration (muon: fig. (c) and photoelectron: fig. (d)) are shown. The muon clusters (a), (b) show reasonable residual distributions between 100 ns, and 250 ns. The photon clusters (c), (d) include a large part of the afterpulsing effect. On the y axis the muon residuals (see fig. (b)) spread than ±5 mm. This can be likely attributed to the smaller charge detected on this layer.
In the case of the standard hodoscope setup, the shape of the measured distributions for the photoelectrons (see Figure 7.27 (b)) is in agreement with the simulation except for afterpulsing (see Figure 6.20 (b)). The measured muon cluster distribution (see Figure 7.27 (a), (c)) is in agreement with the simulation (see Figure 6.20 (c)).
The cluster timing for the primary cluster is compared to the residual distribution for all detector layers and the x layer of the reversed detector.
Also visible in (see Figure 7.27 (b), (d)) is that the afterpulsing effect spreads over the whole detector region similar to the Cherenkov photons.

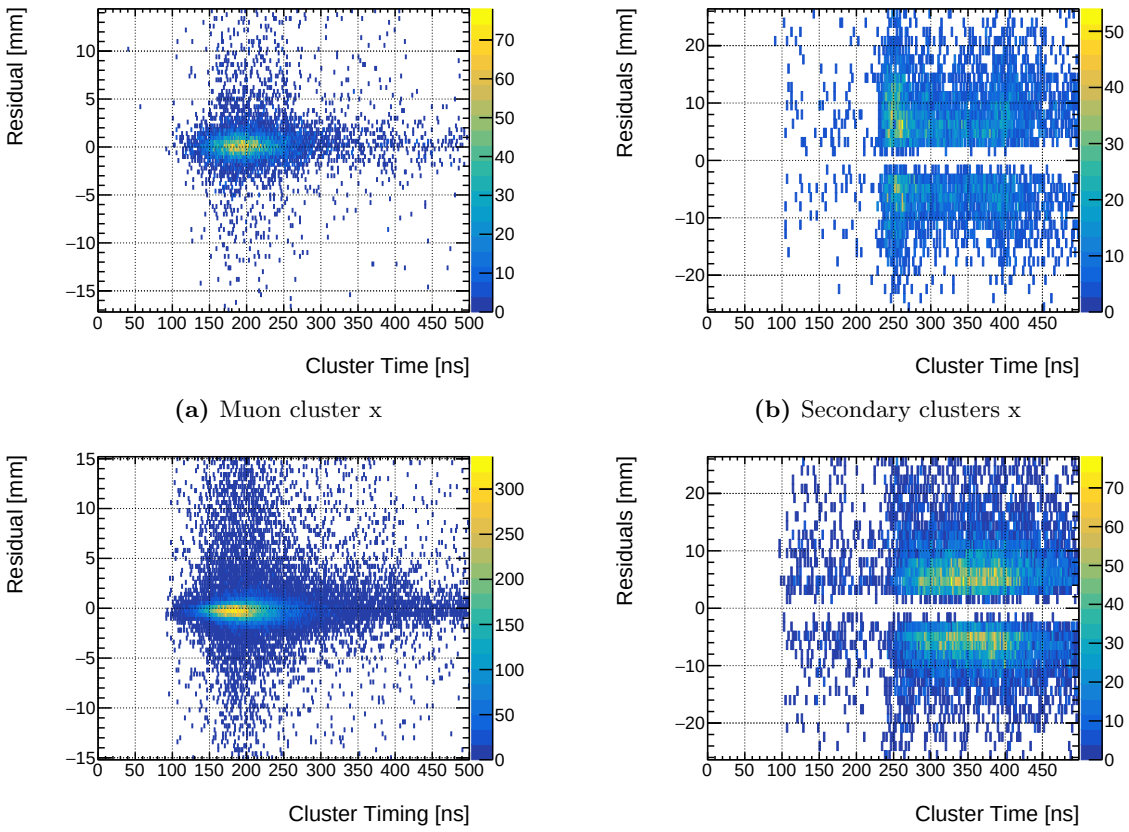

(a) Muon cluster x

(b) Secondary clusters x

(c) Muons x reversed

(d) Secondary x reversed

Figure 7.27: The cluster timing against the residuals is visualized for the muon cluster (see fig. (a)) and secondary cluster (see fig. (b)) for the normal configuration, and a reversed setup for the muon cluster (see fig. (c)) and photoelectron cluster (see fig. (d)). It is visible that the muon signal and the peak at 250 ns can be separated this way, similar to the simulation in Garfield++.

In Figure 7.28, the strip multiplicity was also compared to the cluster timing. The muon cluster in both the reversed and standard configuration has a similar number of addressed strips (see fig. (a) and (b)) from 100 to 250 ns. The wrongly as cluster accounted afterpulsing signals (> 250 ns) has fewer addressed strips on average. This is more clearly visible (see fig.

(c) and (d)), where the difference again is the Cherenkov photon signal at 250 ns (in fig. (c)). The photopeak has, on average 2-4 strips which was also the simulated value (see Figure 6.13 (a)). In general, the measured signatures are similar to the simulated distributions (see Figure 6.21 (a) for the muon and (b) for the photoelectron).

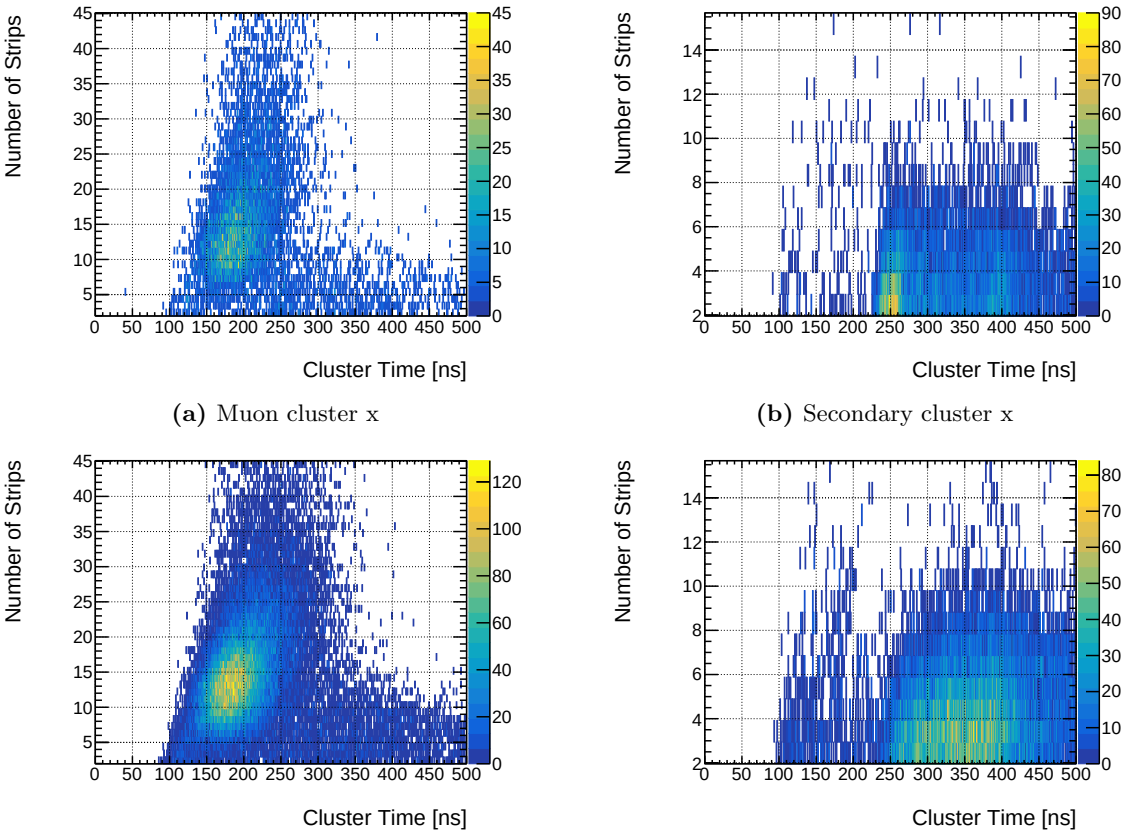

(a) Muon cluster x

(b) Secondary cluster x

(c) Muons x reversed

(d) Secondary x reversed

Figure 7.28: The number of strips is compared to the cluster timing (see fig. (a)) and secondary cluster (see fig. (b)) for the normal configuration and a reversed setup, the muon cluster (see fig. (c)) and photoelectron cluster (see fig. (d)). The after-pulsing effect in all plots for time bins > 250 ns exhibits a generally lower number of addressed strips. Also, the photon peak at 250 ns mostly has 2-4 strips addressed which is in agreement with the simulation (see Figure 6.13 (a)).

7.8 Summary

In this chapter, it was shown that the reference detectors and the Cherenkov Micromegas are all operational. Cherenkov photons have been rudimentary detected.
The spatial resolution of the CHMM detector was determined to be ≈ 700 µm. In the tracking, muon and photon cluster have been well separated.
It is shown that due to distinct photons peak in the timing, information can be used for the separation when reference trackers are used.
Furthermore, the detector reconstructs positions all over its active area within the thickness of the radiator. The photo feedback has to be improved in future iterations as the deposited charge leads to a prolonged signal and could potentially lead to instabilities in a high-rate environment.
Finally, the conversion efficiency of the photons to photoelectrons is another factor that has to be further improved and investigated, as the detector's detection efficiency of this prototype is lower than determined by simulations.

Chapter 8

Cherenkov Cone Reconstruction

This chapter aims to find a reliable momentum or energy reconstruction technique that can be used for the Inverted RICH prototype and its further development.
The analytic description of the Cherenkov cone fit is tested as follows: First, the reconstruction is tested with simulated photoelectron positions at the bottom of the radiator by Geant4 only (see Chapter 6).
Next, the reconstruction is tested with Garfield++ simulation results taking the processes inside the Micromegas and the strip readout into account. This reconstruction is also tested on measured data (see Chapter 7).
Finally, Geant4 simulations from muons arriving at an incidence angle in the radiator are also investigated to reconstruct the Cherenkov angle θ_C and the muon's inclination angle α.
Two other techniques not discussed in this chapter are: A two-dimensional fit of a Gaussian distribution (see Section D) and the application of a Machine Learning algorithm (see Section C). Both methods require further refinement for reliable momentum reconstruction.
A fit is quite challenging for individual events as it requires a stable fit for a meager amount of data points. For the simulated events, the average amount of Cherenkov photons is $N_{pe} = 75 \pm 11$ Geant4 data and $N_{clu,gar} = 21 \pm 4$ for Garfield++ simulation for the into the gas extracted photoelectrons (see Figure 6.6 (a) and (b)) and for the measured data $N_{clu,meas} = 2 \pm 1$ on average in the Cherenkov detector (see Section 7.6).
In the Garfield++ simulation (see Figure 8.1 (b)), a significant overlap between the photons closest to the muon (yellow square) is visible as the electron avalanches inside the Micromegas lead to a spread compared to the position of the photoelectrons at the photocathode (see Figure 8.1 (a)).
With $N_{clu} = 2 \pm 1$ the measured amount of data points per event is too low for a fit. Therefore the fit of multiple events was used for the Garfield++ simulation and measurement results in Figure 8.4 and the following figures.

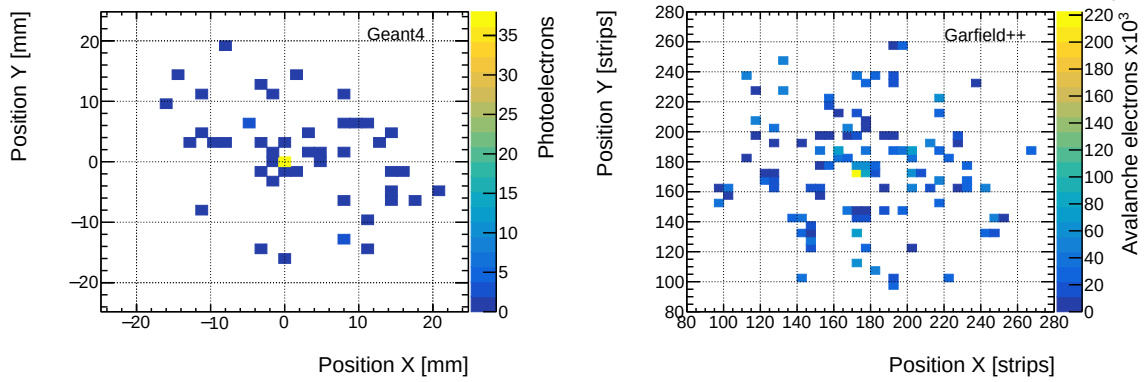

(a) Cherenkov event for a 4 GeV muon in Geant4 in units of mm centered at the muon's position

(b) Cherenkov event for a 4 GeV muon in Garfield++ in units of strips

Figure 8.1: In Geant4, the photoelectrons are created and read out at the bottom of the 20 mm LiF radiator (see fig. (a)). Another event in Garfield++ demonstrates the avalanche behavior where photoelectrons overlap a 4 GeV muon (see fig. (b)).

8.1 Analytical Cherenkov Cone Fit

The following section discusses the fit function used for the momentum reconstruction. In the case of a perpendicular incident muon, the number of photons n_0 created on each path length Δz is constant along the path of a muon in the Cherenkov medium. Thus the number of photons on each circular element for radius $\Delta r + r$ with $\Delta r \approx \Delta z \cdot \tan\theta_C$, is constant. Assuming the number of photons n_0 as homogenously distributed over a circular ring segment, then $\frac{dn}{d\phi}$ stays constant for different azimuth angles ϕ (see Figure 1.5).

$$\frac{dn}{d\phi} = \frac{n_0}{2\pi} \tag{8.1}$$

The distribution of photons on the photocathode plane projected along the x or y axis can be calculated with polar coordinates $\phi = \arccos(\frac{x}{r})$ as follows:

$$\frac{dn}{dx} = \frac{dn}{d\phi} \cdot \frac{d\phi}{dx} = -\frac{n_0}{2\pi} \cdot \frac{1}{\sqrt{r^2 - x^2}} \tag{8.2}$$

The total amount of Cherenkov photons N parametrized by Cartesian coordinates is the integral of Equation 8.2 with the inclusion of x_0 to account for displacements of the peak position integrated over the Cherenkov cone with radius R:

$$N = \int_0^R \frac{dn}{dx} dr = C \cdot \ln\left(\frac{R + \sqrt{R^2 - (x - x_0)^2}}{|x - x_0|}\right) \tag{8.3}$$

The parameter R of the function defines the radius of the Cherenkov cone. The fit function is only applied in areas where $x < R$. Otherwise, the function is set to 0 as the function becomes complex-valued.
A good fit at 4 GeV is shown in Figure 8.2 for 1000 muon events, thus including around 50000 photons produced in Geant4. Excluding reflections at the border, the function fits well with the data points.
Also, the prediction of the fit gives a radius of $R = (22.571 \pm 0.004)$ mm for a 20 mm thick radiator which is in agreement with the theoretical value of (21 ± 2) mm (see Figure 5.22 (b) blue values).

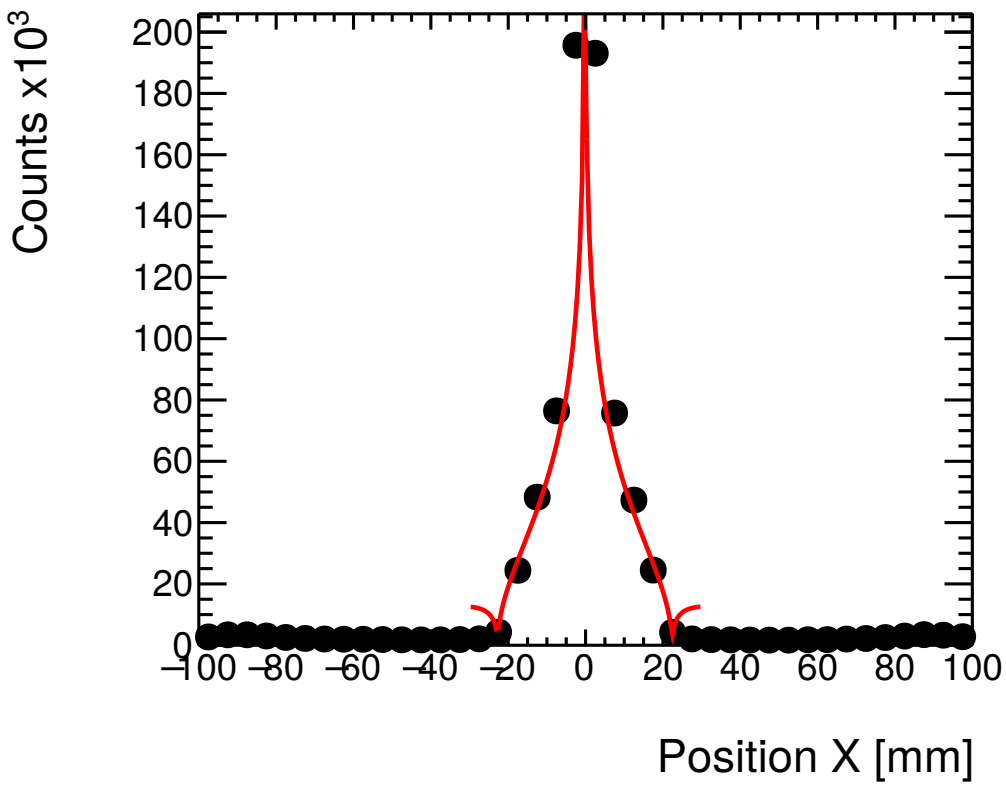

Figure 8.2: Application of the Cherenkov fit function for 1000 cosmic muons at 4 GeV with a perpendicular incidence in a 20 mm LiF radiator produced by Geant4. The radius determined via this method is $R = (22.571 \pm 0.004)$ mm, which agrees with the theoretical calculations.

8.2 Energy Variation

The goal of the detector is to determine the energy of a single incident muon.
As in Section 5.5 explained, the radius of the Cherenkov cone depends on the traversing particle's energy. Thus the fit function (see Equation 8.3) is ideal for separating energies of various Cherenkov events by determining the cone size.
The function from Equation 8.3 was applied to individual Cherenkov events from Geant4, as visible in the two examples (see Figure 8.3).
Photons far away ($> R_{C,max} = 21 \pm 2$ mm) from the expected distribution stem from reflections inside the radiator and are not distributed along the Cherenkov cone (see Figure 6.9 (a) and (b)). These are excluded from the fit.
In the case of the 4 GeV muon (see Figure 8.3 (a)) the radius fit results in $R = (25 \pm 15)$ mm and for the 100 MeV case (see Figure 8.3 (b)) in (13 ± 3) mm. This result agrees with the theoretical radius of $R_{4GeV} = (21 \pm 2)$ mm and $R_{100MeV} = (17 \pm 2)$ mm within errors. The fit is unstable for this low number of data points, leading to a larger uncertainty. However, an improvement is visible when comparing the function to the larger uncertainties shown by the Gaussian fit (see Appendix D).

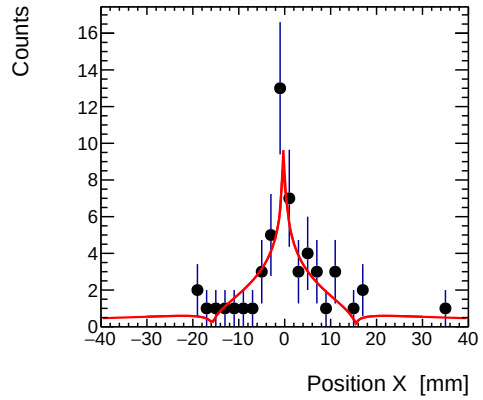

(a) fit of the x axis of a single Cherenkov Event for a 4 GeV muon in Geant4

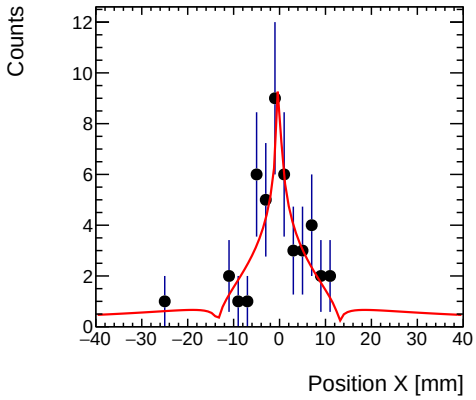

(b) Exemplary fit of a 100 MeV muon event in Geant4

Figure 8.3: For two events the function defined by Equation 8.3 is shown for a 4 GeV muon (a) and a 100 MeV muon (b). The radius determined via fit for fig. (a) yields $R_{4GeV} = 21 \pm 2$ mm and for fig. (b) yields $R_{100MeV} = 17 \pm 2$ mm. This is still a large uncertainty but much smaller than the Gaussian fit.

In the following 10000 muons and for comparison, single muon events were simulated as a function of the kinetic energy in Geant4. In Figure 8.4, the accumulation of the 50000 photoelectrons created was fit (black curve). In comparison, the individual muons creating around 50 photoelectrons were fit (green curve) and then compared to the theoretically calculated radius (blue).
In the case of all distributions, an increase in the reconstructed kinetic energy is visible. The uncertainty is the largest for the fits of single events, as to be expected due to the low statistics. This makes it impossible to differentiate between single events with a low number of photoelectrons at low energies below 100 MeV. The fit for many muons has the same issue. However, above 100 MeV, the fit is much closer to the theoretical curve than for individual muons.
Due to the significant deviation of individual muons, the following photon accumulations from around 10000 muons are used for the fit.

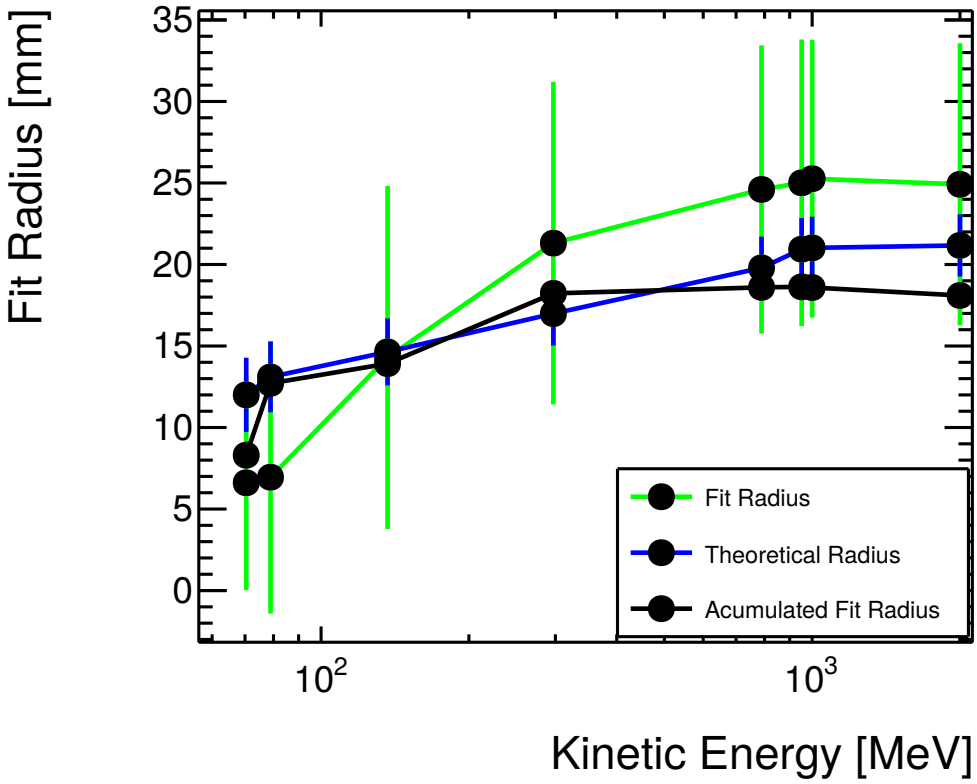

Figure 8.4: The determined radius from the fit function is shown for 10000 muons (black) and for single muons (green) produced by Geant4, where the radius deviates for low energies from the theoretical curve. In all cases, an increase is visible with larger kinetic energies, while for individual event fits, the uncertainty is too large for exact radius determination. This uncertainty is low when fitting multiple events. A deviation between the theoretical and the radius for the accumulation can be seen for energies approaching 1 GeV. This is however in agreement with the simulated radii as shown in Figure 5.22 (b).

8.3 Comparison of Garfield++ Simulation and Measured Data

The accumulated events from the simulated avalanche electrons from Garfield++ and the experimental data obtained with the CHMM in chapter 7 are fit.
As discussed, significant uncertainties arise in individual events making the fit result inaccurate. An accumulation of individual events is used. The fit is applied to the residual distributions from Garfield++ and the measured data.
The muon cluster is in the following separated from the photon cluster leading to a dip in the center of the position distribution as the overlapping photoelectrons are lost as well (see simulated distribution Garfield++ in Figure 8.5).
In Figure 8.5 (a), events created by Garfield++ fitted for a 100 mm sized radiator with 20 mm thickness are shown. Figure 8.5 (a) is for perpendicular incident muons with an energy variation Gaussian distributed between 63 MeV and 4 GeV. The radius is for perpendicular inclination $R = (24.72 \pm 0.01)\,\text{mm}$. The Gaussian energy distribution above was mapped to the corresponding Cherenkov radius dependent on the kinetic energy to also calculate a theoretical radius (see Figure 5.22 (a)). The radius calculated this way is $R_{theo} = (20 \pm 1)\,\text{mm}$. Individual events must be fit for the exact determination of the radius due to the accumulation of different particle energies. The goal, however, here is to compare the measured and simulated distribution's extent.
However, it is still possible to compare the radius of the fit function from the simulation to the measured data.

The measured data acquired with the detector hodoscope (see Chapter 7) is fit in the following. The focus is on a slight inclination angle with an acceptance angle of $\pm 1°$ in Figure 8.5 (b). The fit also works well for the data resulting in $r_{1°} = (20.7 \pm 0.2)\,\text{mm}$.
The radius determined this way is closer to the theoretical calculated radius but deviates from the simulation. Reasons for this might be due to the CsI cathode in the simulation covering the whole radiator. In contrast, in reality, a small area is not covered with CsI due to a minor defect, and the Cr is applied around a diameter of 2 mm on the edge of the radiator (see Section 7.4).

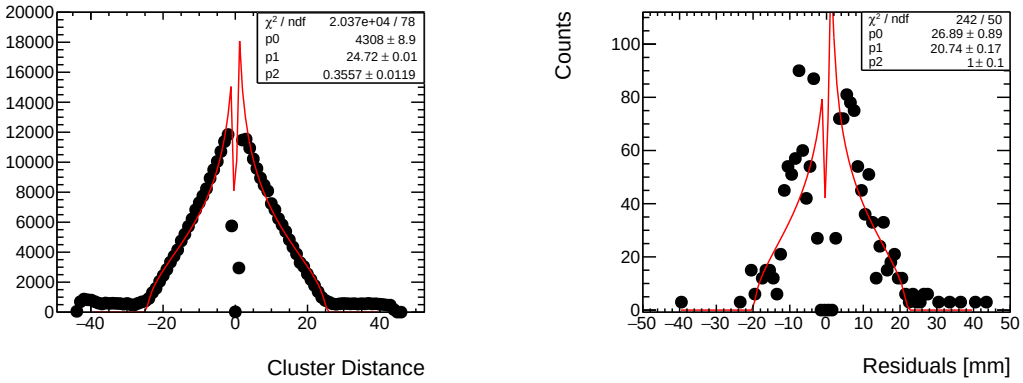

(a) 2 GeV Gaussian energy variation for a perpendicular muon with crossing point in the center of the radiator along the detector's x axis in Garfield++

(b) Fit on the measured data from the CHMM detector of the detector hodoscope between [-1, 1]°

Figure 8.5: The signature of 10000 muon events produced in Garfield++ was fit for the variation of different muon energies resulting in a radius $R = (24.72 \pm 0.01)\,\text{mm}$ (see fig. (a)). The fit function is applied to the measured residual (see fig. (b)), including 20000 muons of Cherenkov Micromegas with different acceptance angles chosen for the hodoscope in case of $\alpha = 1°$ yields $(20.7 \pm 0.2)\,\text{mm}$.

8.4 Variation of the Muon Incidence Angle

In addition to the energy variation, the angular distribution of cosmic muons in the Cherenkov Micromegas follows a $\cos^2 \alpha$ law (see Chapter 7). For this reason, it is of interest to study the signature for inclined tracks so that the fit can be used to differentiate between the incidence angle of the muon and its kinetic energy.
The two-dimensional photon hit distribution for 10000 muons created in Geant4 are shown in Figure 8.6 for varied incidence angles α in a LiF radiator with 10 mm thickness. For small angles, e.g., of 5°, the photon distribution is nearly symmetric at the center of the distribution, similar to a perpendicular incident muon (see Figure 8.6 (a) and (c)). For larger angles along one axis, the distribution becomes asymmetric.
Reflections are visible as a ring around the borders of the crystal at every angle. Also visible is that the steep centered peak becomes smeared with increasing angle.

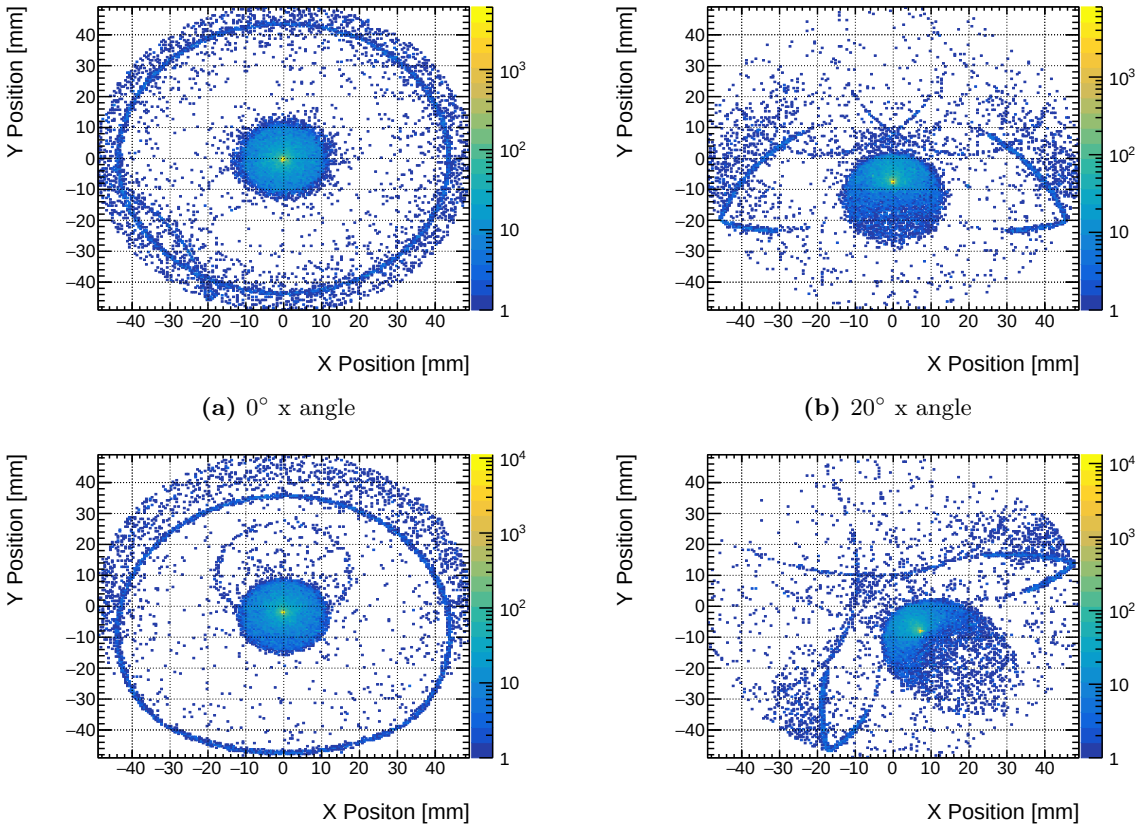

(a) 0° x angle

(b) 20° x angle

(c) 5° x angle

(d) 20° x angle and y angle

Figure 8.6: 1000 muons were simulated in Geant4 for a LiF radiator with 10 mm thickness. The incidence angle of the muon was varied: Fig. (a) shows perpendicular incidence, fig. (b) has 20° along one axis, fig. (c) 5° and fig. (d) along both axis 20°. The shape of the Cherenkov cone alters with increased inclination angles. If the tilt is significant, the cone is reflected visible for a 20° angle on the y-axis (b) and both axes (d). The noticeable large rings at the borders are also a result of reflection.

The projection of the 2D hit position for multiple inclined particles is shown in Figure 8.7. The tails of the function are becoming more significant with increasing α leading to an asymmetry between the left and right tails.
For the momentum reconstruction at incidence angle, $\alpha = 0°$, the width of this hit distribution can be directly used. When reconstructing the momentum for inclined particles, another variable that also characterizes the angles has to be found. This new variable can serve as a foundation for the reconstruction process. The asymmetry between both sides of the distribution increases due to a longer tail on one side while the other only marginally changes relative to the peak of the distribution. This could be used for the reconstruction of the incidence angle. In order to study the impact of different angles, the photon distribution and asymmetry variance are analyzed.

For different angles along the x and y axis the average photon distances $d_x = \sum_i \frac{1}{N_{pe}}(x_{pe} - x_\mu)$ (see Section 5.1) were simulated in Figure 8.8 (a) As expected, the distance of the radius increases with a higher angle on the respective axis. It stays relatively constant if the angle on the x axis changes. To find out if the inclination of a particle with a variation of both the x and y axis angle leads to an independent result along both axis, an asymmetry is defined as the distances of the photons compared to the muon position d_x along x and d_y along y:

$$A = \frac{d_x - d_y}{d_x + d_y} \tag{8.4}$$

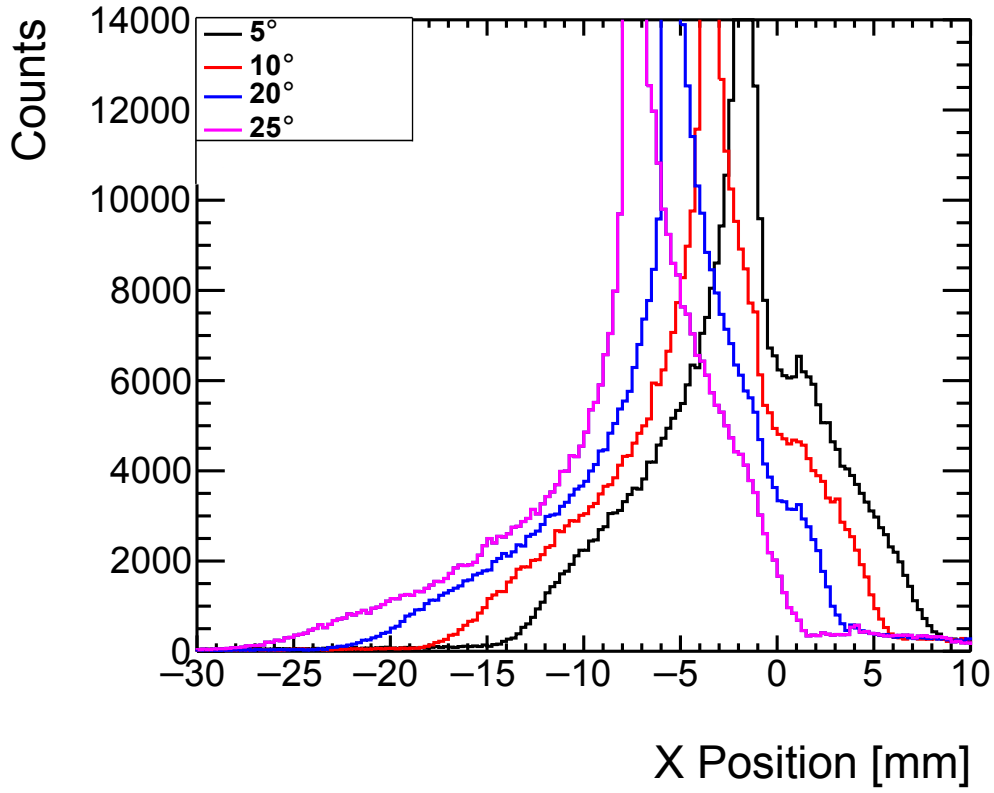

Figure 8.7: The 1D projection of the photon intensity exhibits longer tails in the direction the incident muon traverses through the radiator. For larger angles e.g., 25°, this tail nearly covers the whole detector. The asymmetry between both sides of the distribution increases due to a longer tail on one side. At the same time, the other only marginally changes relative to the distribution's peak. This could be used for the reconstruction of the incidence angle.

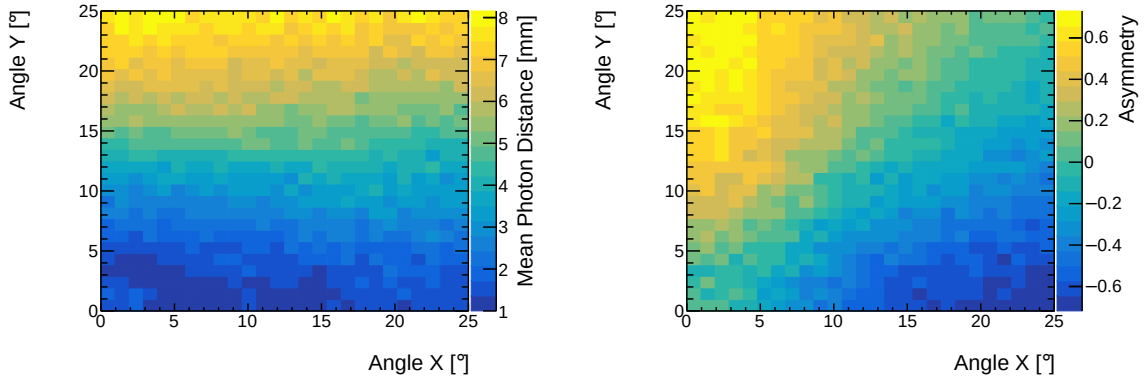

(a) The mean photon distance to the respective muon along the y axis

(b) Asymmetry A as a function of x and y angle

Figure 8.8: For different incidence angles along x and y, the mean distance of the photons away from the muon is shown in fig. (a), the asymmetry (see Equation 8.4) is determined in fig. (b), by using the mean photon distance determined in fig. (a) for a Cherenkov angle of $\theta_C = 46.8°$ in LiF (see Table 1.1). The asymmetry along both axis for the same angles is interchangeable.

For 1D reconstruction, asymmetry along the x-axis must be independent of the y axis and vice versa. This behavior can be seen in the graph in Figure 8.8 (b), where interchanging the x and y inclinations result in similar asymmetry values. Since the asymmetry value only slightly varies when interchanging x and y angles, it is possible to reconstruct inclined

particles by projecting the distributions onto the x and y axis of the detector and solving the problem in 1D.
The cone size as a 1D projection could be used to determined the incidence angle. In the following, the size of the Cherenkov cone is calculated by applying Equation 1.11. A radiator thickness d along the y axis results in 1D projected cones with size r along the x axis. Thus the equation can be rewritten as a function of x and y (see Figure 8.9 (a)):

$$y = (\tan(\theta_C))^{-1} \cdot |x| \tag{8.5}$$

Equation 8.5 only accounts for perpendicular muon tracks (see Figure 8.9 (a)). To determine also muons inclined by α a rotations matrix is used to rotate the 1d projected cone (see Equation 8.8) into a new coordinate system x' and y'

$$\begin{pmatrix} x' \\ y' \end{pmatrix} = \begin{pmatrix} \cos\alpha & -\sin\alpha \\ \sin\alpha & \cos\alpha \end{pmatrix} \cdot \begin{pmatrix} x \\ y \end{pmatrix} = \begin{pmatrix} x\cos\alpha - y\sin\alpha \\ x\sin\alpha + y\cos\alpha \end{pmatrix} \tag{8.6}$$

Equation 8.5 is then transformed $x \to x'$ and $y \to y'$ into the new coordinate system

$$y'(x') = \begin{cases} \frac{\frac{\cos\alpha}{\tan\theta_C} - \sin\alpha}{\frac{\sin\alpha}{\tan\theta_C} + \cos\alpha} \cdot x' & \text{if } x' < 0 \\ \\ -\frac{\frac{\cos\alpha}{\tan\theta_C} - \sin\alpha}{-\frac{\sin\alpha}{\tan\theta_C} + \cos\alpha} \cdot x' & \text{if } x' > 0 \end{cases} \tag{8.7}$$

After a translation of the radiator size $d = 20\,\text{mm}$ along the y axis, the zero crossing x_L and x_R of $y'(x')$ are determined. The difference $dist_x$ of these values gives the size of the projected cone:

$$dist_x = |x_R - x_L| = \left| \frac{2d}{\tan\theta_C - \tan\alpha} \right| \tag{8.8}$$

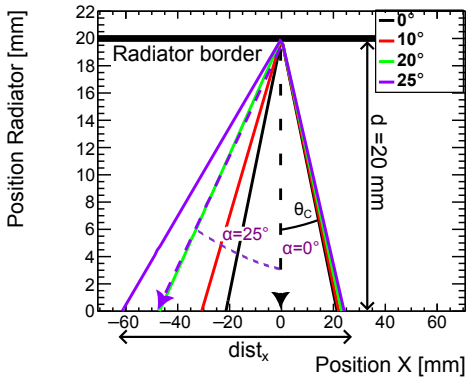

(a) Intersection of a Cherenkov cone as described by Equation 8.5 for different inclination angles of a cosmic muon with 4 GeV kinetic energy. Fig. (a) shows that the distance of the left side of the cone changes drastically with increasing angle while the distance of the right side of the cone only varies slightly. The first line could be used to determine the angle, while the other could be used to determine the kinetic energy.

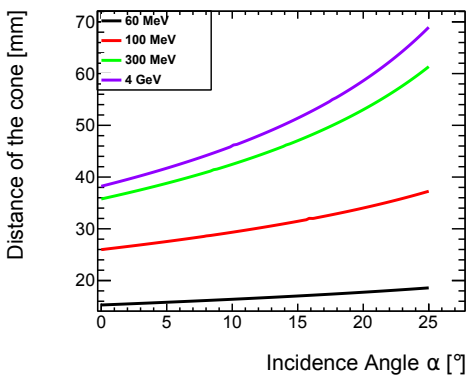

(b) Distance for 1D Cherenkov cones for a variation of the incidence angles α. The radius is half of the calculated value.

Figure 8.9: For different incidence angle α and energies of the muon, the theoretical distance $dist_x$ of the cone is plotted for different kinetic energies of the incident muon in LiF $d = 20\,\text{mm}$.

In Figure 8.9 (a), it is visible that only slight variation for the position of the right side exists. The left side of the cone varies strongly for increasing incidence angles. For larger incidence angle α, a higher distance $dist_x$ is covered by the cone on the detector's surface (see Figure 8.9 (b)).
With an average Cherenkov angle of 44.6° (see Table 1.1) the distance changes from 20 mm to 40 mm for 1 GeV muons ranging from 0° to 25° (radii taken from Section 5.5). One side (left) of the photon distribution could be used to determine the incidence angle. In contrast, the other one (right) could be used for the determination of the kinetic energy (see Figure 8.9 (a)) due to its marginal change.

8.5 Incidence Angle Reconstruction

Now also, an attempt is made to fit 10000 accumulated Geant4 events to inclined particles. It is essential to separate both quantities (Cherenkov angle θ_C and incidence angle α) otherwise, the determination of a particle's kinetic energy is not accurately possible (see Figure 8.9).
With the introduction of the inclination, a dependency for the fitted radius with the kinetic energy E_{kin} and the inclination angle has to be found to determine the particle's kinetic energy.

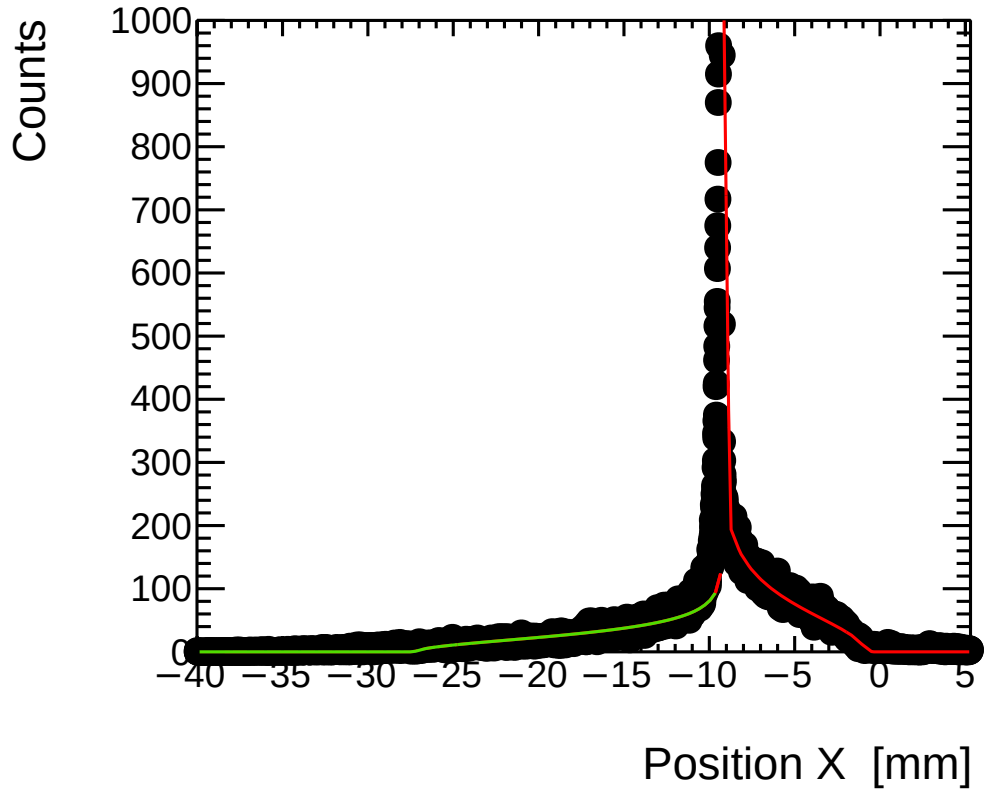

Figure 8.10: Example of the Cherenkov fit in Geant4 for a 25° inclined muon with $E_\mu = 4\,\text{GeV}$ in a 10 mm thick radiator using the two functions from Equation 8.3 to determine an asymmetry between the left and right and combined radius of the curve. The right fit (red) has a radius determined as $R_R = (8.492 \pm 0.003)\,\text{mm}$, and the left fit (green) has a radius $R_L = (17.943 \pm 0.008)\,\text{mm}$.

The effect described by Figure 8.7 that the distribution along the x axis is asymmetric with larger incidence angles α can be used to distinguish between different inclination angles.
For this reason the intensity distribution seen in Figure 8.10 is fit for 10000 muons two times. First, the left side and then the right side. In this case, the result for the right radius is determined to be $R_R = (8.492 \pm 0.003)\,\text{mm}$, and for the left fit (blue) a radius $R_l = (17.943 \pm 0.008)\,\text{mm}$ inside a 10 mm thick radiator is found.
In the following the asymmetries between left and right fits Figure 8.11 (a)) and the radii of the y axis (see Figure 8.11 (b)) were compared to the inclination angle α.
Applying the asymmetry definition from Equation 8.4 to the fit gives the result shown in Figure 8.11 (a)). When the inclination α_y along the y axis increases, the asymmetry along this axis also changes. In the case of the x axis the asymmetry stays nearly constant with variations expected due to the angular error $\Delta\theta_C$ (see Section 5.4.2). It is visible that the y asymmetry reaches values with a maximum deviation of -0.3 for the largest angle.
For the y axis (see Figure 8.11 (b)), however, a strong increase of the combined and the left radius R_L is visible where the right radius R_R stays nearly constant.
A combined radius R_{comb} is also determined with the right side radius R_R and the left side radius R_L, which shows similar change as both R_L and R_R with different angles:

$$R_{comb} = \frac{R_R + R_L}{2} \tag{8.9}$$

The right radius R_R (green) can be ideally used for the energy determination. In contrast, the left radius R_L (blue) might serve as an indicator for the inclination angle α_Y. R_{comb} (black) shows the combined behavior of both fit parameters increasing with larger α_Y.

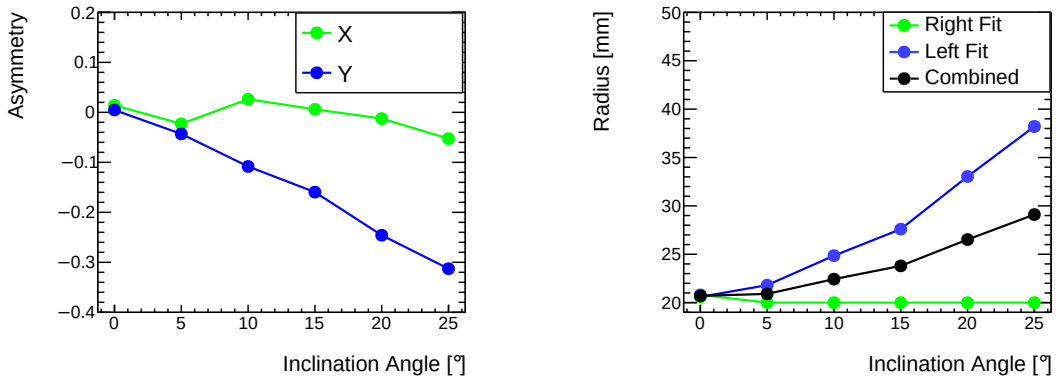

(a) The asymmetry for the x and y axis of the detector

(b) Radius y determined via fit

Figure 8.11: The asymmetry (see Equation 8.4) between both sides of the fit in y shows a clear dependency on the particle's inclination α_Y (see fig. (a)). The angle was varied along the y axis. A decrease to -0.3 is visible along the y axis. Thus this parameter can be used to characterize the inclination angle of the particle. The radii (see fig (b)) determined by fit of the two sides and the average radius are shown for the inclined y position. On the y radius, a clear increase is visible similar to the theoretical calculation (see Figure 8.9 (b)).

The asymmetry between the right and left sides can thus be used to indicate the inclination. In contrast, the smaller radius can be used to determine a particle's energy. This behavior is studied in further detail as the smaller radius must be only proportional to E_{kin} and not dependent on the angle α_Y to be used for energy separation.

8.6 Energy and Incidence Angle Variation

After having been individually varying the energy and inclination angle α_Y of the incoming cosmic muon so far, these parameters are varied simultaneously to determine whether or not the two parameters can be separated.

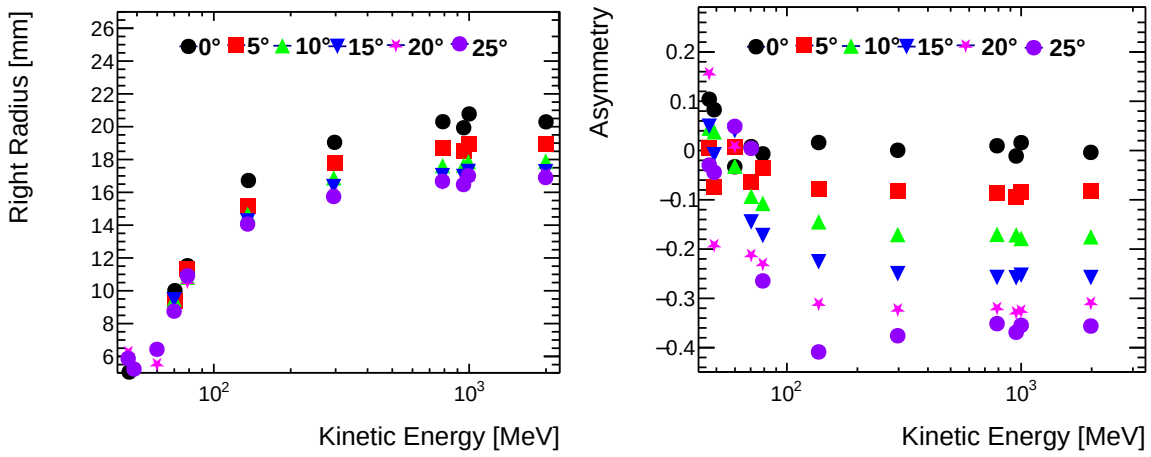

(a) Radius of the right side R_R

(b) Asymmetry

Figure 8.12: The right radius shown in fig. (a) increases with the kinetic energy of the particle while the asymmetry fig. (b) varies with the inclination angle α of the incident particle. As both quantities are distinguishable, this can be used to identify the inclination angle α as well as the kinetic energy of a particle.

As visible in Figure 8.12 (a), the radius of the right side increases with the kinetic energy. It is expected that this radius only increases to a small degree for different angles of incidence (see Figure 8.11 (b) and theoretical calculation see Figure 8.9 (a)).
For low energies, the number of created photons is minimal, as well as the radius. This makes the identification of low-energy particles difficult.
Figure 8.12 (b) shows the different asymmetry values determined as a function of energy. Due to the small number of photons at energies below 100 MeV, the asymmetry varies strongly while staying constant at higher energies. Different angles become distinguishable via asymmetry.
Cherenkov cones created by perpendicular muons are symmetric. Thus, an $A = 0$ is determined for those values. The energy and inclination angle can be distinguished and determined with the right radius R_R and the asymmetry between the left and right sides.

8.7 Summary

In this chapter, a promising analytic description for the Cherenkov cones was studied for accumulations of muon events and individual muon events generated by the simulation. For these accumulations, the fit worked well. Also, the comparison between simulation and measurement data showed some agreement regarding the distribution width. The fits of single events are improvable.
The implication of inclined muons for the photon distribution was discussed initially. The increasing cone size when the muon traverses the detector at an angle α can be utilized to also determine different incidence angles and photon energies simultaneously with the fit function.

Chapter 9

Potential Detector Optimizations

In the following possible optimizations for the Inverted RICH detector prototype are proposed. These include possibilities to resolve ambiguities, improvements concerning quantum efficiency, and options for reaching different momentum ranges.

9.1 Ambiguity of the Position Reconstruction

Different reconstruction techniques have been discussed in (see Chapter 8). These relied on a 1D strip information. Complete 2D position information is desired for the many Cherenkov photons to resolve all ambiguities.
A pixel detector with a fine spatial resolution $\sigma_{pix} = \frac{\text{pitch}}{\sqrt{12}}$ would introduce very many electronic channels to reach a comparable resolution to a strip detector [Kolanoski and Wermes, 2016]. Comparing a potential pixel anode to an anode with 358 strips per layer, the required electronic channels would be around $strips_x \cdot strips_y = 358 \cdot 358 \approx 128000$ electronic channels.
Alternatively, introducing another strip readout plane rotated by 45° can decrease the ambiguities. Jagfeld [2023] proposed such a detector in the form of a Segmented Gaseous Electron Multiplier readout (SGR) that reads out an XYV triple plane (see Figure 9.1).

Similar to a Micromegas detector, a Gaseous Electron Multiplier (GEM) invented by F. Sauli in 1997 is a micropattern gaseous electron multiplier with high rate capabilities.
GEM foils are made out of thin 50 µm Kapton foils sandwiched by 5 µm metal layers. In periodic distances, holes allow electrons to traverse through the GEM foil. An electric field created by the voltages applied between the top and bottom side leads to gas amplification in the holes.
The design by Jagfeld [2023] as a hybrid detector of GEM and Micromegas allows for a third position information added to the two created at the readout strips of the Micromegas detector (see Figure 9.2).

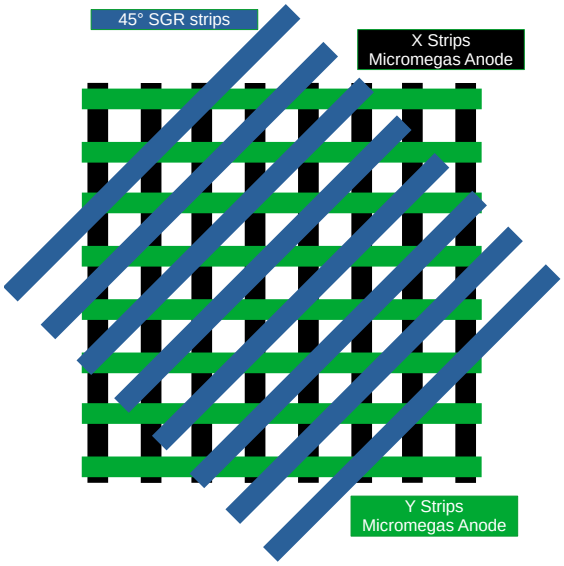

Figure 9.1: Schematic of a xyv strip design. In addition to the readout strips of the Micromegas anode, a third detector plane allows the separation of multiple particles as the layer is turned relative to the anode strips. The third detector plan can be used with a pixel anode [Jagfeld, 2023].

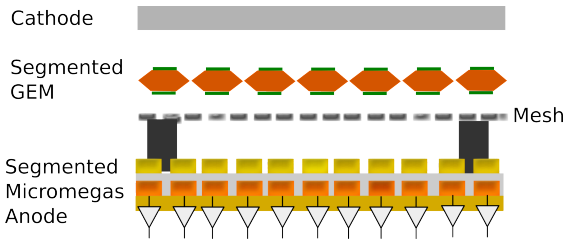

Figure 9.2: Layout of a potential next development step of the readout anode. This detector would allow for a fine detector resolution while also narrowing down the ambiguities on a pixel or a strip Micromegas [Jagfeld, 2023].

The GEM foil is segmented and can be read out via the APV25 readout electronics. If the readout strips of the SGR are turned relative to the anode strips by 45° the detector's readout would allow for a reduction of the ambiguities while multiple particles are traversing the detector (see [Jagfeld, 2023]).
Another advantage is that the GEM defines another separate gas region with a different electrical field. With a small size of about ≈1 mm photoelectron could be amplified in this region.

9.2 Detection Efficiency

Increasing the photon detection efficiency is another critical step in optimizing this detector. A straightforward method of increasing the detection efficiency would be using a gas with higher extraction efficiency ϵ than Ar:CO_2 93:7 vol% with $\epsilon_{Ar} = 55\%$ (see Section 6.2.2) like a Ne mixture of Ne:CF_4 with $\epsilon_{Ne} = 78\%$ (see Figure 2.11) or COMPASS gas also used by the Picosec Micromegas (see Section 2.4).
Another improvement without a complete change of the design can be made with the photocathode. Applying thinner layered Chromium could improve the transmission however, the electrical conductivity might decrease in the process.
Also of interest might be the use of Ni with transmission $T_{Ni} = 75\%$ at 350 nm and for Chromium with $T_{Cr} = 60\%$ for the 3.5 nm of layer thickness [Ghosh et al., 2009].
Finally, the photocathode material itself can be changed so that visible light is transmitted however, in transmissive mode CsI is already the best choice for the wavelength of 100 - 200 nm (see Section 5.1).
The combination of these improvments when applying (see Equation 9.1) the peak detection effiency ϵ_{det} including the peak quantum efficiency $QE = 9\%$ for CsI from Hamamatsu [2007]

is

$$\epsilon_{det} = T_{Ni} \cdot \epsilon_{Ne} \cdot QE = 5.4\% \tag{9.1}$$

This is a good improvement compared to the simulated detection efficiency with Ar:CO_2 93:7 vol% and 4 nm Cr layer of $\epsilon = 2.28\,\%$ (see Section 6.2.2).
Another option would be using a reflective photocathode evaporated onto a GEM foil (see Figure 9.3). Compared to the transmissive mode, the photon does not have to traverse the whole cathode in a reflective photocathode. Thus the quantum efficiency QE is increased. The position of the photocathode will limit the angular acceptance of the detector to only perpendicular incidence. The photons must pass from the radiator with a large refractive index to the gas with a much lower refractive index close to 1. Here the photons will experience total reflection. For a LiF radiator with $n = 1.46$ (see Table 1.1), the critical angle θ_T at which total reflection will occur when light is guided into a gas $n_g \approx 1$ is:

$$\theta_T = \arcsin\left(\frac{1}{n}\right) = 43.23^\circ \tag{9.2}$$

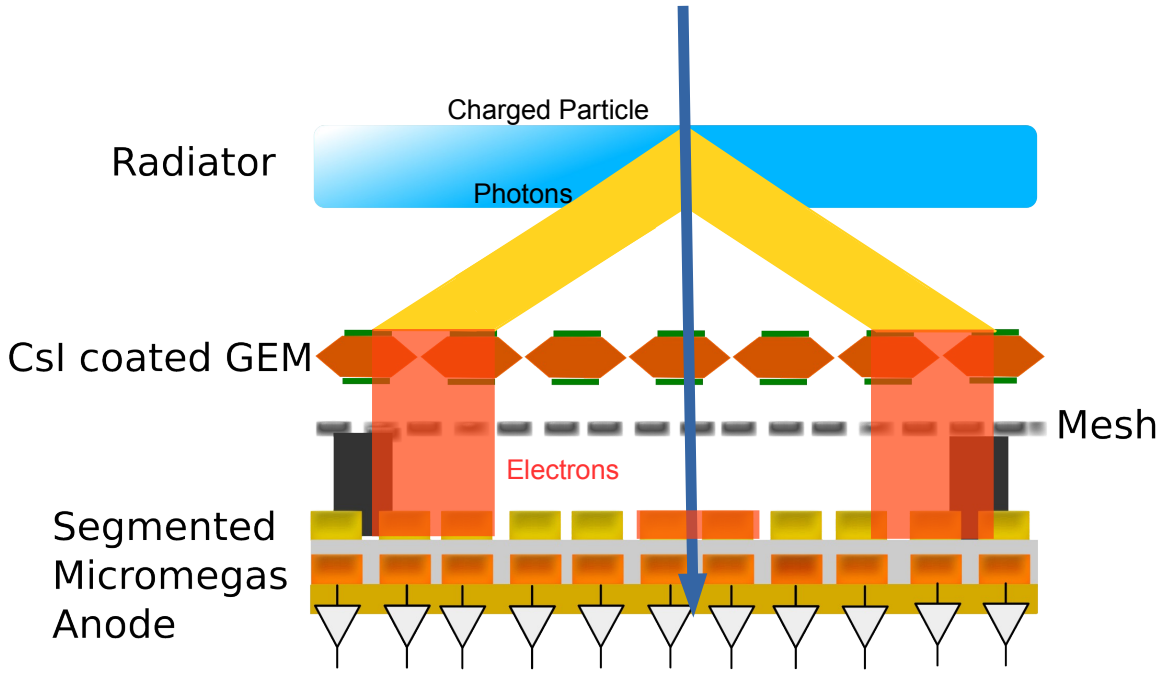

Figure 9.3: Another layout involves changing the photocathode to a reflective photocathode on top of a GEM foil, increasing the quantum efficiency, and achieving a ring form on the detector readout.

It would be possible to apply standard RICH reconstruction methods [Muresan, 2007] , as the Cherenkov photons can fly through the gas volume. No further Cherenkov photons are created inside the gas, and a ring shape becomes visible. Similar detector types in this form have been successfully studied [Martinengo et al., 2011]. Also possible in another step would be the combination of the SGR with a CsI layer. This design will require a second GEM foil in the detector covered by the CsI and where the photoelectrons will be preamplified.

9.3 Kinematic Range

A drawback of the initial design is that the energy range of the detector is limited, e.g., in LiF starting around $E_{kin} = 40\,\text{MeV}$ (see Section 1.1).
A material with a low refractive index $n < 1.1$ will be necessary to make also the high energy

regions accessible such as cosmic muons around an energy of a few GeV. Because of this lower refractive index, however, the photon yield will be lower according to the Frank Tamm formula (see Equation 1.5).
A design quite similar to the ARICH of Belle II called proximity focusing RICH could be used (see Figure 9.4).
This design stacks different radiator materials on top, thus making it possible to differentiate between different particles due to the alternating refractive indices leading to different Cherenkov angles (see Figure 1.2). If CsI is the used photocathode, then an alternation between a liquid, gaseous and solid radiator has to be made.
Another option would be using an aerogel that is manufactured without containing air so that transmission of VUV photons is possible.

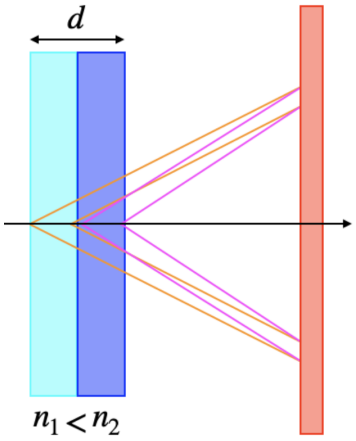

Figure 9.4: Example of a proximity focusing RICH. The detector uses the Cherenkov angle in two different media differs. Taken from [Yonenaga, 2020]. The overlap of Cherenkov rings on the photodetector is desired for a fine resolution of the Cherenkov photons.

Chapter 10

Characterization of a 10x10 cm^2 Pixel Micromegas

As an alternative to strip anodes, an option for the Cherenkov detector might be to use a pixelated Micromegas detector[1]. Such a type of anode could be suited for direct reconstruction of the two-dimensional Cherenkov cone for the momentum of a particle (see Chapter 9). In this chapter, a pixel detector prototype with 8x10 mm^2 sized readout pixels underneath a resistive strip anode is characterized with a ^{55}Fe source using a 6 mm drift region. The pixel size is certainly too coarse to be used in Cherenkov applications. This study aims, therefore, to demonstrate the feasibility of pixel Micromegas detectors.
The technical drawing of the detector's anode is shown in Figure 10.1. The 120 pixels are connected to the APV25 chip via a Panasonic connector. The detector functions as described in Section 2.3 except the readout strips are replaced by readout pixels.

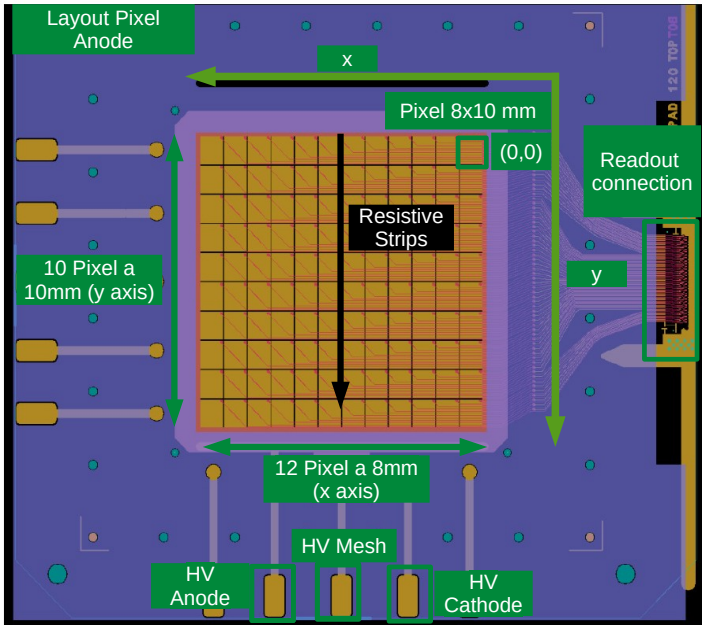

Figure 10.1: The pixelated detector has an active area of 10x10 cm^2 with 120 pixels. The pixels are asymmetric and have a size 8x10 mm^2. One APV25 readout hybrid is required. The resistive strips are guided to the HV supply on top of the pixels. Along the y axis a v-shaped spread along the 10 mm sized pixel is expected due to the resistive strips.

[1]The anode is manufactured at CERN

Along the y axis where the pitch is 10 mm the v-shaped spread across the resistive strip anode is expected as the resistive strips are perpendicular to this axis (see Section 2.3).
The detector is filled with an Ar:CO_2 gas mixture of 97:3 vol%. The voltage applied on the cathode is $U_{drift} = 350\,\text{V}$ while the anode voltage U_{ampl} is varied to determine the working point.

10.1 Measurement Setup

The experimental setup is demonstrated in Figure 10.2. A guide rail is used on top of the pixel detector to precisely place the ^{55}Fe source to measure signal sharing between the individual pixels. An Ortec Model 142PC preamplifies a trigger signal for the readout electronics. [Ortec, 1970] is used. Using dense scintillators is impossible as the photons created by the ^{55}Fe source are stopped inside the scintillator material and can not reach the gaseous volume. For this reason, the preamplifier picks-up a trigger signal from the micro-mesh of the detector.

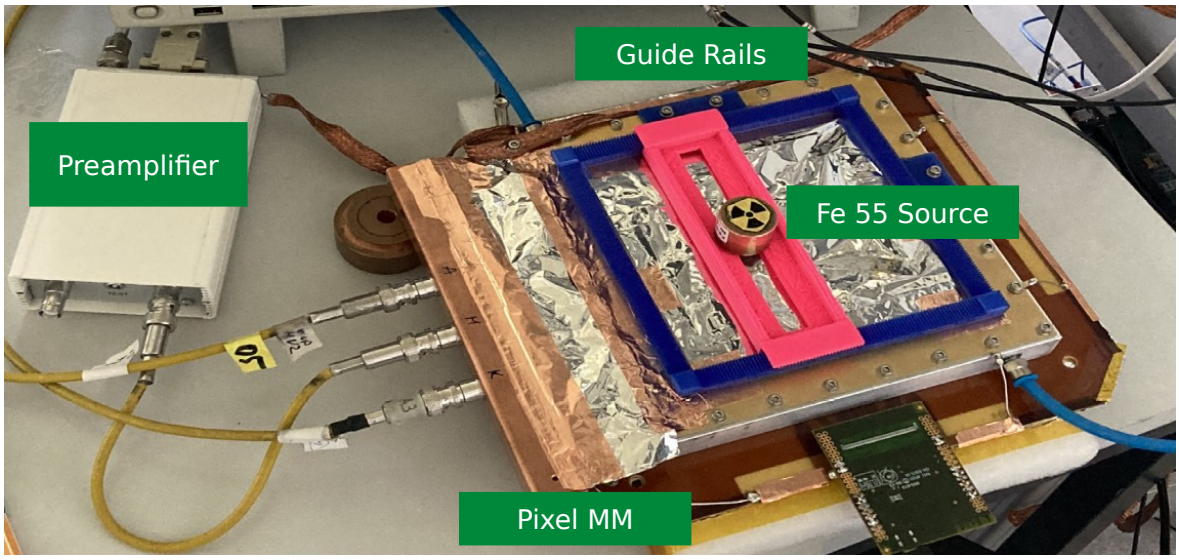

Figure 10.2: Picture of the ^{55}Fe measurement setup with the pixelated Micromegas detector. The ^{55}Fe is positioned on a guiding rail to scan the pixels with the source. The trigger signal is obtained via the signal on mesh amplified by a preamplifier.

The trigger chain for this setup is shown in Figure 10.3. The charge signal from the micro-mesh is converted to a voltage signal in the preamplifier and then amplified and shaped. A CAEN CFD N843B [CAEN, 2021] constant fraction discriminator converts the charge signal to a NIM standard pulse which is used as a trigger signal [Leo, 1987]. The signal has to reach a certain threshold to be gated through. The dual timer (CAEN N93B [CAEN, 1991]) ensures that the trigger rate is manageable for the FEC. In another operational mode, a randomized trigger signal was used created by a pulse generator. The randomization allows the detector to run at low anode voltages, where the mesh trigger no longer provides a reliable trigger signal.

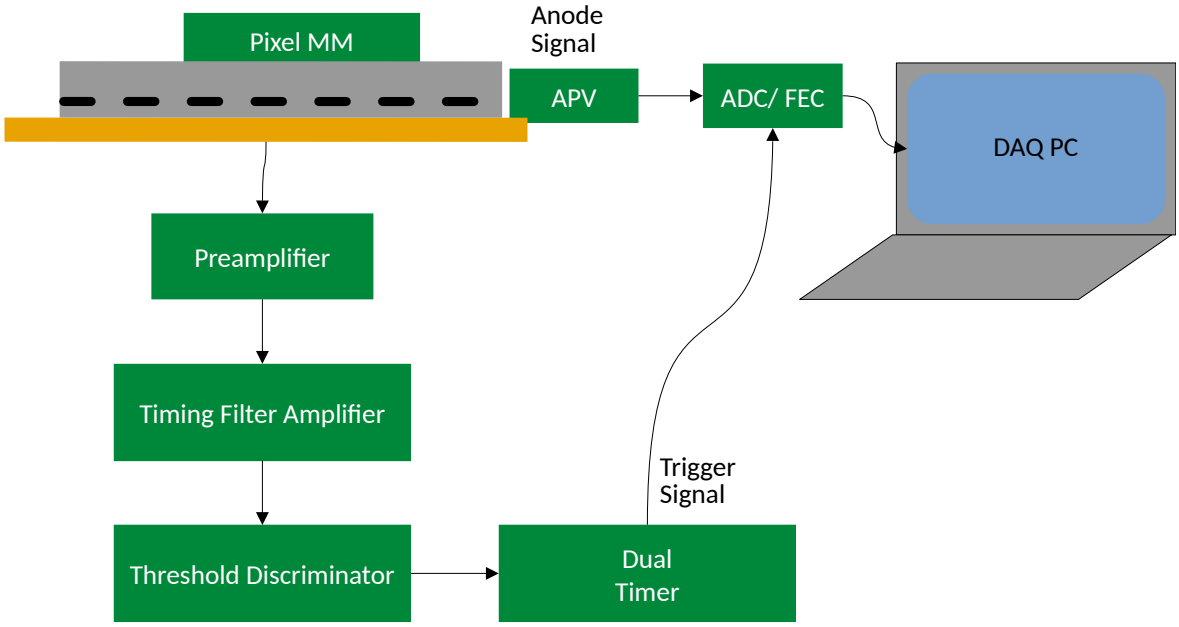

Figure 10.3: Readout chain of the ^{55}Fe measurement with the pixelated Micromegas. The detector signal is read out via the APV25 SRS hybrid after the readout system receives the trigger signal. The timing filter amplifier amplifies and shapes the signal, while the threshold discriminator filters events above a chosen threshold value. The dual timer extends the trigger signal duration to be longer than the time needed to read out an entire event.

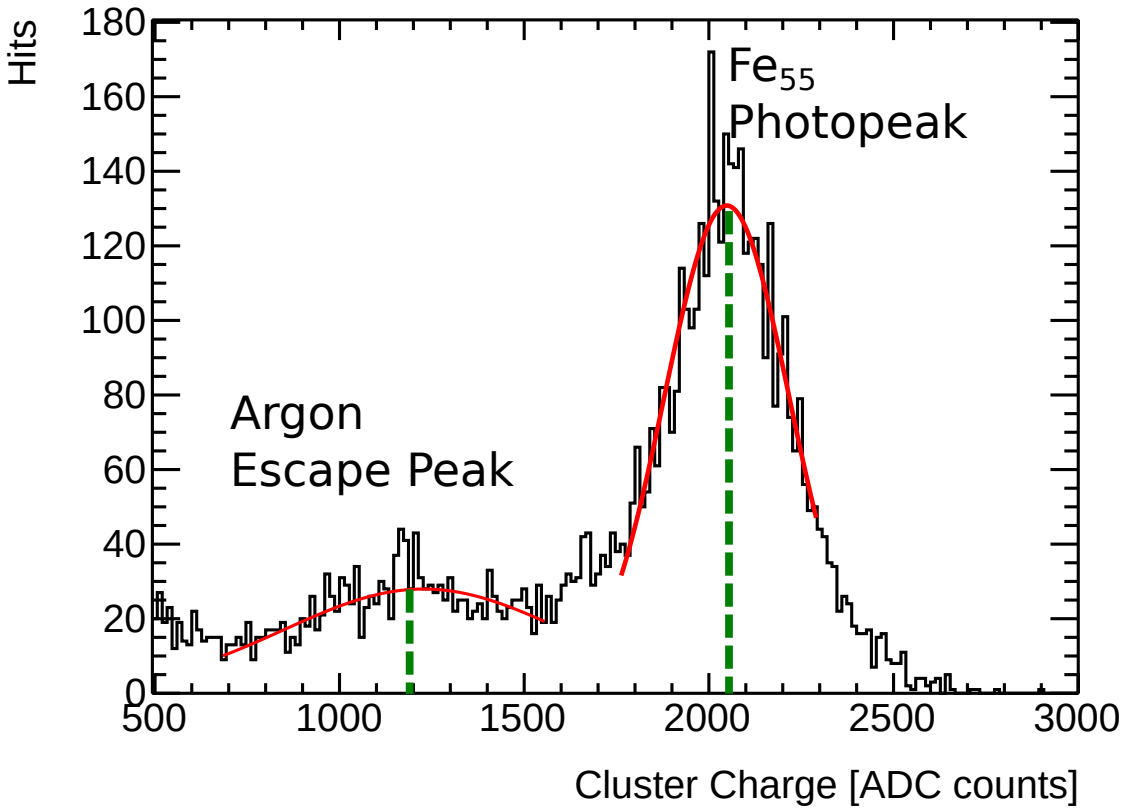

Figure 10.4: The measuredenergy spectrum of ^{55}Fe is shown in units of ADC counts at $U_{ampl} = 460\,\mathrm{V}$ for 10000 photons. The K_α photon peak (2049 ADC counts) in the energy spectrum and the Ar escape peak (1200 ADC counts) are both resolvable.

The decay of the ^{55}Fe source produces two distinct peaks in its spectrum (see Figure 10.4). Via electron capture, ^{55}Mn is created. The most probable emission is the K_α line with an energy of the created photon of $E_\gamma = 5.9\,\text{keV}$. The created photon interacts via photoeffect with the gas (see section 1.3). Depending on the de-excitation process, the total photon energy $E_\gamma = 5.9\,\text{keV}$ is deposited in the detector or some energy, the de-excitation of an Ar atom of 3 keV, leaves the detector in the form of a photon so that only the so-called Ar escape peak $E_{Ar} = 2.9\,\text{keV}$ is measurable [Danger, 2014]. This discrete energy spectrum is ideal for energy calibration as the fraction between the two peaks is expected to be:

$$\frac{E_\gamma}{E_{Ar}} = \frac{5.9\,\text{keV}}{2.9\,\text{keV}} = 2.03 \tag{10.1}$$

10.2 Raw Signal

A typical raw signal for $U_{amp} = 520\,\text{V}$ of a ^{55}Fe photon covering the middle of the detector is shown in Figure 10.5. A strong saturation (above 1600 ADC channels) is visible over three pixels along the y axis. Eight pixels detect a pixel charge higher than the chosen threshold. The number of electrons created by the photons of a ^{55}Fe source were determined by Danger [2014] to be around 120 - 200 electrons in a drift gap region of 5 mm in Ar:CO_2 93:7 vol%. This high electron number leads to a saturation of the APV25 amplifier. A time-resolving

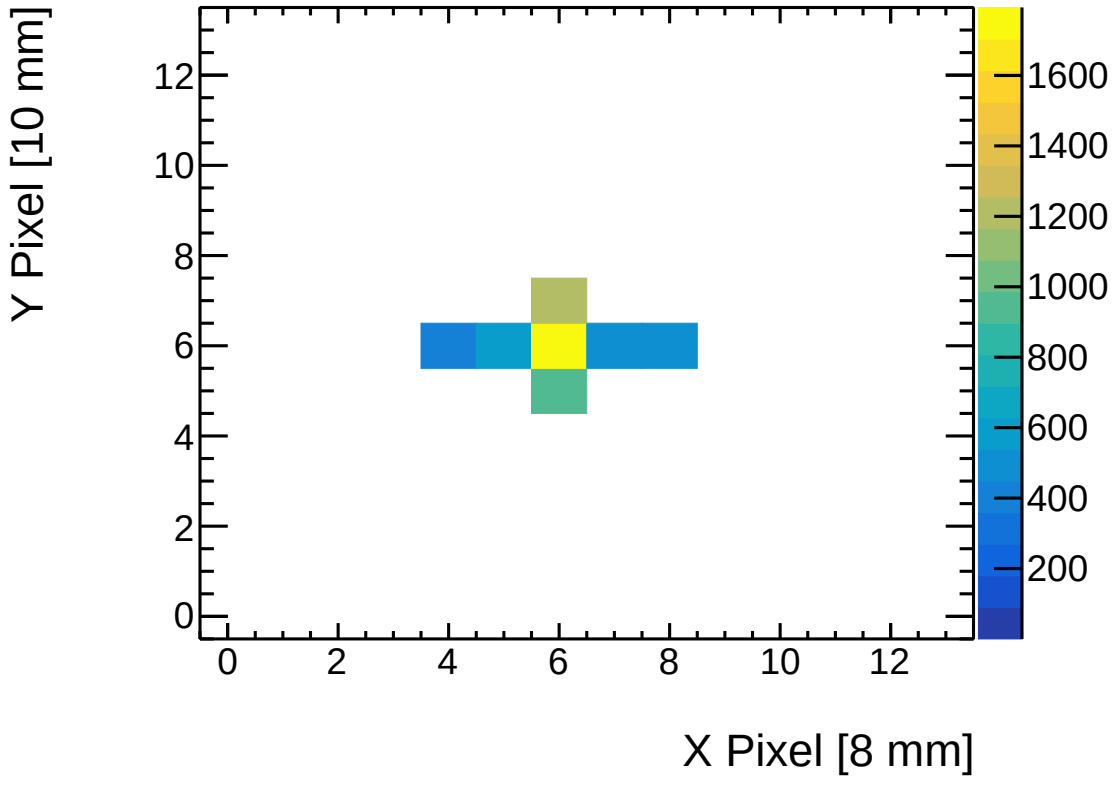

Figure 10.5: A single event of a ^{55}Fe decay where the highest charge on each pixel is color coded at 520 V amplification voltage. The highest charge is strongly saturated. It is visible for this particular event that the strongest signal is located on two neighboring pixels in y. Along the x pixels, charge sharing effects seem to be induced between channels.

projection of the same event onto the x and y axis of the detector parameterized by the APV channel is shown along the x plane (see Figure 10.6) and the y plane (see Figure 10.7). The neighboring pixels in Figure 10.6 along x are 1 APV channel apart, while in Figure 10.7 along

y they are 12 APV channel apart.
On the x axis (see Figure 10.6), the pixel experiencing the most charge seems to share the charge with its neighboring pixel. The arrival time of the charge on every pixel is of similar order.
The x position shows a strong charge-sharing effect between the pixel with the highest charge and its neighbors. This effect is likely induced by capacitive coupling. The main reason for capacitive coupling is a coupling between the detector channels going to the Panasonic connector for the readout electronics. The timing of this charge effect is expected to be the same as the original responding readout channel. This behavior is further investigated (see Section 10.5).
The y axis (see Figure 10.7) perpendicular to the resistive strips is also where the v shape of the signal is visible (see Section 2.3). The propagation of the signal as a v shape leads to a staggered signal propagation time. The signal sharing effect on both axes is further studied in Section 10.5.

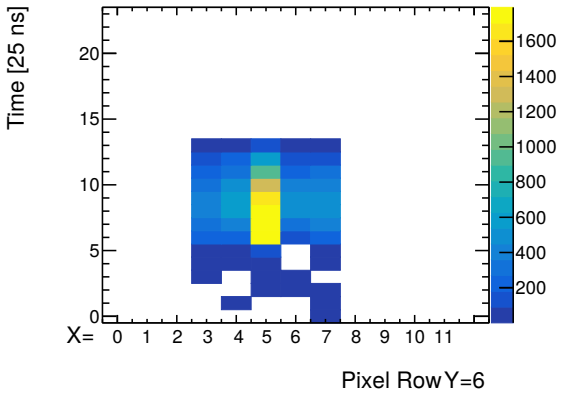

Figure 10.6: The same event as in fig. 10.5 sorted along the x pixel compared to time on y pixel 6. The charge sharing induced by the pixels with the highest charge to its neighbors is visible.

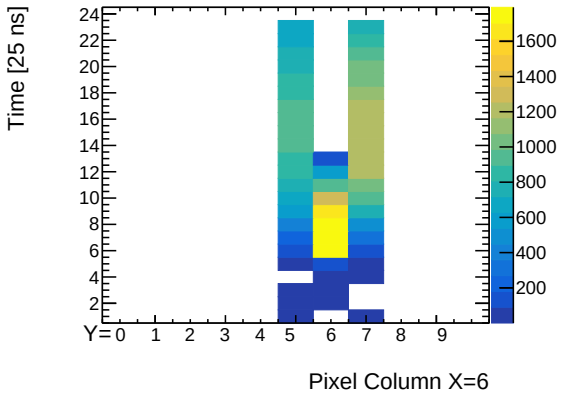

Figure 10.7: The same event as in fig. 10.5 shown are the 10 y channels of a detector column multiplied by the considered x row compared to time. The expected v shape between the strips is visible for x pixel 6.

10.3 Pixel and Cluster Charge

First, the pixel and cluster charge distributions are investigated to determine a working point defined by the amplification voltage U_{ampl}. A threshold above 80 ADC counts is required for the pixel charge. Otherwise, the pixel is regarded as noise.
The pixel charge for different amplification voltages is visible in Figure 10.8 (a) and (b). The effect of the saturation of the readout electronics (see section 3.1) for large U_{ampl} is visible in Figure 10.8 (a) where a large amount of saturation is created. A channel is accounted for as saturated when the pixel charge exceeds 1800 ADC counts. Saturated signals are set around this value by the readout electronics.
Thus, many events can not be used to reconstruct the energy spectrum as visible in the form of the dominant peak around $\approx$ 1800. ADC counts for amplification voltages of 470 V and 500 V. When decreasing the voltage, the saturation also decreases (see Figure 10.8 (b)).

An optimum is reached for the pixel charge at $U_{ampl} = 460$ V where the whole dynamic range of the APV25 is utilized. Only a small amount of saturation is determined for this voltage.
For lower U_{ampl} also, the maximum pixel charge decreases, which is expected to negatively affect the energy resolution as the readout chip does not utilize the full charge range.
The cluster charge should contain the complete deposited charge inside the detector. This

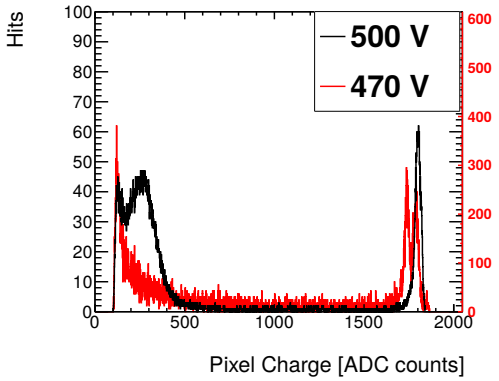

(a) Pixel charge with high saturation (scaled)

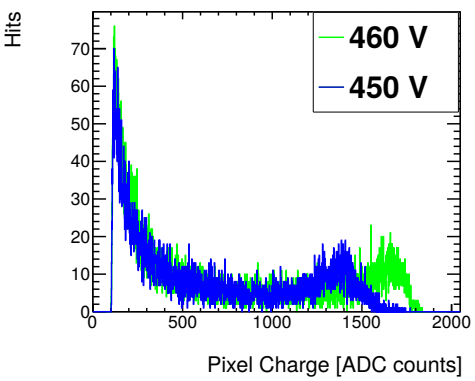

(b) Pixel charge close to the working point

Figure 10.8: The pixel charge exhibits high saturation for voltages $\geqslant 470\,\mathrm{V}$. The voltage has to be decreased for optimal detector operation using APV25 readout electronics. 460 V is the highest U_{ampl} such that no saturation is observed.

means that the ^{55}Fe spectrum with its distinct energy peaks should be visible for the cluster charge (see Figure 10.9 (a) and (b)).
For the amplification voltages of 500 V only one peak in the detector is visible as the K_α overlaps with the smaller Ar escape peak (see Figure 10.9 (a)). This effect is already visible for $U_{ampl} = 470\,V$. This effect is increased by saturation as the charge of the K_α peak only increases marginally.
For the working point at around 460 V, the Argon escape peak becomes prominent, qualifying it as the working point (see Figure 10.9 (b)).

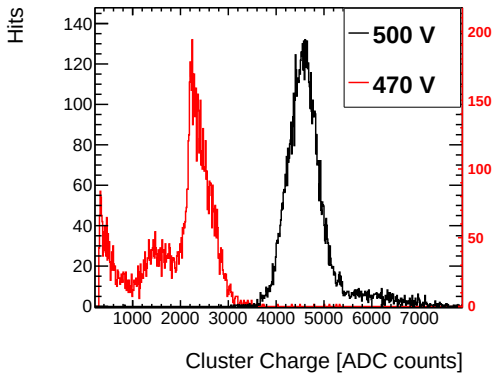

(a) Cluster charge with over saturation on single pixels (scaled) (see Figure 10.8)

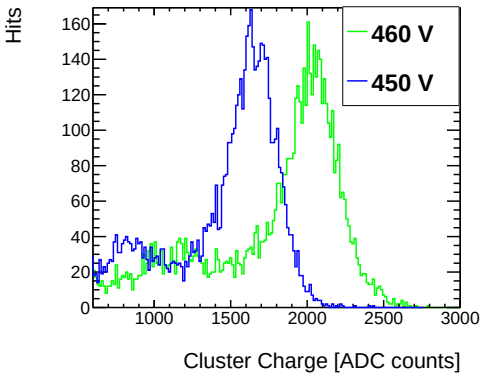

(b) Cluster close to the working point

Figure 10.9: Cluster charge of the pixel detector for saturated amplification voltages of 500 V and 470 V in fig. (a). The $K\alpha$ and the Ar escape peak would be expected for the energy spectrum of the ^{55}Fe source in the cluster charge. Due to the saturation, the smaller Ar Escape peak can not be resolved above 470 V. In fig. (b) this peak is well resolvable for voltages of 460 V and 450 V.

The mean value obtained by a Gaussian fit of the K_α peak and the Ar escape peak is shown as a function of the applied anode voltage U_{ampl} (see Figure 10.10).
It is increasing exponentially due to the gas gain (see Section 2.2.2) inside the detector up to U_{ampl} around 470 V for both peaks. Both peaks should increase similarly. Above those voltages, a substantial deviation from the exponential increase is visible due to the high saturation of the readout electronics. Also, above 470 V, the Ar escape peak is no longer resolvable due to the overlap of the two peaks.

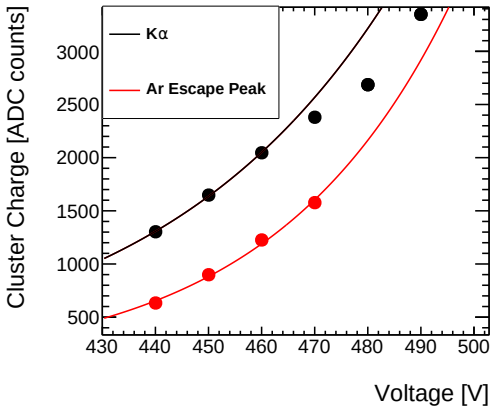

Figure 10.10: The mean value of the cluster charge determined by a Gaussian fit was determined for several amplification voltages. An exponential increase is visible as expected up to 470 V. Above 480 V the K_α peak vanishes due to saturation.

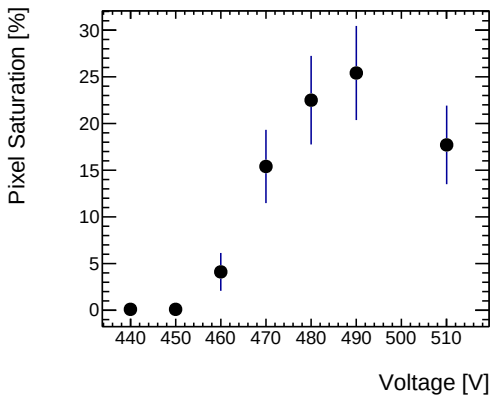

Figure 10.11: Fraction of saturation of all readout pixels per event for 20000 events. Saturation starts at a voltage of 470 V. A decrease is visible as charge sharing effects induce an observable charge on pixels neighboring the saturated ones and increasing the number of hit pixels.

The slope of the exponential fit $c \cdot e^{ax}$ yields for the K_α line $a = (0.0299 \pm 0.001)\,\frac{1}{V}$ and a constant of $c = (-6.6 \pm 0.7)$ ADC counts. The fit of the Ar escape peak values yields a slope of $a = (0.0225 \pm 0.02)\,\frac{1}{V}$ and a constant of $c = (-6.7 \pm 0.7)$ ADC counts.
The resulting exponential increase for the K_α line is roughly of the same order. The lower gain might be because of saturation effects influencing the K_α peak. The saturation effects are the reason for the deviation of the data from the exponential increase above 470 V.
The before mentioned saturation (see Figure 10.11) increases when amplification voltages of 470 V. Up to 460 V this effect is negligible only reaching 5 % of all addressed pixel integrated over 20000 events. For 510 V the saturation effect decreases. As the voltage increases, crosstalk effects stemming from the saturated pixel affect the signal more strongly, leading to an increased number of addressed pixel (see Figure 10.16). For this reason, the saturation of all addressed pixels may decrease.
The fraction of the Ar escape peak and the K_α photon peak at 5.9 keV should result in a fraction of 2.03 (see Equation 10.2). At every voltage possible to fit both of these peaks, the fraction was determined (see Figure 10.12).
The theoretical fraction of 2.03 is the closest reached by the voltages 440 V and 450 V. For higher U_{ampl}, a deviation from this value exists due to saturation inside the detector, and thus the Ar peak can not be resolved well at those voltages.
The energy resolution res_E is defined by the width σ of the K_α peak and the reconstructed pulse height E_γ:

$$res_E = \frac{\sigma}{E_\gamma} \tag{10.2}$$

The energy resolution was determined for varying amplification voltages U_{ampl} (see Figure 10.13). For $U_{ampl} < 460$ V the energy resolution is 11%. When reaching $U_{ampl} = 460$ V a minimum of 9 % is reached. For increasing voltages, the energy resolution also worsens.

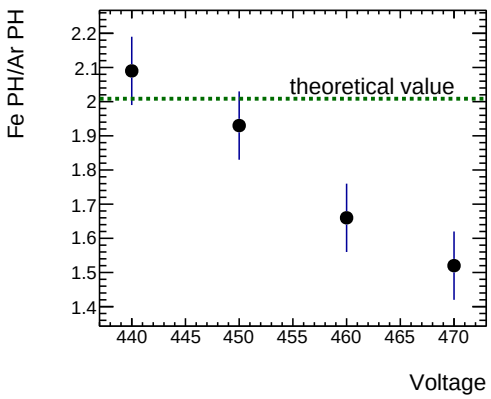

Figure 10.12: The nominal ratio between the K_α peak and the Argon escape peak is expected at 2.03. The data points for voltages 440 V and 450 V almost reach this ratio but follow an overall trend.

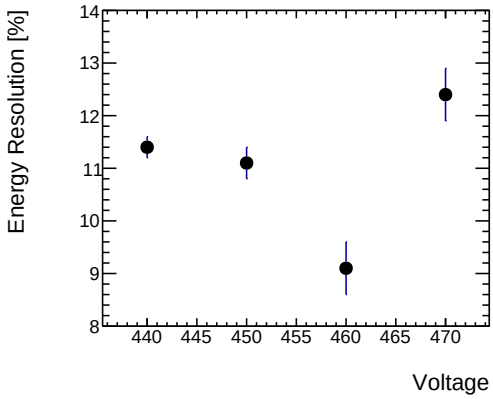

Figure 10.13: Equation 10.2 for the K_α peak can be used to determine the energy resolution res_E of the detector. The lowest point is at the working point of 460 V corresponding to a finer energy resolution. After this point, the saturation increases. Thus, the energy resolution decreases.

10.4 Hit Position and Pixel Multiplicity

In the following, the position reconstructed by the detector and the number of addressed pixels is studied.
The ^{55}Fe source is centered in the middle of the detector (see Figure 10.14). The reconstructed position for $U_{ampl} = 460$ V is concentrated around four pixels on both the x and y axis.

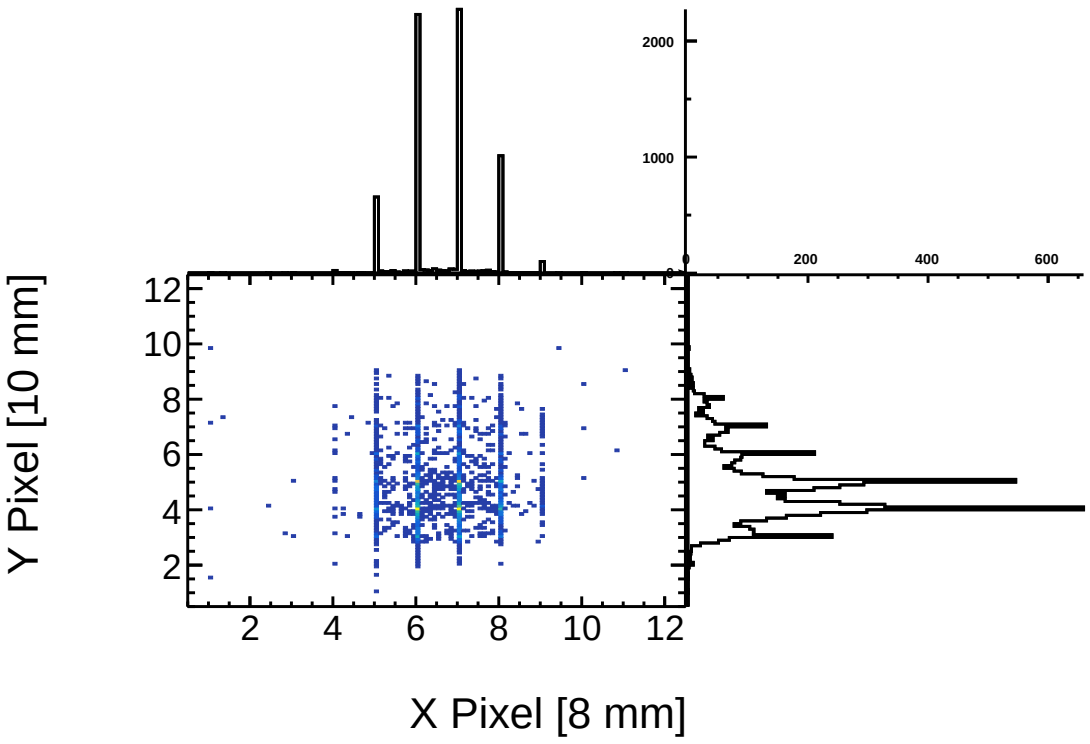

Figure 10.14: The reconstructed centroid position for a ^{55}Fe measurement at $U_{ampl} = 460$ is shown for 10000 events. The spot irradiated by the source is located around four pixels. On the y pixels, the v shape of the signal leads to a smearing effect for the centroid position, while this effect is not visible along the x axis.

Along the x axis of the detector, discrete peaks are visible along x and to a weaker extent on the y pixels. The discrete structure indicates that the signal of most photons addresses only one x pixel. Here only marginal charge sharing exists, likely due to the low voltage applied. This charge sharing effect is investigated in section 10.5.
In contrast, the y layer where the v shape of the signal exists shows a more continuous hit distribution.
The expansion of the beam spot $2 \cdot r_{src}$ can be determined by geometrical considerations of the maximum allowed emission angle by the source (see Figure 10.15). This angle α is defined by the radius of the source's pinhole 2.5 mm and its depth within the housing of the source 5 mm. The angle is then given as $\tan\alpha = \frac{2.5}{5} = 0.5$. The irradiated spot can then be determined as $2 \cdot r_{src} = 2 \cdot d_{src} \tan\alpha = 2 \cdot 25\,\text{mm} \cdot 0.5 = 25\,\text{mm}$. Along the x axis with a 8 mm pixel size this corresponds to 3 pixels and along y with a 10 mm pixel size, this corresponds to 3 responding pixels.
Figure 10.14 roughly agrees for the x pixels, while for the y pixels, a larger number of responding pixels is visible in the measurement. This deviation between measurement and calculation can be explained due to the signal's v shape.

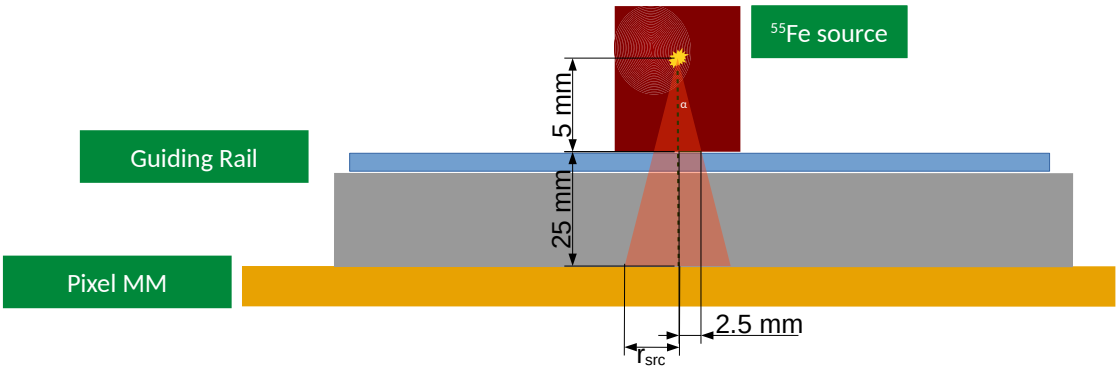

Figure 10.15: The irradiated position $2 \cdot r_{src}$ along an axis on the Pixel Micromegas' anode can be calculated by determining the maximum angle α of photons irradiated by the ^{55}Fe source. Using that, the pinhole of the source is 2.5 mm in radius and placed 5 mm deep in its housing $\tan\alpha = \frac{2.5}{5} = 0.5$ is calculated. As the source is distanced $d_{src} = 25\,\text{mm}$ from the readout plane, the irradiated spot is then $2 \cdot r_{src} = 2 \cdot d_{src} \tan\alpha = 2 \cdot 25\,\text{mm} \cdot 0.5 = 25\,\text{mm}$.

The number of pixels addressed per event is shown in Figure 10.16. Along the x and y axis the row or column with the maximum number of pixels per event was used. The number of addressed pixels stays constant up to the working point voltage of 460 V. Above this value, an increase is visible up to 7 pixels for all pixels at the highest amplification voltage. For the individual rows along x and y directions, a maximum of 3-4 addressed pixels is visible. These values agree with the theoretical calculation for the beam spot Figure 10.15.
Along the y axis, the number of addressed pixels is up to 500 V higher than for the x layer as expected due to the v shape. The induced v shape leads to a smeared-out effect also for the position reconstruction (see Figure 10.14) along this layer as exhibited already at $U_{ampl} = 460\,\text{V}$.
From 500 V onwards the amount of capacitive coupling along the x layer increases and can be seen by a larger number of addressed pixels. The crosstalk effects between neighboring pixels are studied in the following.

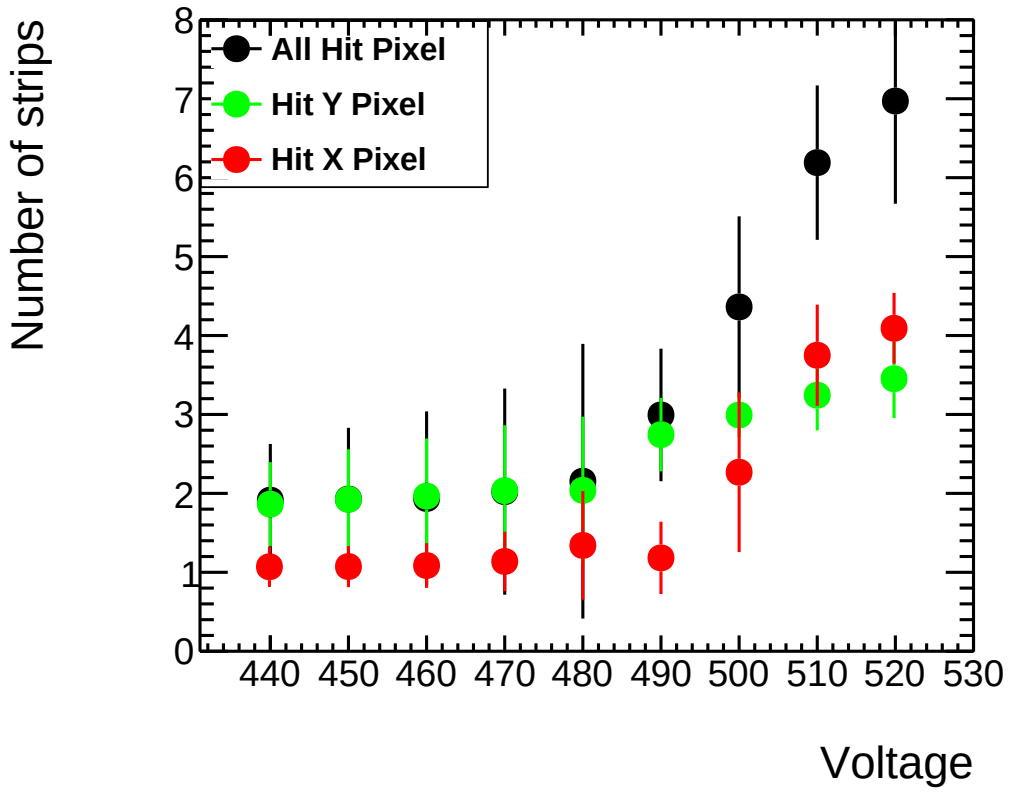

Figure 10.16: The responding number of pixels in the detector is shown for the number of all pixels (black) as well as a maximum of all rows on the x pixel (green) and columns on the y pixel (red) for 10000 events. As long as the detector is operated below 480 V the number of addressed pixels stays constant. In y direction, the signal drifts along the HV channels. At the same time, the crosstalk on the x pixels increases with increasing HV due to capacitive coupling between the connection lines from the pixels to the Panasonic connector.

10.5 Crosstalk between Neighboring Pixels

As demonstrated in the previous section, multiple effects lead to more responding readout pixels than expected for one reconstructed ^{55}Fe event. The charge sharing between neighboring pixels and the time difference of neighboring signals is investigated to quantify the underlying effect. Only non-saturated events below an ADC count of 1600 are used in the following.
The pixel with the highest amount of charge collected is used as reference q_{max} and compared to the charge between neighboring pixel q_i. The charge factor between two pixel is

$$C_q = \frac{q_i}{q_{max}} \tag{10.3}$$

For a voltage of 460 V the relative charge factor (see Equation 10.3) is shown in Figure 10.17 with the center chosen as the pixel with the highest charge $q_i = q_{max}$ at 100%. Along the resistive strips in the y direction, a significant contribution of around 14% in both directions of the y axis is visible. The effect is much weaker for neighboring pixels along the x-axis, and it becomes almost negligible for pixels further away, such as the secondary neighbors. On the diagonal, well below 1% of the charge q_{max} is shared. In the following, only the direct neighbors of the pixels with the highest charge are discussed. For 10000 events the diagonal and secondary neighbors are statistically insignificant e.g. "2*Left" responded seven times. Furthermore, along one axis mostly only two pixels are hit up to voltages of 480 V (see Figure 10.16).

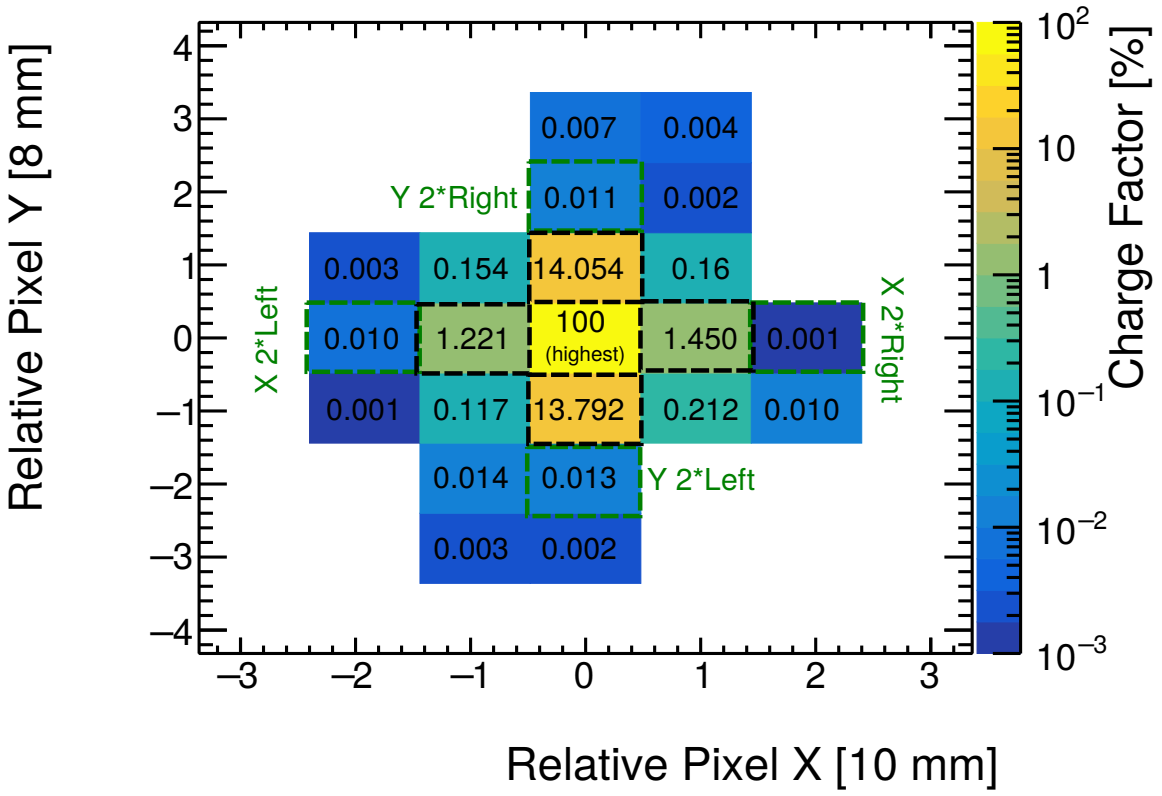

Figure 10.17: The pixel charge relative to q_{max} in percent is indicated for the relative position along x and y pixels for $U_{ampl} = 460\,\text{V}$ averaged for 10000 events. The center of this distribution at (0,0) is the highest pixel per event. Indicated are also the pixels (black dashed lines) that are investigated in the following.

In Figure 10.18 charge factor C_q (see Equation 10.3) increases for the direct right and left neighbor pixel on the x and y axis of the detector with a higher voltage. For the detector's y axis, the charge factor is 12% and grows to 24%. The x axis between 1% and up to 4% is reached at maximum. The effect along y is more prominent than along x due to the influence of the resistive strips.
In both cases, the left and right neighbors see a similar amount of charge sharing. The effect is almost symmetric. Above 480 V, the pixel becomes saturated. Thus, these voltages are not included in the measurement.

The time difference Δt between the pixels with the highest accumulated charge t_{qmax} and the investigated neighbor pixel t_i is defined as

$$\Delta t = t_i - t_{qmax} \tag{10.4}$$

Along the x axis all signals arrive simultaneously as the highest charge is independent of the voltage (see Figure 10.19). Along the y axis there is a clear tendency for a later signal timing of around 7 to 8 time bins relative to the pixel with the highest charge. The prolonged signal timing indicates a v shape of the signal along the y axis due to the resistive strip layer (see Section 2.3). At around U_{ampl} =480 V the value for the left and right neighbors along y is not equal anymore, which might be due to saturation.

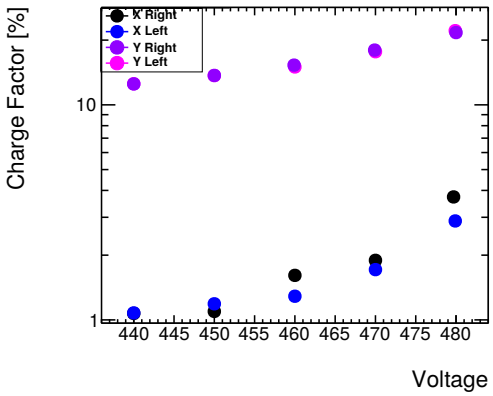

Figure 10.18: The directly neighboring x pixel (left and right) shows increased charge sharing when reaching higher voltages above the working point of 460 V. The same situation is visible for the y pixels. However, the factor is 10 times higher along the resistive strip layer.

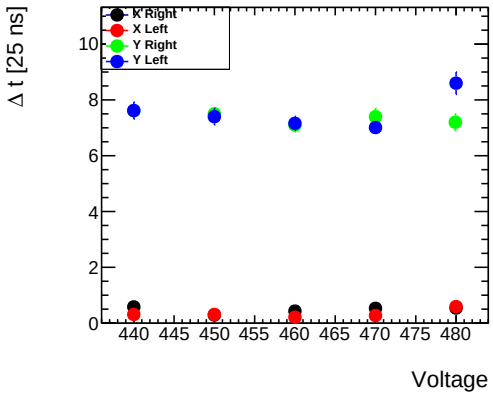

Figure 10.19: On the x pixel the timing arrives simultaneously at neighboring pixels due to crosstalk as visible by $\Delta t = 0$ for all neighboring pixels for all voltages. On the y pixel, due to the signal traveling the resistive strips towards the HV connection, the time difference Δt between the pixel with the highest charge and its neighbors differs.

The electron velocity spread along the resistive strips for two-dimensional strip detectors was investigated by Jagfeld [2023] and 0.4 $\frac{\text{mm}}{\text{ns}}$ for a resistive area instead of strips 0.05 $\frac{\text{mm}}{\text{ns}}$ were determined. Comparing the value for a spread along two readout pixels underneath resistive strips along y with 10 mm size would yield:

$$\Delta t_{theo,strips} = \frac{10\,\text{mm}}{0.4\frac{\text{mm}}{\text{ns}}} = 50\,\text{ns} = 2 \cdot 25\,\text{ns} \tag{10.5}$$

When applying the above Equation 10.5 to the resistive area velocity $\Delta t_{theo,area} = 16 \cdot 25\,\text{ns} = 400\,\text{ns}$ are expected for the spread tine. The measured value for resistive strips by Jagfeld [2023] strongly deviates from the measured $7 \cdot 25\,\text{ns}$ (Figure 10.19).
If the pitch size of the resistive strips is different than measured in Jagfeld [2023], the electron velocity is expected to be different. Further, as the readout pixels are coarse compared to readout strips with $p_s = 250\,\mu\text{m}$, it is challenging to reconstruct the electron velocity on the pixels accurately. These factors must be considered for better position reconstruction and can be used when analyzing the detector.

10.6 Summary

The pixel detector was demonstrated to be operational. The charge sharing effects along x and y were studied. While the y pixels experience the influence of the anode charges moving on the resistive strips, capacitive coupling influences the x axis. For this detector to be an alternative to a strip anode for the Cherenkov Micromegas, the position reconstruction must be verified, e.g., with a detector hodoscope. Due to its coarse pixel, this prototype is not ideal for determining the position distribution of a Cherenkov cone in two dimensions with low ambiguity. The resolution of these ambiguities has to be provided in another way, as discussed in Chapter 9.

Chapter 11

Conclusion

This thesis successfully studied and simulated the Inverted RICH Micromegas prototype and identified possible optimizations for later stages of development.
The detector consists of a 20 mm thick LiF Cherenkov radiator coated double-layer of 4 nm Cr and 15 nm CsI. A Micromegas detects the electrons produced by the Cherenkov photons inside the CsI. Simulations investigated the photocathode material, including the photon yield, and the whole detector system, including the signal response.
When aiming for a high photon yield, it is crucial to choose a solid radiator because of its high refractive index $n \approx 1.5$ and the high photon yield. As a tradeoff, the Cherenkov angle resolution degrades compared to gaseous or liquid radiators. The most suitable radiators are LiF and MgF_2. A theoretical quantum efficiency for the CsI of 9% was determined in the VUV 100 nm - 200 nm range. When a good momentum resolution is desired, gaseous radiators or aerogel should be used as the variation of their refractive index is small. Aerogel could be applied when produced without being filled with air.
Simulation studies predicted the detector's behavior. The signal timing distribution and their correlations to the residuals and strip multiplicity were close to data recorded with the detector hodoscope measuring cosmic muons. The agreement between simulation and measurement demonstrated that the Inverted RICH Micromegas had detected Cherenkov photons.
The detection efficiency of photoelectrons is considerably lower in measurements than theoretically determined. There could be multiple causes for the issue, including the aging of the photocathode and the presence of gas pollution. It is essential to eliminate these factors to avoid them in future iterations.
Finally, reconstruction methods showed promising results regarding the simulation and the measured data. These reconstruction methods can also be further adapted for new prototypes of this detector. The Cherenkov cone was fit analytically in 1D, and a successful approach was tested to discover the relationship between the Cherenkov angle and the muon incidence angle.
Also, the photon feedback created by recombination photons hitting the photocathode has to be improved in future iterations.
The before-mentioned simulations enabled a good distinguishment between photons and muon signals which could be reproduced in the experiment. Here it was proven that the photocathode works homogeneously and detects Cherenkov photons. Thus, the prototype works successfully.
A pixelated Micromegas prototype has been tested, showing very high pulse height and, thus, considerable crosstalk. The anticipated v shape on the resistive layer led to additional crosstalk. Unfortunately, the detector's spatial resolution is not fine enough to distinguish the Cherenkov cone.

Alternatively, if a detector is employed which allows for XYV readout using a Segmented GEM Readout (SGR), its potential application is the detection of Cherenkov cones.

Appendix A

Detector Alignment

To guarantee precise tracking and a clear separation between muon clusters and photoelectron clusters for the Cherenkov detector, it is important to account for shifts and rotations in the experimental setup. The hodoscope consists of two reference detectors. Thus, the alignment is relative to the track these two detectors define.

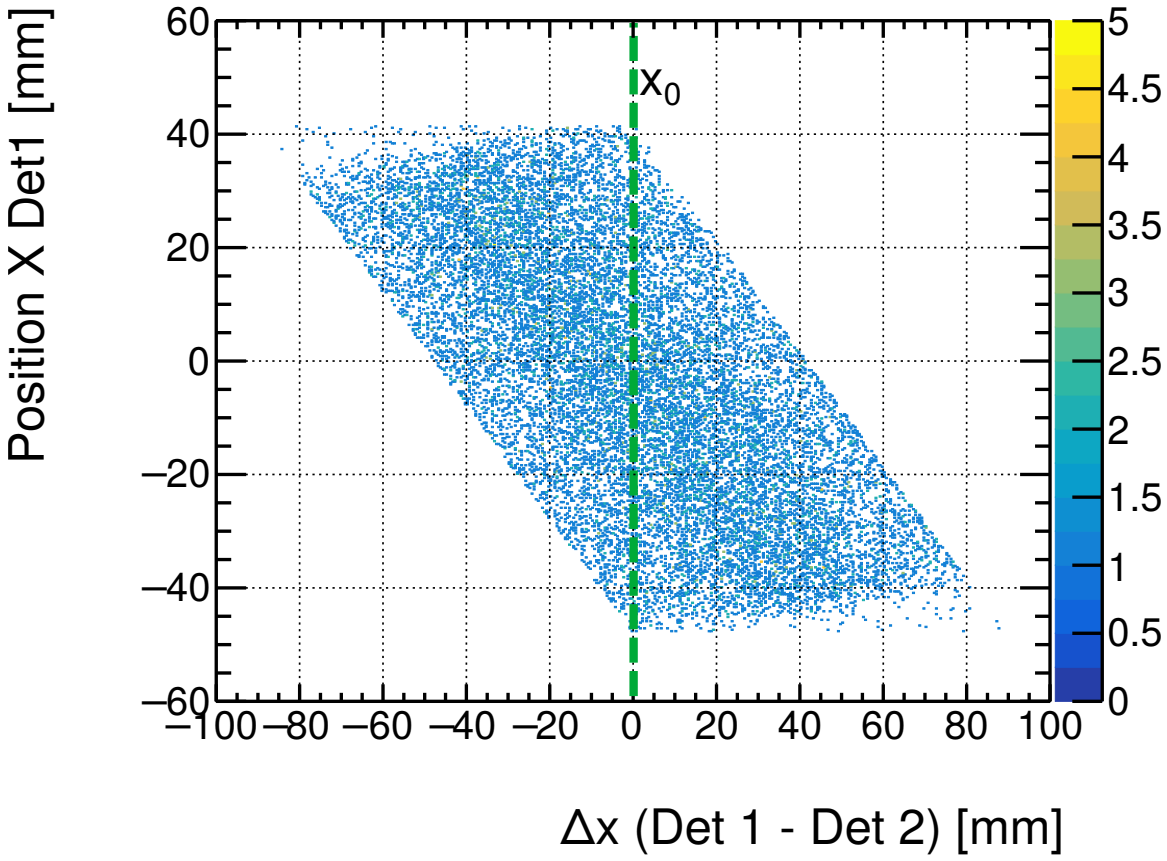

Figure A.1: A good alignment of the detectors leads to $\Delta x = x_{Det2} - x_{Det1} = 0$ having the largest variation along y (position X). Both corners of the distributions have the same values for Δx.

Aligning two detectors for cosmic muons is more challenging than perpendicular particle beams as the particles are not confined to a small beam spot. Δx is the position difference in detectors 1 and 2. The two detectors are aligned in Figure A.1.
$\Delta x = 0$ for perfect alignment is expected to be the distribution center. The dashed green

line is also parallel to the y axis of the plot going through the two corners of the distribution when no rotation exists.

Translation along ΔX and ΔY

A shift along the x or y axis can be compensated as the reference position in the test detector x_{ref} compared to the measured position x_{meas} e.g., along the x axis will yield a constant offset in the residual distribution $\Delta x = x_{meas} - x_{ref}$ (see Figure A.3). The detector shift can be corrected by applying the shift on Δx in Figure A.3.

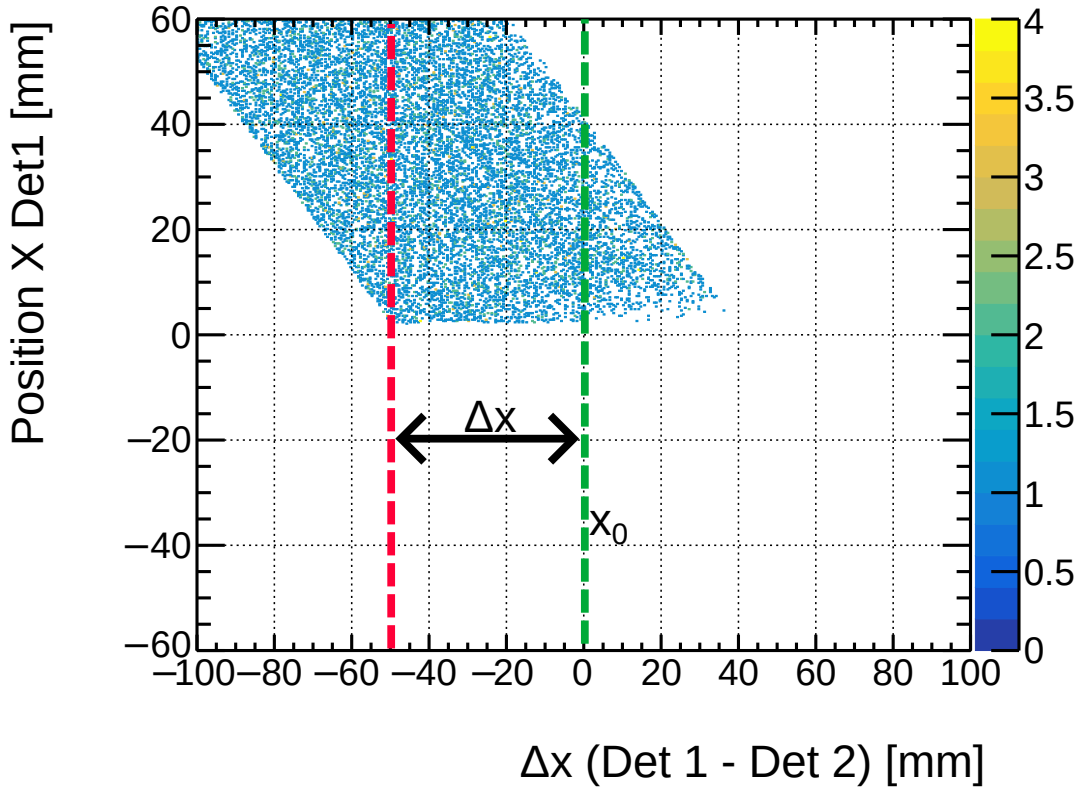

Figure A.2: A relative shift between the reference detectors of Δx is visible in the two-dimensional position difference of the detector.

Rotation around the X and Y axis

Rotations of angle α along the x and y axis can be handled by comparing Δx and the position x measured in the detector (see Figure A.3). The rotation is corrected when determining the angle δ between the correct alignment of the two edges (green dashed line) and the rotated edges (red dashed line) (see Figure A.3).

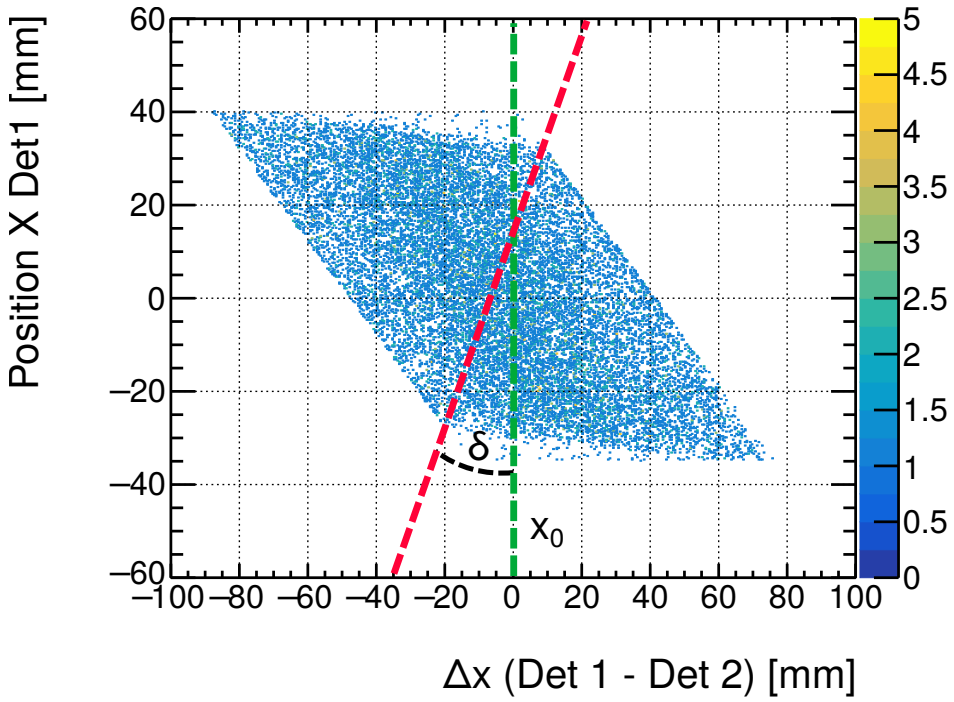

Figure A.3: A tilt of the detector along x or y lead to a rotation by δ of the 2D distribution. The distribution has to be rotated such that the red dashed line is identical to the green dashed line.

Translation along Z

A linear correlation exists between the x and y residual and the associated slope if a shift is along the x and y axis. The slope m corresponds to the displacement along the z axis (see Figure A.4). This correction is only possible for the test detector when the reference detectors are aligned.

$$m = \frac{\Delta y}{slope} = \Delta z \tag{A.1}$$

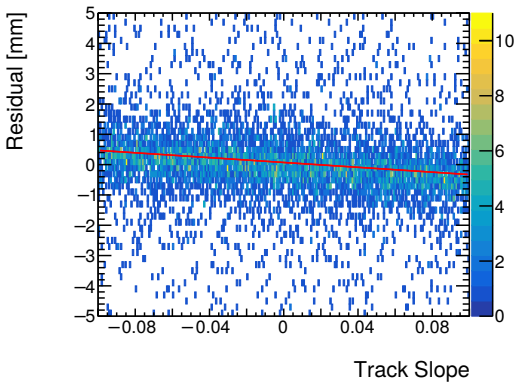

(a) Measured shift along the z axis compared to the residual

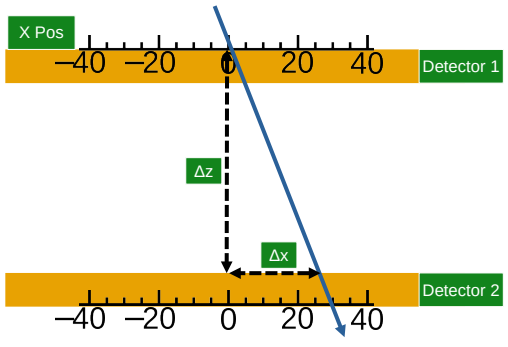

(b) Sketch of a dis-positioned detector along the z axis

Figure A.4: A shift across the z axis leads to a dependency for the residual $\sigma = x_{ref} - x_{meas}$ as the detector is displaced by the resulting slope. x_{ref} is the position inside the test detector determined by the line fit, and x_{meas} is the actual position reconstructed by the test detector.

Appendix B

Detector Resolution for Different Particle Energies

To determine which momenta can be differentiated in a LiF radiator with a certain detector spatial resolution for two muons with kinetic energy E_1 and E_2 the resulting difference in diameter $\Delta r = 2d(\tan(\theta_1) - \tan\theta_2)$ of the Cherenkov cone is shown on the z axis of fig. B.1. The white area for $E_1 \approx E_2$ is not resolvable. This is also applicable for Δr between intervals of $[E_1 = 1500\,\text{MeV}, E_2 = 2000\,\text{MeV}]$. For high energy differences $[E_1 = 100\,\text{MeV}, E_2 = 500\,\text{MeV}]$ even a coarse spatial resolution of a few mm would be enough to resolve the momentum.

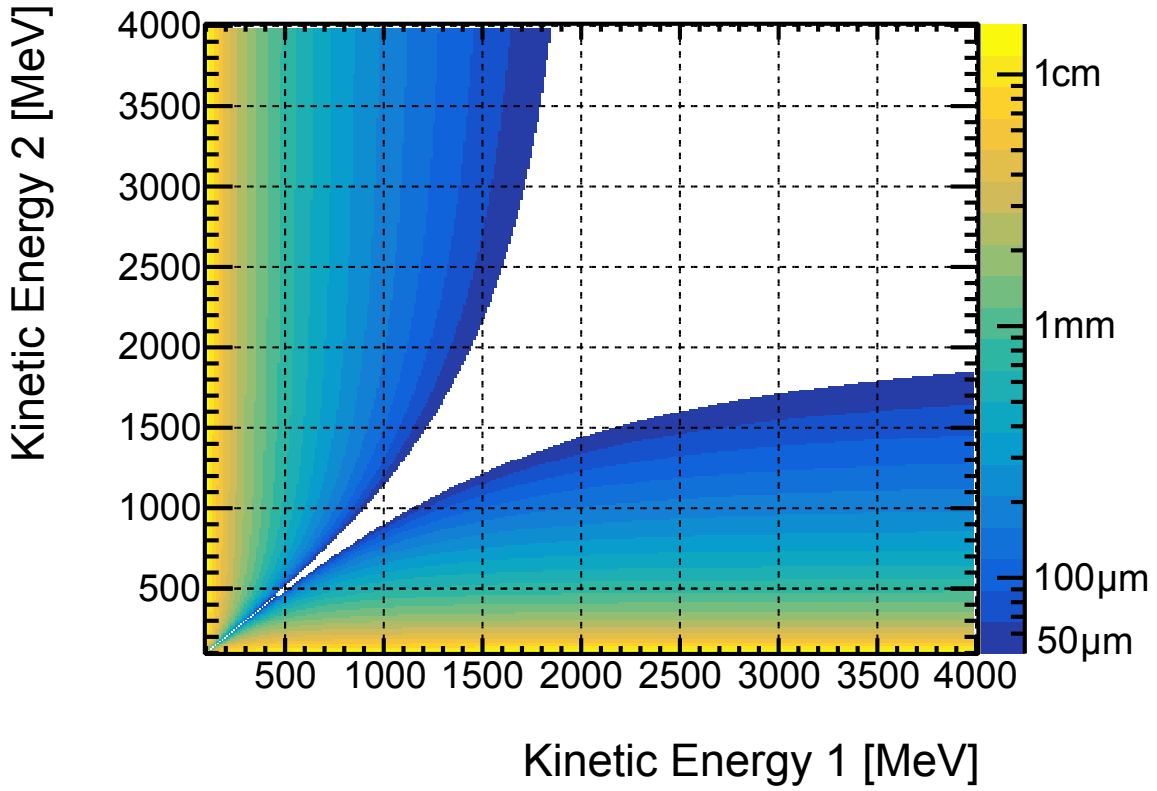

Figure B.1: For the mean refractive index of LiF ($n = 1.45$) for two different momenta the resulting radius difference was plotted logarithmically. The white area is not resolvable for Micromegas detectors with assumed spatial resolution of 50 µm. Beginning at 1500 MeV it becomes impossible to resolve the different momenta up to 4000 MeV with this medium and this detector setup.

Appendix C

Outlook: Neural Networks for Momentum Reconstruction

One reconstruction method uses the help of neural networks to determine the particle energy and the incident angle of the traversing particle. Neural networks are modeled after biological neurons and have also been applied in RICH imaging techniques [Muresan, 2007].
In this thesis, the sci-kit framework using a neural network built with the PyTorch library was used and written in Python [Pedregosa et al., 2011] [Ketkar, 2017]. These so-called neurons are interconnected using an input, hidden, and output layer (see Figure C.1).
The input layer receives the data with weights added in the process. Each line represents a free parameter (weight w) to be optimized during the training
The hidden layer processes the information from the input layer and makes decisions based on which information. Moreover, the output layer provides the final result of the Cherenkov detector, the energy of a charged particle.

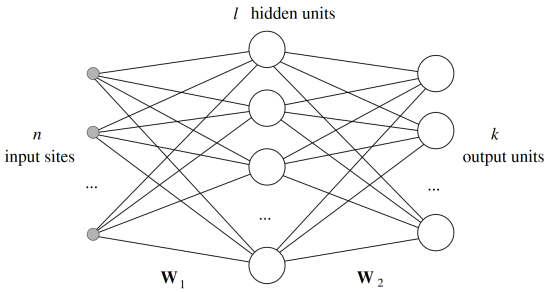

Figure C.1: Sketch of a generic neural network with input sites n and hidden layers in the middle l. Multiple hidden layers can be connected to the output layers. Taken from Rojas [1996].

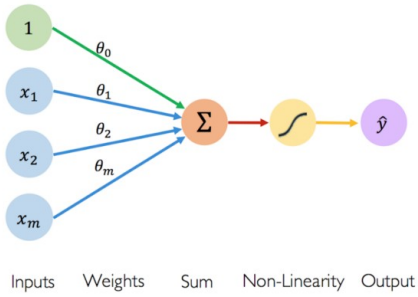

Figure C.2: Sketch of a singular neuron. It accepts an input which is then weighted. The sum of the weighted inputs is then applied to a non-linear activation function. Its result is then the output of the neuron. Taken from Benoit Liquet [2022]

A sketch of a single neuron is shown in Figure C.2. It takes the input values x as a m-sized vector or an mxn-sized matrix. With weights w_i applied, the sum of the input values is applied to an activation function ϕ with an added threshold θ. After this step, the output value $\hat{y}$ can be retrieved as

$$y = \phi(\theta + \sum_i x_i \cdot w_i) \tag{C.1}$$

The activation function is chosen non-linear. Otherwise, the neural network can always be reduced to a linear combination, thus requiring only one layer (see Equation C.1). Here the Rectified Linear Unit (ReLU) is used

$$f(x) = max(0, x) = \begin{cases} x \text{ if } x > 0 \\ 0 \text{ else} \end{cases} \tag{C.2}$$

Before the performance of neural networks, it has to be trained with the training data. In the scope of this thesis, a vector with the size of the number of detector strips is filled with the number of photons detected on the strips and receives the kinetic energy of the muon as a label.
This aims to optimize the weight for the given problem. Afterward, a different set than the training data is used to validate the neural network. The loss defines the difference between the predicted output of the neural network and the labeled output values. The goal of the network is to minimize the loss by varying its weights during the training. In linear regression, this is often defined by mean root square:

$$RMS = \sqrt{\frac{\sum_i (x_{1,i} - x_{2,i})^2}{N}} \tag{C.3}$$

The goal for the validation data set is to minimize the loss but keep the neural network's weights static.
Two machine learning algorithms were implemented for the reconstruction. One was tested for different muon incidence only with a pixel anode and one for energy variation only with a strip anode, both using simulations by Geant4.
The studies with the neural network for angles were performed to identify the inclination angle with $\alpha = \{0, 3, 4, 8, 12, 16, 20\}$ [°]. For this reason, the two-dimensional photon distribution shown in Figure 8.6 was packed into a 256x256 sized matrix. The bin size or pixel size was then chosen as 3 mm, with the entries being the collected photons on the pixel.
The forward sequential neural network uses four layers. For the sequential forward network, a training loss of 0.0364 is reached, whereas the test loss goes to a similar value of 0.0354 (see Figure C.3). This convergence implies good training without over or under-training of the model, as visible by the similar conversion of training and test loss.
The confusion matrix on the right shows the predicted angle by the model compared to the actual label given in advance. The algorithm correctly labeled the validation data except for incidence angle of 3° and 4° (visible in the confusion matrix), likely because they are nearly indistinguishable. However, this model is a good base for a more refined model [Strasser, 2021].

Also tested was a variation of only the energy of the incoming particle with a strip anode. Here the one-dimensional hit distribution on a strip-based Micromegas was used to test the machine learning algorithm.
For the binning, the pitch of the Micromegas was used $p = 0.25$ mm. Here the training converges close to zero, but the losses increase instead of decreasing. This overtraining effect can be overcome with a statistic size and by optimizing the neural network. As a next step, combining the neural networks to retrieve the angle and energy of a traversing muon is possible.

A significant disadvantage is, however, the high number of training data required to test it to actual data for good weight estimation of the neural network. In the training procedure, the number of events for a stable convergence was larger than 500000 for the algorithm applied to the energy variation. Furthermore, the data test was only simulated.
For real data, the electronic noise must be thoroughly cleaned from data. Also, labeling would require measurements with reference detectors (e.g., chapter 7) for the training data.

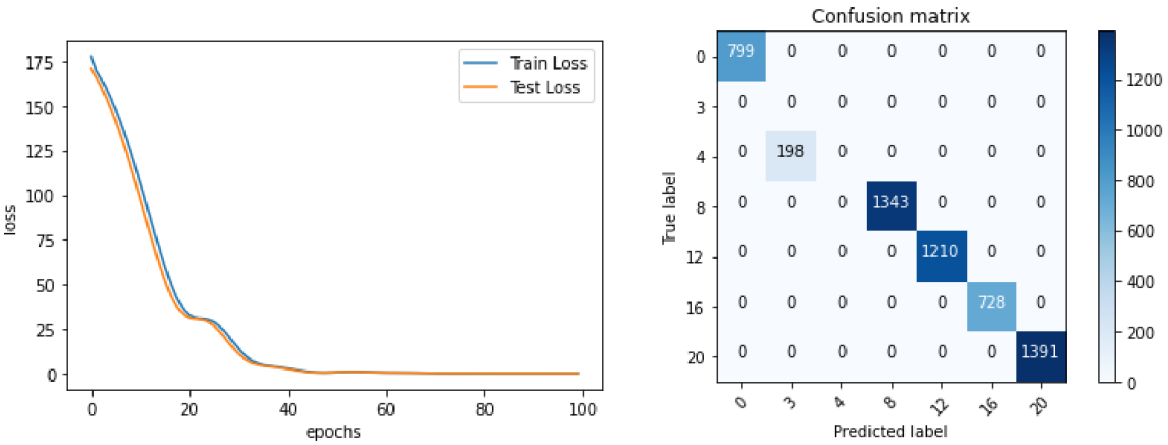

Figure C.3: The achieved confusion matrix and loss by Strasser [2021] for a neural network trained on differentiating between the muon incidence angle. Here the loss converges and has a good prediction, as visible in the confusion matrix.

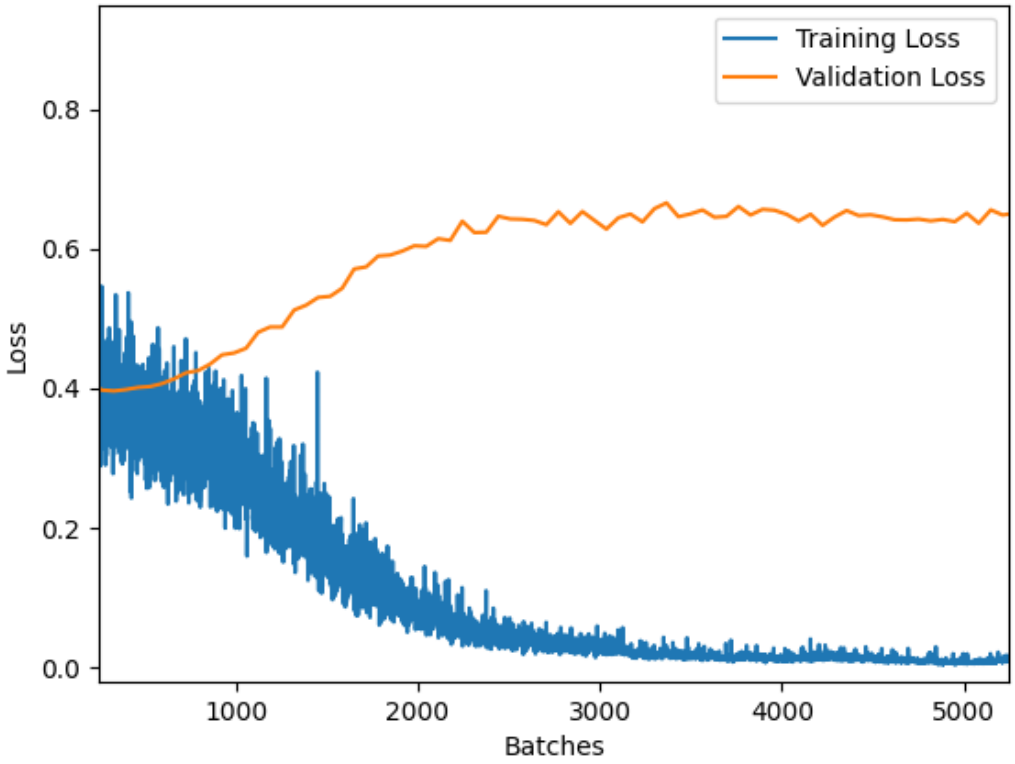

Figure C.4: Training loss and validation loss are shown for the machine learning algorithm training on six energies. It is visible that over-training occurs.

Appendix D

Momentum Reconstruction with a Bigaussian Fit

As a simple first approach, a two-dimensional Gaussian was used as a fit function to Geant4 simulations. The two dimensional Gaussian $f(x, y)$ is described by five parameters an amplitude C, the center x_0, y_0 and the standard deviation σ_x, σ_y:

$$f(x,y) = C \cdot \exp\left(-0.5 \cdot \left(\frac{x - x_0}{\sigma_x}\right)^2\right) \cdot \exp\left(-0.5 \cdot \left(\frac{y - y_0}{\sigma_y}\right)^2\right) \tag{D.1}$$

The radius of the Gaussian along one axis was defined at the intersection of a parabolic approximation of the Gaussian distribution via Taylor expansion with the x axis (see Figure D.1)

$$f(x) \approx f(x_0) + f'(x_0) \cdot (x - x_0) + \frac{f''(x_0)}{2} \cdot (x - x_0)^2 = C + \frac{C}{4\sigma_x^2} \cdot (x)^2 \stackrel{!}{=} 0 \tag{D.2}$$

The intersection on the x (or y axis) Figure D.1 yields a radius $r = 2\sigma_x$. The results of this fit are shown in Figure D.2 (a) for photoelectrons created by an $E_{kin} = 100\,\text{MeV}$ muon and in Figure D.2 (b) for photoelectrons of an $E_{kin} = 4\,\text{GeV}$ muon and they are listed in Table D.1.

Energy [GeV]	σ_x [mm]	σ_y [mm]	Radius y [mm]	Radius x [mm]	Theoretical radius [mm]
0.1	1.86±4.7	1.70±4.3	3.72±9.4	3.4±8.6	9.30
4	3.52±8.89	3.04±7.667	7.04±17.79	6.08±35.58	11

Table D.1: The radii are determined via a 2D Gaussian fit shown in Figure 8.2 for a 10 mm thick LiF radiator crystal. The radii are calculated as $r = 2\sigma_x$. The theoretical radii were calculated from Figure 5.22 for a 10 mm crystal.

Regrettably, the fit's performance is highly unreliable, exhibiting significant uncertainty for energy values ranging from 100 MeV to 4 GeV. Furthermore, the calculated radius does not correspond with the theoretically predicted radius. Therefore, an alternative analytical fit was attempted.

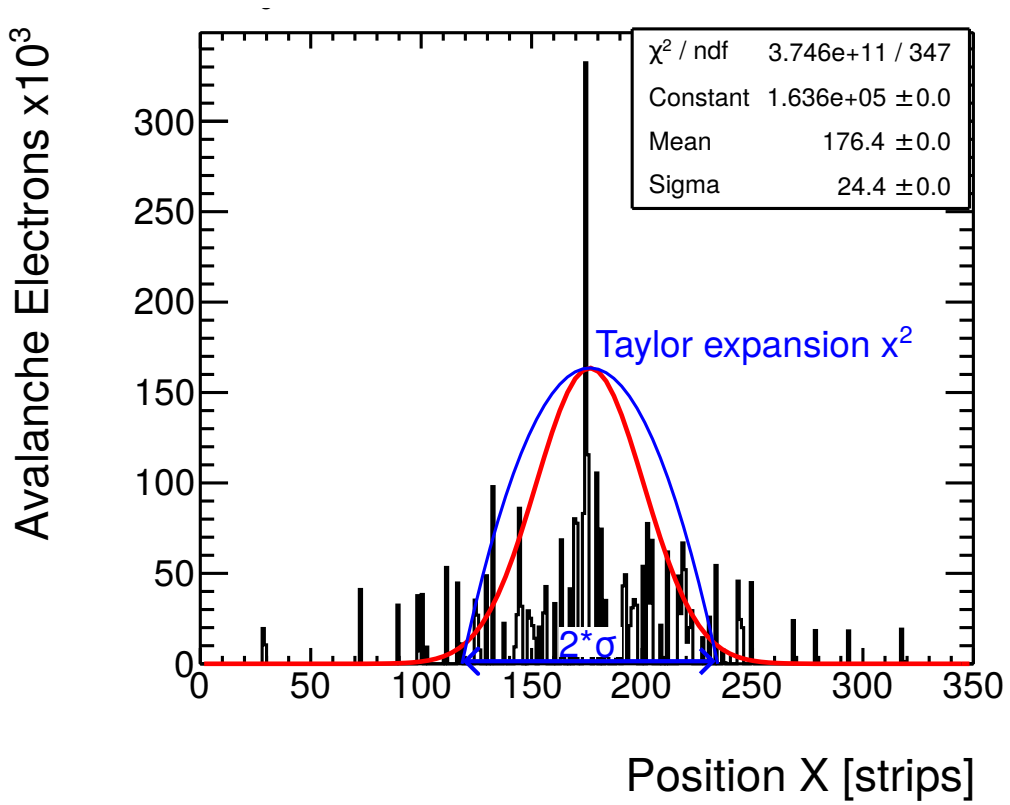

Figure D.1: 1D Projection along the x axis of a 4 GeV muon event from Garfield++. In red, the projection of the 2D Gaussian fit is shown. The black curve represents the avalanche hits. The blue line represents the parabolic approximation via Taylor expansion to determine the radius $r = 2\sigma_x$.

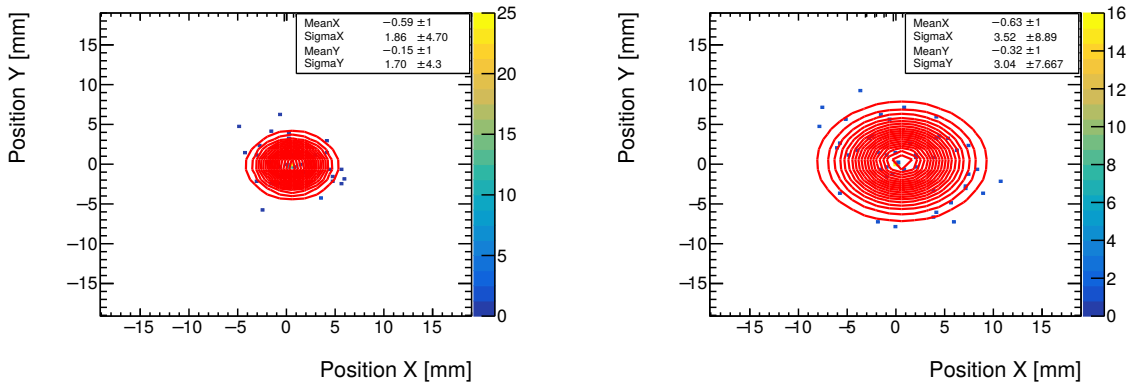

(a) 100 MeV Geant4 **(b)** 4 GeV Geant4

Figure D.2: A two-dimensional Gaussian (contour lines) was fit to single Cherenkov events in a 10 mm thick LiF crystal simulated by Geant4. The resulting error for the individual fit of the muon events is large. The taylor expansion was used to extract a radius.

Appendix E

List of Abbreviations

ADC	Analog-to-Digital Converter
APV25	Analog Pipeline Voltage readout chip
BaF_2	Barium Fluoride
CaF_2	Calcium Fluoride
CHMM	Prototype Cherenkov Micromegas
CsI	Cesium Iodide
FEC	Front End Concentrator cards
FWHM	Full Width Half Maximum
LHC	Large Hadron Collider
LiF	Lithium Fluoride
MgF_2	Magnesium Fluoride
NaF_2	Natrium Fluoride
Micromegas	Micro Mesh Gaseous Structure Detectors
MPGD	Micro Pattern Gaseous Detector
SRS	Scalable Readout System
SiO_2	Silicon Dioxide
RICH	Ring Imaging Cherenkov Detector

Bibliography

[Abbon et al.(2007)] Abbon, P., Albrecht, E., Alexakhin, V.Yu., et al. The COMPASS experiment at CERN. *Nuclear Instruments and Methods in Physics Research Section A: Accelerators, Spectrometers, Detectors and Associated Equipment*, 577(3):455–518, 2007. doi:10.1016/j.nima.2007.03.026. URL https://doi.org/10.1016%2Fj.nima.2007.03.026.

[Adinolfi et al.(2013)] Adinolfi, M., Aglieri Rinella, G., Albrecht, E., et al. Performance of the LHCb RICH detector at the LHC. *European Physical Journal C*, 73:2431, 2013. doi:10.1140/epjc/s10052-013-2431-9.

[Agostinelli et al.(2003)] Agostinelli, S., Allison, J., Amako, K., et al. Geant4—a simulation toolkit. *Nuclear Instruments and Methods in Physics Research Section A: Accelerators, Spectrometers, Detectors and Associated Equipment*, 506(3):250–303, 2003. ISSN 0168-9002. doi:https://doi.org/10.1016/S0168-9002(03)01368-8. URL https://www.sciencedirect.com/science/article/pii/S0168900203013688.

[Alexopoulos et al.(2014)] Alexopoulos, T., Iakovidis, G., Leontsinis, S., et al. Examining the geometric mean method for the extraction of spatial resolution. *Journal of Instrumentation*, 2014.

[Allison et al.(2006)] Allison, J., Amako, K., Apostolakis, J., et al. Geant4 developments and applications. *IEEE Transactions on Nuclear Science*, 53(1):270–278, 2006. doi:10.1109/TNS.2006.869826.

[Allison et al.(2016)] Allison, J., Amako, K., Apostolakis, J., et al. Recent developments in geant4. *Nuclear Instruments and Methods in Physics Research Section A: Accelerators, Spectrometers, Detectors and Associated Equipment*, 835:186–225, 2016. ISSN 0168-9002. doi:https://doi.org/10.1016/j.nima.2016.06.125. URL https://www.sciencedirect.com/science/article/pii/S0168900216306957.

[Bauer(1995)] Bauer, Burkhard B. *Eigenschaften reflektiver und transmittiver CsI-Photokathoden*. Master's thesis, Physik-Department der Technischen Universität Munchen Institut E12, 1995.

[Bellunato et al.(2008)] Bellunato, T., Calvi, M., Matteuzzi, C., et al. Refractive index of silica aerogel: Uniformity and dispersion law. *Nuclear Instruments and Methods in Physics Research Section A: Accelerators, Spectrometers, Detectors and Associated Equipment*, 595(1):183–186, 2008. ISSN 0168-9002. doi:https://doi.org/10.1016/j.nima.2008.07.072. URL https://www.sciencedirect.com/science/article/pii/S0168900208009716. RICH 2007.

[Benoit Liquet(2022)] Benoit Liquet, Sarat Moka Yoni Nazarathy. The mathematical engineering of deep learning. 2022. URL https://deeplearningmath.org/.

[Berglund and Spicer(1964)] Berglund, C. N. and Spicer, W. E. Photoemission studies of copper and silver: Theory. *Phys. Rev.*, 136:A1030–A1044, 1964. doi:10.1103/PhysRev.136.A1030. URL https://link.aps.org/doi/10.1103/PhysRev.136.A1030.

[Biagi(2023)] Biagi, S. Magboltz - transport of electrons in gas mixtures. 2023. URL https://magboltz.web.cern.ch/magboltz/.

[Bideau-Mehu et al.(1981)] Bideau-Mehu, A., Guern, Y., Abjean, R., et al. Measurement of refractive indices of neon, argon, krypton and xenon in the 253.7–140.4 nm wavelength range. dispersion relations and estimated oscillator strengths of the resonance lines. *Journal of Quantitative Spectroscopy and Radiative Transfer*, 25(5):395–402, 1981. ISSN 0022-4073. doi:https://doi.org/10.1016/0022-4073(81)90057-1. URL https://www.sciencedirect.com/science/article/pii/0022407381900571.

[Bortfeldt(2014)] Bortfeldt, J. *Development of Micro-Pattern Gaseous Detectors - Micromegas*. Ph.D. thesis, Ludwig-Maximilians-Universität München, 2014.

[Bortfeldt et al.(2017)] Bortfeldt, J., Biebel, O., Flierl, B., et al. Low material budget floating strip micromegas for ion transmission radiography. *Nuclear Instruments and Methods in Physics Research Section A: Accelerators, Spectrometers, Detectors and Associated Equipment*, 845:210–214, 2017. ISSN 0168-9002. doi:https://doi.org/10.1016/j.nima.2016.05.003. URL https://www.sciencedirect.com/science/article/pii/S0168900216303606. Proceedings of the Vienna Conference on Instrumentation 2016.

[Bortfeldt et al.(2018)] Bortfeldt, J., Brunbauer, F., David, C., et al. Picosec: Charged particle timing at sub-25 picosecond precision with a micromegas based detector. *Nuclear Instruments and Methods in Physics Research Section A: Accelerators, Spectrometers, Detectors and Associated Equipment*, 903:317–325, 2018. ISSN 0168-9002. doi:https://doi.org/10.1016/j.nima.2018.04.033. URL https://www.sciencedirect.com/science/article/pii/S0168900218305369.

[Braem et al.(2005)] Braem, A., De Cataldo, G., Davenport, M., et al. Results from the ageing studies of large csi photocathodes exposed to ionizing radiation in a gaseous rich detector. *Nuclear Instruments and Methods in Physics Research Section A: Accelerators, Spectrometers, Detectors and Associated Equipment*, 553(1):187–195, 2005. ISSN 0168-9002. doi:https://doi.org/10.1016/j.nima.2005.08.059. URL https://www.sciencedirect.com/science/article/pii/S0168900205015962. Proceedings of the fifth International Workshop on Ring Imaging Detectors.

[Byszewski(2012)] Byszewski, M. Mmdaq q and a-atlas micromegas daq. 2012. URL https://indico.cern.ch/event/218341/contributions/1519619/attachments/352429/491014/mmdaq_QA.pdf.

[CAEN(1991)] CAEN. Technical Information Manual, Mod. N93B, Dual Timer. 1991. URL https://www.caen.it/?downloadfile=3941.

[CAEN(2011)] CAEN. Technical Information Manual, Revision n.7, Mod. N845. 2011. URL https://www.caen.it/?downloadfile=3947.

[CAEN(2021)] CAEN. Technical Information Manual, Revision n. 7, Mod. N405. 2021. URL https://www.caen.it/?downloadfile=6340.

[Covita et al.(2011)] Covita, D.S., Azevedo, C.D.R., Caldas, C.C., et al. Photoelectron extraction efficiency from cesium iodide photocathodes in a pressurized atmosphere of argon and xenon up to 10 bar. *Physics Letters B*, 701(2):151–154, 2011. ISSN 0370-2693.

doi:https://doi.org/10.1016/j.physletb.2011.05.056. URL https://www.sciencedirect.com/science/article/pii/S0370269311005879.

[Danger(2014)] Danger, Helge. *Untersuchung von Aufladeeffekten und Alterungsstudie an einem Micromegas Detektor mit resistiver Streifenanode*. Ph.D. thesis, Ludwig-Maximilians Universität München, München, 2014. URL https://www.etp.physik.uni-muenchen.de/publications/theses/download/dipl{_}hdanger.pdf.

[Derré et al.(2000)] Derré, J, Giomataris, Y, Rebourgeard, Ph, et al. Fast signals and single electron detection with a micromegas photodetector. *Nuclear Instruments and Methods in Physics Research Section A: Accelerators, Spectrometers, Detectors and Associated Equipment*, 449(1):314–321, 2000. ISSN 0168-9002. doi:https://doi.org/10.1016/S0168-9002(99)01452-7. URL https://www.sciencedirect.com/science/article/pii/S0168900299014527.

[Di Mauro et al.(2005)] Di Mauro, A., Andres, Y., Belin, B., et al. Status of the hmpid csi-rich project for alice at the cern/lhc. *IEEE Transactions on Nuclear Science*, 52(4):972–979, 2005. doi:10.1109/TNS.2005.852743.

[Di Mauro et al.(1995)] Di Mauro, A, Nappi, E, Posa, F, et al. Photoelectron backscattering effects in photoemission from CsI into gas media. 1995. doi:10.1016/0168-9002(95)01146-3. URL https://cds.cern.ch/record/291107.

[Dietz-Laursonn(2016)] Dietz-Laursonn, Erik. Peculiarities in the simulation of optical physics with geant4. *arXiv*, 2016.

[Einstein(1905)] Einstein, Albert. Über einen die Erzeugung und Verwandlung des Lichtes betreffenden heuristischen Gesichtspunkt. *Annalen der Physik*, 322(6):132–148, 1905. ISSN 15213889. doi:10.1002/ANDP.19053220607.

[Escada et al.(2009)] Escada, J, Coelho, L C C, Dias, T H V T, et al. Measurements of photoelectron extraction efficiency from csi into mixtures of ne with ch4, cf4, co2 and n2. *Journal of Instrumentation*, 4(11):P11025, 2009. doi:10.1088/1748-0221/4/11/P11025. URL https://dx.doi.org/10.1088/1748-0221/4/11/P11025.

[Flierl(2018)] Flierl, B.F. *Particle Tracking with Micro-Pattern Gaseous Detectors*. Ph.D. thesis, Ludwig-Maximilians-Universität München, 2018.

[FLUKE(1993)] FLUKE. Fluke 289 True-rms Industrial Logging Multimeter with TrendCapture. 1993. URL https://www.fluke-direct.com/pdfs/cache/www.fluke-direct.com/289/datasheet/289-datasheet.pdf.

[Francke and Peskov(2016)] Francke, Tom and Peskov, Vladimir. *Position-Sensitive Gaseous Photomultipliers*. IGI Global, 2016. doi:10.4018/978-1-5225-0242-5.

[Frank and Tamm(1937)] Frank, I. M. and Tamm, I. E. Coherent visible radiation of fast electrons passing through matter. *Compt. Rend. Acad. Sci. URSS*, 14(3):109–114, 1937. doi:10.3367/UFNr.0093.196710o.0388.

[Ghosh et al.(2009)] Ghosh, D. S., Martinez, L., Giurgola, S., et al. Widely transparent electrodes based on ultrathin metals. *Opt. Lett.*, 34(3):325–327, 2009. doi:10.1364/OL.34.000325. URL https://opg.optica.org/ol/abstract.cfm?URI=ol-34-3-325.

[Giomataris et al.(1996)] Giomataris, Y., Rebourgeard, P., Robert, J., et al. Micromegas: a high-granularity position-sensitive gaseous detector for high particle-flux environments. *Nuclear Instruments and Methods in Physics Research, Section A , 376:29–35*, 1996.

[Grupen and Shwartz(2008)] Grupen, Claus and Shwartz, Boris. *Particle Detectors*. Cambridge Monographs on Particle Physics, Nuclear Physics and Cosmology. Cambridge University Press, 2 edition, 2008. doi:10.1017/CBO9780511534966.

[Hamamatsu(2007)] Hamamatsu. Photomultiplier tubes basics and ampplications third edition (edition 3a). Technical report, Hamamatsu Photonics K.K., 2007.

[Hartbrich(2019)] Hartbrich, Oskar. Particle id in belle ii arich and top. In *Spring B2SKW, KEK*. 2019.

[Henneken et al.(2000)] Henneken, H, Scholze, F, Krumrey, M, et al. Quantum efficiencies of gold and copper photocathodes in the vuv and x-ray range. *Metrologia*, 37(5):485, 2000. doi:10.1088/0026-1394/37/5/31. URL https://dx.doi.org/10.1088/0026-1394/37/5/31.

[H.H.Li(1976)] H.H.Li. Refractive index of alkali halides and its wavelength and temperature derivatives. *Journal of Physical and Chemical Reference Data 5, 329*, 1976.

[Horvat(2005)] Horvat, S. *Study of the Higgs Discovery Potential in the Process $pp \to H \to 4\mu$*. Ph.D. thesis, University of Zagreb, 2005.

[Čerenkov(1937)] Čerenkov, P. A. Visible radiation produced by electrons moving in a medium with velocities exceeding that of light. *Phys. Rev.*, 52:378–379, 1937. doi:10.1103/PhysRev.52.378. URL https://link.aps.org/doi/10.1103/PhysRev.52.378.

[Jagfeld(2023)] Jagfeld, Christoph Simon Maximilian. *Research and Development of a Segmented GEM Readout Detector*. Ph.D. thesis, Ludwig-Maximilians-Universität München, 2023.

[Jones et al.(1999)] Jones, L.L., French, M.J., Morrissey, Q., et al. The APV25 Deep Submicron Readout Chip for CMS Detectors. 1999. doi:10.5170/CERN-1999-009.162.

[Kawamoto et al.(2013)] Kawamoto, T. et al. New Small Wheel Technical Design Report. 2013.

[Ketkar(2017)] Ketkar, Nikhil. *Introduction to PyTorch*, pages 195–208. Apress, Berkeley, CA, 2017. ISBN 978-1-4842-2766-4. doi:10.1007/978-1-4842-2766-4_12. URL https://doi.org/10.1007/978-1-4842-2766-4_12.

[Kleinknecht(1992a)] Kleinknecht, K. *Detektoren fuer Teilchenstrahlung: mit 20 Tabellen*. Teubner-Studienbücher : Physik, 1992a.

[Kleinknecht(1992b)] Kleinknecht, K. *Detektoren fuer Teilchenstrahlung: mit 20 Tabellen*. Teubner-Studienbücher : Physik, 1992b.

[Klitzner(2019)] Klitzner, Felix Fidelio. *Development of Novel Two-Dimensional Floating Strip Micromegas Detectors with an In-depth Insight into the Strip Signal Formation*. Ph.D. thesis, Ludwig-Maximilians-Universität München, 2019.

[Kolanoski and Wermes(2016)] Kolanoski, Hermann and Wermes, Norbert. *Teilchendetektoren: Grundlagen und Anwendungen*. Springer, 2016. ISBN 978-3-662-45349-0, 978-3-662-45350-6. doi:10.1007/978-3-662-45350-6.

[Korff(1946)] Korff, Serge Alexander. *Electron and nuclear counters*. Van Nostrand, Toronto, 1946.

[Korth(a)] Korth. Datasheet, Lithiumfluorid. a. URL https://www.korth.de/material/detail/Lithiumfluorid.

[Korth(b)] Korth. Datasheet, Magnesiumfluorid. b. URL https://www.korth.de/material/detail/Magnesiumfluorid.

[Korth(c)] Korth. Datasheet, Natriumfluorid. c. URL https://www.korth.de/material/detail/Natriumfluorid.

[Leo(1987)] Leo, W. R. *Techniques for Nuclear and Particle Physics Experiments: A How to Approach*. 1987. ISBN 978-3-540-57280-0.

[Li(1980)] Li, H. H. Refractive index of alkaline earth halides and its wavelength and temperature derivatives. *Journal of Physical and Chemical Reference Data 9, 161*, 1980.

[Lippert(2012)] Lippert, Benedikt. Studien zur Signalentstehung und Parametrisierung der Gasverstärkung in einem Micromegas-Detektor. 2012. URL https://www.etp.physik.uni-muenchen.de/publications/bachelor/download{_}auth{_}etp/bac12{_}blippert.pdf.

[Loesel(2017)] Loesel, Phillip. *Precision Calibration of Large Area Micro Pattern Gaseous Detectors*. Ph.D. thesis, LMU Muenchen, 2017.

[M. Tanabashi et al. (Particle Data Group)(2018)] M. Tanabashi et al. (Particle Data Group). Review of particle physics. *Phys. Rev. D 98, 010001*, 2018.

[Maier-Komor et al.(1995)] Maier-Komor, P, Bauer, B.B, Friese, J, et al. Preparation of reflective csi photocathodes with reproducible high quantum efficiency. *Nuclear Instruments and Methods in Physics Research Section A: Accelerators, Spectrometers, Detectors and Associated Equipment*, 362(1):183–188, 1995. ISSN 0168-9002. doi:https://doi.org/10.1016/0168-9002(95)00314-2. URL https://www.sciencedirect.com/science/article/pii/0168900295003142. Proceedings of the 17th World Conference of the International Nuclear Target Development Society.

[Malitson(1963)] Malitson, Irving H. A redetermination of some optical properties of calcium fluoride. *Appl. Opt.*, 2(11):1103–1107, 1963. doi:10.1364/AO.2.001103. URL https://opg.optica.org/ao/abstract.cfm?URI=ao-2-11-1103.

[Manthos et al.(2020)] Manthos, I, Bortfeldt, J, Brunbauer, F, et al. Recent developments on precise timing with the picosec micromegas detector. *Journal of Physics: Conference Series*, 1498(1):012014, 2020. doi:10.1088/1742-6596/1498/1/012014. URL https://dx.doi.org/10.1088/1742-6596/1498/1/012014.

[Martinengo et al.(2011)] Martinengo, P., Peskov, V., Breskin, A., et al. R&d results on a csi-coated triple thick gem-based photodetector. *Nuclear Instruments and Methods in Physics Research Section A: Accelerators, Spectrometers, Detectors and Associated Equipment*, 639(1):126–129, 2011. ISSN 0168-9002. doi:https://doi.org/10.1016/j.nima.2010.10.033. URL https://www.sciencedirect.com/science/article/pii/S0168900210022722. Proceedings of the Seventh International Workshop on Ring Imaging Cherenkov Detectors.

[Martoiu et al.(2013)] Martoiu, S, Muller, H, Tarazona, A, et al. Development of the scalable readout system for micro-pattern gas detectors and other applications. *Journal of Instrumentation*, 8(03):C03015–C03015, 2013. doi:10.1088/1748-0221/8/03/c03015.

[Muresan(2007)] Muresan, R. Cherenkov Ring Reconstruction Methods. Technical report, CERN, Geneva, 2007. URL https://cds.cern.ch/record/1057872.

[Nappi and Seguinot(2005)] Nappi, E. and Seguinot, J. Ring imaging Cherenkov detectors: The state of the art and perspectives. *Riv. Nuovo Cim.*, 28(8-9):1–130, 2005. doi:10.1393/ncr/i2006-10004-6.

[Ntekas(2016)] Ntekas, Konstantinos. Performance characterization of the Micromegas detector for the New Small Wheel upgrade and Development and improvement of the Muon Spectrometer Detector Control System in the ATLAS experiment. 2016. URL http://cds.cern.ch/record/2143887. Presented 2016.

[Ortec(1970)] Ortec. Instruction Manual 452 Spectroscopy Amplifier. 1970.

[Pedregosa et al.(2011)] Pedregosa, Fabian, Varoquaux, Gaël, Gramfort, Alexandre, et al. Scikit-learn: Machine learning in python. *Journal of Machine Learning Research*, 12(85):2825–2830, 2011. URL http://jmlr.org/papers/v12/pedregosa11a.html.

[Pinto(2010)] Pinto, Serge Duarte. Micropattern gas detector technologies and applications, the work of the RD51 collaboration. 2010. doi:10.1109/NSSMIC.2010.5873870.

[Radhakrishnan(1947)] Radhakrishnan, T. The dispersion, birefringence and optical activity of quartz. *Proc. Indian Acad. Sci. 25, 260-265*, 1947.

[Raether(1964)] Raether, H. *Electron Avalanches and Breakdown in Gases*. Butterworths advanced physics series, 1964.

[Rajani et al.(2010)] Rajani, K. V., Daniels, S., McNally, P. J., et al. Ultrathin chromium transparent metal contacts by pulsed dc magnetron sputtering. *physica status solidi (a)*, 207(7):1586–1589, 2010. doi:https://doi.org/10.1002/pssa.200983732. URL https://onlinelibrary.wiley.com/doi/abs/10.1002/pssa.200983732.

[Ratcliff(2003)] Ratcliff, Blair N. Imaging rings in ring imaging cherenkov counters. *Nuclear Instruments and Methods in Physics Research Section A: Accelerators, Spectrometers, Detectors and Associated Equipment*, 502(1):211–221, 2003. ISSN 0168-9002. doi:https://doi.org/10.1016/S0168-9002(03)00276-6. URL https://www.sciencedirect.com/science/article/pii/S0168900203002766. Experimental Techniques of Cherenkov Light Imaging. Proceedings of the Fourth International Workshop on Ring Imaging Cherenkov Detectors.

[Rojas(1996)] Rojas, Raúl. *Neural Networks*. Springer Berlin Heidelberg, 1996. doi:10.1007/978-3-642-61068-4.

[Rolandi et al.(2008)] Rolandi, Luigi, Riegler, Werner, and Blum, Walter. *Particle Detection with Drift Chambers*. Springer Berlin Heidelberg, 2 edition, 2008. ISBN 978-3-540-76683-4. doi:10.1007/978-3-540-76684-1. URL http://link.springer.com/10.1007/978-3-540-76684-1.

[Seguinot and Ypsilantis(1977)] Seguinot, J. and Ypsilantis, T. Photo-ionization and cherenkov ring imaging. *Nuclear Instruments and Methods*, 142(3):377–391, 1977. ISSN 0029-554X. doi:https://doi.org/10.1016/0029-554X(77)90671-1. URL https://www.sciencedirect.com/science/article/pii/0029554X77906711.

[Smirnov(2005)] Smirnov, I. Heed - modeling of ionization produced by fast charged particles in gases. 2005. URL http://ismirnov.web.cern.ch/ismirnov/heed.

[Sohl et al.(2020)] Sohl, L., Aune, S., Bortfeldt, J., et al. Single photoelectron time resolution studies of the picosec-micromegas detector. *Journal of Instrumentation*, 15(04):C04053, 2020. doi:10.1088/1748-0221/15/04/C04053. URL https://dx.doi.org/10.1088/1748-0221/15/04/C04053.

[Sohl(2020)] Sohl, Lukas. Overview on recent picosec-micromegas developments and performance tests. In *RD51 Miniweek*. 2020.

[Strasser(2021)] Strasser, Timo. Simulations and angle reconstruction for a cherenkov positionsensitive micromegas. 2021. URL https://www.etp.physik.uni-muenchen.de/publications/bachelor/download_auth_etp/bac21_tstrasser.pdf.

[The National Institute of Standards and Technology()] The National Institute of Standards and Technology. The National Institute of Standards and Technology (NIST). URL https://www.nist.gov/pml/xcom-photon-cross-sections-database.

[Thorlabs(2017)] Thorlabs. GaP photodiode - UV wavelength. 2017. URL https://www.thorlabs.de/drawings/528bae729314cc14-3DEFBDEC-B709-F3CC-47F574C8C98448DC/FGAP71-SpecSheet.PDF.

[Townsend(1910)] Townsend, T.S. *The Theory of Ionization of Gases By Collision*. Constable & Company Ltd, 1910.

[Va'vra et al.(1997)] Va'vra, J., Breskin, A., Buzulutskov, A., et al. Study of csi photocathodes: volume resistivity and ageing. *Nuclear Instruments and Methods in Physics Research Section A: Accelerators, Spectrometers, Detectors and Associated Equipment*, 387(1):154–162, 1997. ISSN 0168-9002. doi:https://doi.org/10.1016/S0168-9002(96)00980-1. URL https://www.sciencedirect.com/science/article/pii/S0168900296009801. New Developments in Photodetection.

[Veenhof(1998)] Veenhof, Robert. Garfield, recent developments. *Nuclear Instruments and Methods in Physics Research Section A, 419, 726-730*, 1998.

[Vladimirov et al.(2001)] Vladimirov, S. V., Kaftanov, V. S., Nilov, A. F., et al. Characteristics of baf2 scintillation crystals. *Atomic Energy*, 90(1):55–62, 2001. ISSN 1573-8205. URL https://doi.org/10.1023/A:1011391923801.

[Yonenaga(2020)] Yonenaga, Masanobu. *Particle Identification using the Aerogel RICH Counter at the Belle II Experiment*. Ph.D. thesis, Hachioji, Tokyo Metropolitan University, Hachioji, 2020. Presented on 31 08 2020.

[Zinth and Zinth(2018)] Zinth, Wolfgang and Zinth, Ursula. *Optik*. De Gruyter, 2018. doi:10.1515/9783110495034.

Acknowledgments

After so many pages, you likely want to get to know the stars of this Ph.D. thesis. Unfortunately, due to this page's limited space, it is impossible to mention all of my colleagues, friends, and family. Now I dearly want to thank:

- ... Prof. Dr. Otmar Biebel, who allowed me to write my bachelor, master, and Ph.D. thesis in the detector physics group. Our coffee discussions on physics were engaging, and inputs for my thesis were invaluable. I also appreciate his unwavering support during the difficult times of the pandemic.
- ... Prof. Dr. Thomas Kuhr, who agreed to write the second review of my thesis.
- ... Dr. Ralf Hertenberger for possibly working on the CHMM and for many important inputs, fruitful discussions, and a helping hand. As well as many fun discussions about bicycles and the Giro.
- ... Roman Gernhaeuser and Sonja Winkler for the evaporation of the Crystal substrate and Thomas Klemenz for using the transmission measurement setup at TUM.
- ... Juergen Friese for valuable input about RICH detectors and for borrowing the MAPMT from Christian Pauly at GSI.
- ... Timo, Sebastian, and Edis were exceptional bachelor students who supported my thesis. Their contributions will always be remembered.
- ... Nikolai Hartmann for helping me do some fun stuff with machine learning.
- ... Christoph for proofreading my thesis.
- ... Makis saving me in dire times with a beautiful cookie
- ... our great hardware group, which is also one of the main reasons I looked forward to arriving every day at Garching for a coffee (or Radler): Christoph, Fabian, Katrin, Alex Lory and Stefanie :)
- ... of course, I also want to thank our Hardware group veterans: Bernhard, Ralph, Phillip, Maximilian H., Felix K.
- ...of course, also the rest of the veterans, especially the analysis people (alumni) of the LS Schaile, for a good time during my master thesis and Ph.D. thesis!
- ... all of my friends, however, especially Mathias, who also supported me emotionally during this time of my Ph.D. and Corona, who I could join for a lot of my greatest road biking trips, and Patrick, with whom I had fun commuting rides to Garching as well as our Meddleearth group led by Moritz.
- ... my parents, Gerhard and Michaela, who supported me the whole time during my studies at LMU.
- ... I want to thank the many zip ties which "hang everything together" - especially cable salad - and the roles of Panzertape that gave their lives in an effort to make a great detector setup.

Declaration of academic integrity

Development of an Inverted Ring Imaging Cherenkov Micromegas

selbständig verfasst zu haben und keine anderen als die angegebenen Quellen und Hilfsmittel verwendet zu haben.

Maximilian Paul Rinnagel

Munich, Juni 7, 2023